NASA
Technical
Paper
2205

November 1983

Investigation of Installation Effects on Twin-Engine Convergent-Divergent Nozzles

E. Ann Bare and
Bobby L. Berrier

NASA

25
25th Anniversary
1958-1983

NASA
Technical
Paper
2205

1983

Investigation of Installation Effects on Twin-Engine Convergent-Divergent Nozzles

E. Ann Bare and
Bobby L. Berrier

Langley Research Center
Hampton, Virginia

INTRODUCTION

Most current operational military aircraft have been designed for efficient subsonic cruise and subsonic-transonic maneuverability, whereas supersonic performance has been considered a "fallout" or off-design condition. Analysis of the air operations during recent conflicts indicates considerable aircraft vulnerability over enemy territory; one method proposed to reduce aircraft vulnerability is to provide efficient supersonic cruise capability to future combat aircraft (ref. 1). Supersonic cruise with reduced engine power (dry or partial afterburning) has been suggested as one method of improving supersonic cruise efficiency. Results of parametric wind-tunnel investigations of convergent-divergent nozzles applicable to supersonic cruise military aircraft have been reported in references 2 and 3. The nozzles of reference 2 were mounted on an isolated nacelle with no afterbody closure ahead of the nozzle and no control surfaces present. Past experimental investigations (refs. 4 to 6) on current high performance fighter aircraft have shown that sizable airplane performance penalties are associated with the installation of the propulsion system into the airframe. Adverse interference effects originating from empennage surfaces have been found to be a major contributor to the afterbody/nozzle drag problem (refs. 6 to 10), especially when the nozzle operates in a closed-down, low-power (dry or partial afterburning) mode. (See ref. 7.) The installation effects, including empennage interference, on single-engine convergent-divergent nozzles are examined in reference 3. For the investigation of reference 3, six reduced-power nozzle configurations, investigated previously on an isolated nacelle and reported in reference 2, were tested on a typical single-engine fighter afterbody model. Twin-engine nozzle installations create the additional complexities of mutual nozzle/jet exhaust interference effects, interfairings, and/or base regions between the nozzles and often additional vertical tail surfaces.

An experimental investigation was conducted to examine installation effects on twin-engine convergent-divergent nozzles applicable to reduced-power supersonic cruise aircraft. For the current investigation, six reduced-power nozzle configurations, investigated previously on an isolated nacelle and a typical single-engine fighter afterbody model (refs. 2 and 3, respectively), were selected for installation on a typical twin-engine fighter afterbody model. The effects of nozzle geometry (length and closure) and empennage surface location on twin-engine aft-end drag were investigated.

The investigation was conducted in the Langley 16-Foot Transonic Tunnel at Mach numbers from 0.50 to 1.20 with nozzle throat areas corresponding to dry power and partial afterburning power. Nozzle pressure ratio was varied from 1.0 (jet off) up to approximately 8.0, depending on Mach number, and angle of attack was varied from -5° to 9° at selected Mach numbers. The horizontal tails were tested in mid and aft afterbody axial locations and the twin vertical tails were tested in forward and mid afterbody axial locations.

A_{an} area of annular clearance gap between inner and outer nozzle parts at model base, m^2

A_e nozzle exit area, m^2

A_{fus} maximum cross-sectional area of model fuselage, $0.0317 \ m^2$

A_o total internal area of outer nozzle exit opening, m^2

A_{seal} cross-sectional area enclosed by metric break seal, $0.0297 \ m^2$

A_t nozzle throat area, m^2

C_D drag coefficient

$C_{D,a}$ afterbody drag coefficient, $\dfrac{D_a}{q_\infty S}$

$C_{D,n}$ nozzle drag coefficient, $\dfrac{D_n \text{ (both nozzles)}}{q_\infty S}$

$C_{D,n,one}$ nozzle drag coefficient, $\dfrac{D_n \text{ (one nozzle)}}{q_\infty S}$

$C_{D,t}$ total aft-end drag coefficient, $\dfrac{D_t}{q_\infty S}$

$C_{D,tails}$ tail drag coefficient, $\dfrac{D_{tails}}{q_\infty S}$

$\Delta C_{D,ia}$ increment in empennage interference-drag coefficient on afterbody

$\Delta C_{D,in}$ increment in empennage interference-drag coefficient on nozzle

$\Delta C_{D,it}$ increment in empennage interference-drag coefficient on total aft end

C_L lift coefficient

$C_{L,n}$ nozzle lift coefficient, $\dfrac{L_n \text{ (both nozzles)}}{q_\infty S}$

$C_{L,t}$ total aft-end lift coefficient, $\dfrac{L_t}{q_\infty S}$

C_p nozzle static-pressure coefficient, $\dfrac{p_n - p_\infty}{q_\infty}$

D_a afterbody drag, N

2

D_{bal} drag measured by balance, positive downstream, N

D_n nozzle drag (pressure + friction), N

D_t total aft-end (afterbody + nozzles + tails) drag, N

D_{tails} tail drag, N

d_b base diameter of nozzle at exit, m

d_e nozzle exit diameter, m

d_m maximum diameter of nozzle, m

d_t nozzle throat diameter, m

L_n nozzle lift, N

L_t total aft-end (afterbody + nozzles + tails) lift, N

ι nozzle length from connect station (FS 165.63) to exit, m

ι_f axial length of nozzle divergent flap (axial distance between nozzle throat and exit), m

M free-stream Mach number

NPR nozzle pressure ratio $\left(\text{ratio of jet total pressure to free-stream static pressure } \dfrac{P_{t,j}}{P_\infty}\right)$

$(NPR)_{des}$ design nozzle pressure ratio (NPR for fully expanded jet exhaust flow)

P_{an} local pressure at nozzle annular clearance gap, N/m^2

P_{es} local static pressure external to the metric break seal, N/m^2

P_{int} local internal static pressure, N/m^2

P_n nozzle external static pressure, N/m^2

$P_{t,j}$ jet total pressure, N/m^2

P_∞ free-stream static pressure, N/m^2

q_∞ free-stream dynamic pressure, N/m^2

S wing reference area, $0.429 \, m^2$

t/c empennage surface thickness ratio (ratio of local maximum thickness to local chord)

x	axial distance from nozzle connect station (FS 165.63), positive downstream, m
α	angle of attack, deg
β	nozzle terminal boattail angle, deg
δ	nozzle divergence angle, deg
θ	nozzle approach angle to throat, deg
Λ_{le}	sweep angle at leading edge, deg
ϕ	meridian angle about nozzle center line (positive for clockwise direction about left-hand nozzle and positive for counterclockwise direction about right-hand nozzle; $\phi = 0°$ at top of each nozzle), deg

Abbreviations:

A/B	afterburning
BL	buttock line
FS	fuselage station
fwd	forward
part	partial
R	radius
sub.	subsonic
super.	supersonic
WL	water line

APPARATUS AND METHODS

Wind Tunnel

The experimental investigation was conducted in the Langley 16-Foot Transonic Tunnel. This tunnel is a single-return atmospheric tunnel with a slotted octagonal test section and continuous air exchange. The wind tunnel has a variable airspeed up to a Mach number of 1.30. Test-section plenum suction is required for speeds above a Mach number of 1.10. A complete description of this facility and operating characteristics can be found in reference 11.

Model and Support System Description

Photographs of the model and support system installed in the Langley 16-Foot Transonic Tunnel are shown in figure 1 and a sketch of the twin-engine fighter model and a portion of the wing-tip-mounted support system is presented in figure 2. A

complete sketch and description of the wing-tip-mounted (or bifurcated sting) support system can be found in reference 11. With the exception of the nozzle hardware, the twin-engine model used for this investigation was utilized previously for an investigation on empennage interference effects (ref. 12). An external high-pressure air supply provides the model with a continuous flow of clean dry air at a controlled temperature of about 360 K, which is used to simulate exhaust flow over a range of jet total pressure. Sketches with important dimensions of the model aft-end components (afterbody, nozzles, and tails) are shown in figure 3.

The bifurcated sting model support system shown in figure 2 consisted of three major portions: the twin support booms, the forebody (nose), and the wing/centerbody. These pieces made up the nonmetric portion (that portion of the model not mounted on the force balance) of the twin-engine fighter model. The centerbody (fuselage) was essentially rectangular in cross section having a constant width and height of 25.40 cm and 12.70 cm, respectively. The four corners were rounded by a radius of 2.54 cm. Maximum cross-sectional area of the centerbody (fuselage) was 317.04 cm^2. The support-system forebody (or nose) was typical of a powered model in that the inlets were faired over. The "wings" of the support system were mounted above the model center line or in a "high wing" position which is also typical of many current fighter designs. The support system wing has a 45° leading-edge sweep, a taper ratio of 0.5, an aspect ratio of 2.4, and a cranked trailing edge. The airfoil was symmetrical and the thickness ratio near the wing fuselage junction at BL 12.70 was realistic (approximately $t/c = 0.067$) to provide as realistic a wake as possible on the model afterbody. From BL 27.94 to the support booms, however, wing thickness ratio increased from $t/c = 0.077$ to $t/c = 0.10$ to provide structural support for the model and to permit transfer of compressed air from the booms to the model propulsion system.

The twin-engine afterbody shown in figure 3(a) was attached to the support-system wing/centerbody by mounting on a six-component strain-gage balance as shown. The term "aft end," as used in this paper, is the metric portion of the model (that portion of the model on which forces and moments are measured) beginning at the metric break seal station (FS 120.04) and includes the afterbody, outer nozzles, and empennage surfaces when present. Note that the model propulsion system (thrust) forces and moments were not measured by the balance as the propulsion system was grounded to the model support system and clearance was provided between the metric and nonmetric portions of the model. A Du Pont Teflon strip inserted in grooves machined in the nonmetric forebody and the metric afterbody was used as a seal to prevent external flow from entering the model. The afterbody lines were chosen to be typical of current close-spaced twin-engine fighter designs and also to fair the afterbody smoothly from the constant cross section of the centerbody down to the nozzles and house the afterbody balance, propulsion simulation system, and related instrumentation.

Figure 3(b) presents a sketch and table giving geometry of the axisymmetric nozzles tested. Nozzle geometries for this investigation simulated two (short, $\iota \approx 8$ cm, and long, $\iota \approx 11$ cm) variable-geometry, convergent-divergent nozzle designs typical of those currently in use on fighter aircraft. However, these nozzles have a larger range of nozzle expansion ratio A_e/A_t in order to satisfy supersonic mission requirements. Each nozzle length was tested at dry power setting with two different nozzle expansion ratios, one ($A_e/A_t = 1.22$) representing subsonic cruise nozzle geometry and the other ($A_e/A_t = 2.24$) representing supersonic cruise nozzle geometry. In addition, the supersonic cruise nozzle expansion ratio was also tested at partial afterburning power setting (larger throat area A_t) for each nozzle length. To isolate the effect of installation (afterbody closure) on nozzle drag,

the six nozzle configurations used for the current investigation were selected from nozzle configurations tested previously on an isolated nacelle (no afterbody closure or empennage surfaces). These results are reported in reference 2. External geometry of the nozzles utilized for the current test duplicated the external geometry of the nozzles selected from reference 2. However, because the balance arrangement of the current investigation required a nominal 0.19-cm annular clearance gap at the nozzle exit to prevent balance-to-model fouling, the nozzle configurations shown in figure 3(b) required a thicker base $(d_b - d_e)$ at the nozzle exit and small changes to nozzle internal geometry $(A_e, A_t,$ and $\delta)$ from the nozzles reported in reference 2. However, nozzle expansion ratio A_e/A_t, which affects exhaust plume shape, was duplicated. The nozzle configurations of the current investigation have also been tested on a typical single-engine fighter afterbody with empennage surfaces, and results from this investigation are reported in reference 3.

One of the objectives of this investigation was to determine the effects of empennage surface location on twin-engine aft-end aerodynamic characteristics. The afterbody had provisions for mounting both the twin vertical tails and the horizontal tails in two axial locations as illustrated in figure 3(c). Forward and mid axial locations of the twin vertical tails were tested; mid and aft axial locations of the horizontal tails were tested.

Sketches of the vertical and horizontal tail surfaces are shown in figures 3(d) and 3(e). These tail surfaces were sized to be representative of current twin-engine fighter aircraft designs. As indicated in the tail sketches, individual root fairings contoured the tails to the afterbody at each tail location. As indicated in figure 3(d) and shown in figures 1(c) and 2, the twin vertical tails were canted outboard 20°. Data from reference 12 indicate that this tail cant angle generally provides lower aft-end drag.

Instrumentation

External aerodynamic forces and moments on the model aft end (including empennage surfaces and outer nozzles) were measured with a six-component strain-gage balance. Forces and moments on the propulsion simulation system (thrust) were not measured.

Eight external seal static-pressure orifices were located in the metric break gap area between the centerbody and afterbody and are denoted p_{es} in figure 3(a). In addition, two internal pressure orifices p_{int} located in the model cavity and eight pressure orifices p_{an} located in the annular gap between inner and outer nozzles were used to measure internal pressures in the model. These pressures were used to correct the balance measurements for pressure-area tares as discussed in the section "Data Reduction."

Each internal nozzle was instrumented with two total-pressure probe rakes located 180° apart and staggered to prevent appreciable flow blockage as shown in figure 3(b). Each rake contained two total-pressure probes. An additional probe was located in each nozzle and contained a thermocouple which was used for the measurement of total temperature.

The outer nozzles each had three rows of external pressure orifices (with five pressure orifices in each row) for measurement of external pressure distributions on the nozzles. Pressure orifice locations are given in figure 4. Note that ϕ is defined differently for left- and right-hand nozzles such that a given value of ϕ

on either nozzle places that row of external orifices in the same location relative to the empennage surfaces and afterbody interfairing.

Tests

Data were obtained at an angle of attack of 0° at Mach numbers from 0.50 to 1.20. Nozzle pressure ratio (ratio of jet total pressure to free-stream static pressure) was varied from approximately 1.0 (jet off) to about 8.0, depending on Mach number. In addition, at Mach numbers of 0.50, 0.90, and 1.20, data were obtained over an angle-of-attack range of -5° to 9° at a nozzle pressure ratio representing typical operating conditions for each Mach number. Reynolds number based on model length varied from approximately 1.62×10^7 at $M = 0.50$ to 2.25×10^7 at $M = 1.20$. All configurations were tested with fixed boundary-layer transition strips on the model nose and wings and on the afterbody empennage surfaces. A 0.254-cm-wide strip of No. 120 silicon carbide grit was located 2.54 cm from the nose of the forebody. Transition strips 0.254 cm wide of No. 120 silicon carbide grit were located 1.27 cm streamwise from the leading edge of the wing and empennage surfaces.

Data Reduction

Data for both model and wind-tunnel test instrumentation were recorded simultaneously on magnetic tape. At each test point, 50 samples of data were recorded over a 5-second period. The samples were averaged; these average values were used for all computations.

Total aft-end drag was measured directly from the six-component strain-gage balance but was corrected for various pressure area terms. Total aft-end drag was computed from the following equation:

$$D_t = D_{bal} - \sum (p_{es} - p_\infty)(A_{fus} - A_{seal}) - \sum (p_{int} - p_\infty)(A_{seal} - A_o)$$

$$- \sum (p_{an} - p_\infty)A_{an} \tag{1}$$

The first two pressure-area terms correct for D_{bal} forces measured by the balance. The last term in equation (1) is not actually measured by the balance but is used to account for the annulus between the internal and external nozzle hardware.

Nozzle drag of both nozzles D_n was obtained by adding nozzle pressure drag to a computed nozzle skin-friction drag. Nozzle pressure drag was determined by integration of nozzle pressure distributions over the nozzle surface area. Nozzle skin-friction drag was computed with the method of Frankl and Voishel as described in reference 13.

Vertical and horizontal tail drag was defined to be the sum of form drag plus skin-friction drag for $M < 0.90$ and wave drag plus skin-friction drag for $M > 1.00$. Skin-friction drag and wave drag were computed by using the methods of

references 13 and 14. The subsonic form factors for the tails were calculated with the following equation from reference 12:

$$\text{Form factor} = 1 + 1.44(t/c) + 2(t/c)^2 \tag{2}$$

The individual root fairings required for each tail location were also figured into the skin-friction and wave-drag calculations. With the use of previously determined drag components, afterbody drag D_a was obtained from the following equation:

$$D_a = D_t - D_n - D_{tails} \tag{3}$$

The tail interference terms used in this report are consistent with those used in references 3 and 7. The total interference increment on the aft end was determined from

$$\Delta C_{D,it} = (C_D)_{tails\ on} - (C_D)_{tails\ off} - C_{D,tails} \tag{4}$$

where $(C_D)_{tails\ on}$ is the measured total aft-end drag for a given configuration, $(C_D)_{tails\ off}$ is the measured aft-end drag for the same configuration with the tails removed, and $C_{D,tails}$ is the computed value of tail drag as discussed previously. Positive values of $\Delta C_{D,it}$ indicate adverse interference effects on aft-end drag. The empennage interference effects on the nozzles were found from the following equation:

$$\Delta C_{D,in} = (C_{D,n})_{tails\ on} - (C_{D,n})_{tails\ off} \tag{5}$$

where the nozzle drags are integrated pressure distributions over the nozzle surface. The empennage interference increment on the afterbody alone was then defined to be the difference between the empennage interference increments on the total aft end and the nozzles alone or

$$\Delta C_{D,ia} = \Delta C_{D,it} - \Delta C_{D,in} \tag{6}$$

It should be noted that any interference effects on the tails themselves (tail on tail or afterbody/nozzle on tail) are included in the afterbody interference drag term $\Delta C_{D,ia}$. Also, because of drag due to lift, empennage interference terms were computed at nominal values of $\alpha = 0°$ only.

The total aft-end lift coefficient $C_{L,t}$ was computed from the balance data after the model angle of attack was corrected for model support deflections and tunnel upflow. No pressure-area corrections are necessary to obtain model aft-end lift coefficients. Nozzle lift coefficient $C_{L,n}$ was obtained from a pressure-area integration by using measured nozzle static pressures over the external surface of the nozzle.

PRESENTATION OF RESULTS

The results of this investigation are presented in plotted coefficient form in figures 5 to 37, which are organized as follows:

Drag and lift coefficient data:

Nozzle length	Power setting	A_e/A_t	Location of horizontal tails	Location of vertical tails	Figure for – Drag	Figure for – Lift
Short	Dry	1.22	Off	Off	5(a)	11(a)
			Mid	Forward	5(b)	11(b)
			Mid	Mid	5(c)	11(c)
			Aft	Mid	5(d)	11(d)
Long	Dry	1.22	Off	Off	6(a)	12(a)
			Mid	Mid	6(b)	12(b)
			Aft	Mid	6(c)	12(c)
Short	Dry	2.24	Off	Off	7(a)	13(a)
			Mid	Forward	7(b)	13(b)
			Aft	Forward	7(c)	13(c)
			Mid	Mid	7(d)	13(d)
			Aft	Mid	7(e)	13(e)
Long	Dry	2.24	Off	Off	8(a)	14(a)
			Mid	Mid	8(b)	14(b)
			Aft	Mid	8(c)	14(c)
Short	Partial A/B	2.24	Off	Off	9(a)	15(a)
			Mid	Mid	9(b)	15(b)
			Aft	Mid	9(c)	15(c)
Long	Partial A/B	2.24	Off	Off	10(a)	16(a)
			Mid	Mid	10(b)	16(b)
			Aft	Mid	10(c)	16(c)

Figure

Nozzle static-pressure distributions:

Effect of nozzle closure (d_b/d_m):
Short nozzles, tails off 17

Effect of nozzle length:
Subsonic dry power nozzles, tails off 18
Supersonic partial A/B power nozzles, tails off 19

Effect of nozzle pressure ratio:
Short subsonic dry power nozzles, tails on 20
Long supersonic dry power nozzles, tails on 21

9

DISCUSSION

Basic Data

Figures 5 through 10 present total aft-end drag coefficient and nozzle drag coefficient for each test configuration. On the left side of each figure, the drag coefficients are presented as a function of nozzle pressure ratio at a nominally constant angle of attack of 0°; on the right side of each figure, as a function of angle of attack at a nominally constant value of nozzle pressure ratio (typical operating NPR for each Mach number). Note that data were not obtained at angles of attack other than 0° at M = 0.80 and 0.85. Total aft-end lift coefficient and nozzle lift coefficient in the same presentation format are shown in figures 11 through 16. Total aft-end coefficients, which include afterbody, nozzle, and empennage (when installed) contributions, were obtained from force balance measurements. Nozzle coefficients were obtained from pressure-area integrations and skin-friction drag calculations.

Nozzle drag and lift coefficients.- Nozzle drag coefficients shown in figures 5 through 10 exhibit similar trends as noted in previous studies (refs. 2 and 3). A significant drag reduction generally occurs with initial jet operation due to a base-bleed effect. Drag then increases with increasing NPR due to the aspiration caused by the pumping action of the jet exhaust. Depending on configuration and Mach number, a maximum jet-on nozzle drag occurs between NPR of 2.0 and 5.0 after which

nozzle drag decreases with increasing nozzle pressure ratio as exhaust plume blockage effects become dominant with the compression region at the nozzle exit increasing in strength. There is no appreciable effect of angle of attack on nozzle drag except at M = 1.20, where small increases in nozzle drag generally occurred with increasing angle of attack.

Pressure recovery on the short and long dry power subsonic nozzles was, in general, sufficient to create thrust (negative drag) on the nozzle boattail surface at subsonic speeds. (See figs. 5 and 6.) Negative drag was measured on the other nozzle configurations at only a few of the subsonic test conditions. Nozzle drag was positive for all configurations at M = 1.20.

Nozzle lift coefficient (figs. 11 through 16) is essentially zero and is unaffected by either nozzle pressure ratio or angle of attack.

Total aft-end drag and lift coefficients.- Total drag coefficient showed basically the same trends with NPR as nozzle drag coefficient. Trends of total aft-end drag with varying angle of attack exhibit typical "drag polar" curves. Since nozzle drag was unaffected by varying angle of attack, the variations shown for total aft-end drag must be attributed to variations in afterbody drag ahead of the nozzle and drag due to lift on the horizontal tails (when installed). As might be expected for the tail-off configurations (fig. 5(a)), the drag polar curves are relatively flat for these configurations except at M = 1.20. For tail-off configurations, minimum total aft-end drag coefficient occurred at angles of attack between 3° and 6° at M < 0.90 and at an angle of attack of 0° at M = 1.20. For tail-on configurations, minimum total drag coefficient occurred near $\alpha = 0°$ at all test conditions except M = 0.90. At M = 0.90, the minimum tail-on total drag usually occurred at a small negative angle of attack ($\alpha \approx -3°$). This shift in angle of attack for minimum drag is probably caused by a different downwash flow field from the support wing at M = 0.90, which results in a significant change in horizontal tail drag due to lift at any given angle of attack. Further evidence of a different downwash flow field at M = 0.90 is indicated by the large shift in angle of attack for zero total lift when compared with data at M = 0.50 and 1.20. (See fig. 11(b).)

Nozzle pressure ratio has essentially no effect on total lift coefficient (figs. 11 through 16). Angle of attack has little or no effect on total lift coefficient of tail-off configurations except at M = 1.20. At M = 1.20, lift increases with increasing angle of attack; since nozzle lift coefficient was independent of angle of attack, this lift increase must occur on the afterbody ahead of the nozzle. Total lift coefficient of tail-on configurations exhibits typical effects of angle of attack; that is, lift increases with increasing angle of attack. However, it should be noted that total lift coefficient data at a Mach number of 0.90 generally show large nonlinearities with increasing angle of attack.

Pressure Distributions

Nozzle closure.- The effect of nozzle closure d_b/d_m on nozzle pressure distributions is presented in figure 17. The data for subsonic dry power nozzle ($d_b/d_m = 0.557$) show a strong external flow expansion near the beginning of the nozzle boattail followed by downstream pressure recovery sufficient to produce negative drag (thrust) at subsonic speeds, as previously discussed. At M = 1.20, the strong external flow expansion over this nozzle results in a standing shock on the nozzle boattail and probable flow separation downstream of the shock. A decrease in closure (supersonic dry power nozzle, $d_b/d_m = 0.752$) decreases the magnitude of the initial

external flow expansion and also decreases the strength of downstream pressure recovery. Pressure recovery is still sufficient at some test conditions (fig. 17(b), M = 0.90) to produce negative drag (fig. 7(a)). The data for supersonic partial A/B power nozzle (d_b/d_m = 0.901) show a weak compression region followed by acceleration of the flow down the nozzle boattail. The weak compression region is caused by a small cusp in the external geometry at the afterbody/nozzle connect station (FS 165.63).

With the exception of the pressure distribution at ϕ = 90° on the subsonic dry power nozzle, all rows of pressure distributions on each nozzle at each Mach number exhibit similar trends. For the subsonic dry power nozzle, data at ϕ = 90° indicate an extensive separation region between the twin nozzles, especially at M > 0.90.

Nozzle length.- Figures 18 and 19 show typical effects of nozzle length on nozzle pressure distributions. In general, increasing nozzle length (which, for a given nozzle power setting and expansion ratio, results in a smaller nozzle boattail angle) increases nozzle static pressures and should result in reduced nozzle drag at most test conditions. The beneficial effect of increasing nozzle length is most pronounced in the external flow expansion region on the subsonic dry power nozzle. (See fig. 18.) The effect of nozzle length on the supersonic partial A/B power nozzle is small except at M = 1.20. (See fig. 19.) The reason for the reduced influence of nozzle length on the nozzle with a higher power setting is clear from examination of the nozzle geometry table in figure 3(b). Increasing nozzle length of the subsonic dry power nozzle reduced nozzle boattail angle (slope) by 6°; a similar increase in nozzle length on the supersonic partial A/B power nozzle resulted in only a 1° reduction in nozzle boattail angle.

It should be noted that effects resulting from changes in nozzle operating conditions or external geometry can feed forward onto the afterbody ahead of the nozzle, especially at subsonic speeds. Thus, although trends of nozzle drag can be hypothesized from nozzle static-pressure distributions, the effect of these changes on total drag must await discussion of the balance data in later sections.

Nozzle pressure ratio.- The effect of NPR on nozzle static-pressure distributions is presented in figures 20 and 21. Jet effects, although small, feed forward over the entire nozzle boattail of both configurations at subsonic speeds. Only the magnitude of pressure is changed and not the shape of the distribution. At M = 1.20, jet effects on the subsonic dry power nozzle are limited to the separated subsonic flow region downstream of the boattail shock. Jet effects on the supersonic dry power nozzle at M = 1.20 are generally limited to the aftmost pressure orifice location (x/ι = 0.95), since downstream disturbances cannot feed forward in supersonic flow except through the boundary layer.

The pressure distributions at ϕ = 45° and 90° which are between the twin nozzles show a difference in behavior with varying NPR at M = 1.20. As discussed previously, a large separated flow region appears to exist between the twin nozzles. Thus, at M = 1.20, jet effects between the nozzles feed almost to the nozzle connect station for the subsonic dry power nozzle and as far upstream as x/ι = 0.514 for the supersonic dry power nozzle.

Empennage arrangement.- The effect of empennage arrangement on nozzle static-pressure distributions is shown in figure 22 for the short subsonic dry power nozzles and in figure 23 for the short supersonic dry power nozzles. It should be noted that results from reference 3 indicate that tail surfaces have a larger impact on after-

body static pressures ahead of the nozzle than on the nozzle itself. Unfortunately, the current model had no afterbody static-pressure instrumentation. The effect of empennage arrangement on total aft-end drag is discussed in a later section.

Examination of figures 22 and 23 indicates that the effects of tail surfaces on nozzle static-pressure distributions at low subsonic speeds (M = 0.50) are generally limited to a small portion of the nozzle located directly behind the tail surfaces (ϕ = 270° and 315°). Data at ϕ = 180° indicate little effect of tail surfaces. As Mach number is increased to transonic and low supersonic speeds, the effects of tail surfaces on nozzle static pressures tend to spread around the nozzle circumference. At M = 1.20, varying empennage arrangement causes large variations in nozzle static pressure around the entire nozzle circumference. (See ϕ = 90° and 180°.)

For the twin-engine afterbody model tested, horizontal tail surface location appears to be the dominant factor influencing nozzle static-pressure level. The mid horizontal tail location (fig. 3(c)) generally has a desired higher nozzle static pressure for tail-on configuration than for tail-off configuration, whereas the aft horizontal tail location generally has an adverse effect on nozzle static pressures. This result is particularly evident on the forward portion (x/ι = 0.0 to 0.5) of the nozzles at M < 0.90. Although these trends were generally independent of vertical tail location, it should be noted that an aft vertical tail location, which reference 7 indicates has a larger impact on nozzle pressures, was not tested during the current investigation.

Aft-End Drag Characteristics

To simplify data analysis, drag data have been cross-plotted at selected nozzle pressure ratios. A typical variation of turbofan-engine nozzle pressure ratio with Mach number is presented in figure 24. This particular schedule was used for comparison purposes in the current investigation.

For the summary figures shown hereafter, cross-plotted values of total aft-end (afterbody, nozzles, and tails) drag, nozzle drag (both nozzles), afterbody drag, and tail drag are presented as a function of Mach number. Also presented are empennage interference-drag coefficient increments on the total aft end, nozzle, and afterbody. All data in the summary figures are at α = 0°.

The nozzle geometries used for the current twin-engine investigation were the same (except for scale) as those investigated on a single-engine configuration reported in reference 3. Several general observations can be made by comparing the data in this report with those in reference 3 and, also, reference 7, which reports the investigation of similar nozzles on a single-engine model. First, the trends of aft-end drag with varying empennage arrangement are not as obvious and consistent on the current twin-engine configurations as observed on the single-engine configurations. Second, tail drag and afterbody drag generally constitute a larger percentage of total aft-end drag on the twin-engine configuration than on the single-engine configuration (note that the twin-engine configuration had twin vertical tails). Last, at subsonic and transonic speeds, empennage interference drag is a larger percentage of total aft-end drag (afterbody, nozzle, and tails) on the twin-engine configuration than on the single-engine configuration. These observations suggest that the complex geometry and flow field of a multiengine configuration probably cause a more difficult aft-end integration task for the airplane designer than a typical single-engine configuration. Detailed discussion of the twin-engine data is contained in the following sections.

Empennage arrangement.- Figures 25 through 30 present the effect of empennage arrangement on the aft-end drag coefficient components for each nozzle configuration tested. At subsonic speeds, these data indicate that most aft-end drag originates on the afterbody and tails, although these two components together constitute only a little over one-half the total aft-facing area of each configuration. Although a significant portion of the total aft-facing area consists of nozzle boattail, nozzle drag contributes very little (less than 10 percent of $C_{D,t}$) to total aft-end drag for $M < 0.90$ and at many test conditions actually reduces total aft-end drag (negative nozzle drag). The small contribution of nozzle drag to total drag at subsonic speeds results from good pressure recovery on the dry power nozzles and from a combination of small pressure coefficients and reduced axial projected area on the partial A/B power nozzles. At $M = 1.20$, the total aft-end drag $C_{D,t}$ is more nearly equally divided among the afterbody, tails, and nozzles except for the partial A/B configurations, for which nozzle drag still contributes only a small portion to total aft-end drag.

Empennage interference-drag coefficient increments on the total aft end, nozzle, and afterbody are presented in the (c) part of figures 25 through 30. These increments were determined by the procedures outlined previously in the section entitled "Data Reduction." The increment in empennage interference-drag coefficient on the total aft end $\Delta C_{D,it}$ was generally adverse (positive) for $M < 0.90$ but was favorable (negative) at $M = 1.20$. Favorable empennage interference also occurs on the nozzle for some configurations at $M < 0.90$ and on the afterbody ahead of the nozzles at $M = 1.20$. Similar to the results on single-engine configurations reported in references 3 and 7, these data show that empennage interference can constitute a significant portion of total aft-end drag for twin-engine configurations, particularly in the high subsonic and transonic speed regime. In fact, as mentioned previously, empennage interference drag constitutes a larger percentage of total aft-end drag for twin-engine configurations (figs. 25 through 30) than reported in reference 3 for single-engine configurations. For example, for the short nozzle configurations at $M = 0.90$, empennage interference drag constitutes from 7 to 15 percent of single-engine total aft-end drag (ref. 3), whereas empennage interference drag constitutes from 17 to 32 percent of twin-engine total aft-end drag (figs. 25, 27, and 29). Most empennage interference effects occur on the afterbody ahead of the nozzles (see $\Delta C_{D,ia}$ values), since empennage interference-drag coefficient increments on the nozzles $\Delta C_{D,in}$ were generally small, especially for those nozzles designed for supersonic operation.

Although examination of component drag coefficients and empennage interference-drag coefficient increments provides an insight into the effects of empennage interference, final evaluation of the effect of empennage arrangement must be made on the basis of total aft-end drag $C_{D,t}$. These values can be found on the top half of part (a) of figures 25 through 30. In general, the effects of empennage arrangement on total aft-end drag coefficient were small. In addition, the empennage arrangement for lowest drag was dependent upon Mach number and nozzle configuration. At subsonic speeds, the lowest total aft-end drag was generally obtained on mid horizontal tail configurations. At $M = 1.20$, the lowest total aft-end drag was obtained on aft horizontal tail configurations except when the subsonic design nozzles were installed. With the subsonic design nozzles installed, the lowest aft-end drag was obtained at $M = 1.20$ on the mid horizontal tail configurations.

Nozzle length.- Figures 31 through 33 show the effect of nozzle length on the aft-end drag coefficient components and empennage interference-drag coefficient increments. As previously discussed, the data are plotted against Mach number at the appropriate scheduled nozzle pressure ratio. For all three nozzle designs (subsonic

dry power, supersonic dry power, and supersonic partial A/B power), increasing nozzle length reduced total aft-end drag with the exception of one empennage arrangement with the supersonic partial A/B power nozzles. Increasing nozzle length also decreased nozzle drag of the subsonic dry power nozzle but had little or no effect on nozzle drag for the two supersonic nozzle designs (figs. 32 and 33). The decrease in drag for the subsonic dry power nozzle with increasing nozzle length results from the accompanying decrease in nozzle boattail angle which causes a weaker expansion of the external flow over the nozzle. However, there is a point of diminishing returns for increasing the nozzle length due to the accompanying increase in nozzle friction drag; the supersonic partial A/B power nozzles (fig. 33(a)) are apparently approaching this point. A small increase in nozzle drag with increased length can be noted for this nozzle at high subsonic Mach numbers.

Although increasing nozzle length only changes nozzle geometry, afterbody drag ahead of the nozzle $C_{D,a}$ is also generally decreased. In fact, for the supersonic nozzle designs, the afterbody drag reduction accounts for nearly all the drag reduction on the total aft end.

As shown in the (c) part of each figure, increasing nozzle length generally tends to decrease empennage interference effects, particularly on the subsonic dry power nozzle design.

Nozzle closure.- Figures 34 and 35 present the effects of nozzle closure on the short and long nozzle designs, respectively. The effect on nozzle drag was found to be dependent on Mach number, empennage arrangement, and nozzle length.

In general, decreasing nozzle closure (increasing d_b/d_m) increased total aft-end drag coefficient $C_{D,t}$ for $M < 0.90$ and significantly decreased total aft-end drag at $M = 1.20$. In the range of Mach number from 0.80 to 0.90, the increase in aft-end drag was small for the short nozzles, particularly with the tails installed. However, in the same Mach number range, decreasing nozzle closure on the long nozzles produced significant increases in total aft-end drag. By examination of nozzle drag coefficient $C_{D,n}$ and afterbody drag coefficient $C_{D,a}$, it can be seen that most of the effects of nozzle closure on total aft-end drag occur on the nozzle itself. The effects of nozzle closure on the afterbody are generally small and a consistent trend is not apparent. Nozzle drag coefficient generally follows the same trends with decreasing nozzle closure as noted previously for total aft-end drag coefficient. Total aft-end drag and nozzle drag probably increase with decreasing nozzle closure at subsonic speeds because of reduced pressure recovery on the nozzles with little boattail closure (larger values of d_b/d_m). Reduced pressure recovery on nozzles with reduced closure can be observed on the static-pressure distributions shown previously in figure 17.

One might expect empennage interference on the aft end to decrease with decreasing nozzle closure because the aft-facing projected area for empennage interference to act on decreases with decreasing nozzle closure. In fact, empennage interference on the total aft-end $\Delta C_{D,it}$ does decrease with decreasing closure at all test Mach numbers when the short nozzle designs were installed (fig. 34(c)). However, with the long nozzle designs installed (fig. 35(c)), a consistent trend of total empennage interference with varying nozzle closure is not apparent.

Comparison of Installed and Isolated Nozzle Drag

Figure 36 presents a comparison of nozzle drag coefficient (one nozzle) for the current investigation with those for the same nozzle geometries installed on a typical single-engine afterbody (ref. 3) and installed on an isolated (no afterbody closure) nacelle (ref. 2). Data are shown for tail-off configurations only. The data of references 2 and 3 have been converted to drag coefficients by using the reference area from the current investigation.

Nozzle drag coefficients of nozzles installed in typical single-engine (ref. 3) and twin-engine (current test) afterbodies are lower than isolated (ref. 2) nozzle drag coefficients at all investigation test conditions. It is obvious from these data that upstream afterbody boattailing has a beneficial effect on nozzle drag. Similar results are reported in reference 15. The reduction in nozzle drag, of course, must be caused by higher static pressures on the nozzle boattail. A comparison of installed and isolated nozzle static-pressure distributions for the short subsonic dry power nozzle is shown in figure 37. This figure indicates that upstream afterbody boattailing produces a stronger nozzle recompression flow field (and thus significantly higher nozzle static pressures) than that which occurs with the cylindrical (isolated) afterbody. With upstream afterbody closure, some of the external flow expansion occurs on the afterbody ahead of the nozzle and the amount of external flow expansion required at the nozzle shoulder is reduced. Thus, the maximum negative static-pressure coefficients on the nozzle are substantially less on the configurations with upstream afterbody closure. The isolated installation also appears to have a fairly strong standing shock on the nozzle boattail which causes downstream external flow separation. The separated flow region on the aft portion of the isolated nozzle installation prevents proper pressure recovery; thus, this configuration also has substantially lower nozzle static pressures in the recompression region than the single- and twin-engine installations. The data of reference 15 indicate that even if external flow separation had not prevented proper pressure recovery on the isolated nozzle installation, this configuration would still not have attained as high static pressures on the aft portion of the nozzle as the configurations with upstream afterbody closure. It is important to note that since part of the external flow expansion process occurs on the afterbody for the single- and twin-engine installations, the drag of the afterbody is dependent on the amount of afterbody closure. The drag incurred on the afterbodies with closure. The beneficial effect on nozzle drag must be traded against a probable increase in afterbody drag ahead of the nozzle. This drag has not been considered in this discussion of figures 36 and 37.

CONCLUSIONS

An investigation has been conducted in the Langley 16-Foot Transonic Tunnel to determine installation effects on convergent-divergent nozzles applicable to twin-engine reduced-power supersonic cruise aircraft. Tests were conducted at Mach numbers from 0.50 to 1.20, angles of attack from $-5°$ to $9°$, and nozzle pressure ratios from jet off to 8.0. The effects of empennage arrangement, nozzle length, and

afterbody closure on total and component drag coefficients were investigated. Results from this study indicate the following conclusions:

1. When compared with a typical single-engine nozzle installation, tail drag, afterbody drag (excluding nozzles), and empennage interference drag (at subsonic and transonic speeds) of a typical twin-engine configuration constitute a larger percentage of total aft-end drag.

2. Empennage interference on aft-end drag can be significant (as high as 32 percent of total aft-end drag at a Mach number of 0.90) in the high subsonic and transonic speed regime.

3. Empennage arrangement generally had only small effects on total aft-end drag. In addition, the empennage arrangement for lowest aft-end drag was dependent upon Mach number and nozzle geometry.

4. Total aft-end drag was generally decreased by increasing nozzle length.

5. Although Mach number and configuration dependent, decreasing nozzle closure generally increased total aft-end drag at subsonic speeds and decreased aft-end drag at low supersonic speeds.

6. Upstream afterbody closure (boattailing) produces significantly higher nozzle static pressures and lower nozzle drag. However, this beneficial effect on nozzle drag must be traded against a probable increase in afterbody drag ahead of the nozzle.

Langley Research Center
National Aeronautics and Space Administration
Hampton, VA 23665
August 31, 1983

REFERENCES

1. Berrier, Bobby L.; and Staff, Propulsion Integration Section: A Review of Several Propulsion Integration Features Applicable to Supersonic-Cruise Fighter Aircraft. NASA TM X-73991, 1976.

2. Berrier, Bobby L.; and Re, Richard J.: Investigation of Convergent-Divergent Nozzles Applicable to Reduced-Power Supersonic Cruise Aircraft. NASA TP-1766, 1980.

3. Burley, James R., II; and Berrier, Bobby L.: Investigation of Installation Effects on Single-Engine Convergent-Divergent Nozzles. NASA TP-2078, 1982.

4. Schmeer, James W.; Lauer, Rodney F., Jr.; and Berrier, Bobby L.: Performance of Blow-in-Door Ejector Nozzles Installed on a Twin-Jet Variable-Wing-Sweep Fighter Airplane Model. NASA TM X-1383, 1967.

5. Reubush, David E.; and Mercer, Charles E.: Effects of Nozzle Interfairing Modifications on Longitudinal Aerodynamic Characteristics of a Twin-Jet, Variable-Wing-Sweep Fighter Model. NASA TN D-7817, 1975.

6. Maiden, Donald L.; and Berrier, Bobby L.: Effect of Airframe Modifications on Longitudinal Aerodynamic Characteristics of a Fixed-Wing, Twin-Jet Fighter Airplane Model. NASA TM X-2523, 1972.

7. Berrier, Bobby L.: Effect of Nonlifting Empennage Surfaces on Single-Engine Afterbody/Nozzle Drag at Mach Numbers From 0.5 to 2.2. NASA TN D-8326, 1977.

8. Runckel, Jack F.: Interference Between Exhaust System and Afterbody of Twin-Engine Fuselage Configurations. NASA TN D-7525, 1974.

9. Glasgow, E. R.: Integrated Airframe-Nozzle Performance for Designing Twin-Engine Fighters. AIAA Paper No. 73-1303, Nov. 1973.

10. Swavely, C. E.; and Soileau, J. F.: Aircraft Afterbody/Propulsion System Integration for Low Drag. AIAA Paper No. 72-1101, Nov.-Dec. 1972.

11. Peddrew, Kathryn A., compiler: A User's Guide to the Langley 16-Foot Transonic Tunnel. NASA TM-83186, 1981.

12. Leavitt, Laurence D.: Effect of Empennage Location on Twin-Engine Afterbody/Nozzle Aerodynamic Characteristics at Mach Numbers From 0.6 to 1.2. NASA TP-2116, 1983.

13. Shapiro, Ascher H.: The Dynamics and Thermodynamics of Compressible Fluid Flow. Volume II. Ronald Press Co., c.1954.

14. Harris, Roy V., Jr.: An Analysis and Correlation of Aircraft Wave Drag. NASA TM X-947, 1964.

15. Bergman, Dave: Implementing the Design of Airplane Engine Exhaust Systems. AIAA Paper No. 72-1112, Nov.-Dec. 1972.
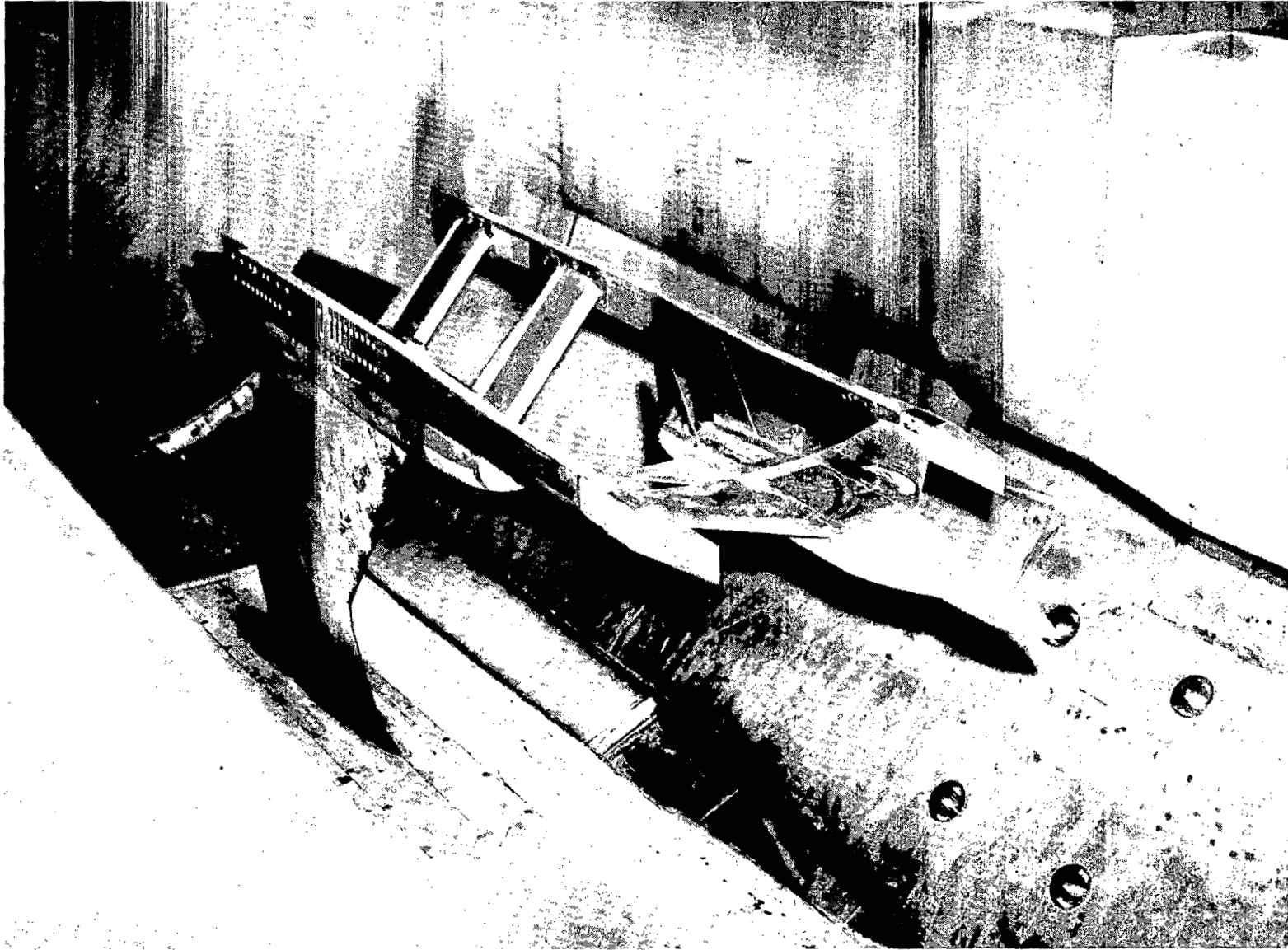
L-79-887

(a) Model and wing-tip support system.

Figure 1.- Twin-engine tail interference model installed in Langley 16-Foot Transonic Tunnel.

L-81-6971

(b) Side view.

Figure 1.- Continued.
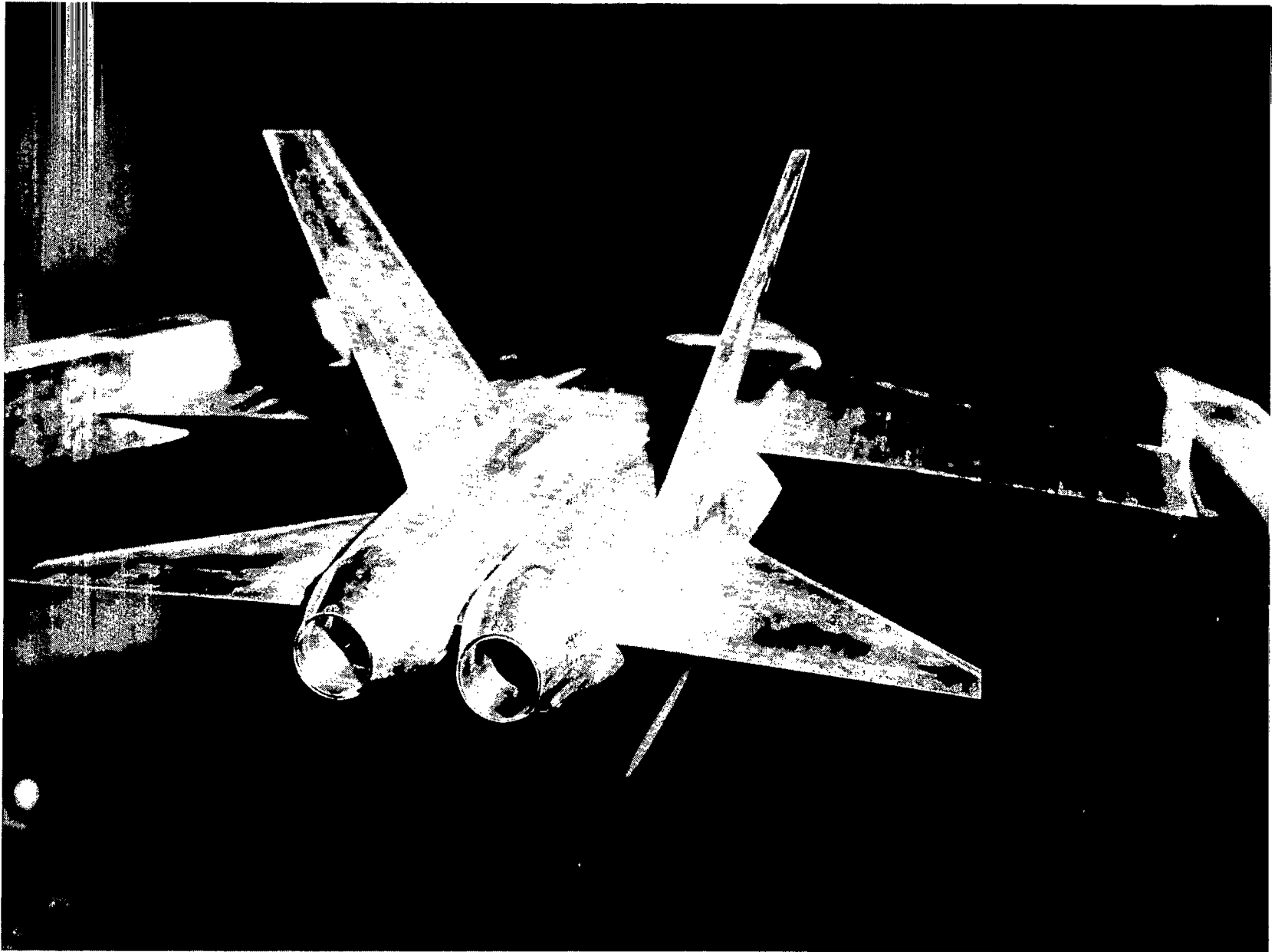
L-81-6973

(c) Rear view.

Figure 1.- Concluded.

BL 50.80

Support booms

Wing/Centerbody

FS 71.12

FS 120.04

FS 165.63

BL 12.70

FS 0.0

BL 5.51 Nozzle center line

BL 0.0

Dry power nozzle

Forebody
and
faired inlets

Afterbody

Engine interfairing

BL 27.94

High-pressure air lines
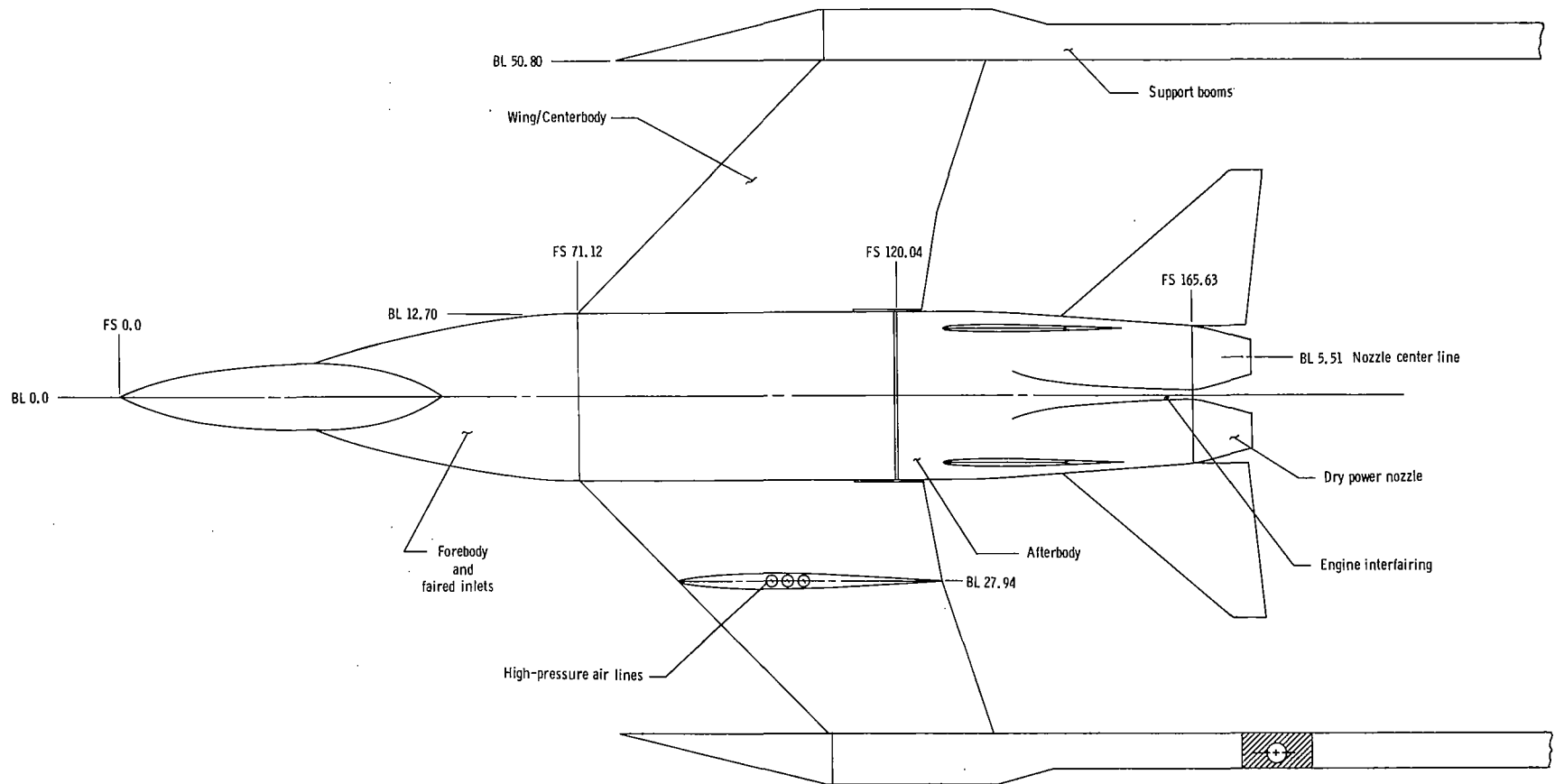
Figure 2.- Sketch of twin tail interference model and wing-tip support system. All dimensions are in centimeters.
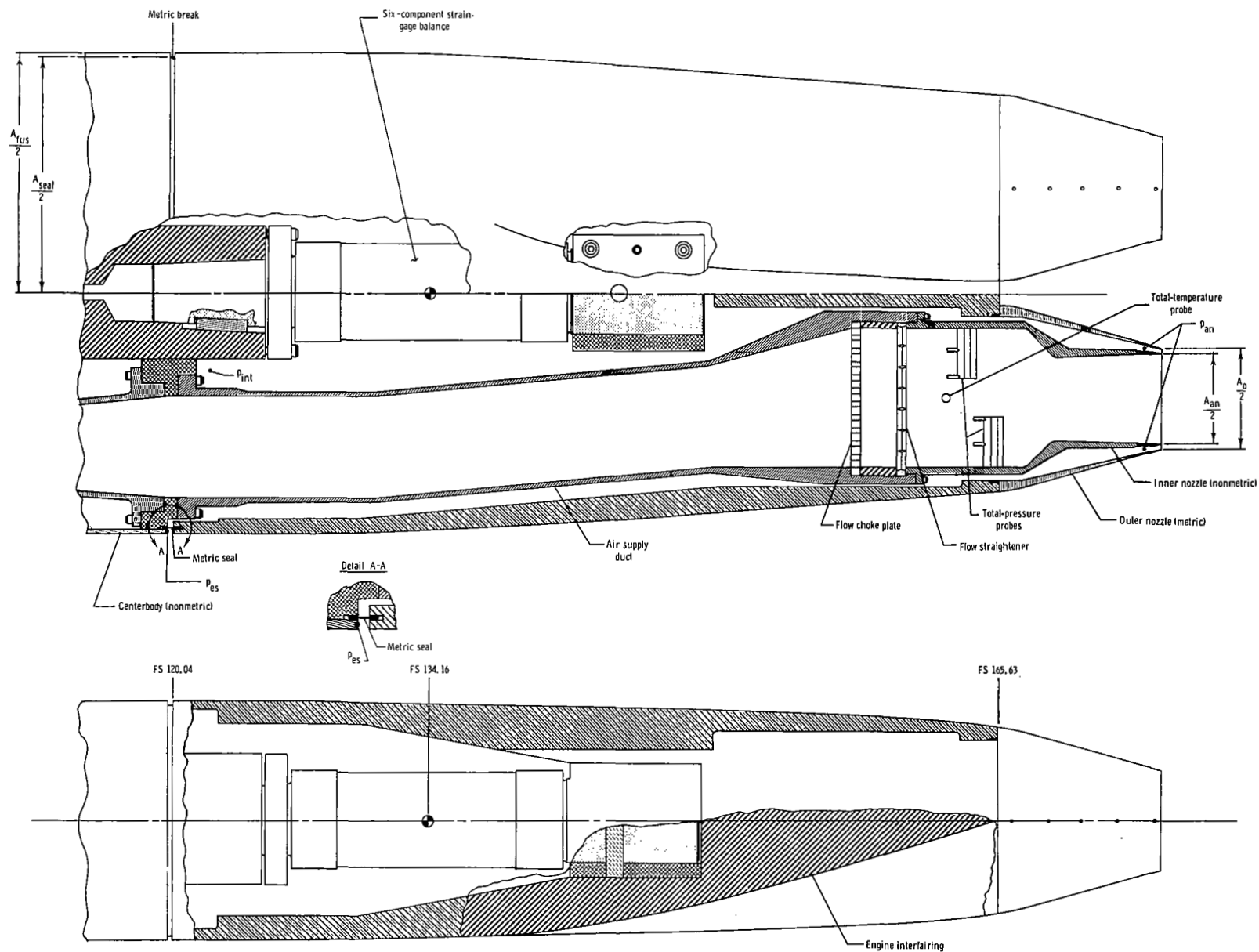
(a) Afterbody.

Figure 3.- Sketches showing model geometry. Linear dimensions are in centimeters.

Flight Segment	Power setting	$(NPR)_{des}$	d_t, cm	d_e, cm	d_b, cm	A_e/A_t	l, cm	l_f, cm	θ, deg	δ, deg	β, deg
Sub. cruise	Dry	4.00	4.51	4.98	5.49	1.22	8.19	4.40	30.00	3.08	18.30
							11.08	7.29		1.87	12.30
Super. cruise		12.90	4.61	6.90	7.41	2.24	8.03	4.24	28.90	15.50	9.65
							10.98	7.20	28.93	9.12	6.72
	Partial A/B		5.59	8.36	8.88		8.21	4.16	16.40	19.02	3.57
							11.19	7.15		11.10	2.57
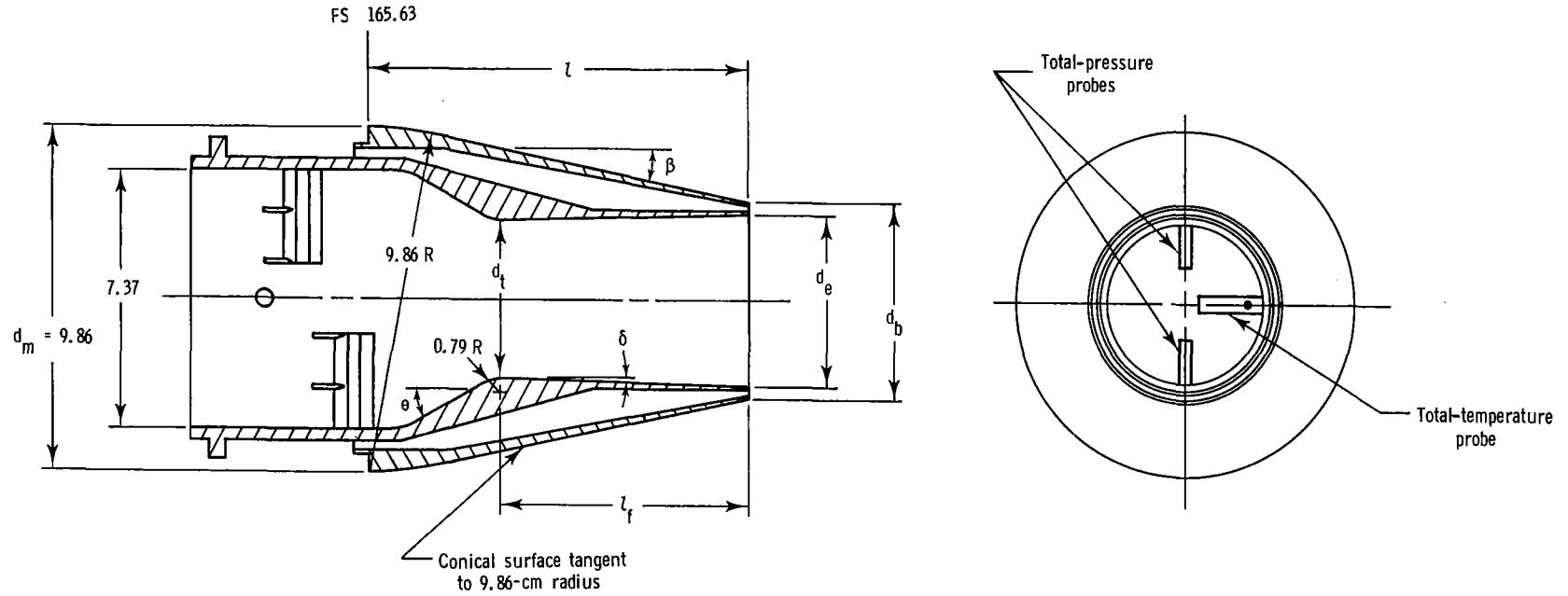
(b) Nozzle.

Figure 3.- Continued.

TOP VIEW

BL 0.0

BL -10.16

Vertical tail
chord plane

Mid

Aft

BL -12.70

FS 120.04

FS 136.68

FS 145.57

Horizontal tail

SIDE VIEW

Vertical tail

FS 120.04   FS 127.00   FS 136.68

Fwd   Mid

WL 6.35

Horizontal tail
chord plane

WL 0.0

WL -6.35
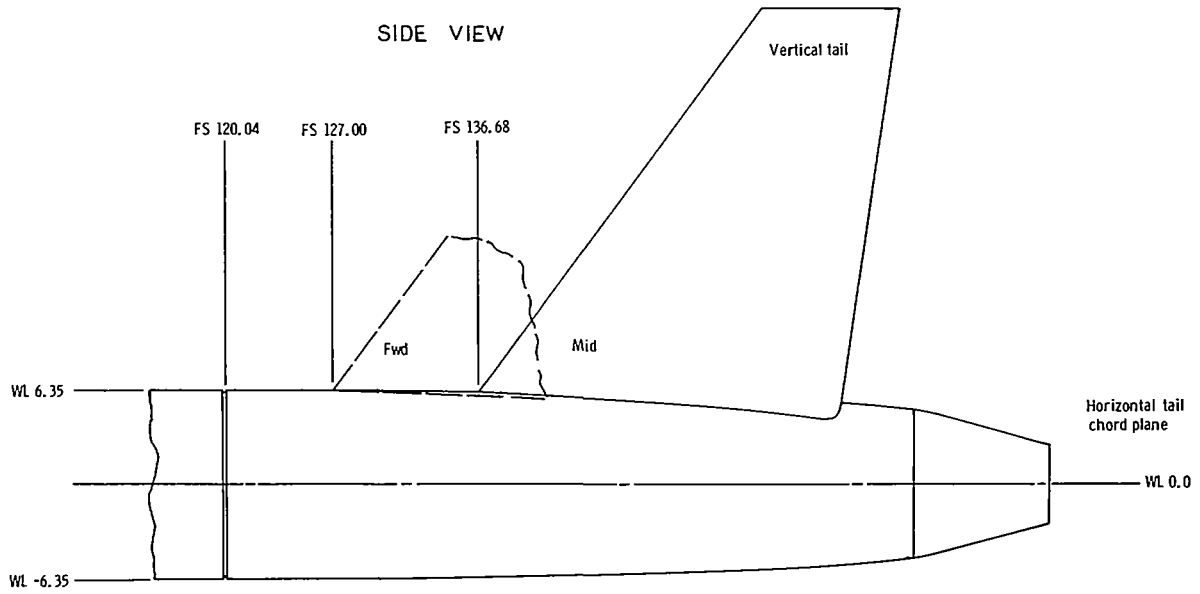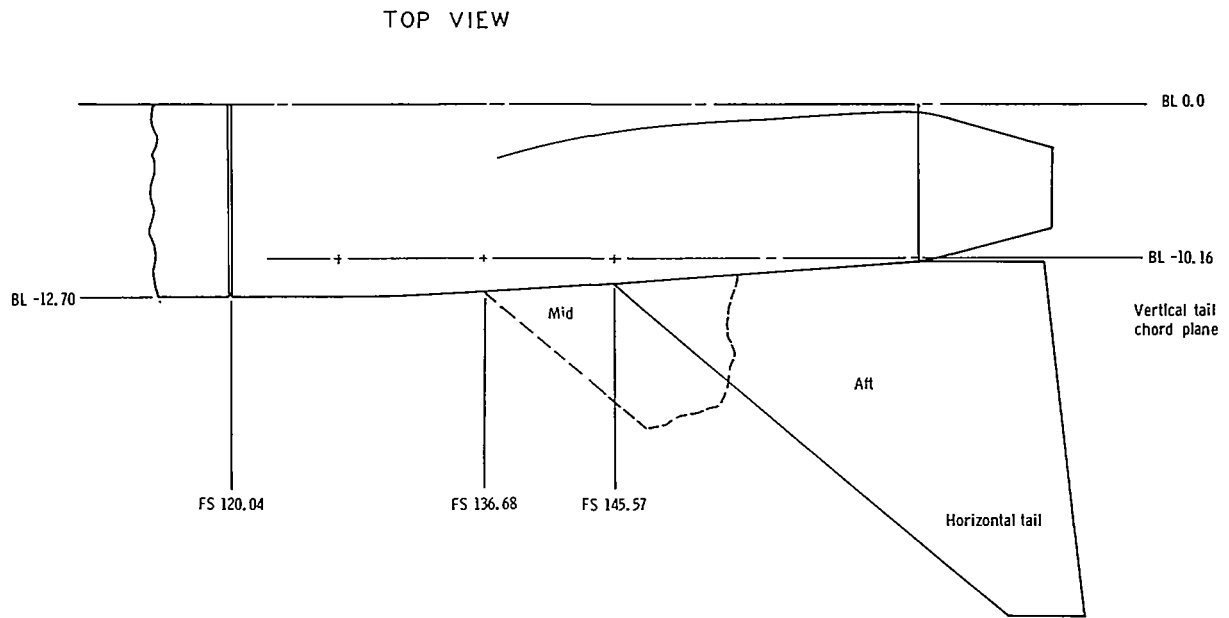
(c) Empennage locations on basic afterbody.

Figure 3.- Continued.

25

Twin Vertical Tail Geometry

Airfoil sections
Tip .... NACA 64-003.5
Root .... NACA 64-005
Tip chord, cm 9.14
Root chord, cm 24.38
Taper ratio .... .375
Tail height (root to tip) , cm 25.40
Planform area (one side exposed, filler excluded) , m^2 .... .0426
Aspect ratio (exposed, filler excluded) 1.514
Λ_{le}, deg 36.52

Toe angle, deg 0.00
Cant angle, deg 20.00

9.14

25.40

36.52°

Distance from model center line
varies slightly with tail location

24.38

Filler contoured for
each tail location

Model
$\mathcal{C}_L$
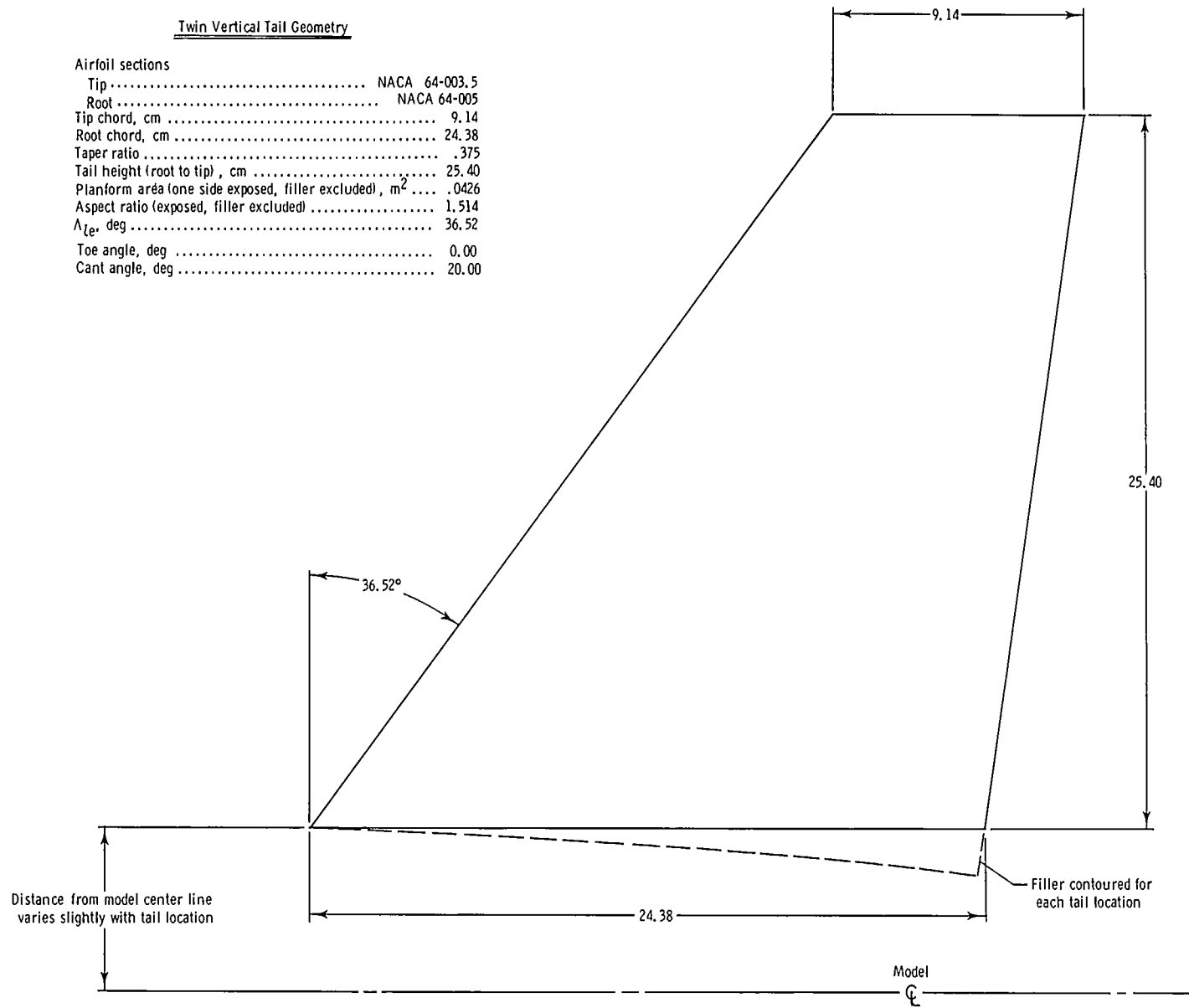
(d) Twin vertical tail.

Figure 3.- Continued.

Horizontal Tail Geometry

Airfoil sections
  Tip .... NACA 64-002.5
  Root .... NACA 64-005.5
Tip chord, cm 5.08
Root chord, cm 28.96
Taper ratio .... .175
Span, cm
  Mid on body 68.58
  Aft on body 67.51
Planform area (one side exposed, filler excluded), m^2 ... .0372
Aspect ratio (exposed, filler excluded) 2.564
Λ_{le}, deg 50.0

5.08

21.84

$50°$

28.96

Filler contoured for
each tail location

Distance from model center line
varies slightly with tail location

$\mathrm{C_L}$
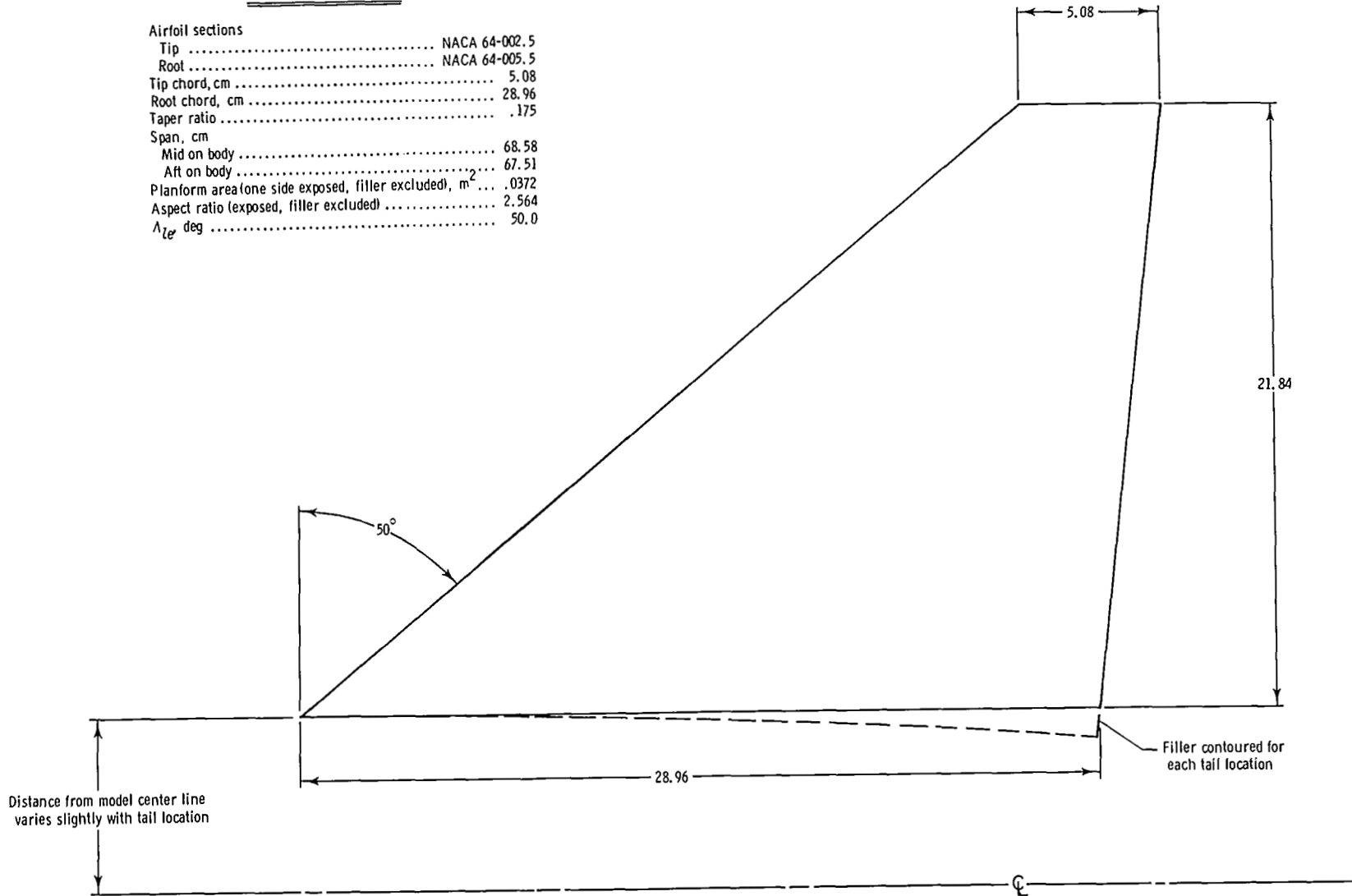
(e) Horizontal tail.

Figure 3.- Concluded.

Orifice x/l = 0.086, 0.300, 0.514, 0.729, and 0.943 for each row
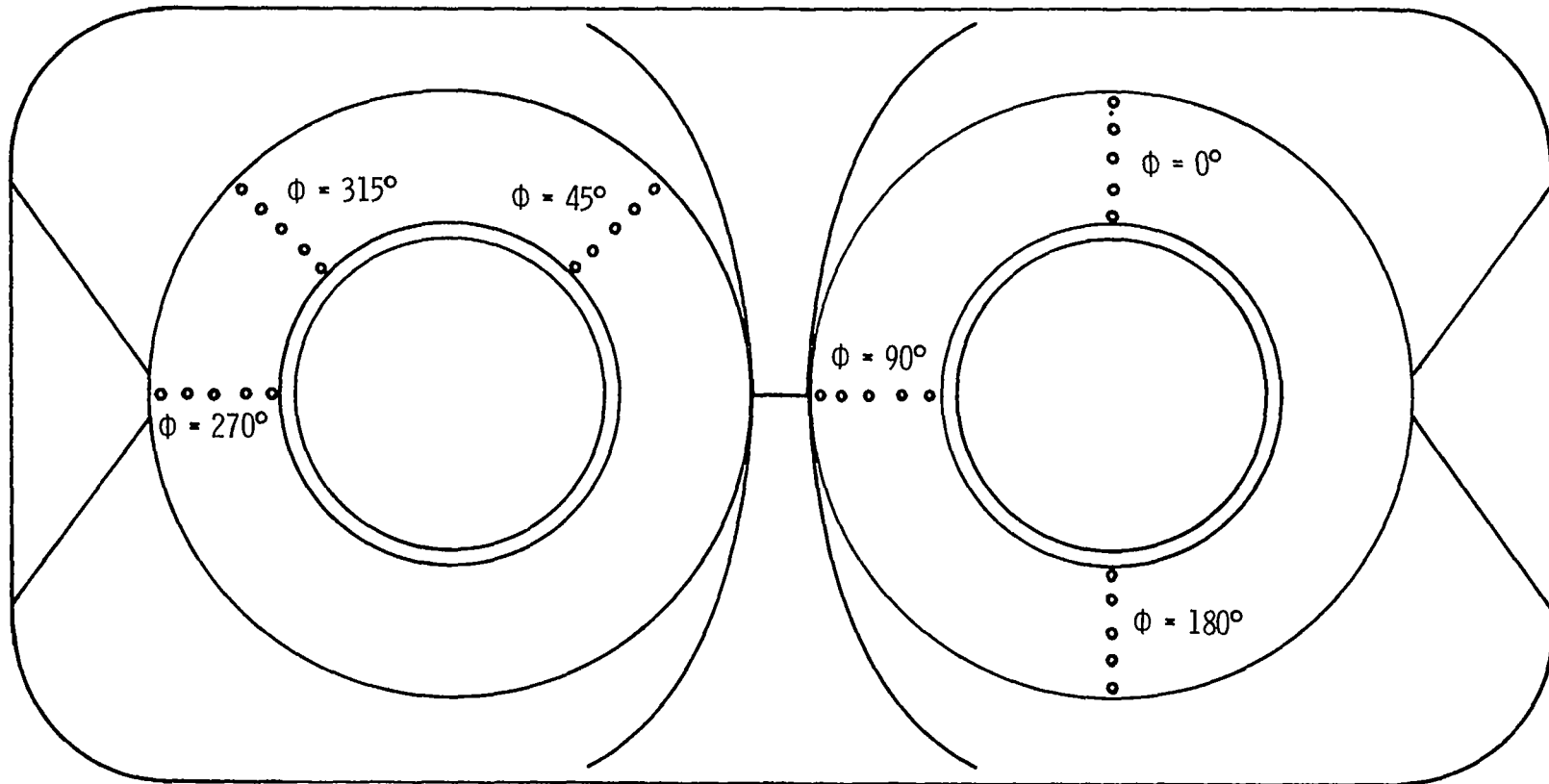
Figure 4.- Orientation of nozzle external static-pressure instrumentation.
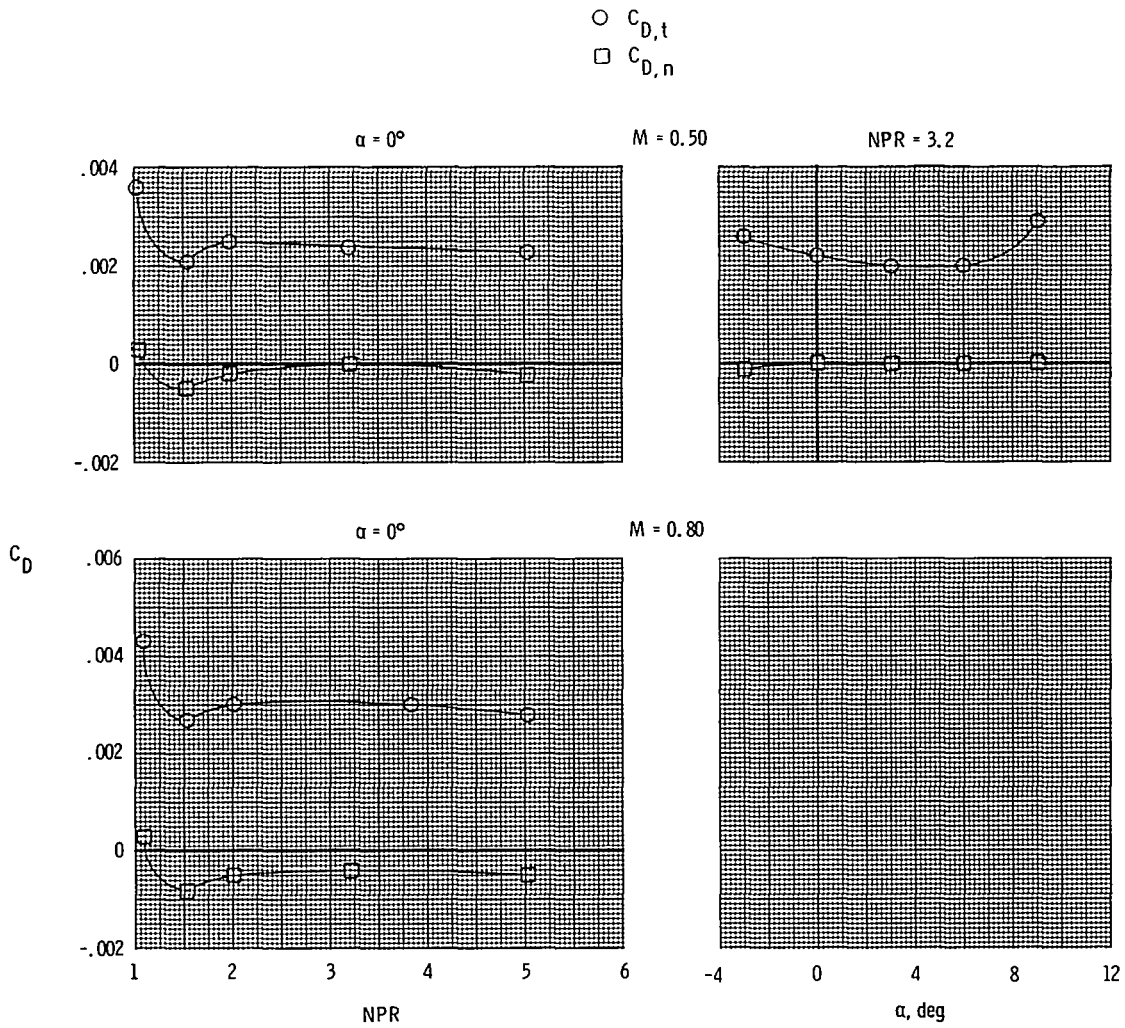
(a) Tails off.

Figure 5.- Variation of total (afterbody + nozzles + tails) and nozzle drag coefficients with nozzle pressure ratio and angle of attack for short subsonic dry power nozzles.
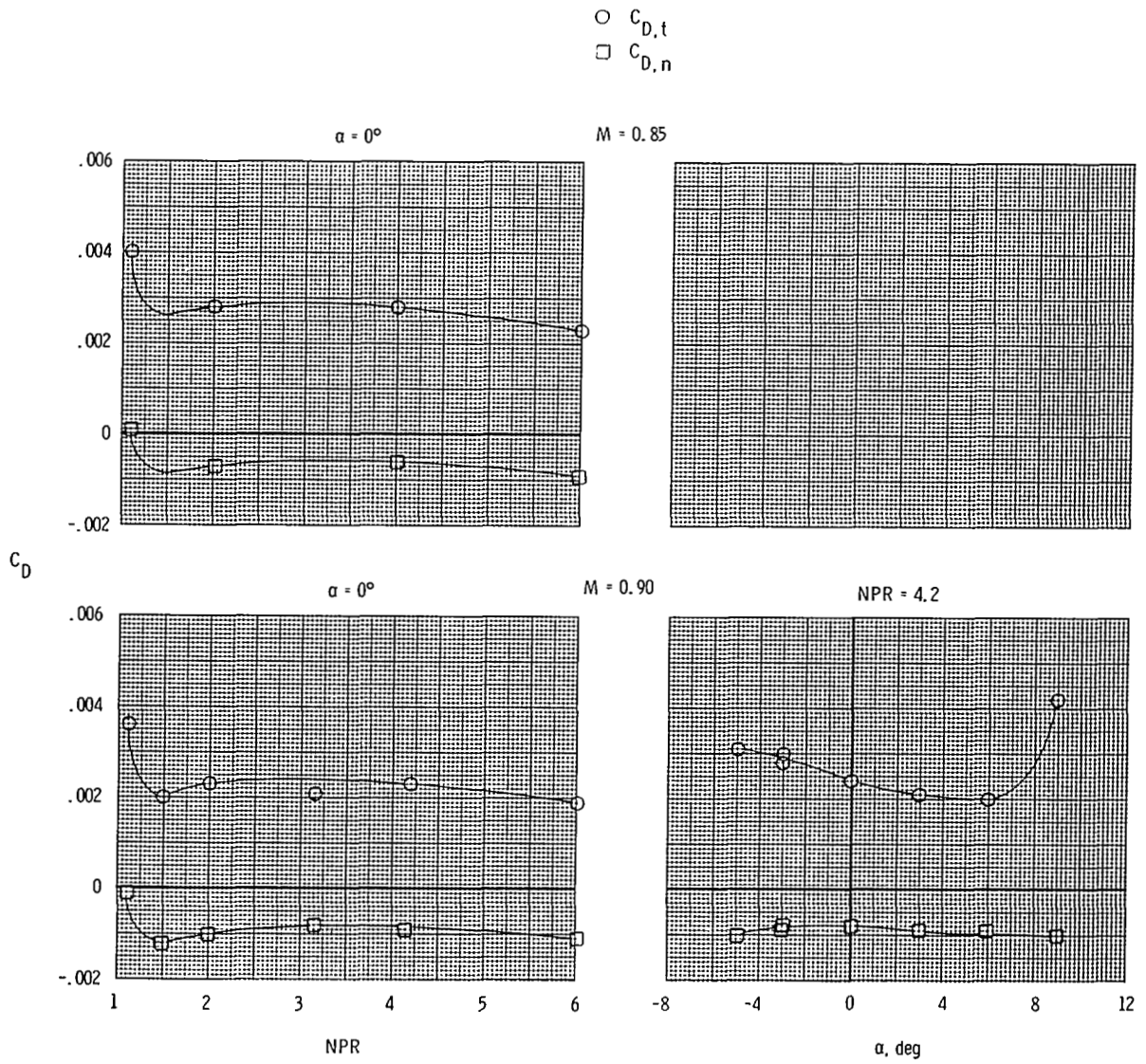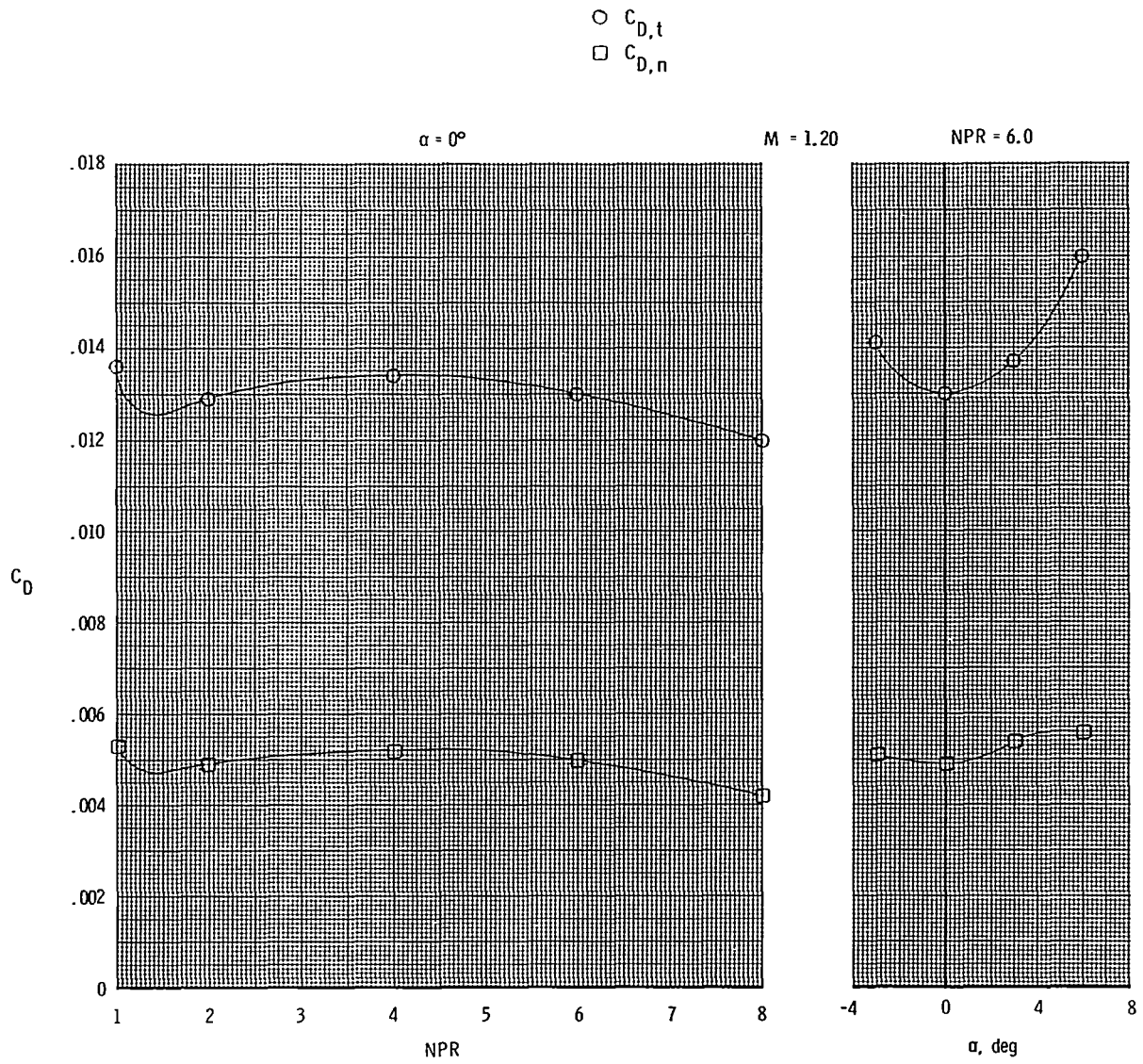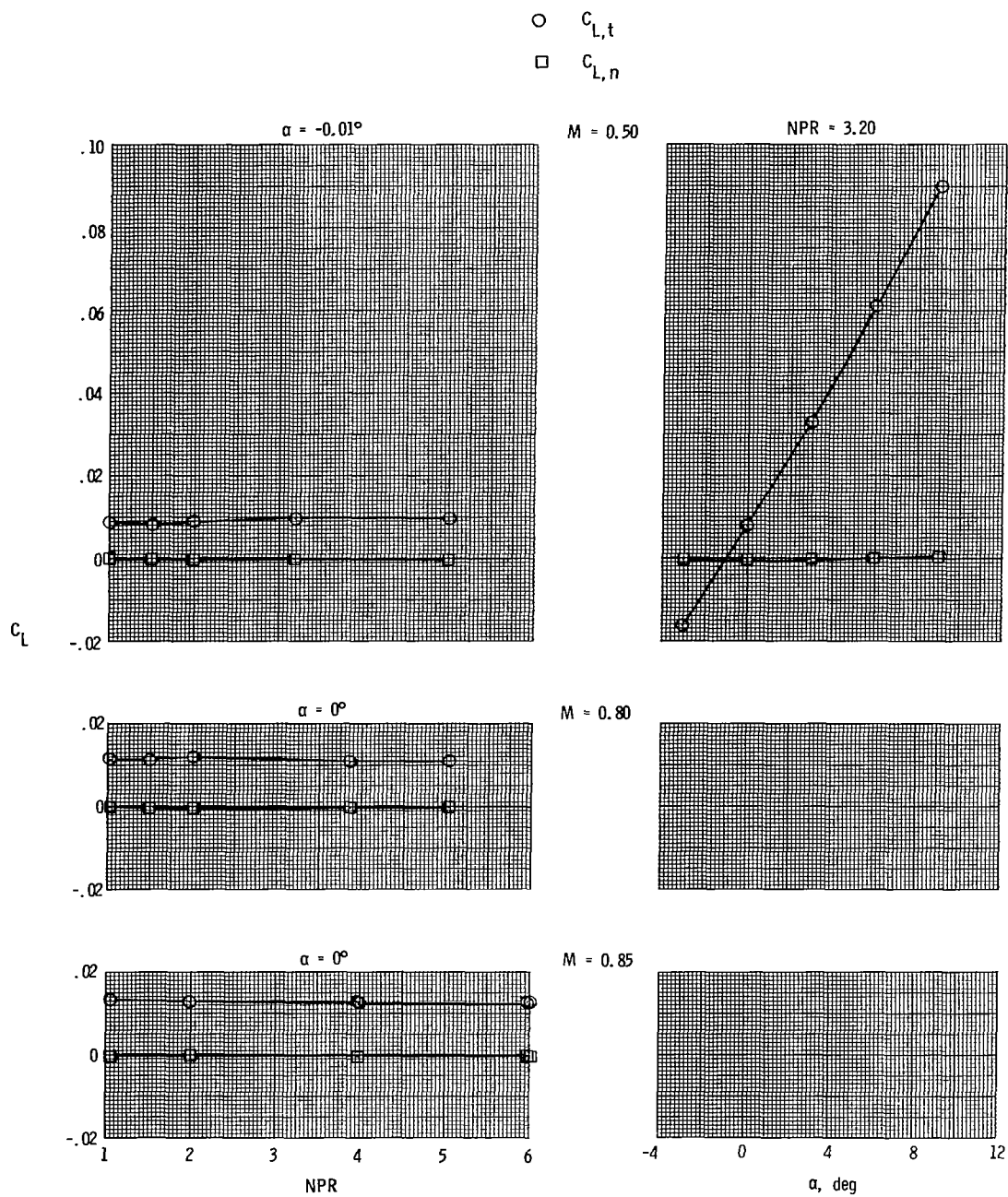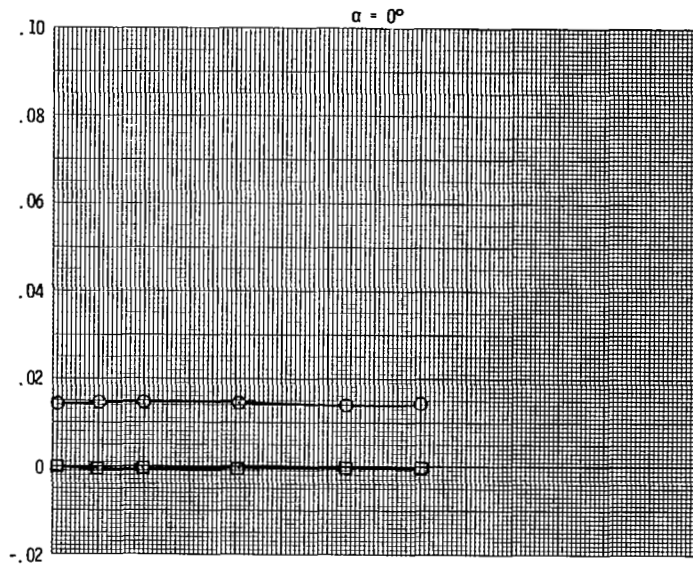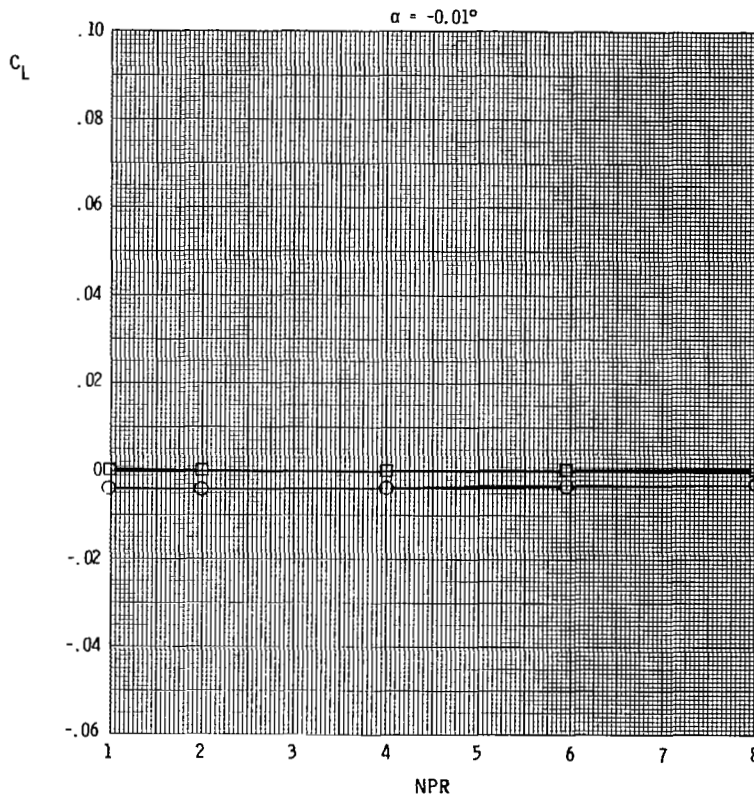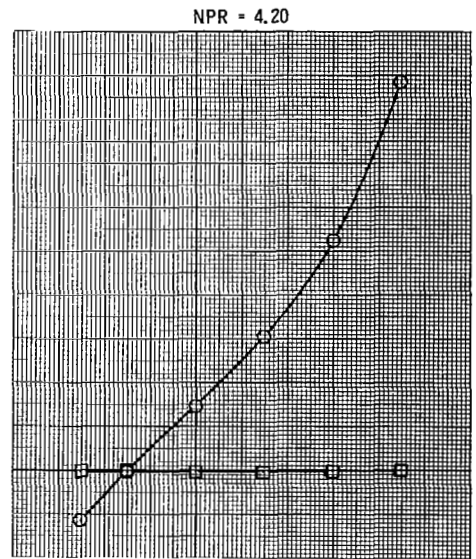
(a) Continued.

Figure 5.- Continued.

(a) Concluded.
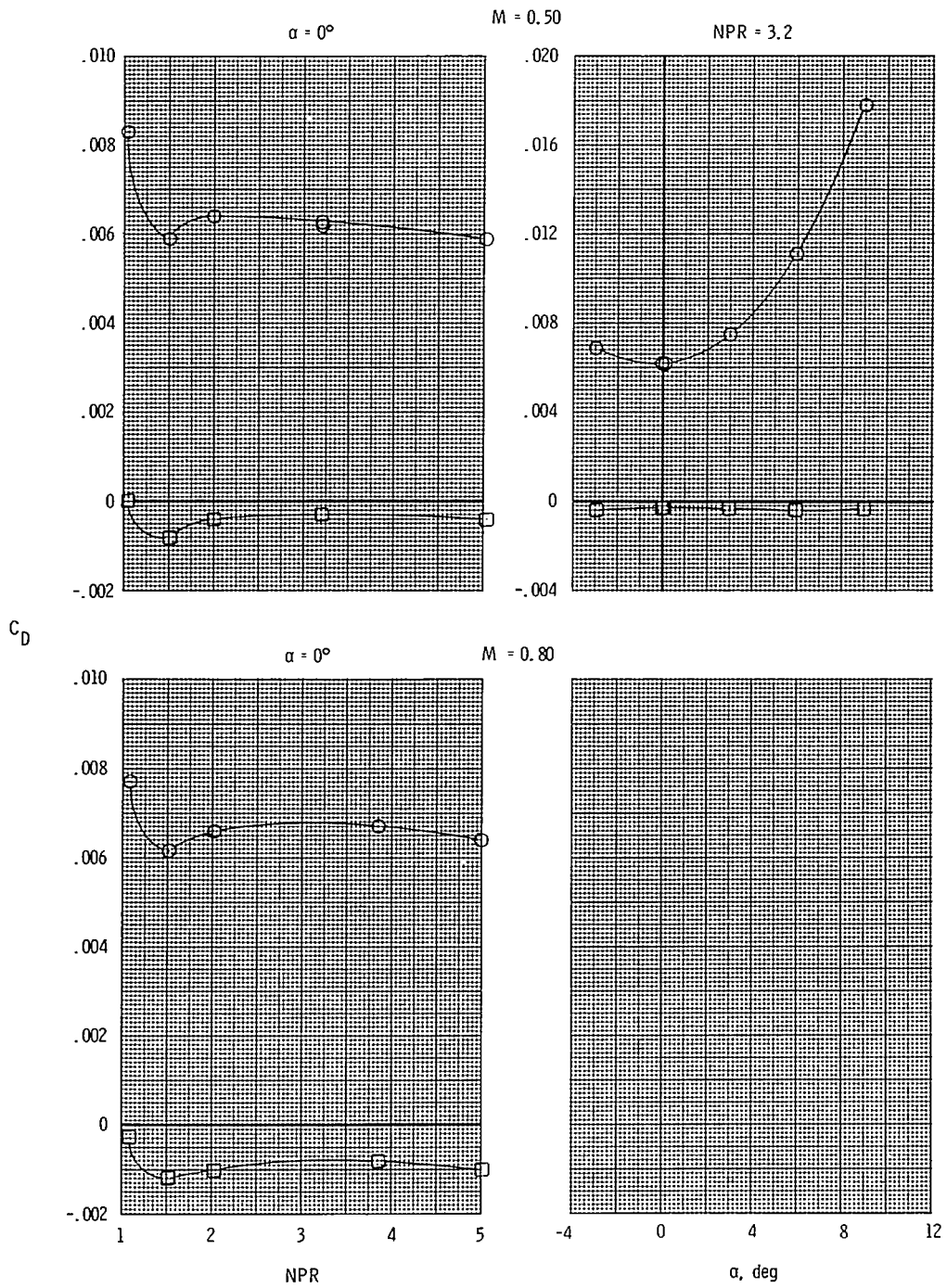
Figure 5.- Continued.

(b) Mid horizontal tails; forward vertical tails.
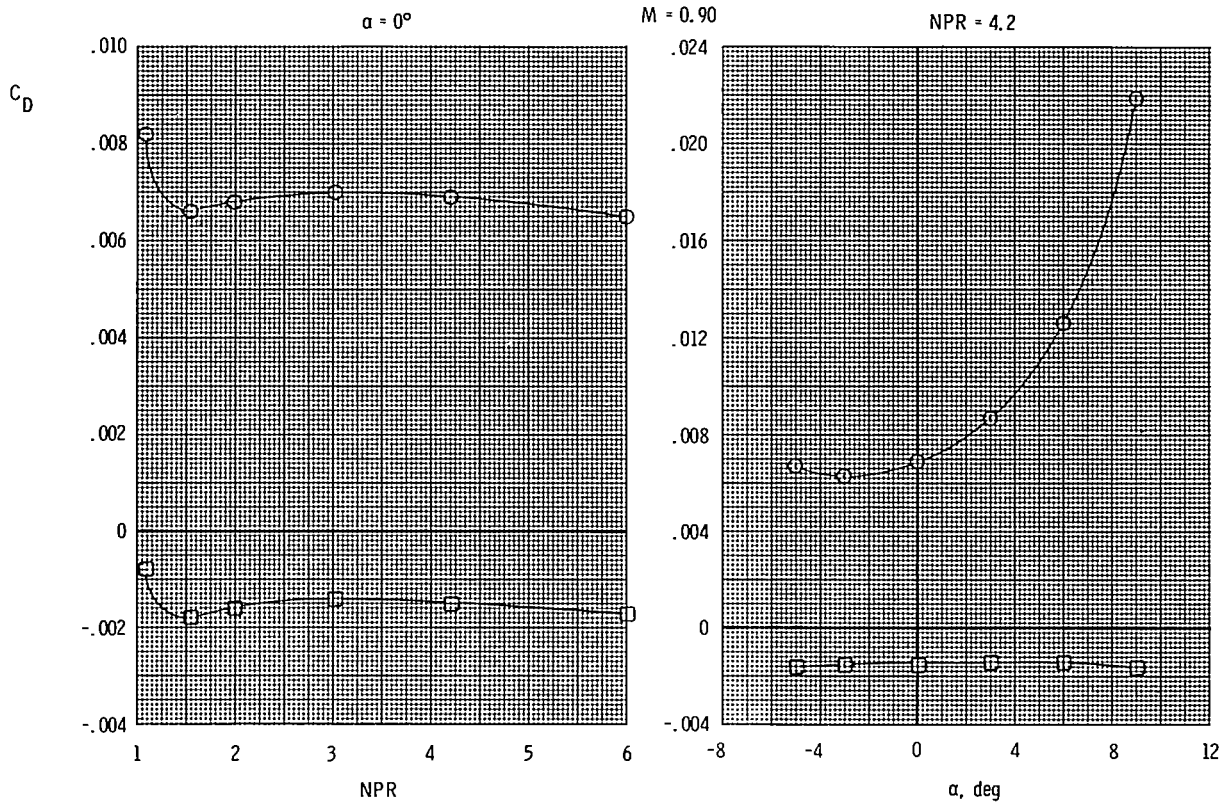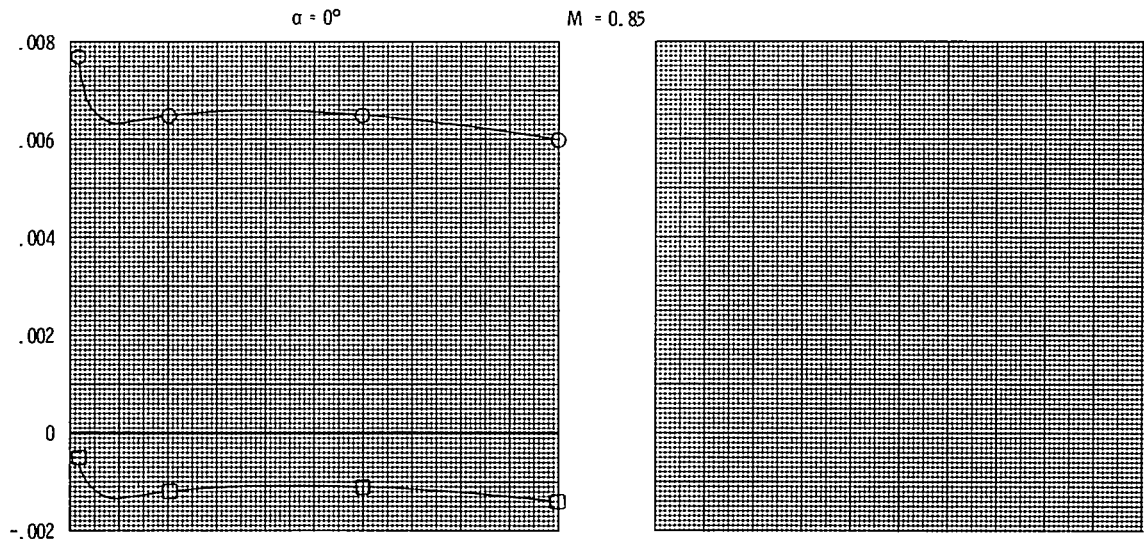
Figure 5.- Continued.

(b) Continued.

Figure 5.- Continued.
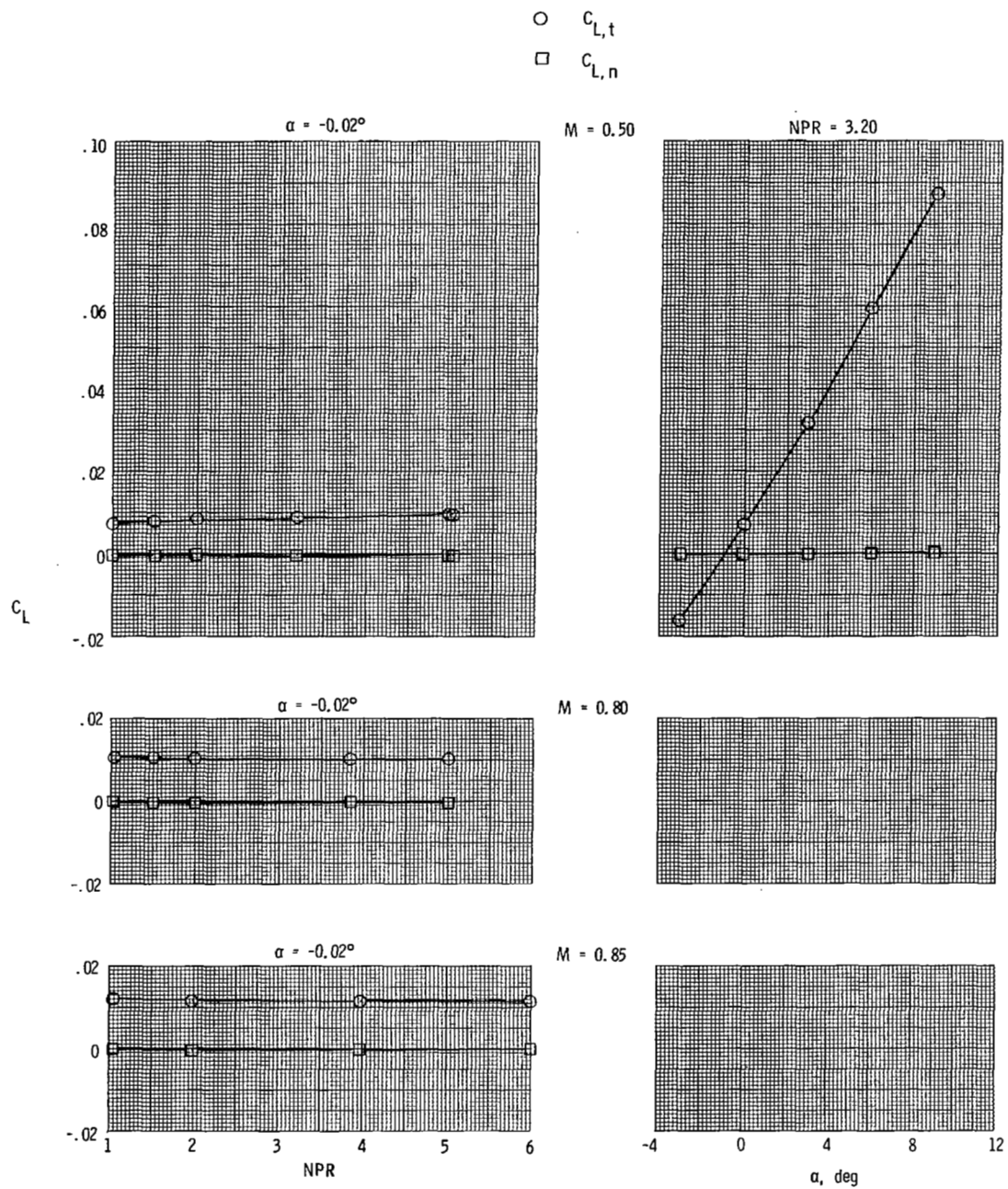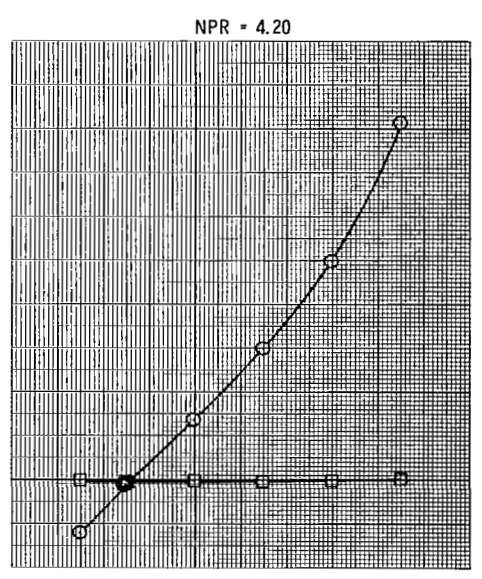
(b) Concluded.

Figure 5.- Continued.

(c) Mid horizontal tails; mid vertical tails.
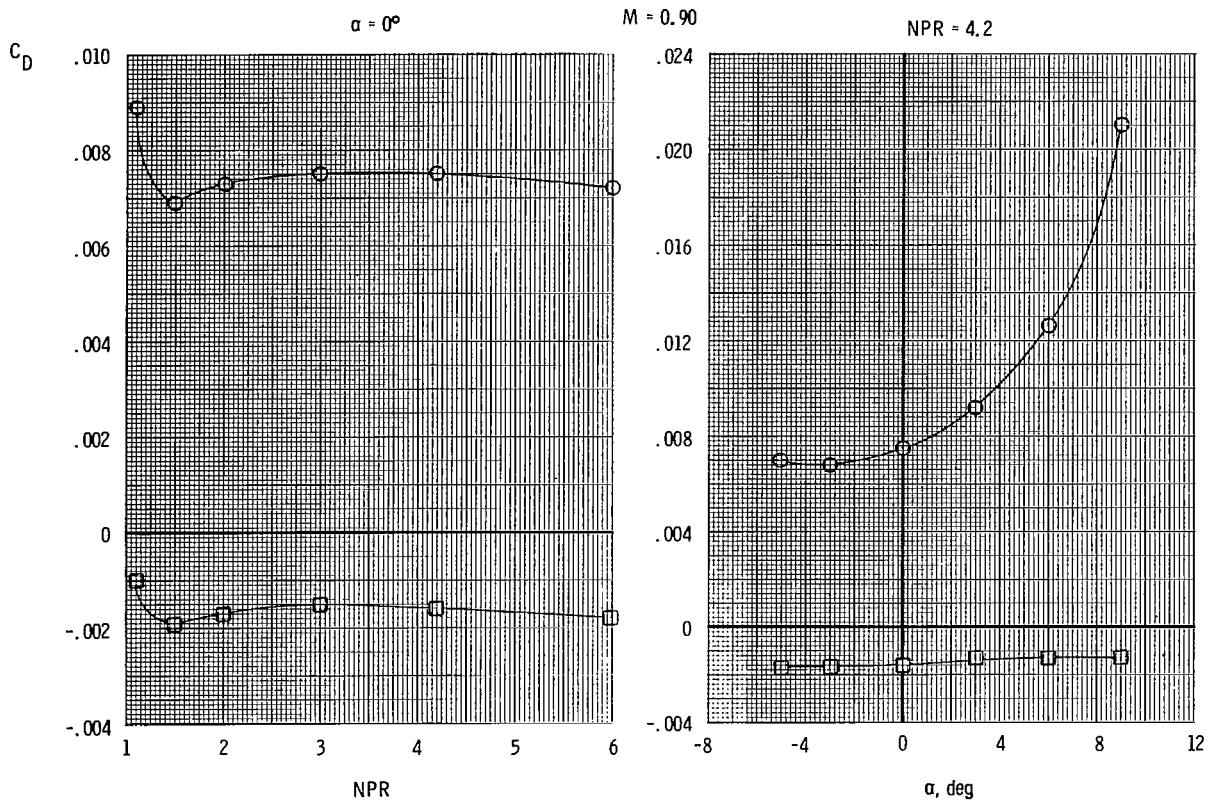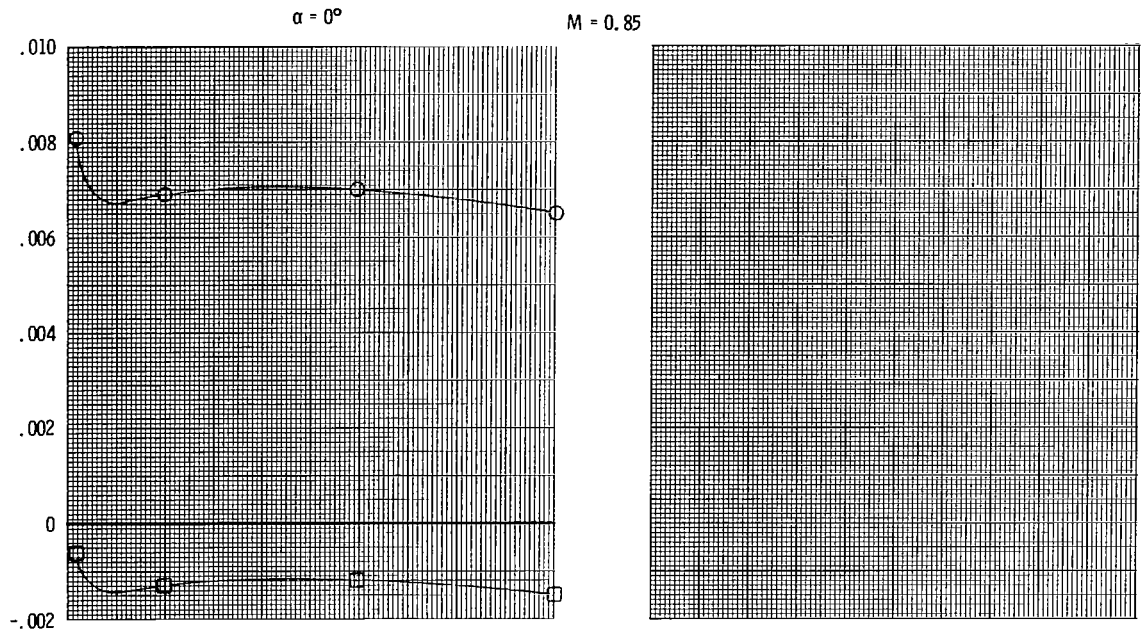
Figure 5.- Continued.
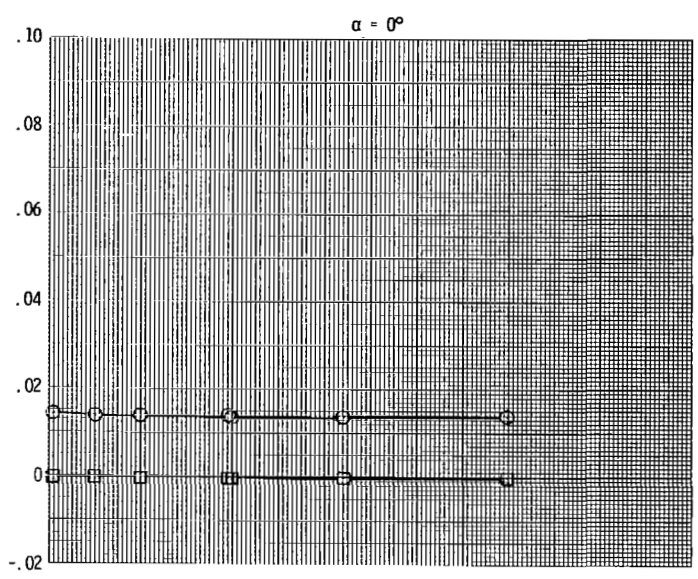
(c) Continued.

Figure 5.- Continued.

(c) Concluded.

Figure 5.- Continued.

(d) Aft horizontal tails; mid vertical tails.

Figure 5.- Continued.

○ $C_{D,t}$
□ $C_{D,n}$

α = 0°   M = 0.85

.010

.008

.006

.004

.002

0

-.002

α = 0°   M = 0.90   NPR = 4.2

C_D

.012   .024

.010   .020

.008   .016

.006   .012

.004

.002   .008

0   .004

-.002   0

1 2 3 4 5 6   -4 0 4 8 12

-.004

NPR   α, deg
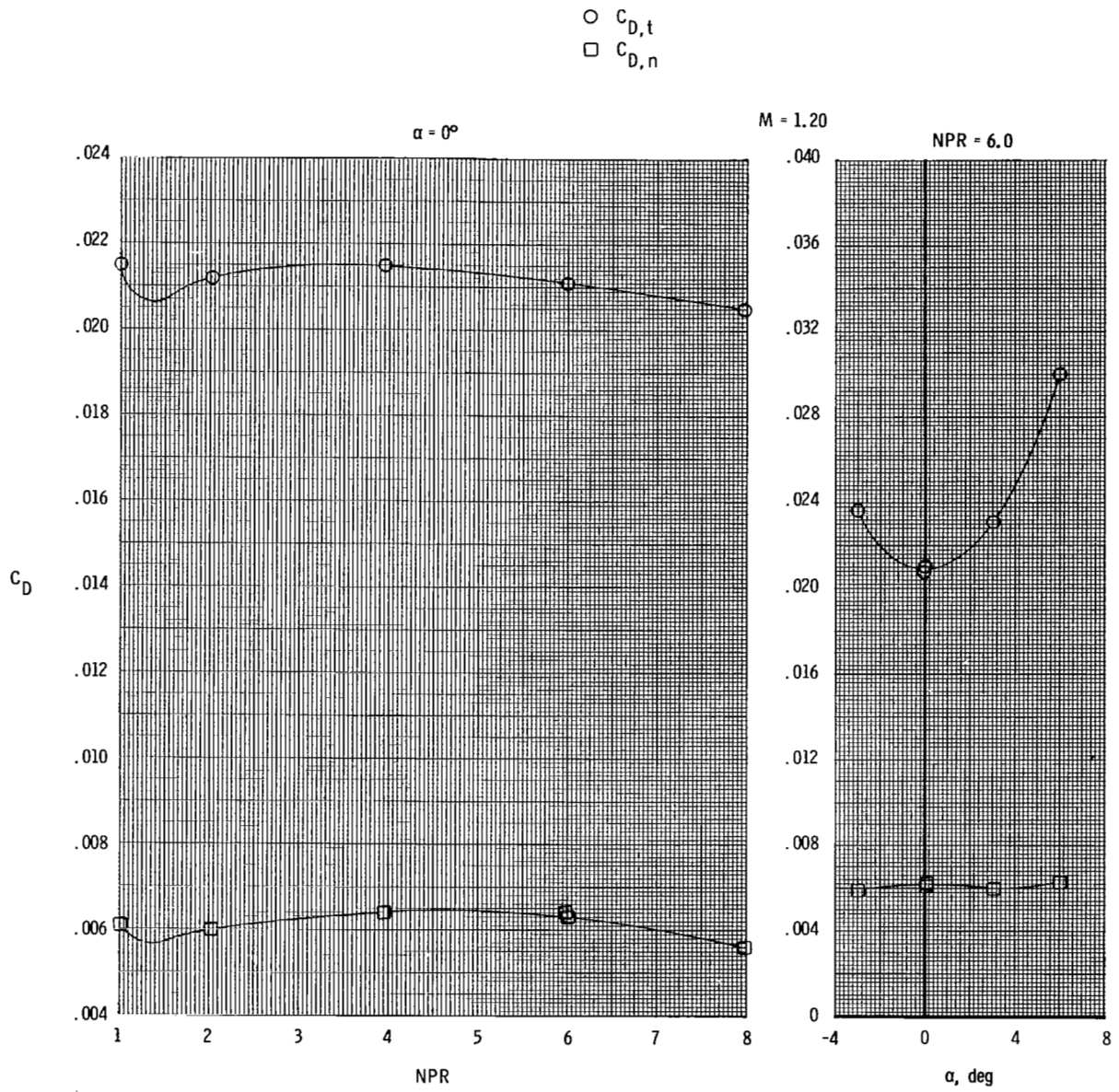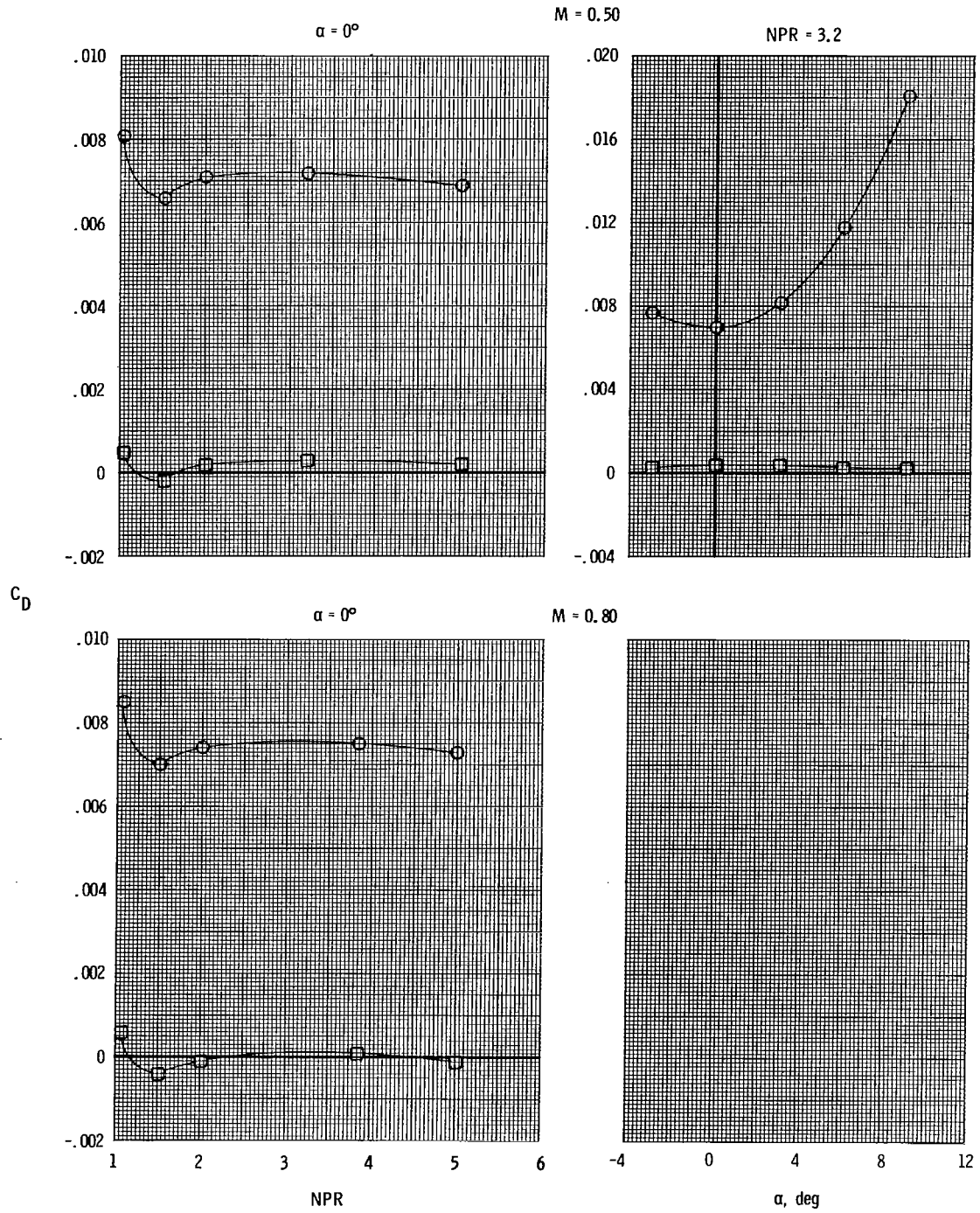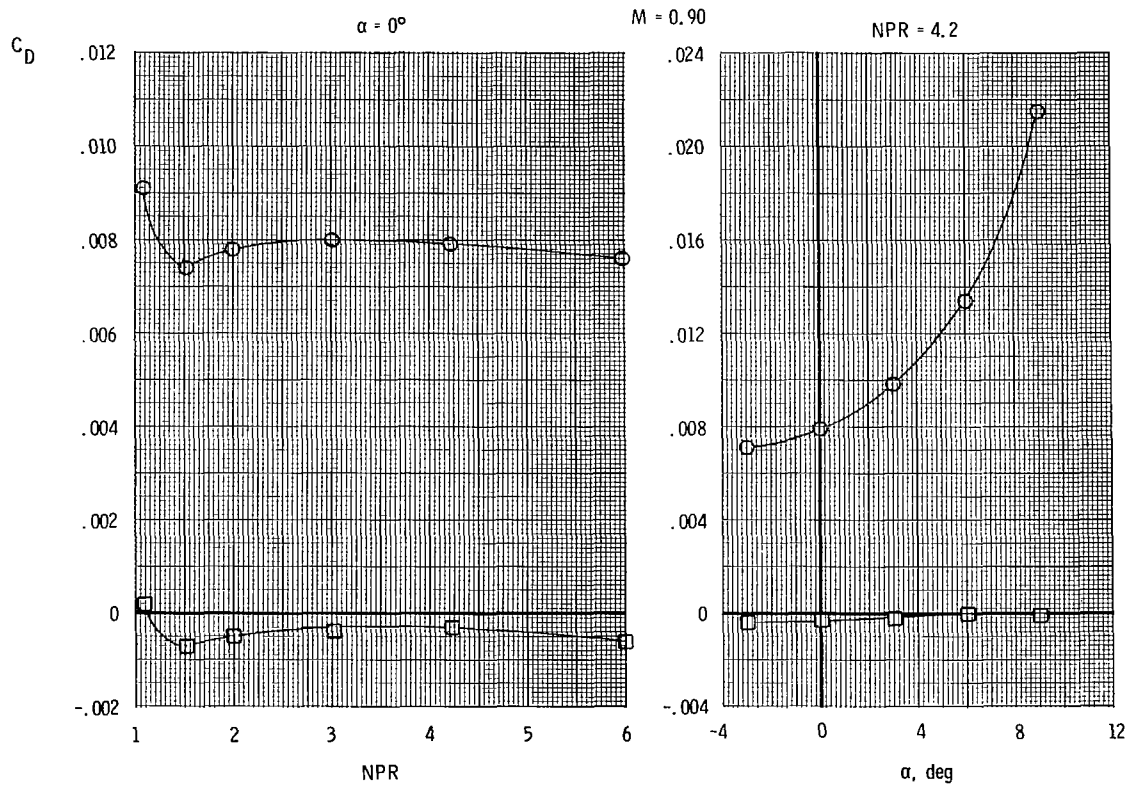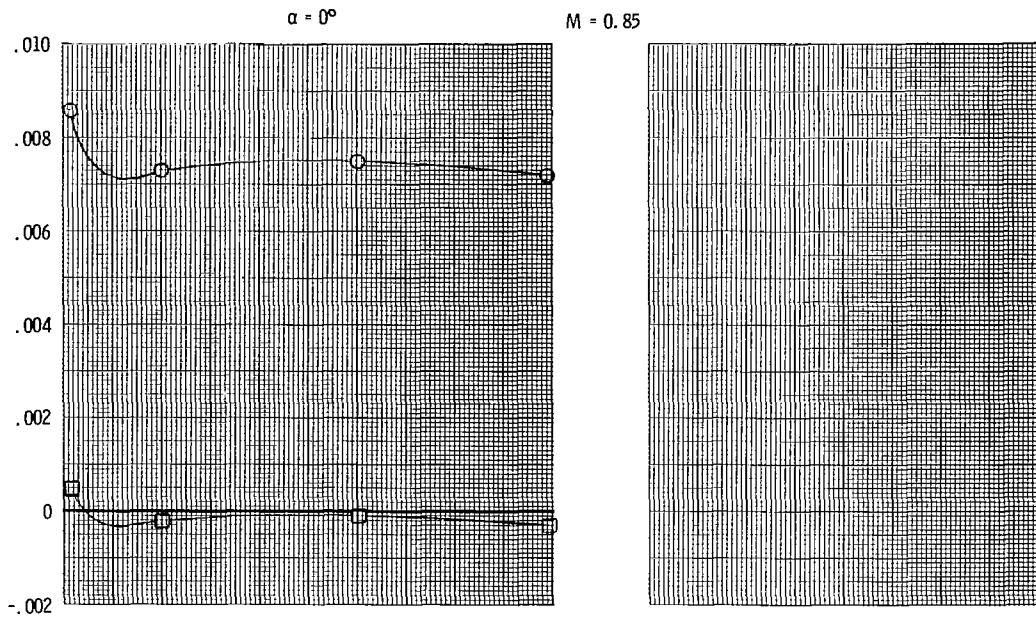
(d) Continued.
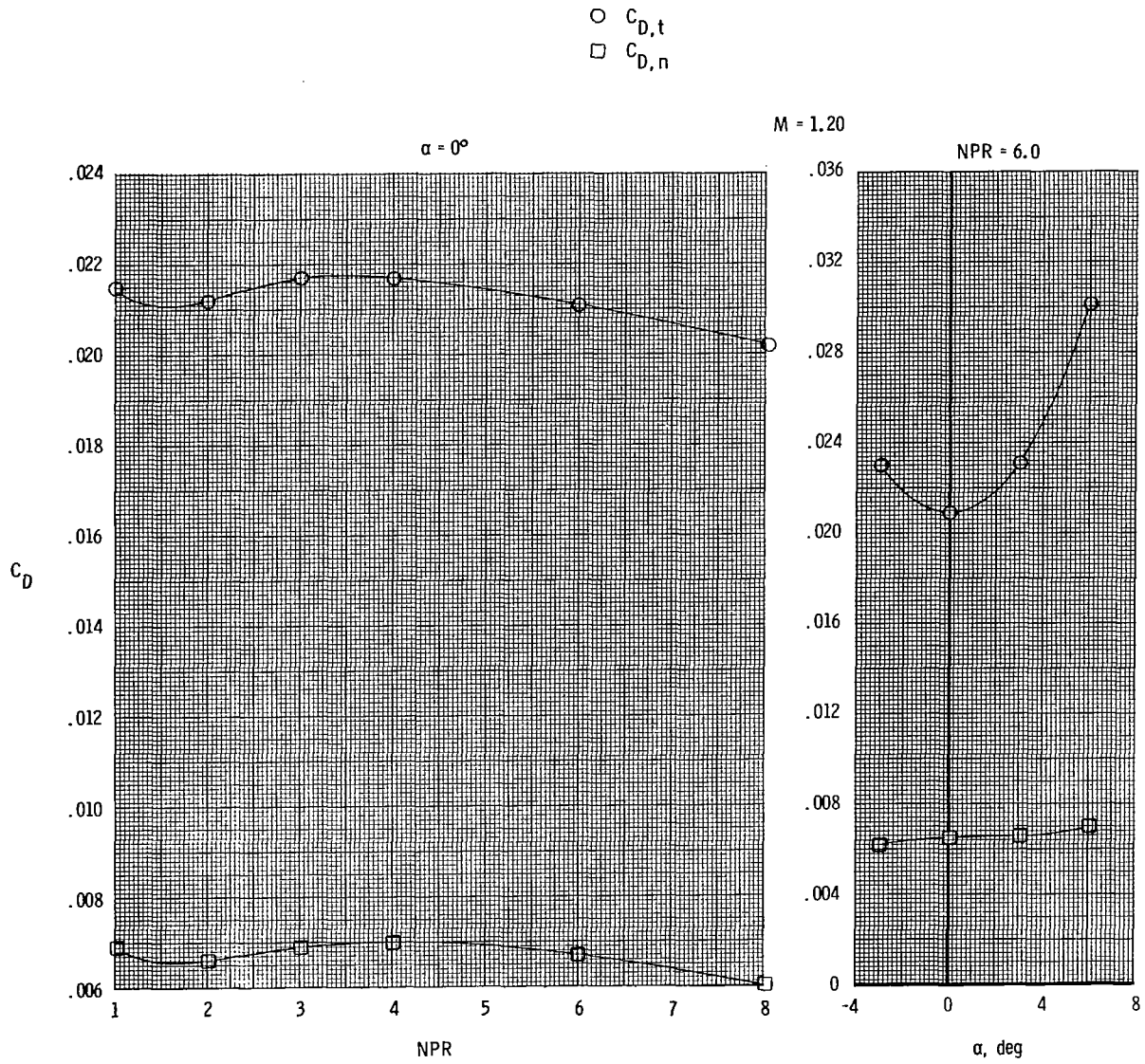
Figure 5.- Continued.

(d) Concluded.

Figure 5.- Concluded.
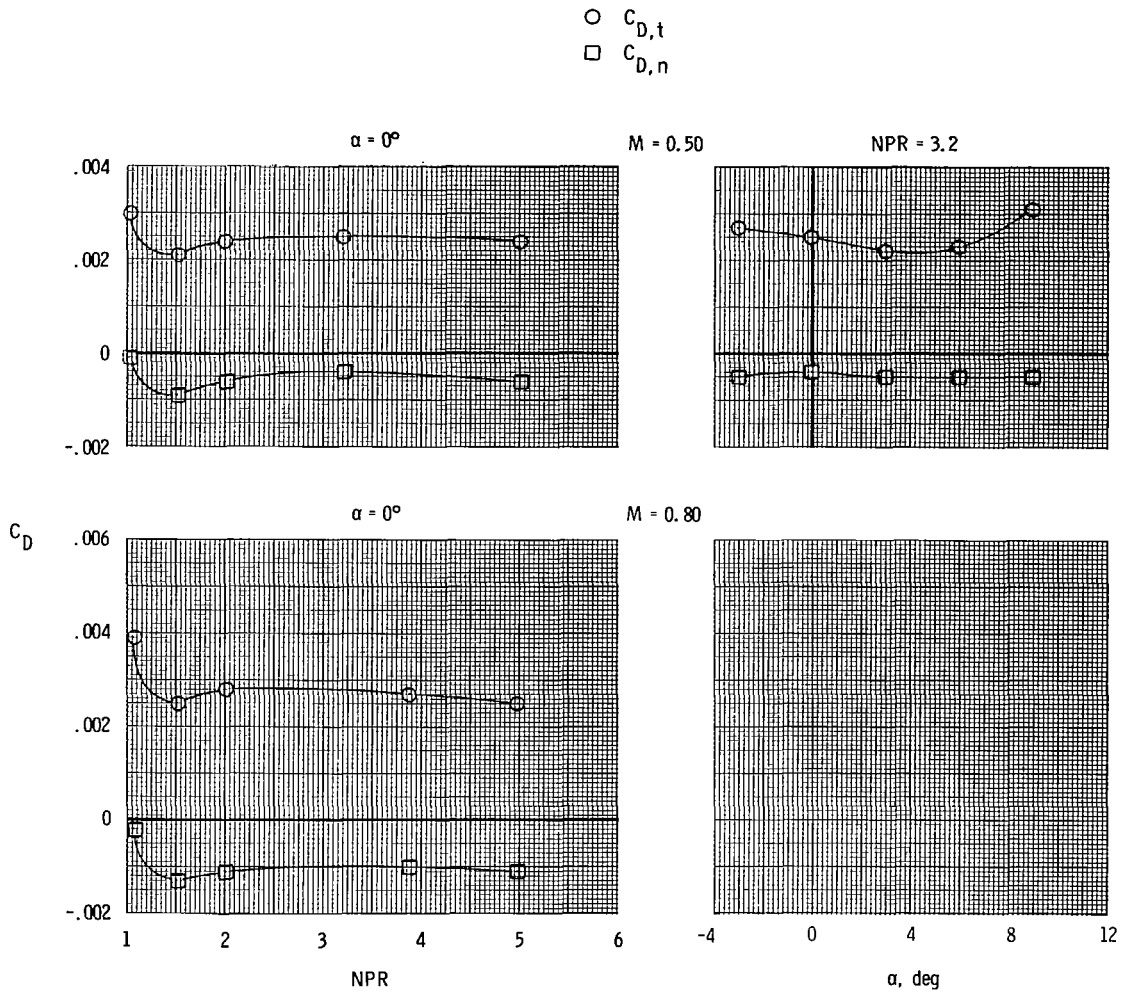
(a) Tails off.

Figure 6.- Variation of total (afterbody + nozzles + tails) and nozzle drag coefficients with nozzle pressure ratio and angle of attack for long subsonic dry power nozzles.
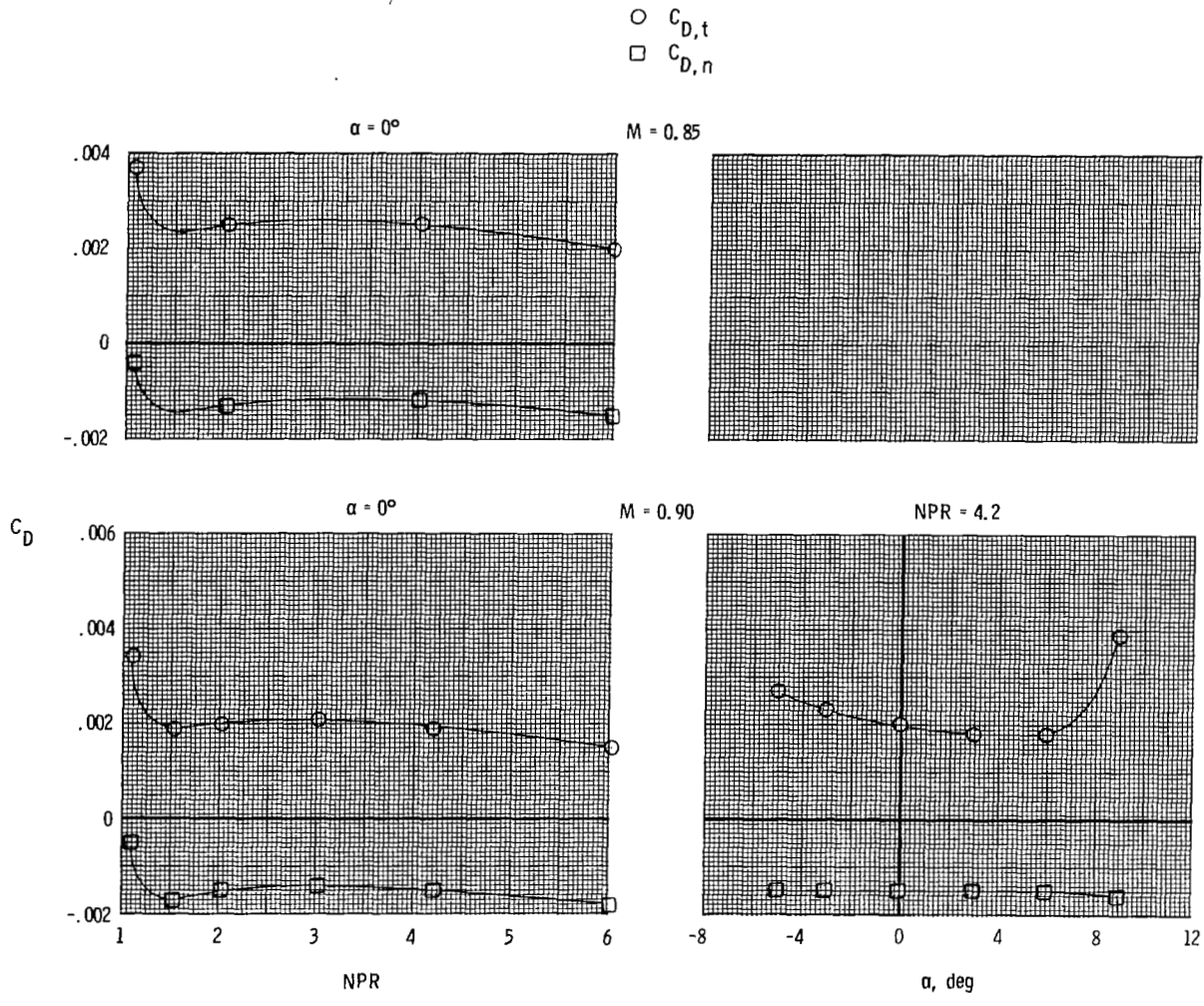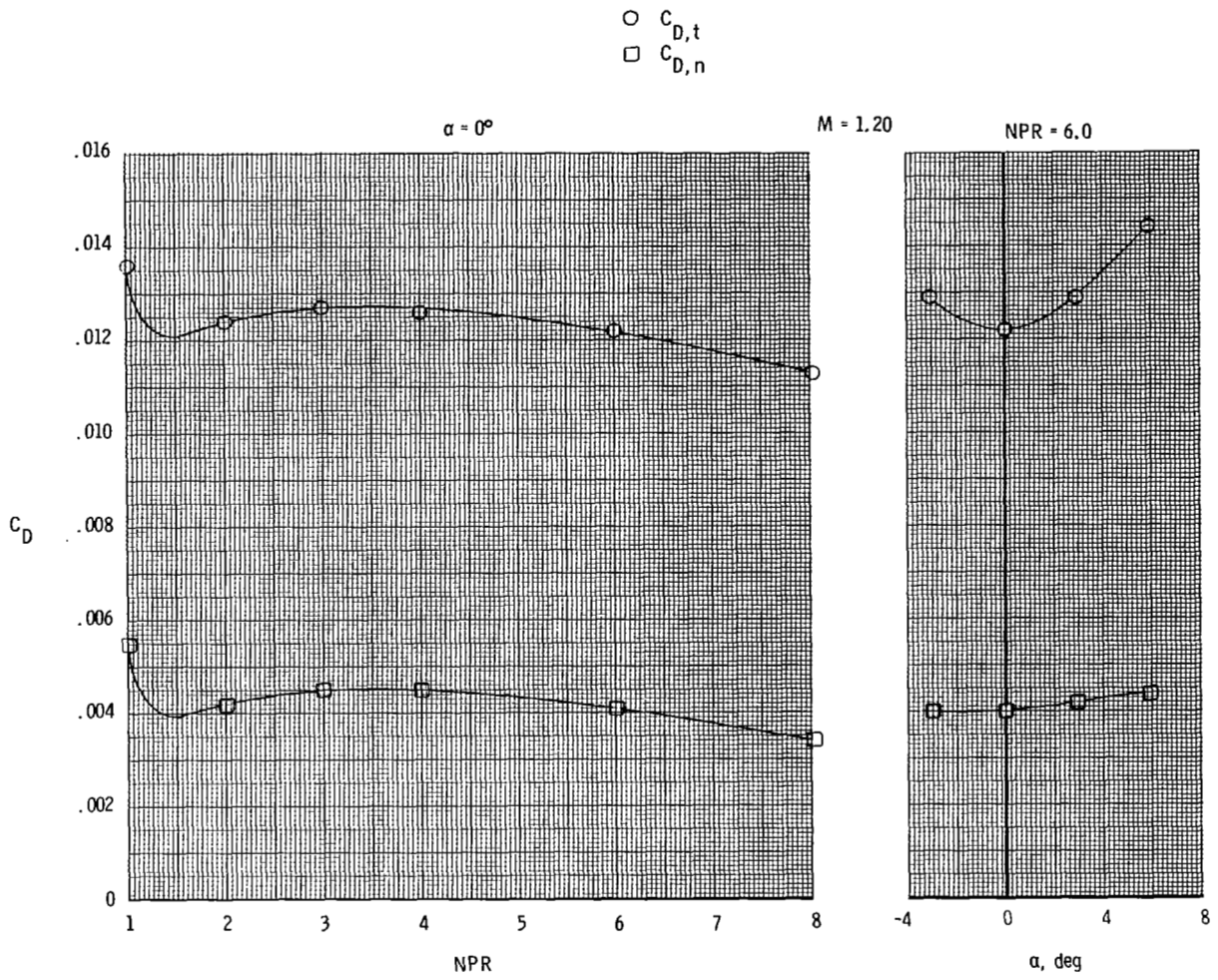
(a) Continued.

Figure 6.- Continued.

(a) Concluded.
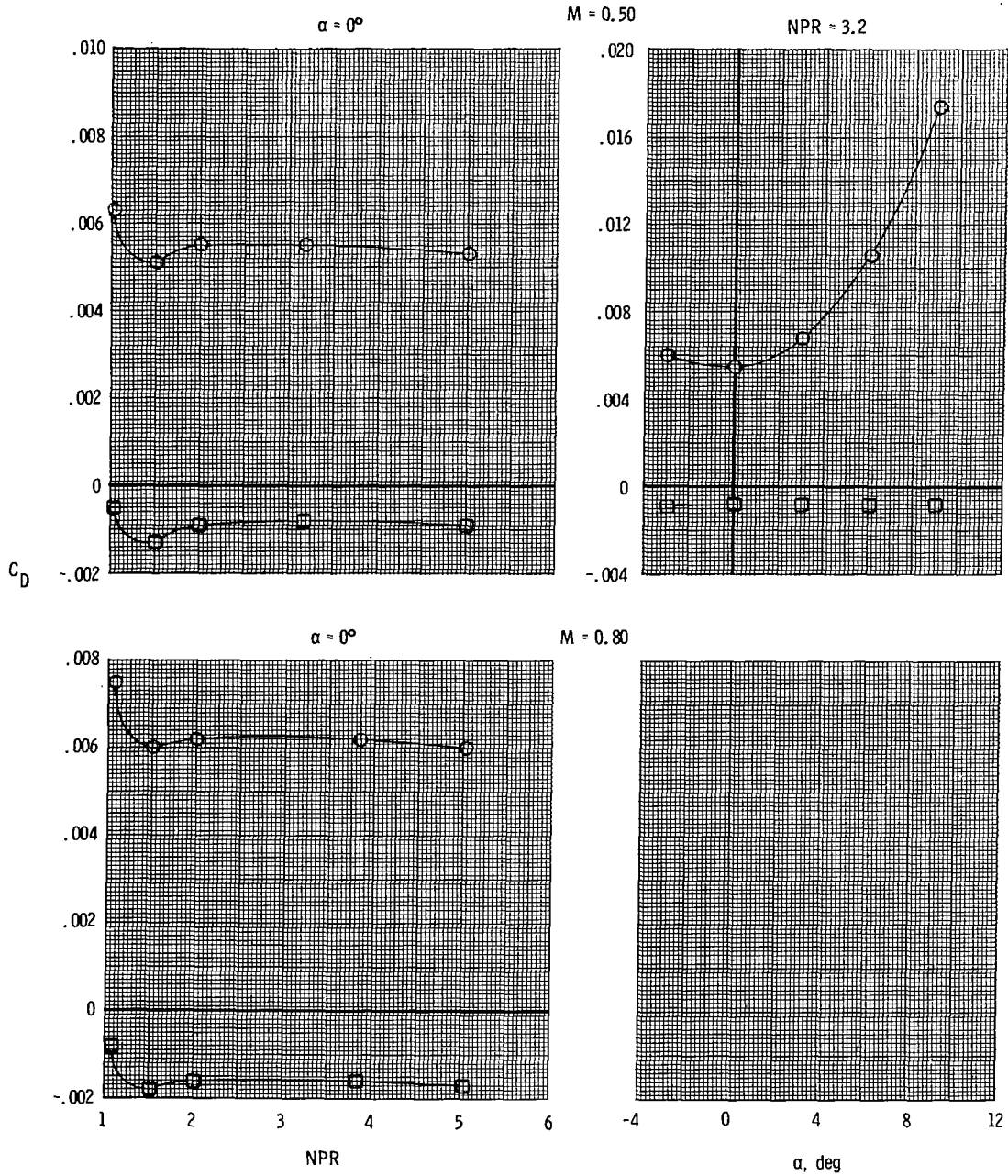
Figure 6.- Continued.

(b) Mid horizontal tails; mid vertical tails.
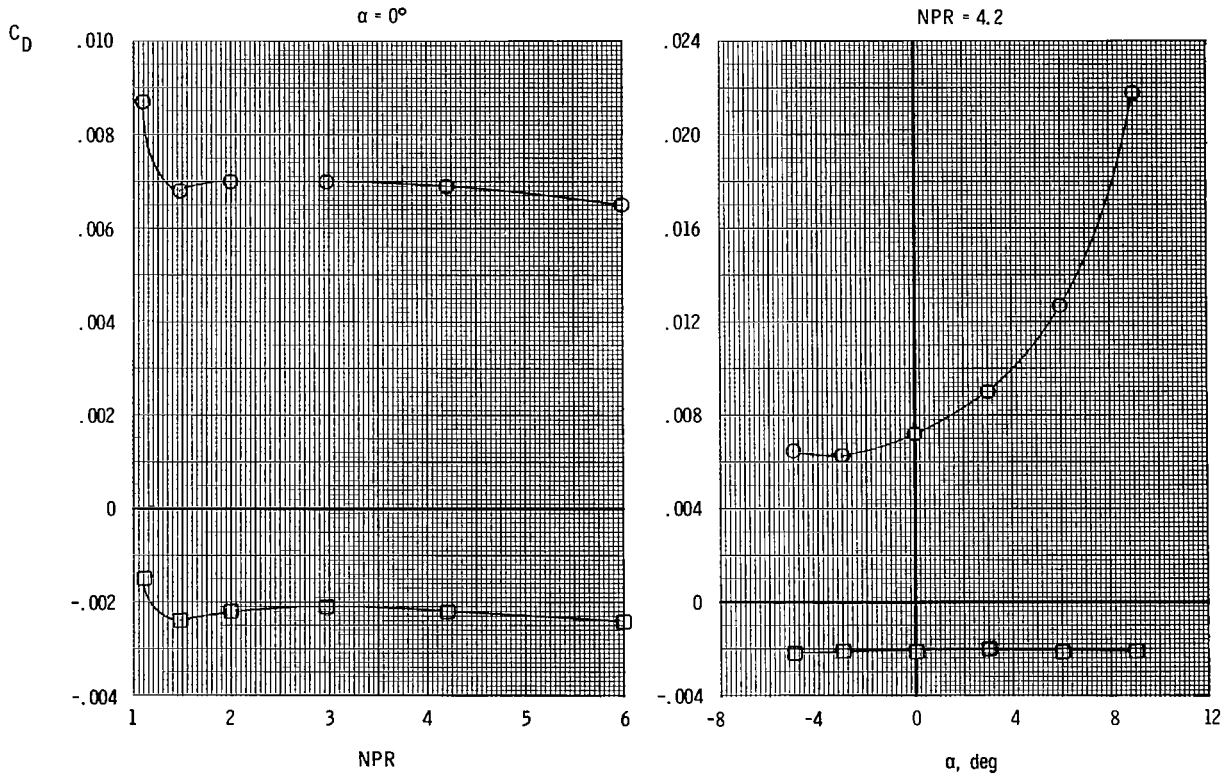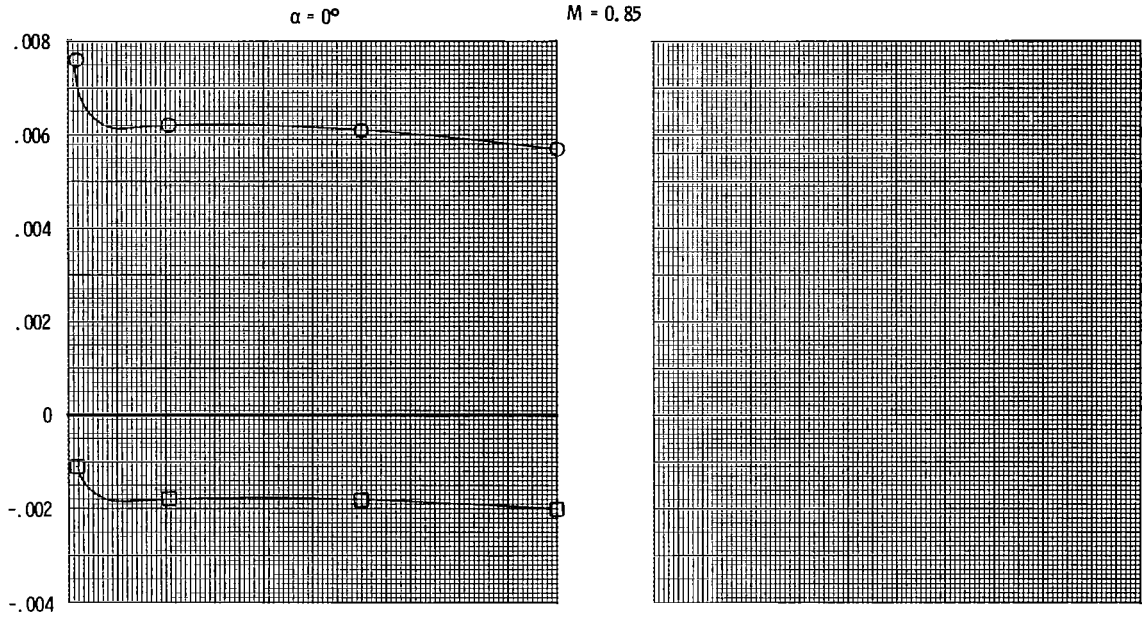
Figure 6.- Continued.

(b) Continued.
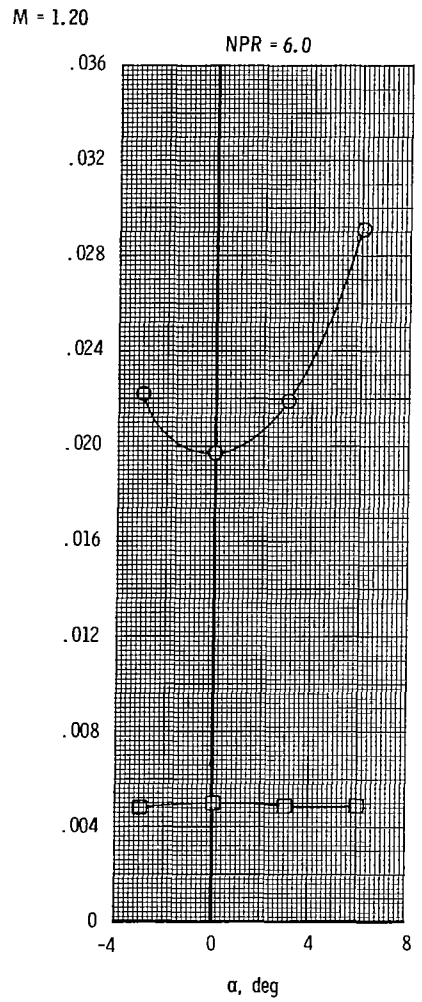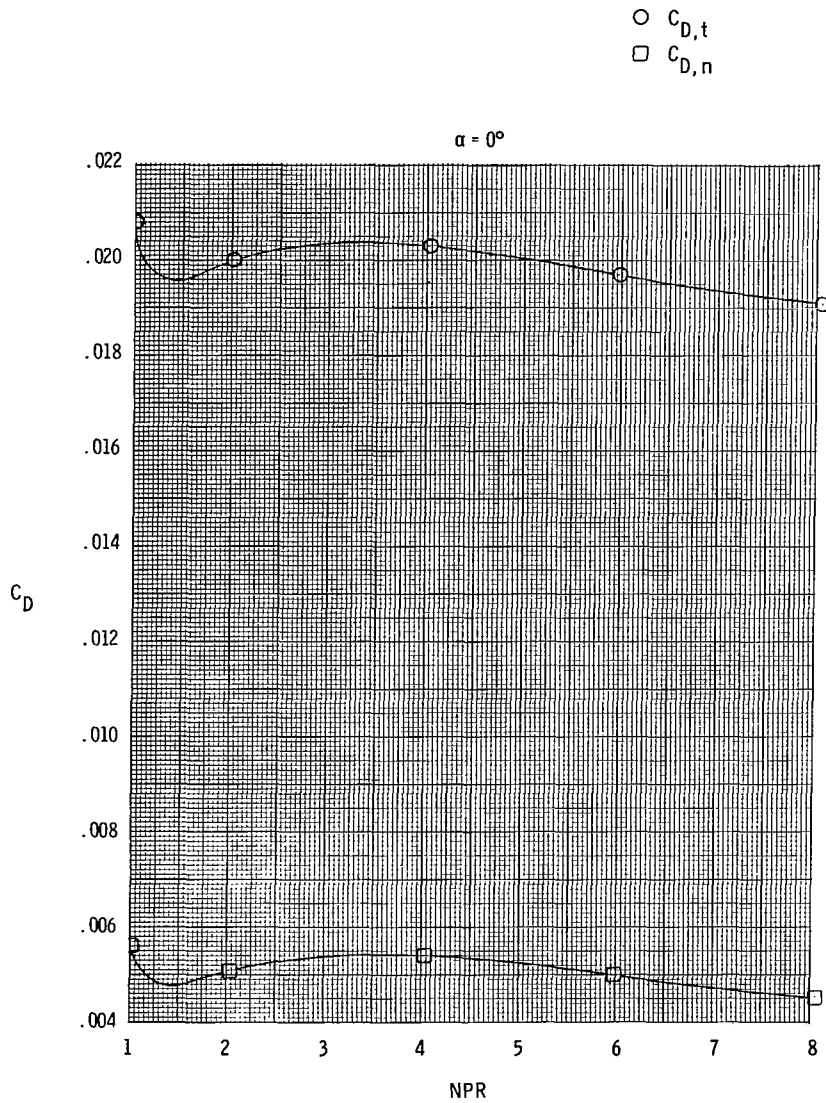
Figure 6.- Continued.

(b) Concluded.
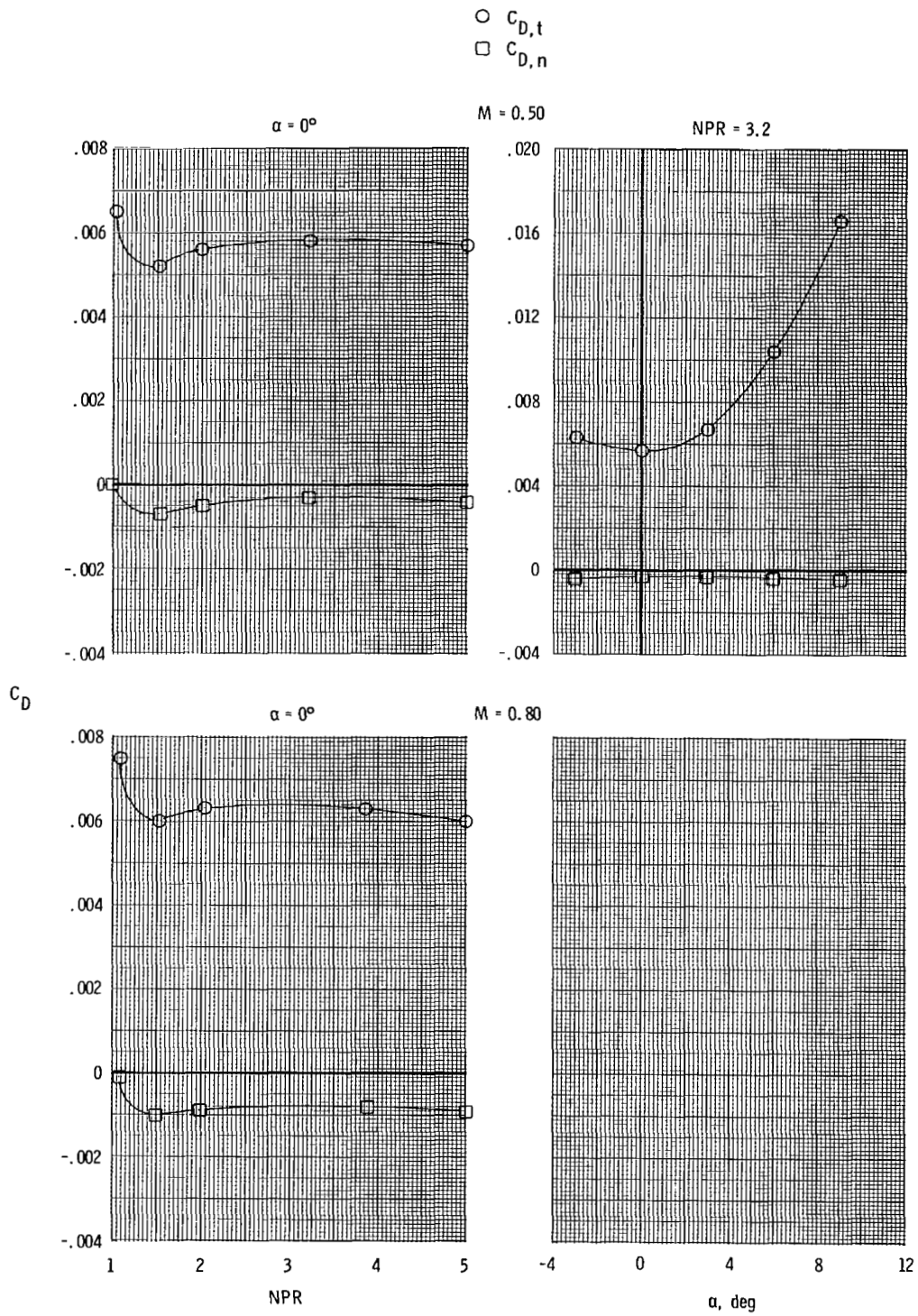
Figure 6.- Continued.

(c) Aft horizontal tails; mid vertical tails.
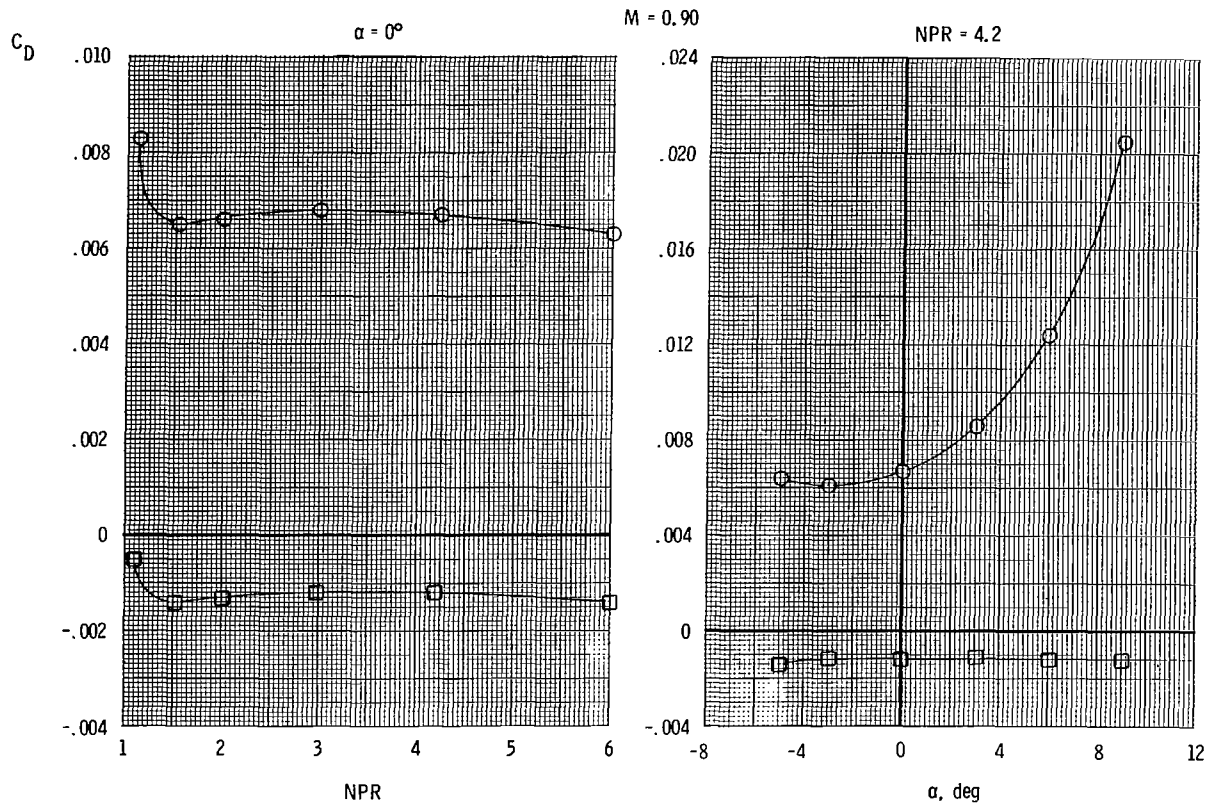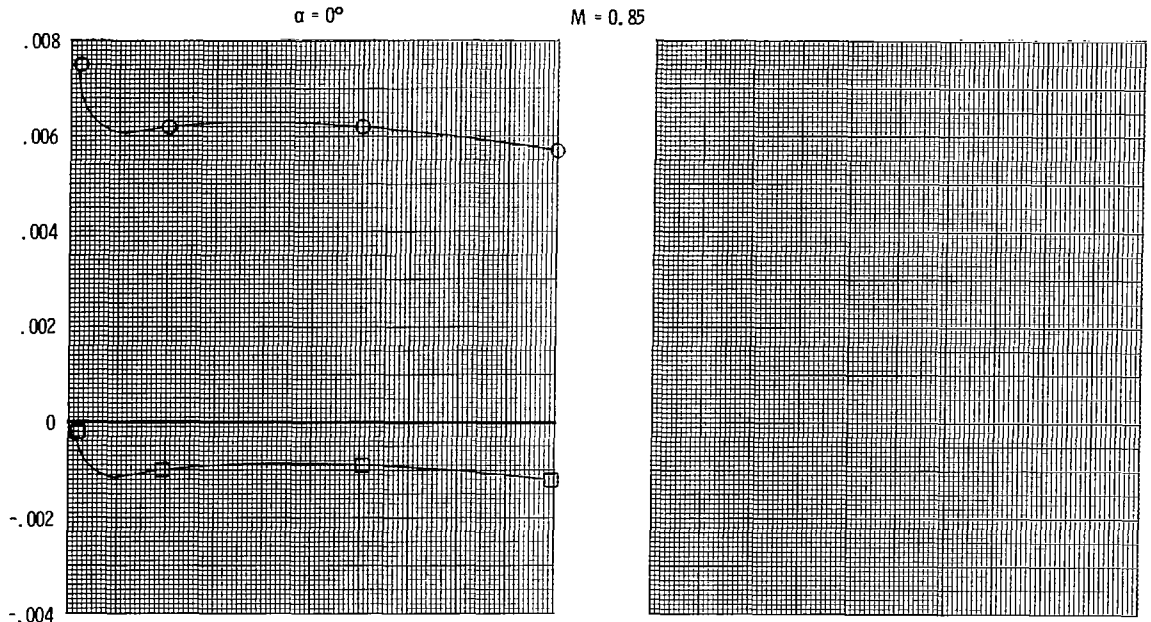
Figure 6.- Continued.

(c) Continued.
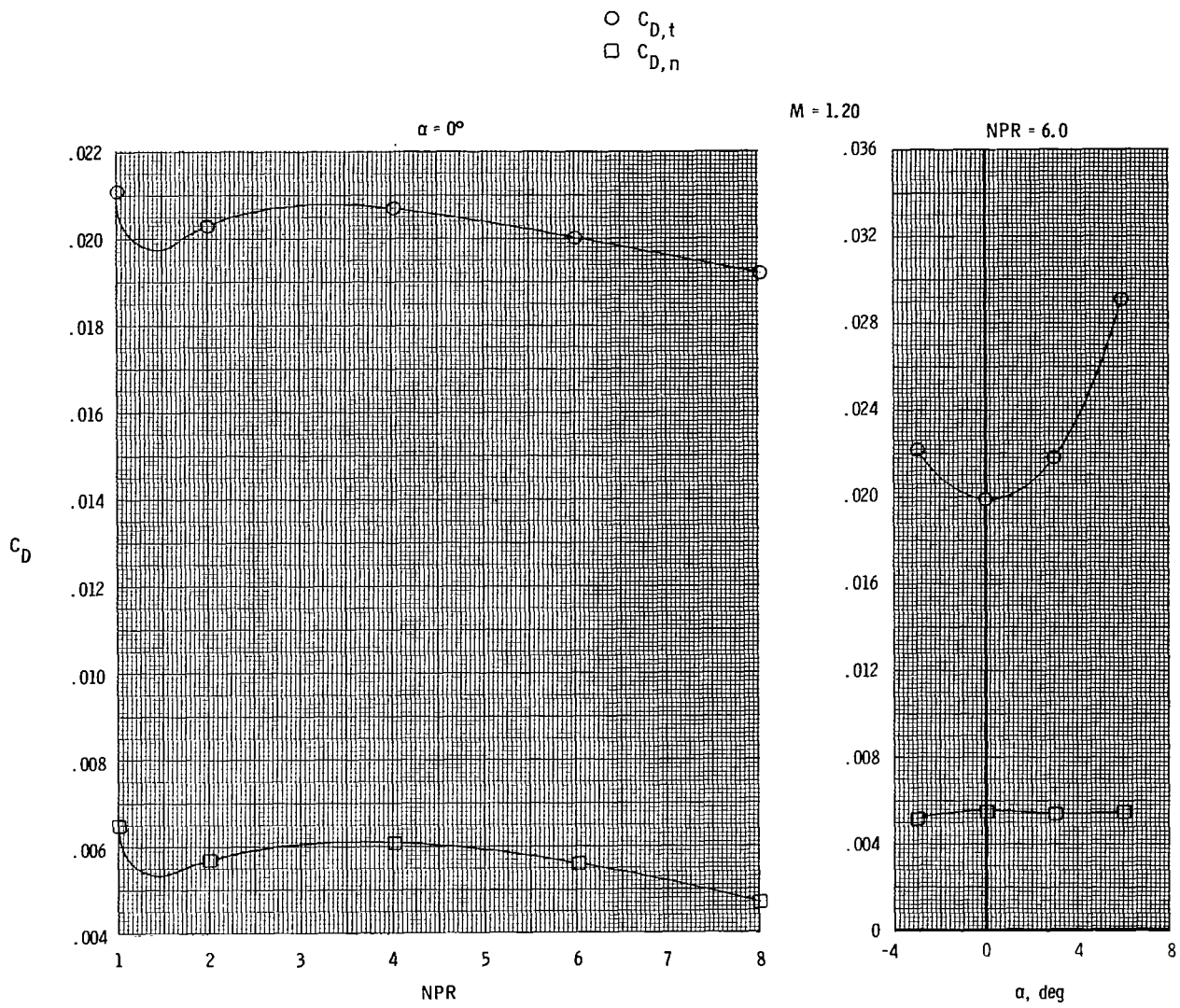
Figure 6.- Continued.

(c) Concluded.
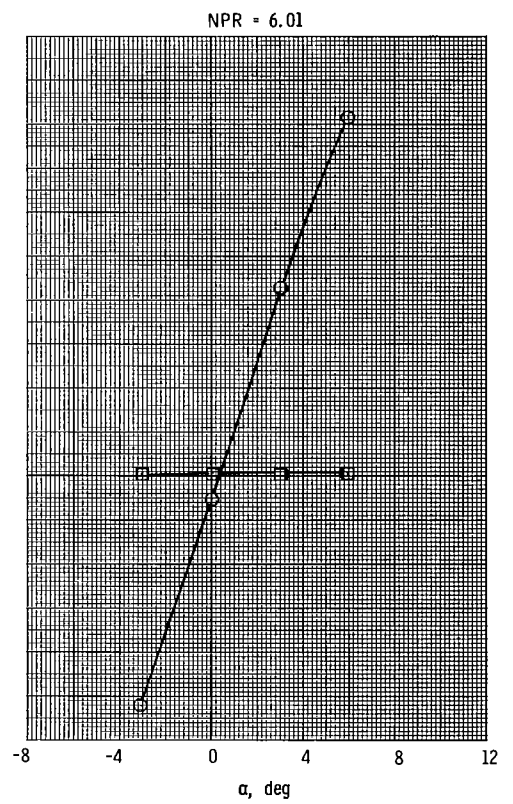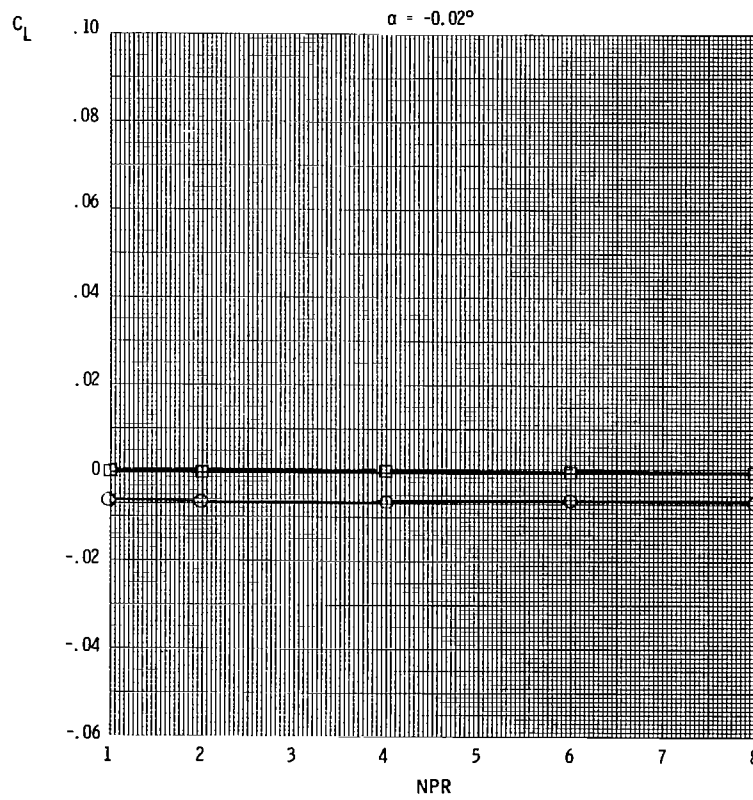
Figure 6.- Concluded.
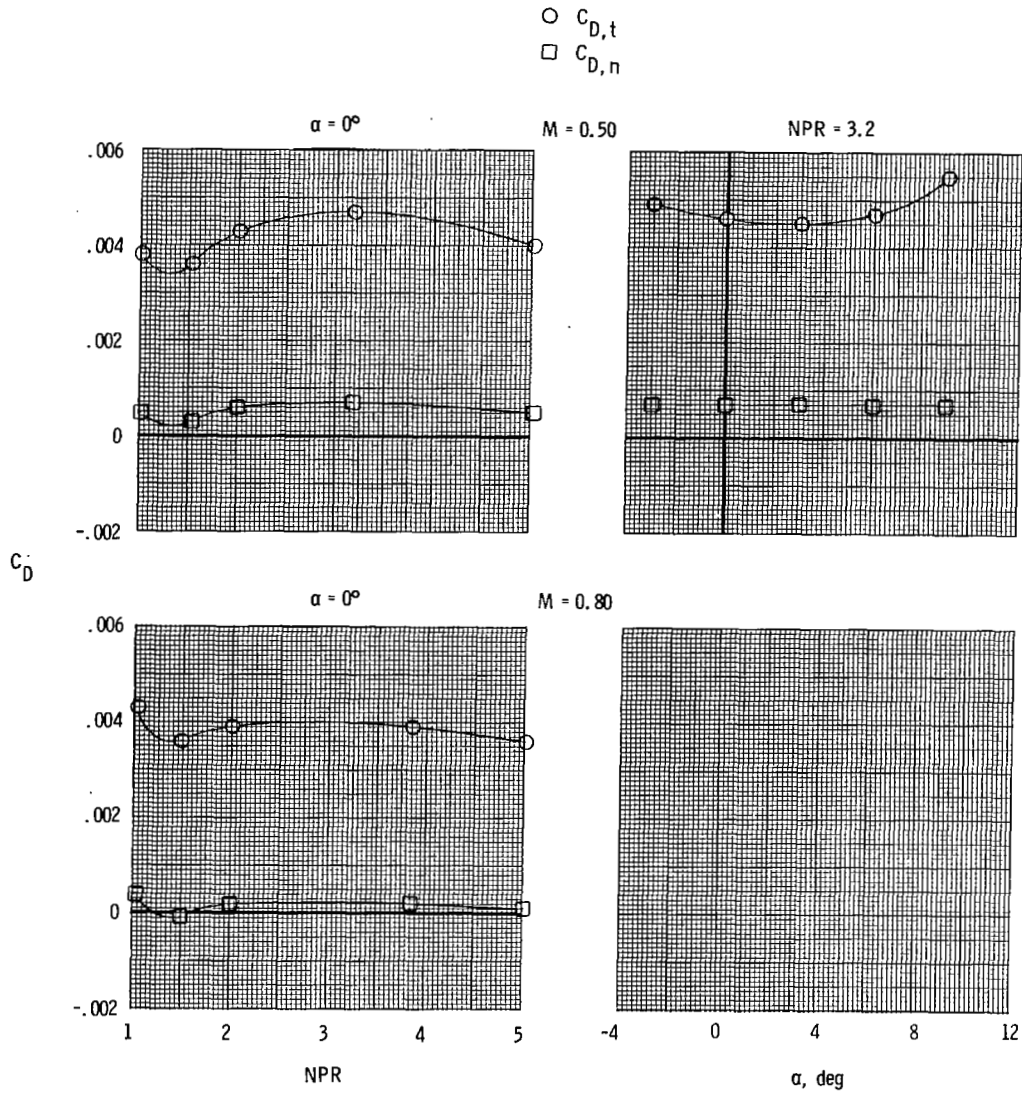
(a) Tails off.

Figure 7.- Variation of total (afterbody + nozzles + tails) and nozzle drag coefficients with nozzle pressure ratio and angle of attack for short supersonic dry power nozzles.
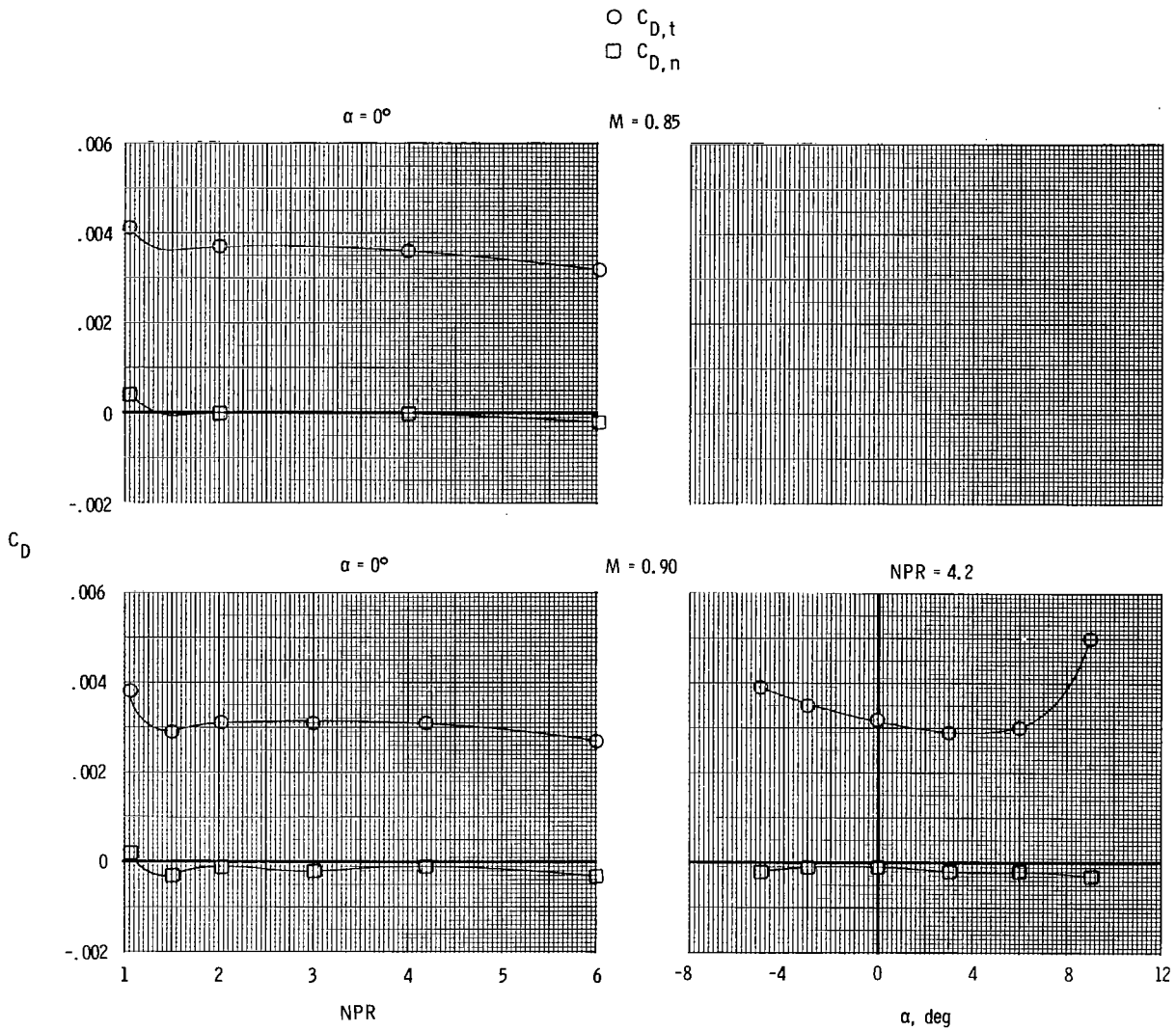
(a) Continued.
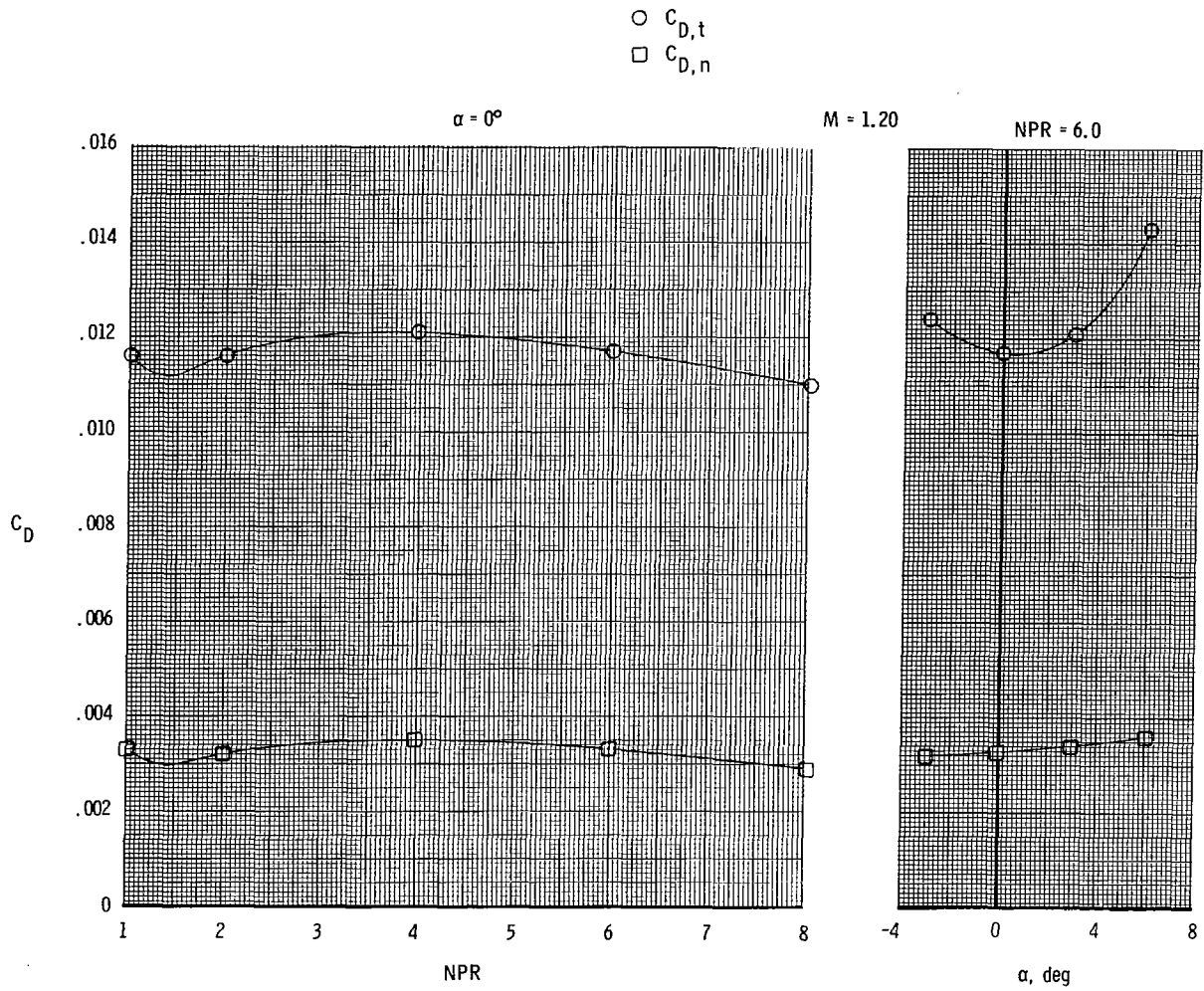
Figure 7.- Continued.

(a) Concluded.
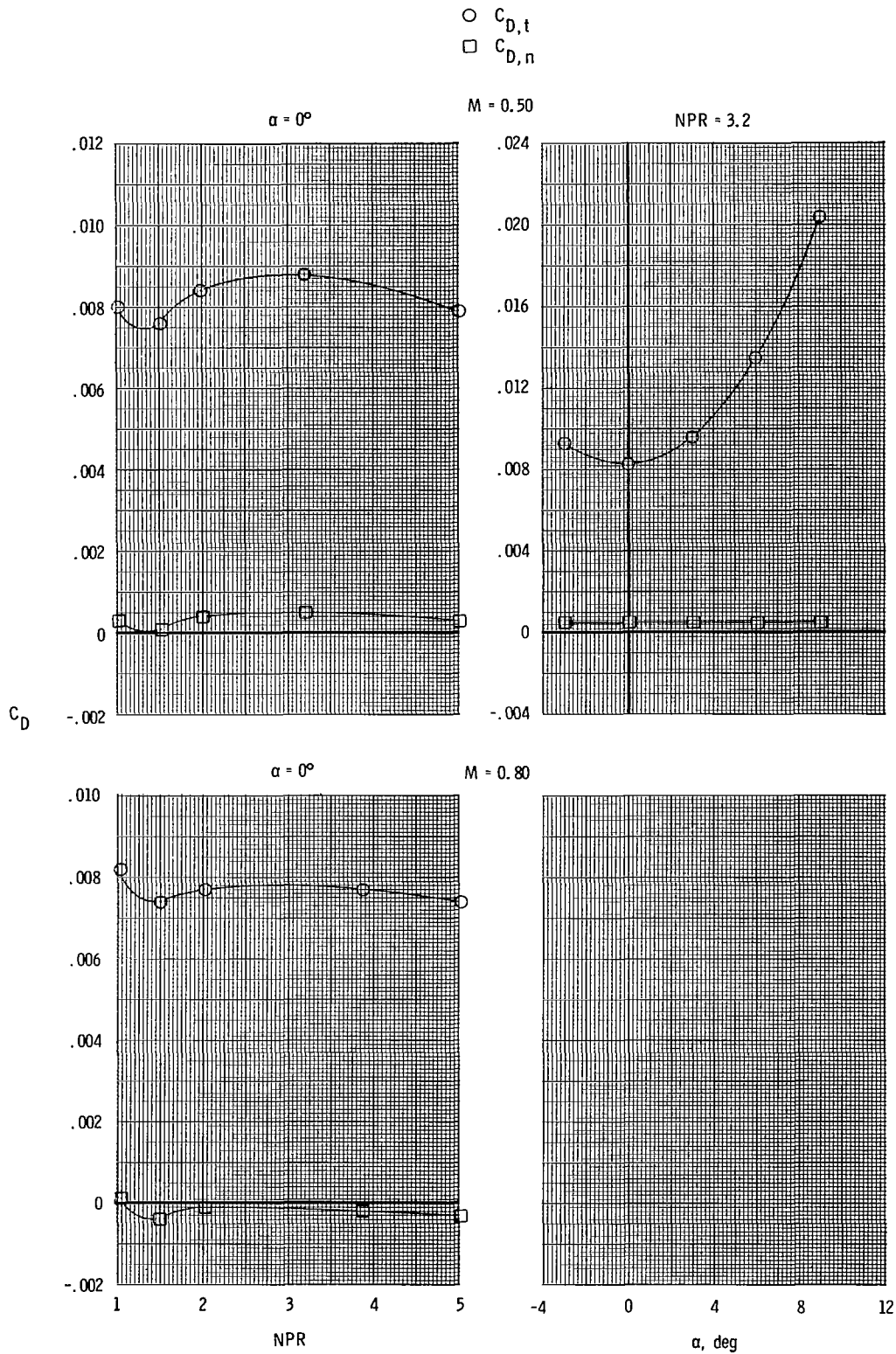
Figure 7.- Continued.

(b) Mid horizontal tails; forward vertical tails.
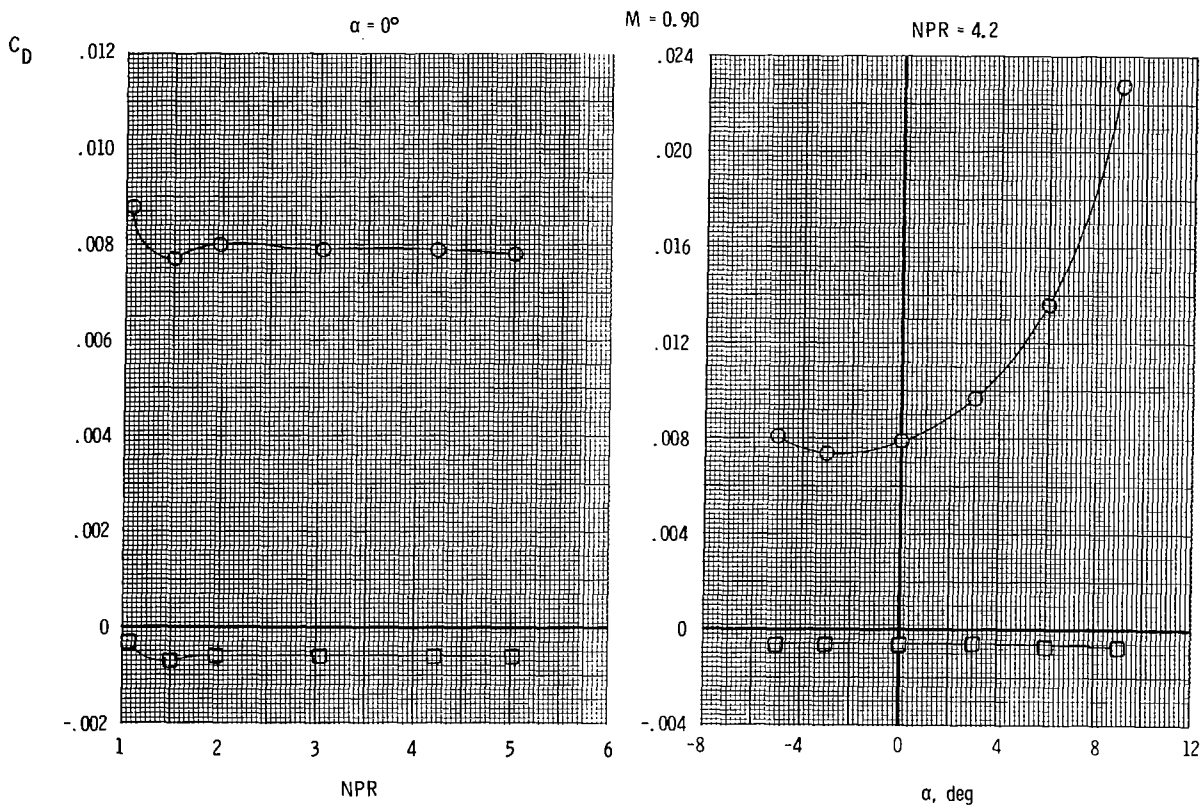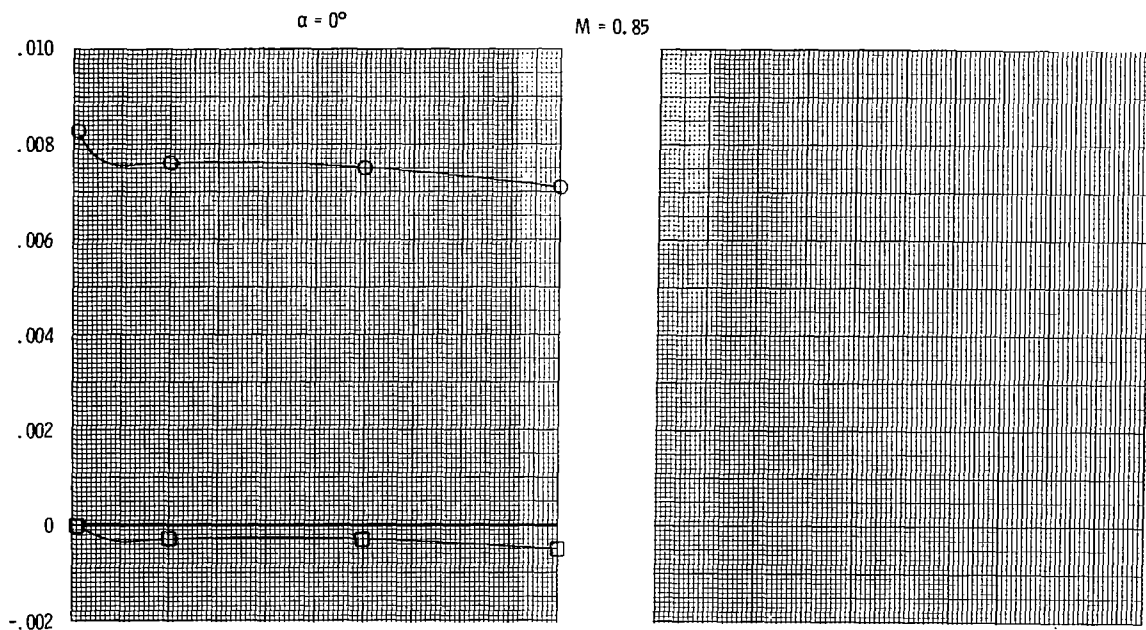
Figure 7.- Continued.

(b) Continued.
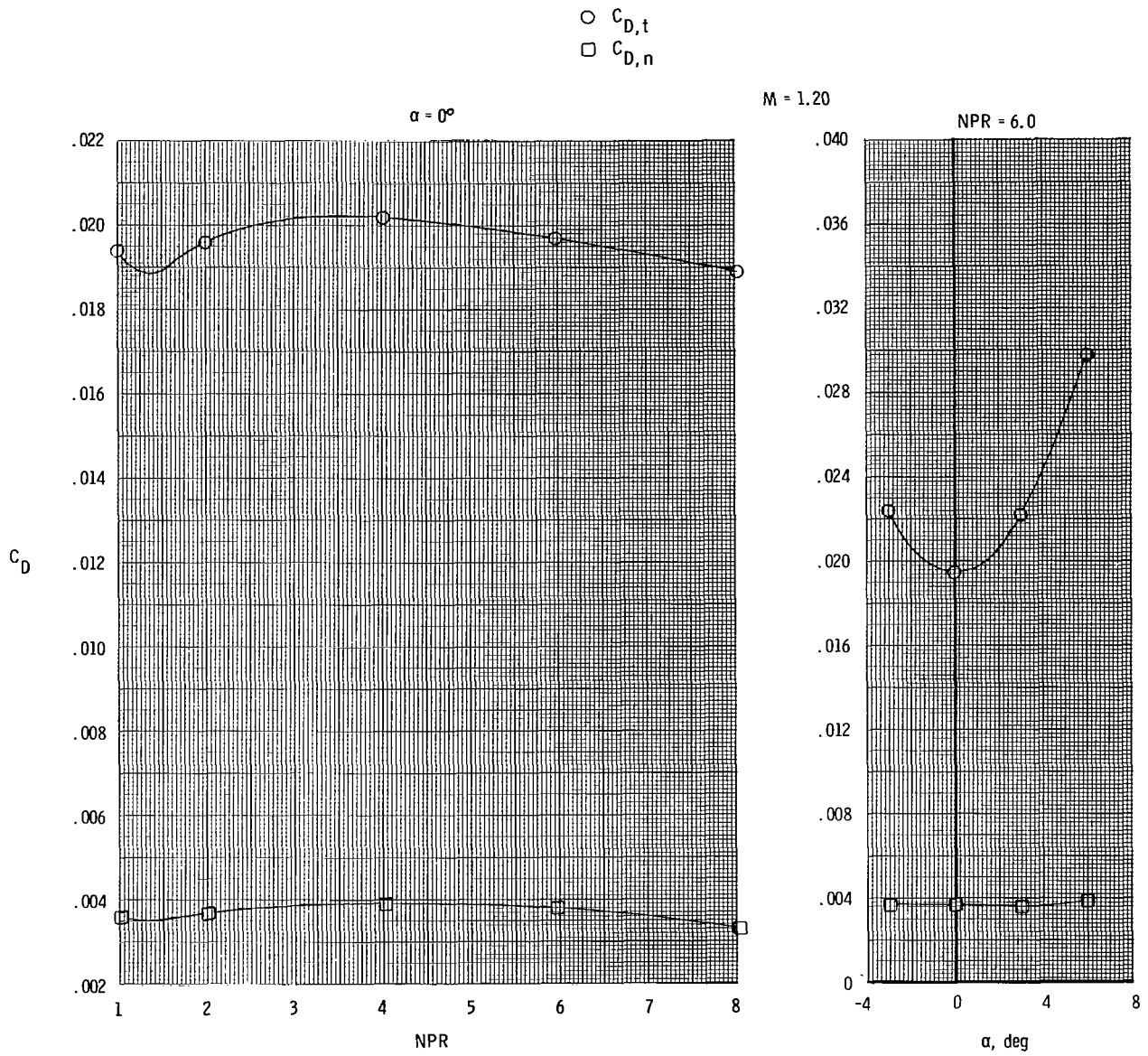
Figure 7.- Continued.

(b) Concluded.

Figure 7.- Continued.

(c) Aft horizontal tails; forward vertical tails.
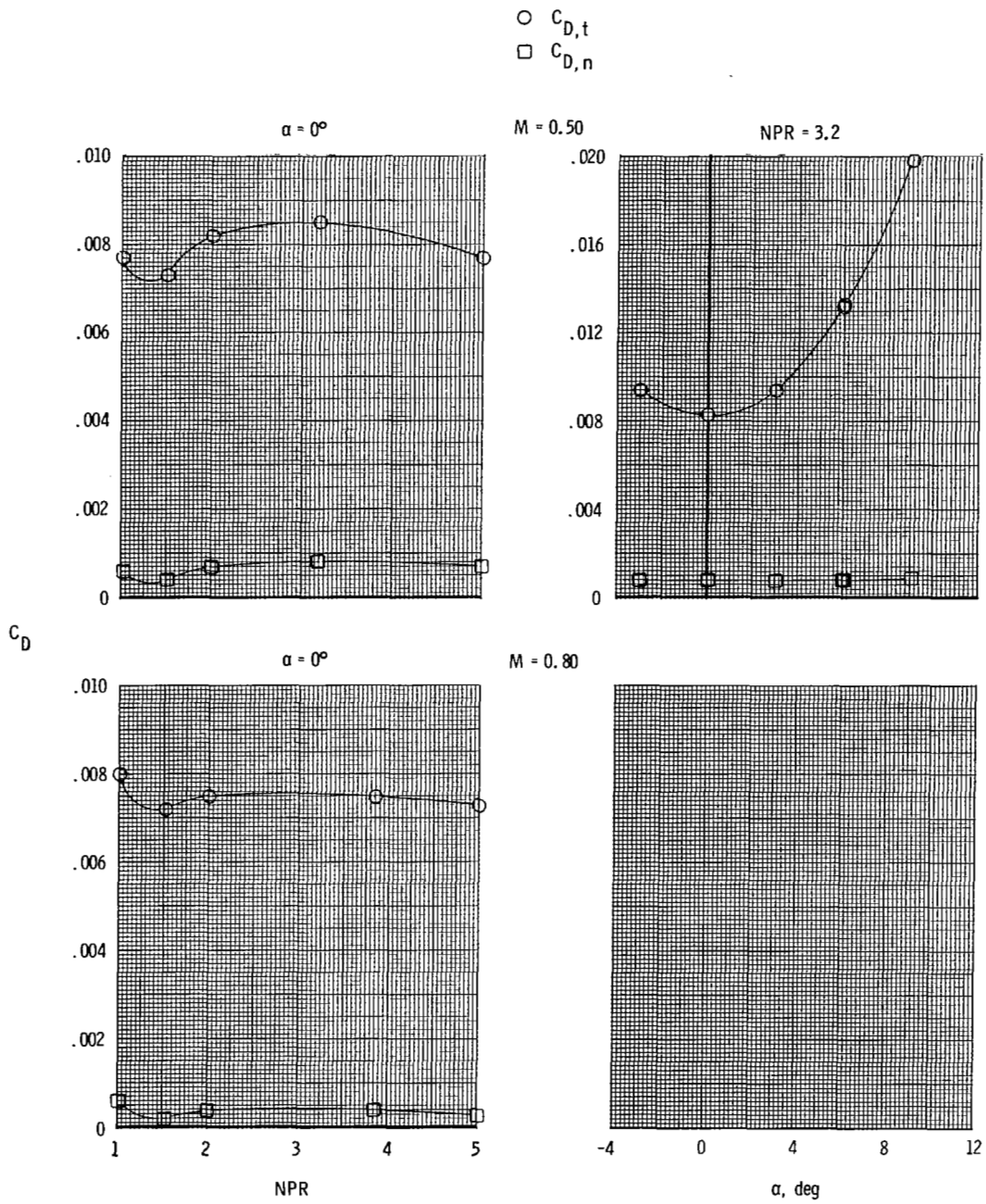
Figure 7.- Continued.

(c) Continued.

Figure 7.- Continued.

$$\circ \quad c_{D,t}$$
$$\square \quad c_{D,n}$$

$\alpha = 0°$ M = 1.20

NPR = 6.0

c_D

NPR

α, deg
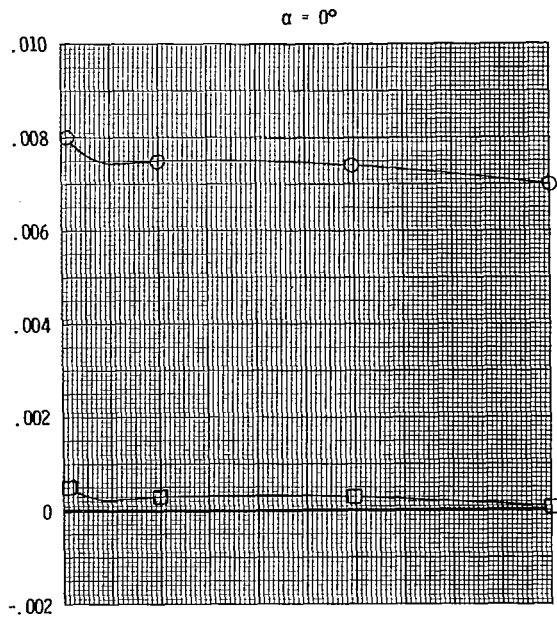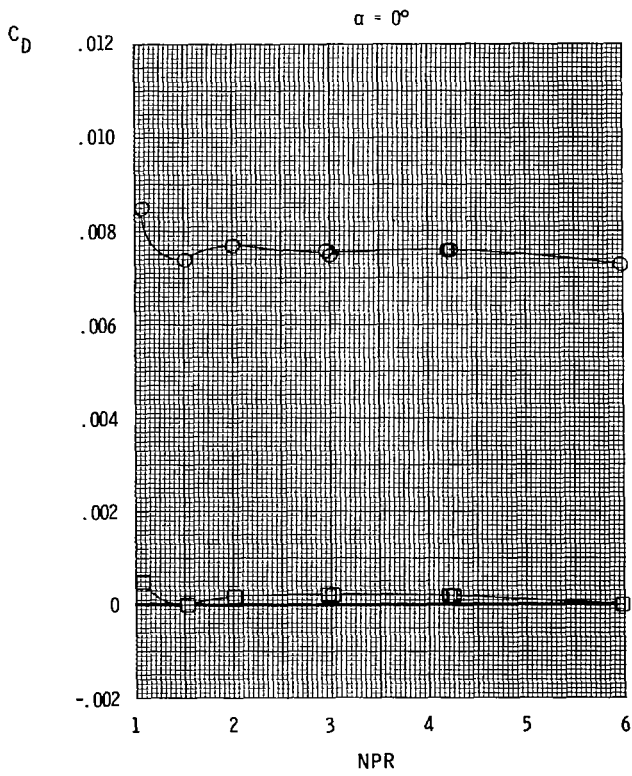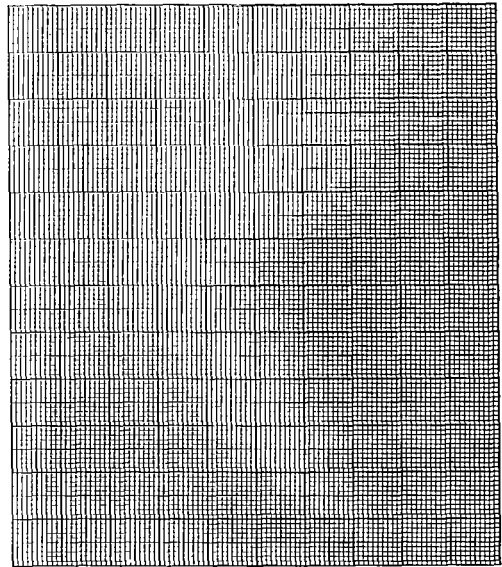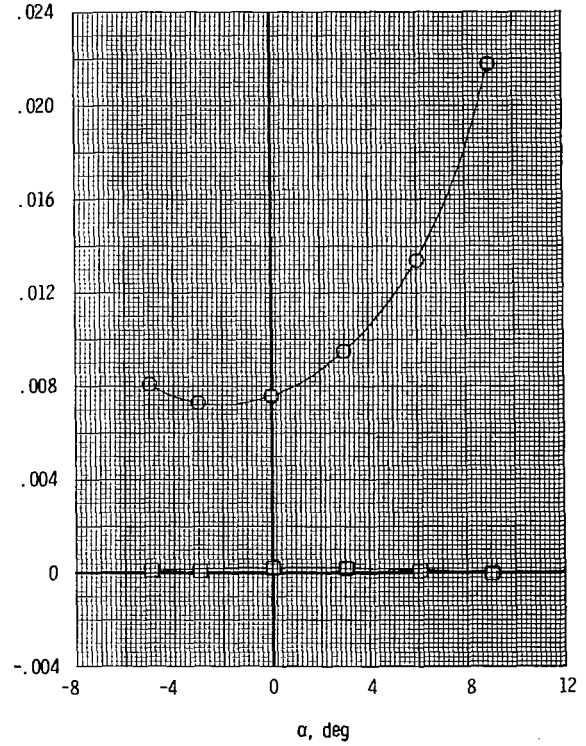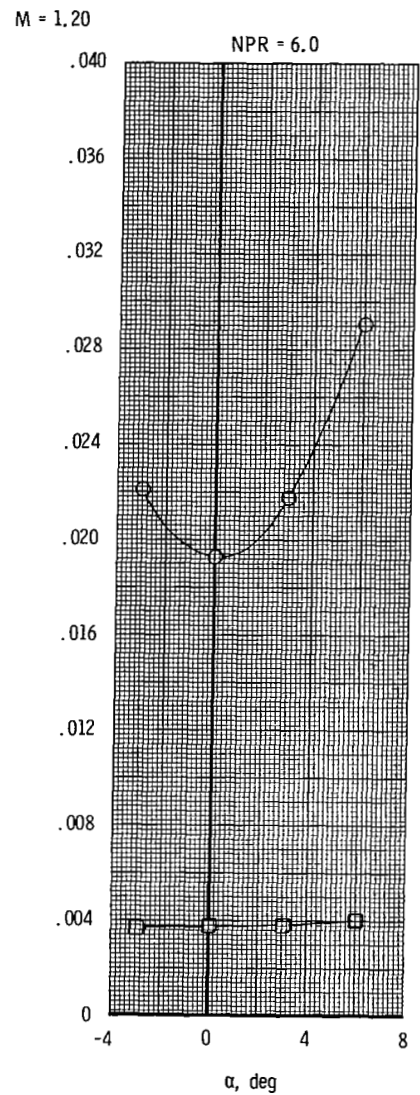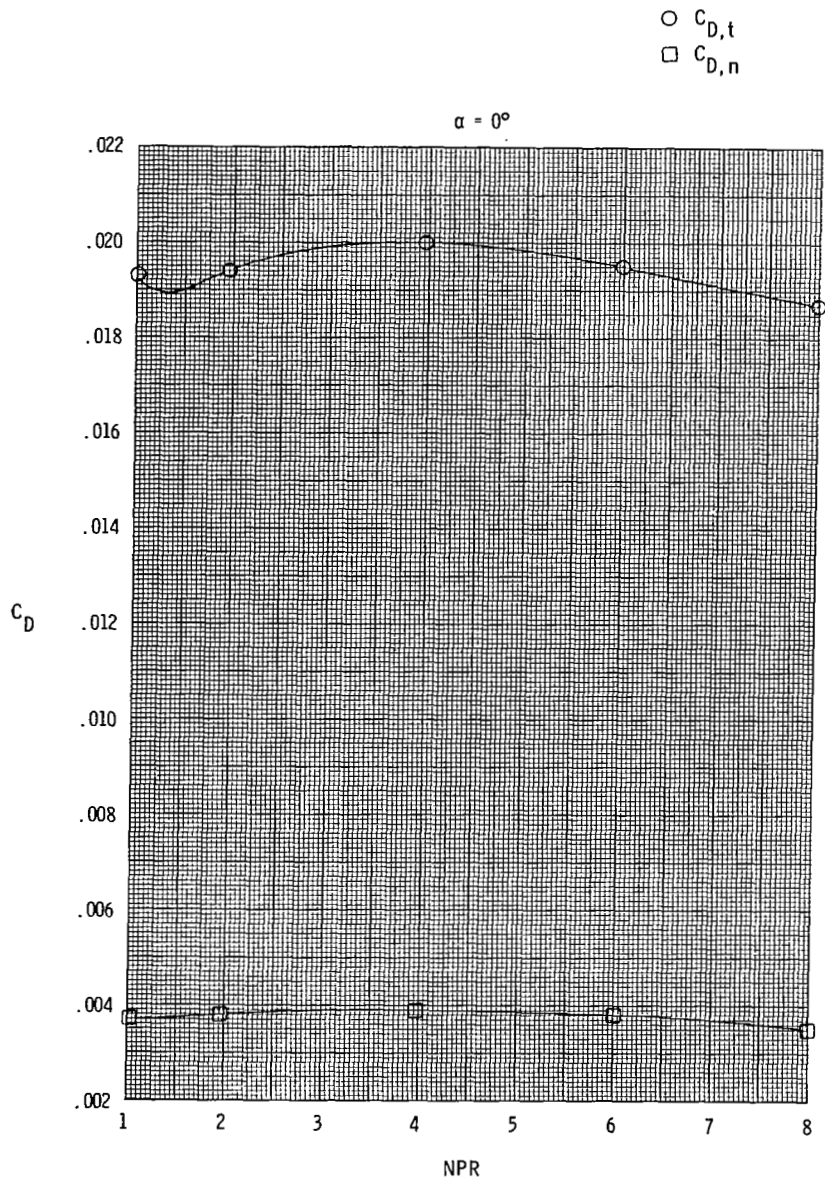
(c) Concluded.
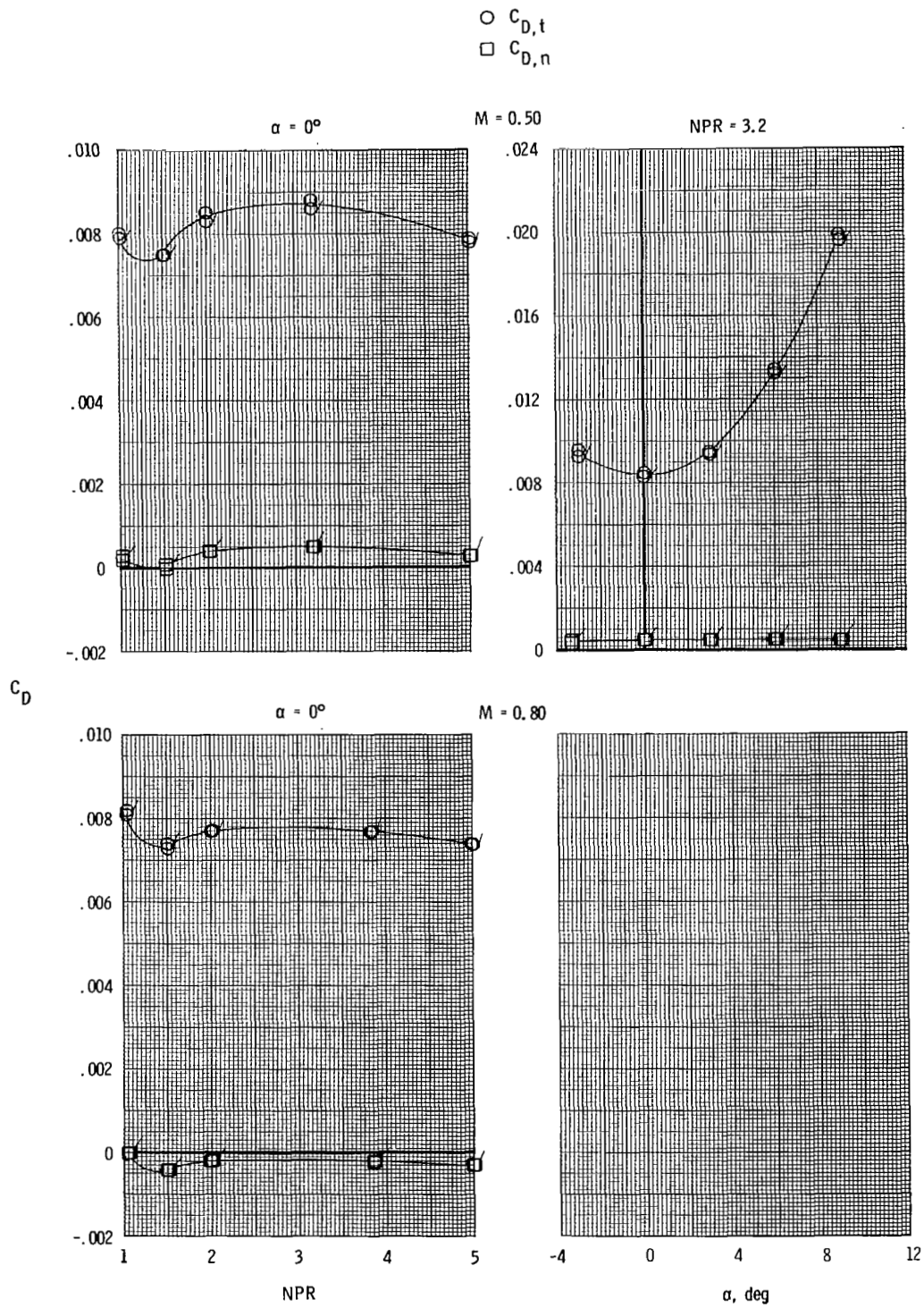
Figure 7.- Continued.

(d) Mid horizontal tails; mid vertical tails.
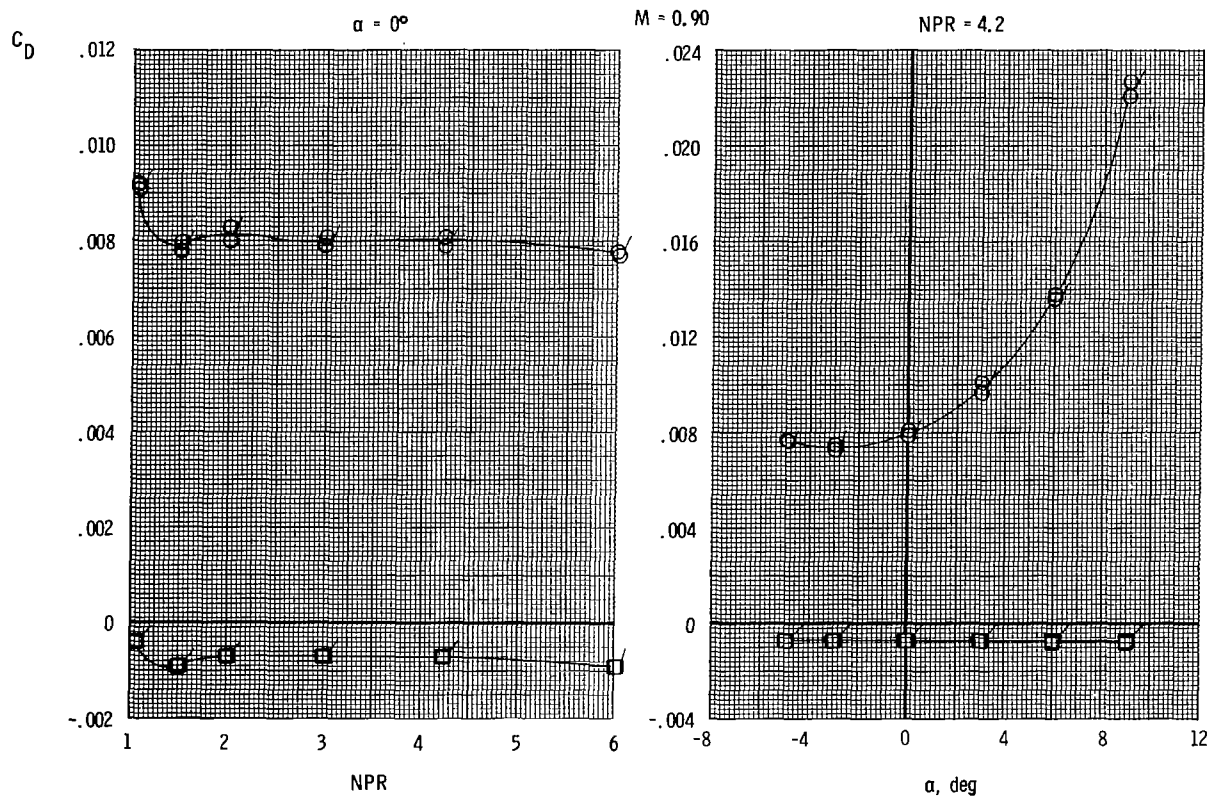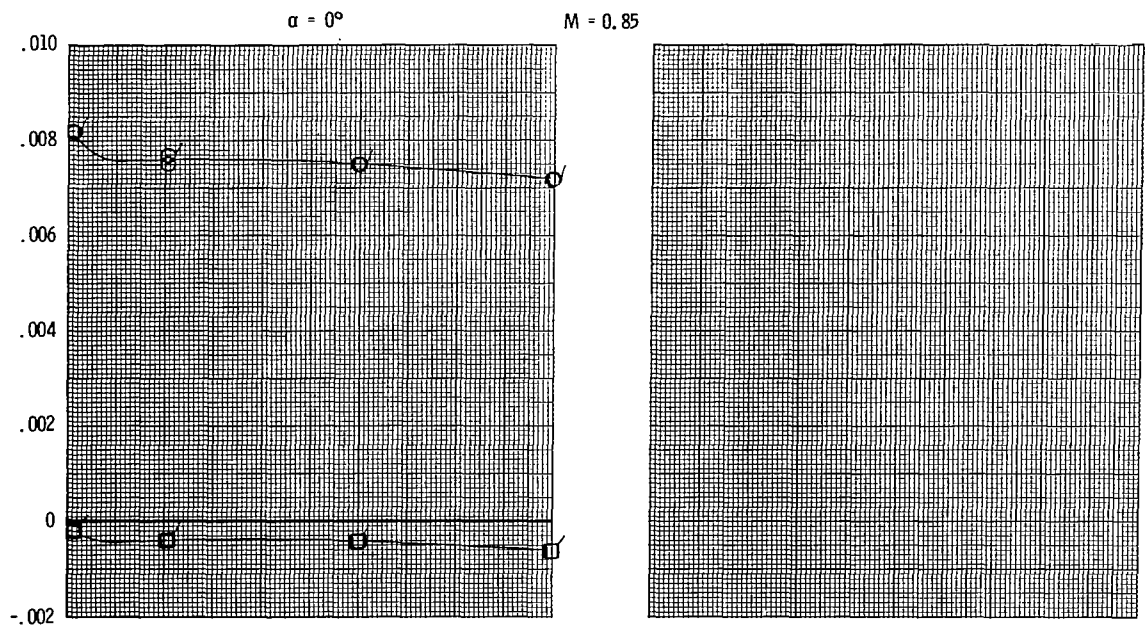
Figure 7.- Continued.

(d) Continued.
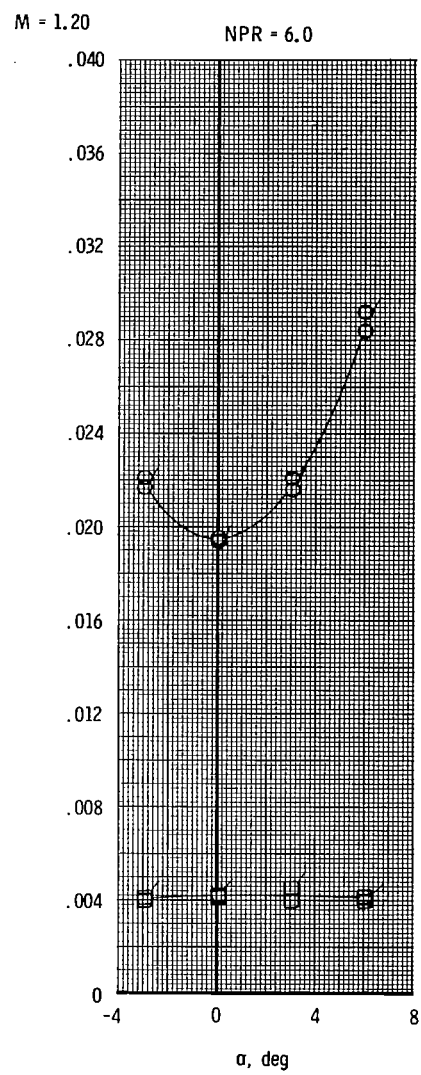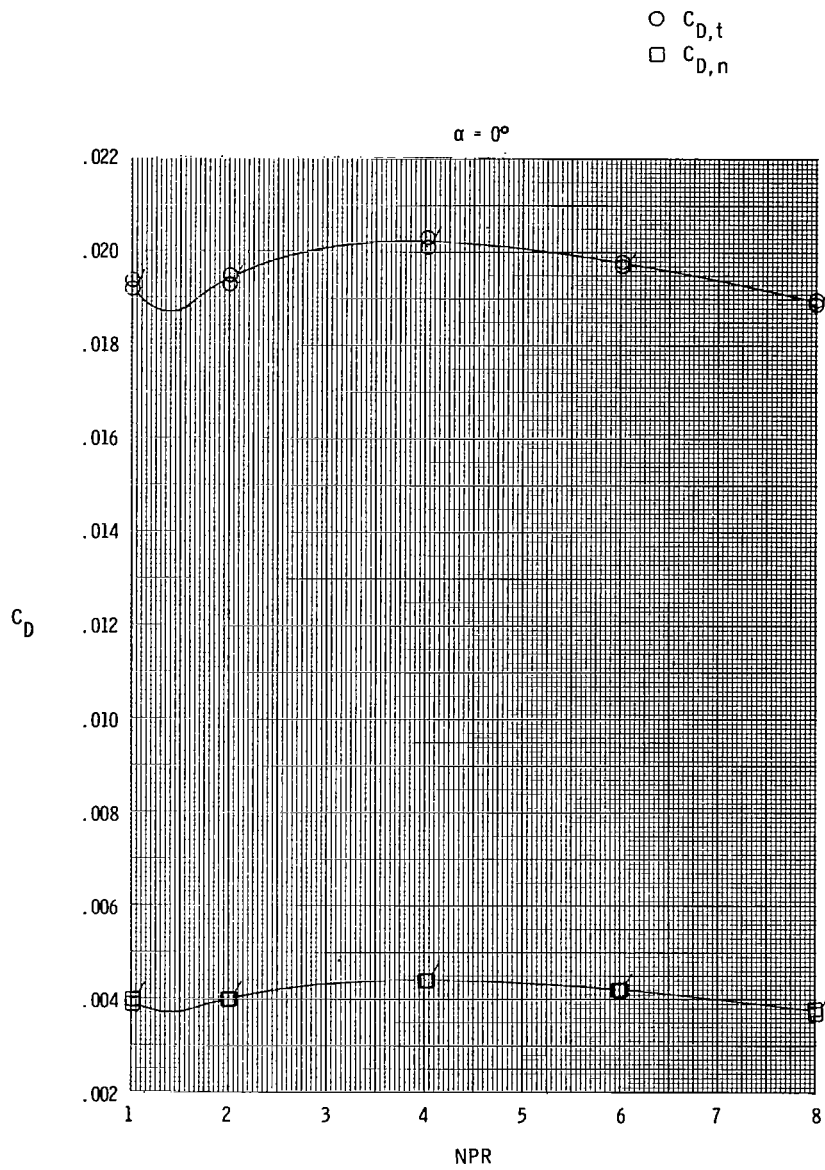
Figure 7.- Continued.

(d) Concluded.
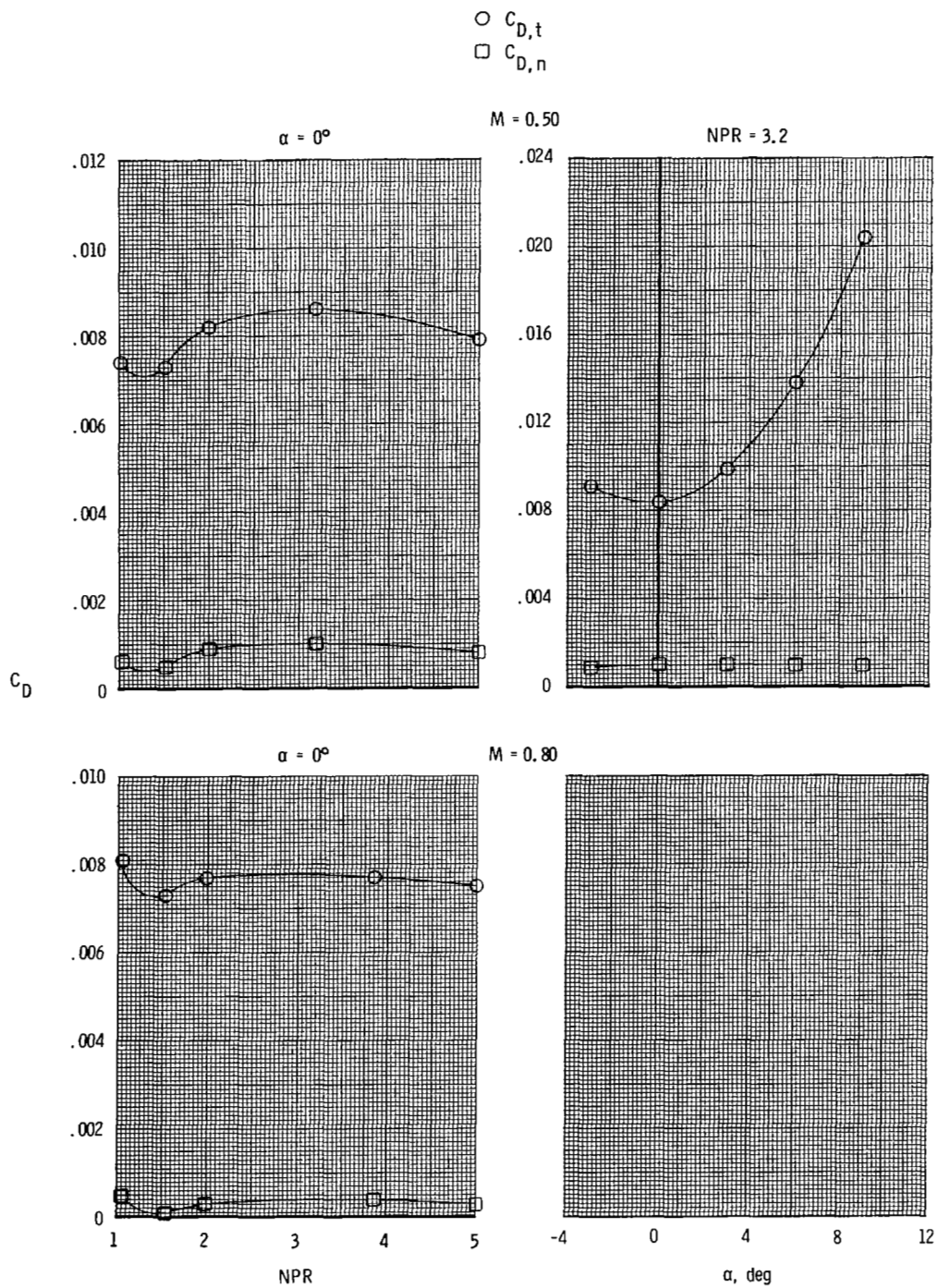
Figure 7.- Continued.

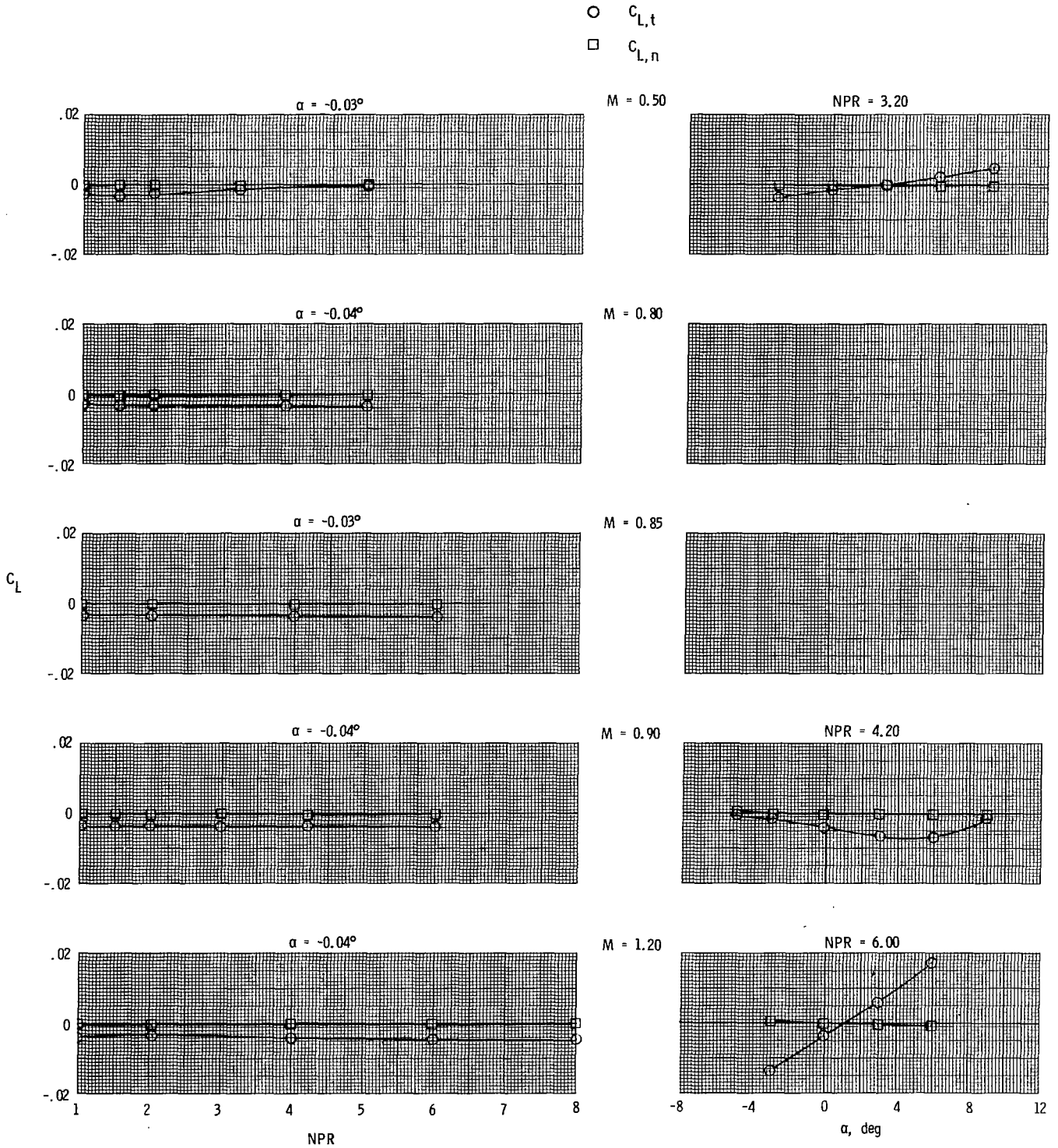(e) Aft horizontal tails; mid vertical tails.
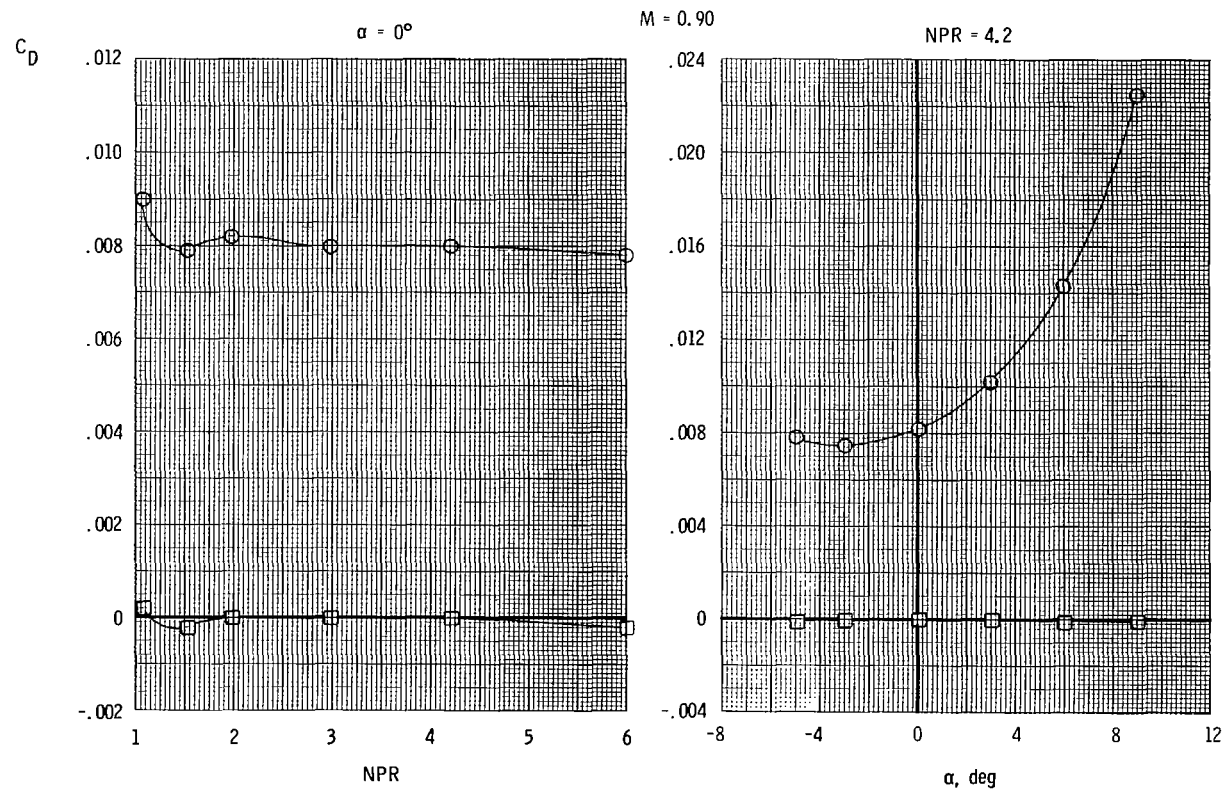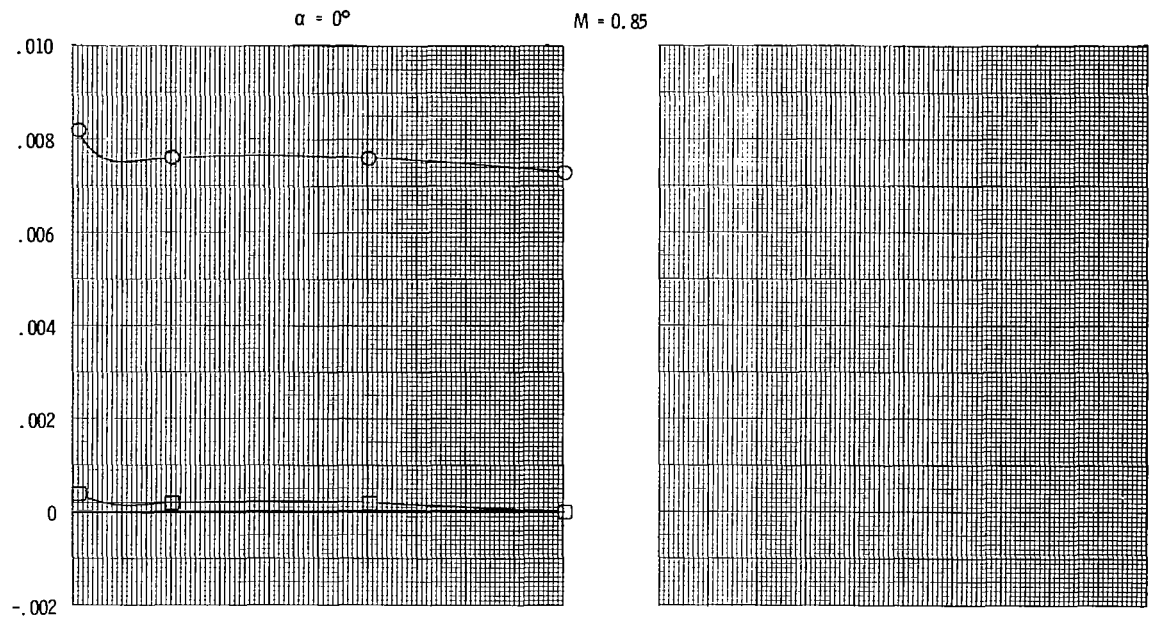
Figure 7.- Continued.

(e) Continued.

Figure 7.- Continued.
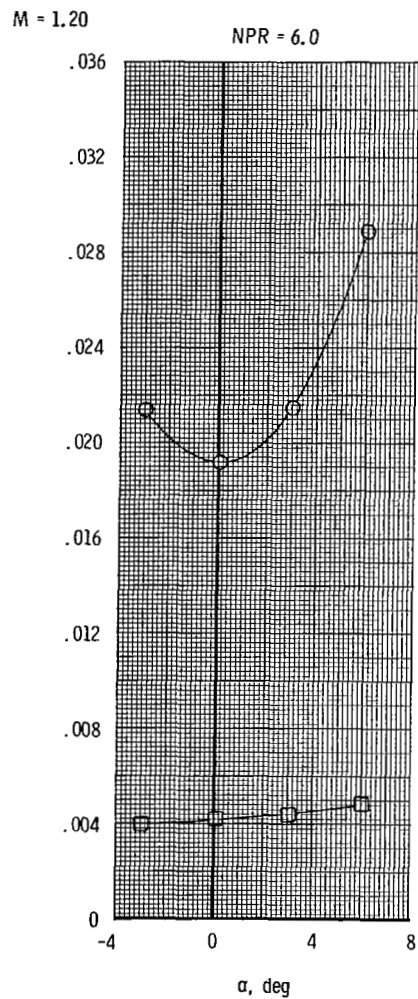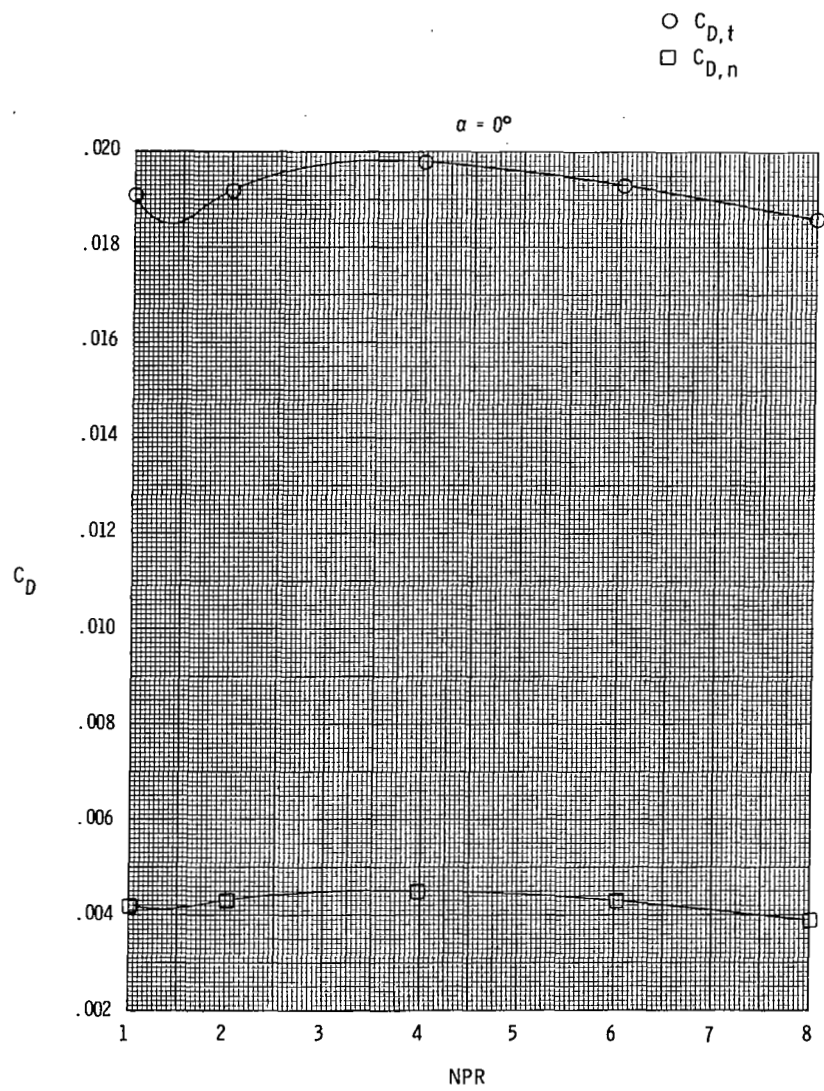
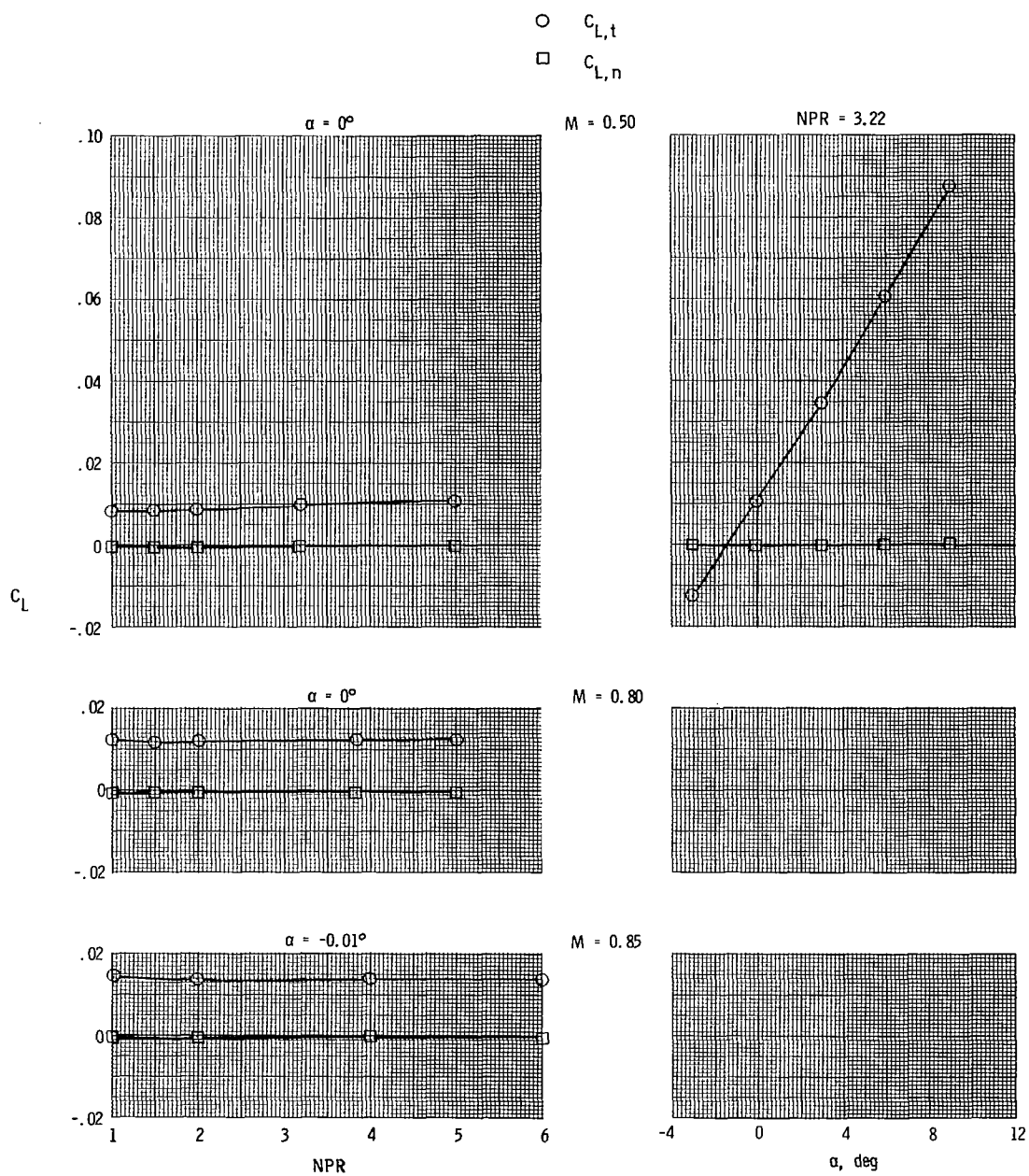(e) Concluded.

Figure 7.- Concluded.
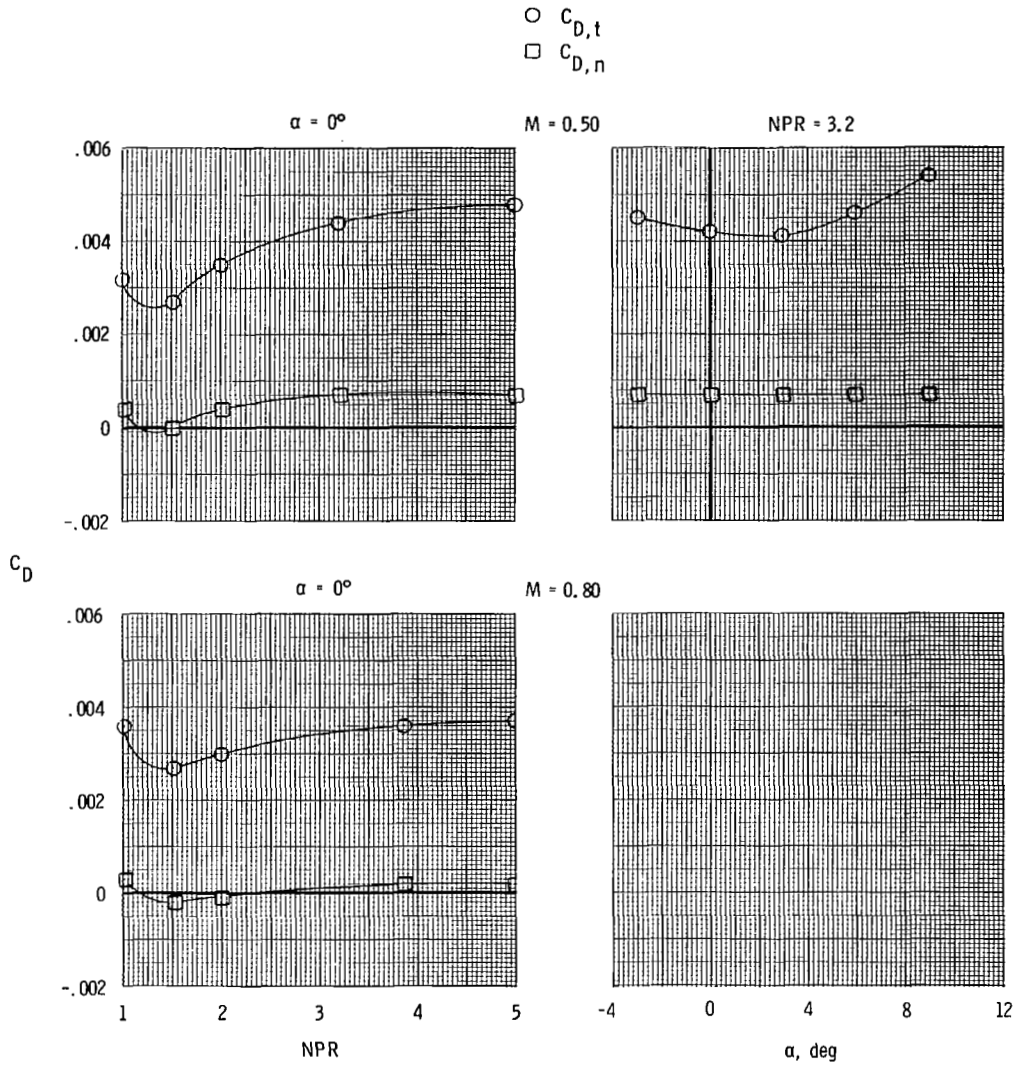
(a) Tails off.

Figure 8.- Variation of total (afterbody + nozzles + tails) and
nozzle drag coefficients with nozzle pressure ratio and angle
of attack for long supersonic dry power nozzles.
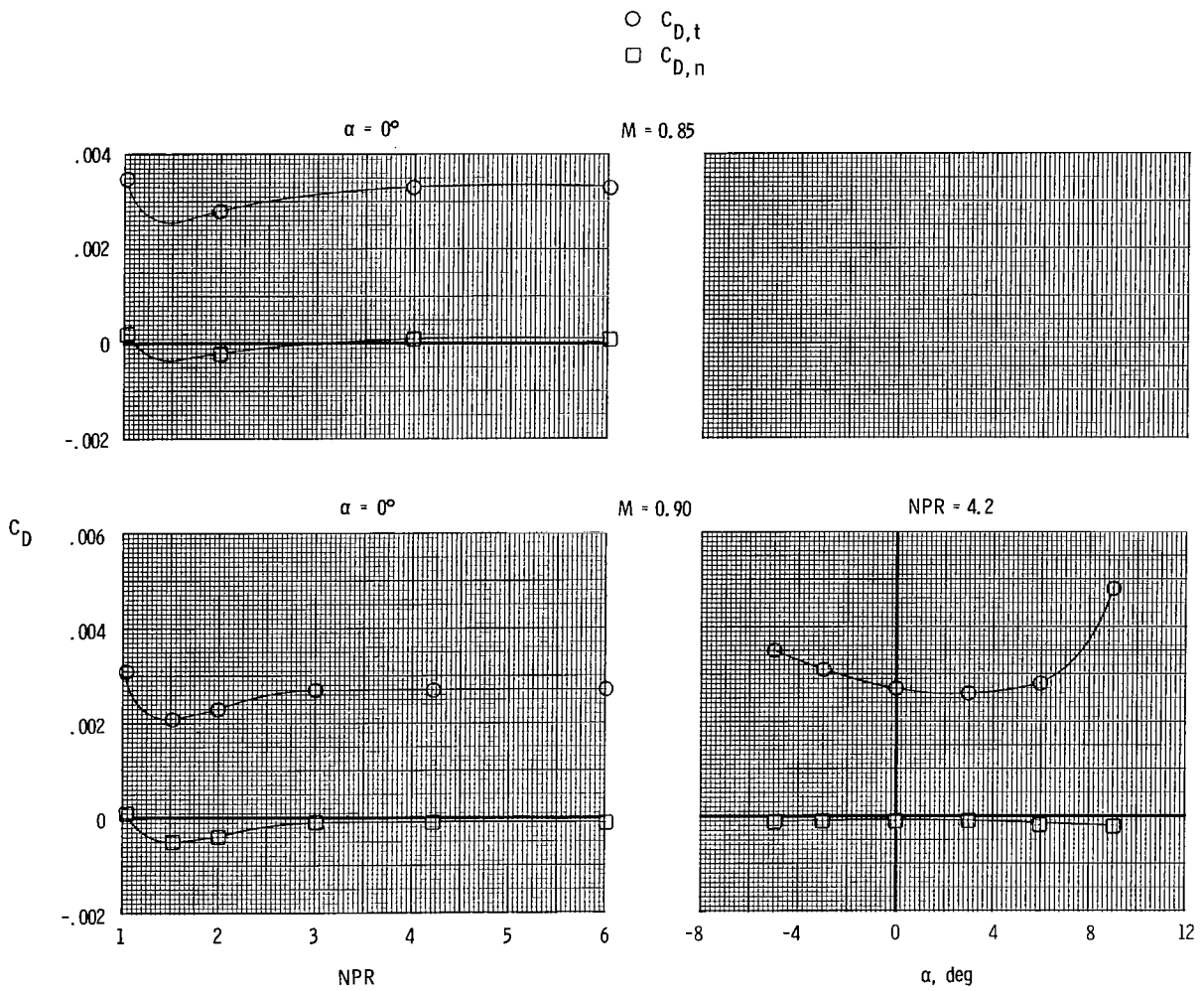
(a) Continued.
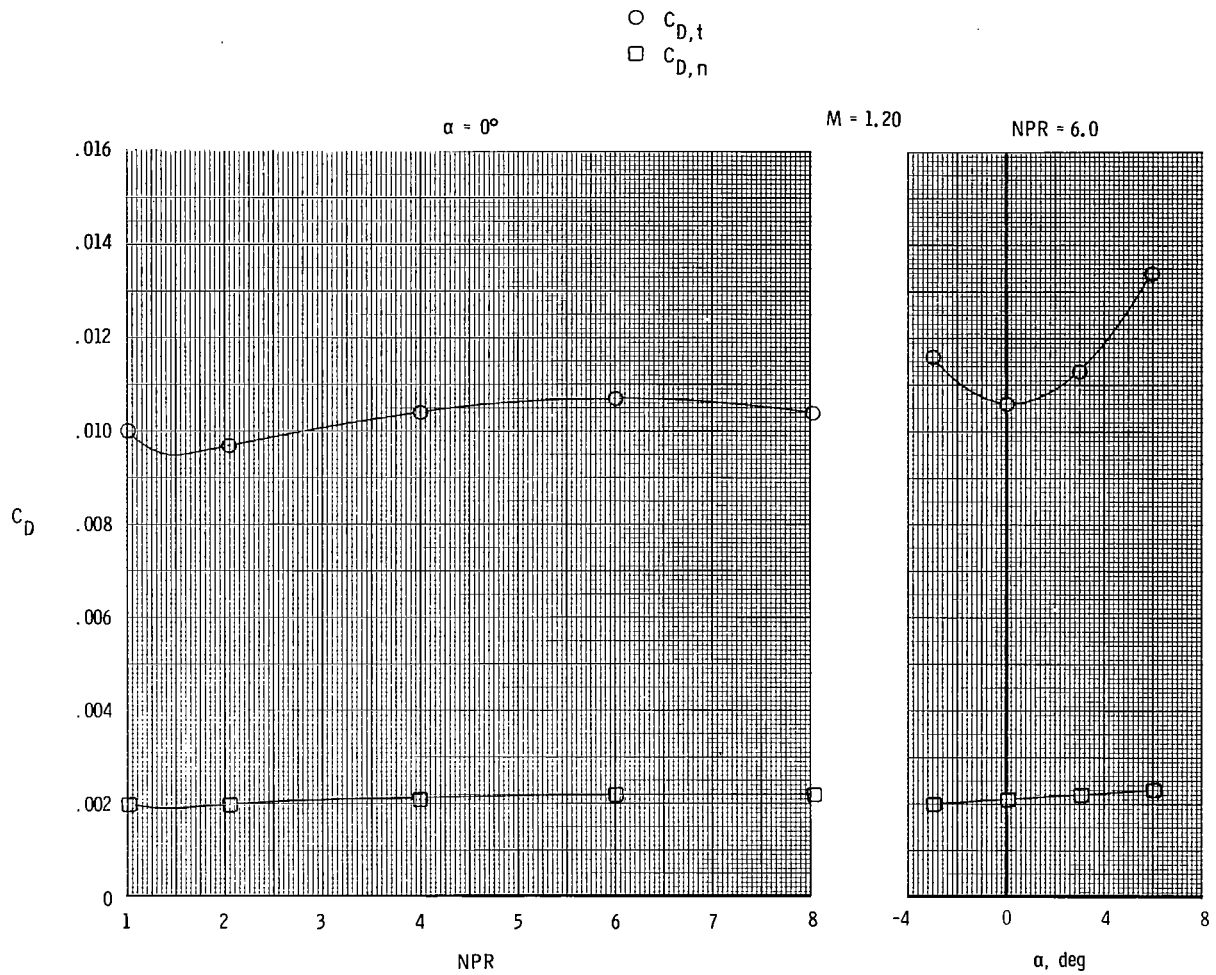
Figure 8.- Continued.

(a) Concluded.
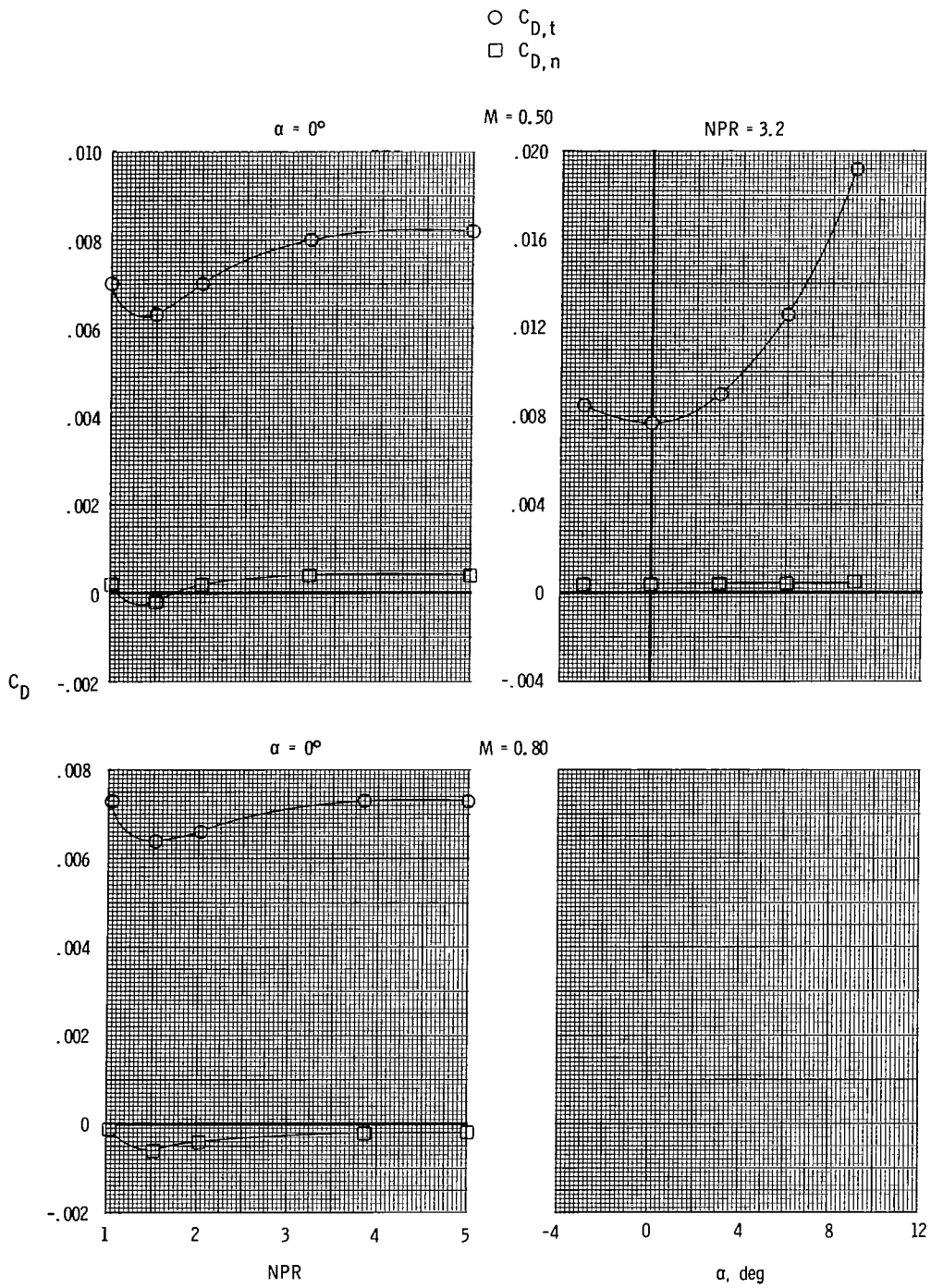
Figure 8.- Continued.

(b) Mid horizontal tails; mid vertical tails.
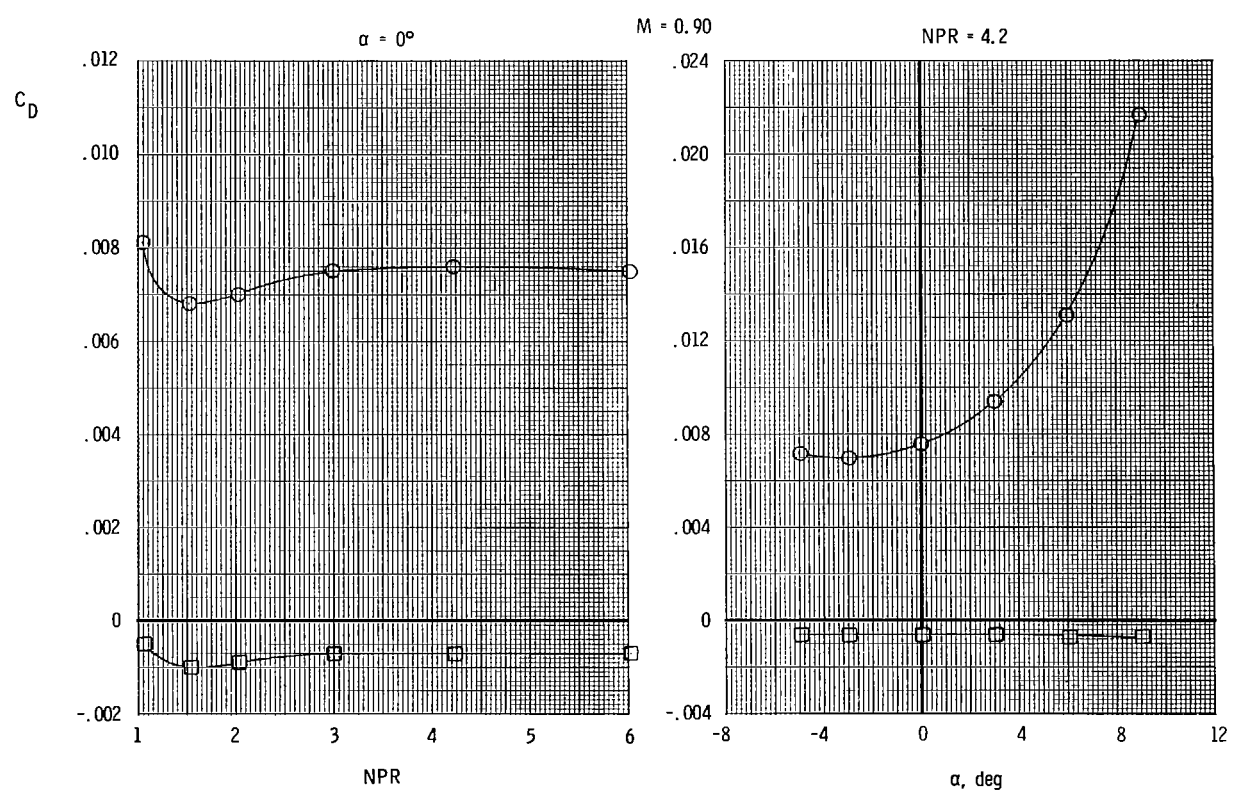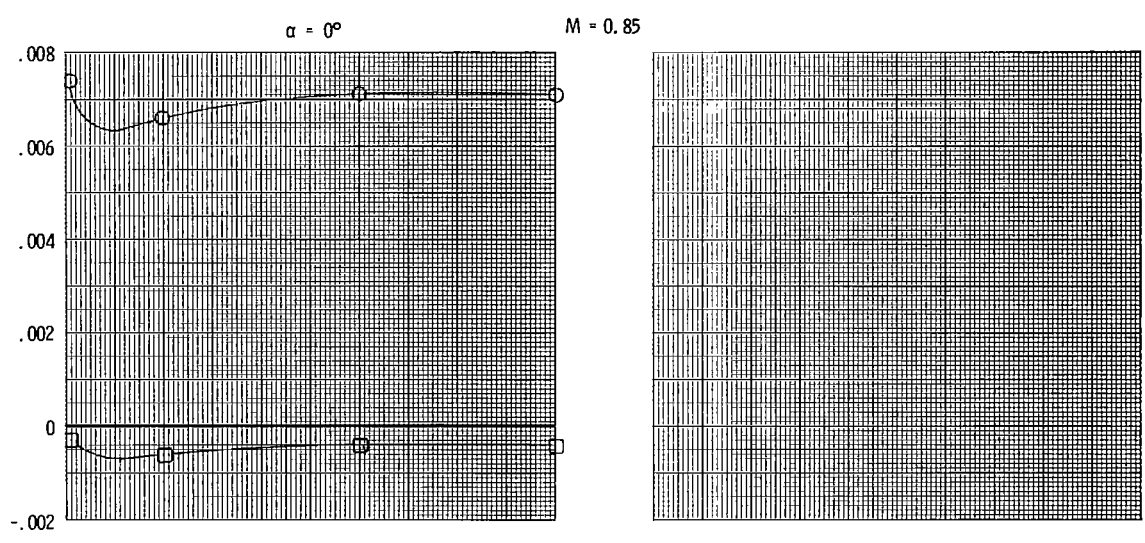
Figure 8.- Continued.

(b) Continued.
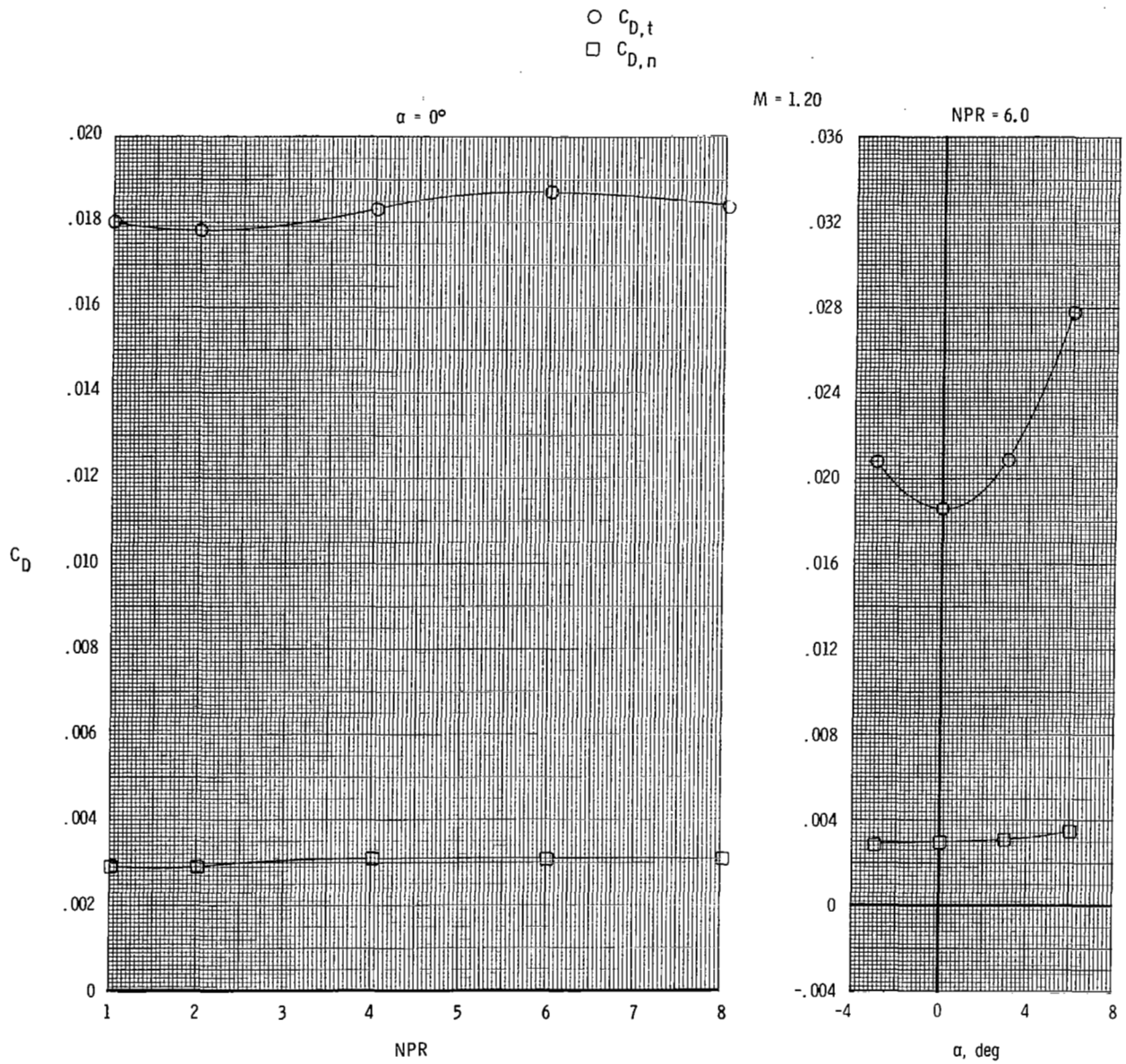
Figure 8.- Continued.

(b) Concluded.
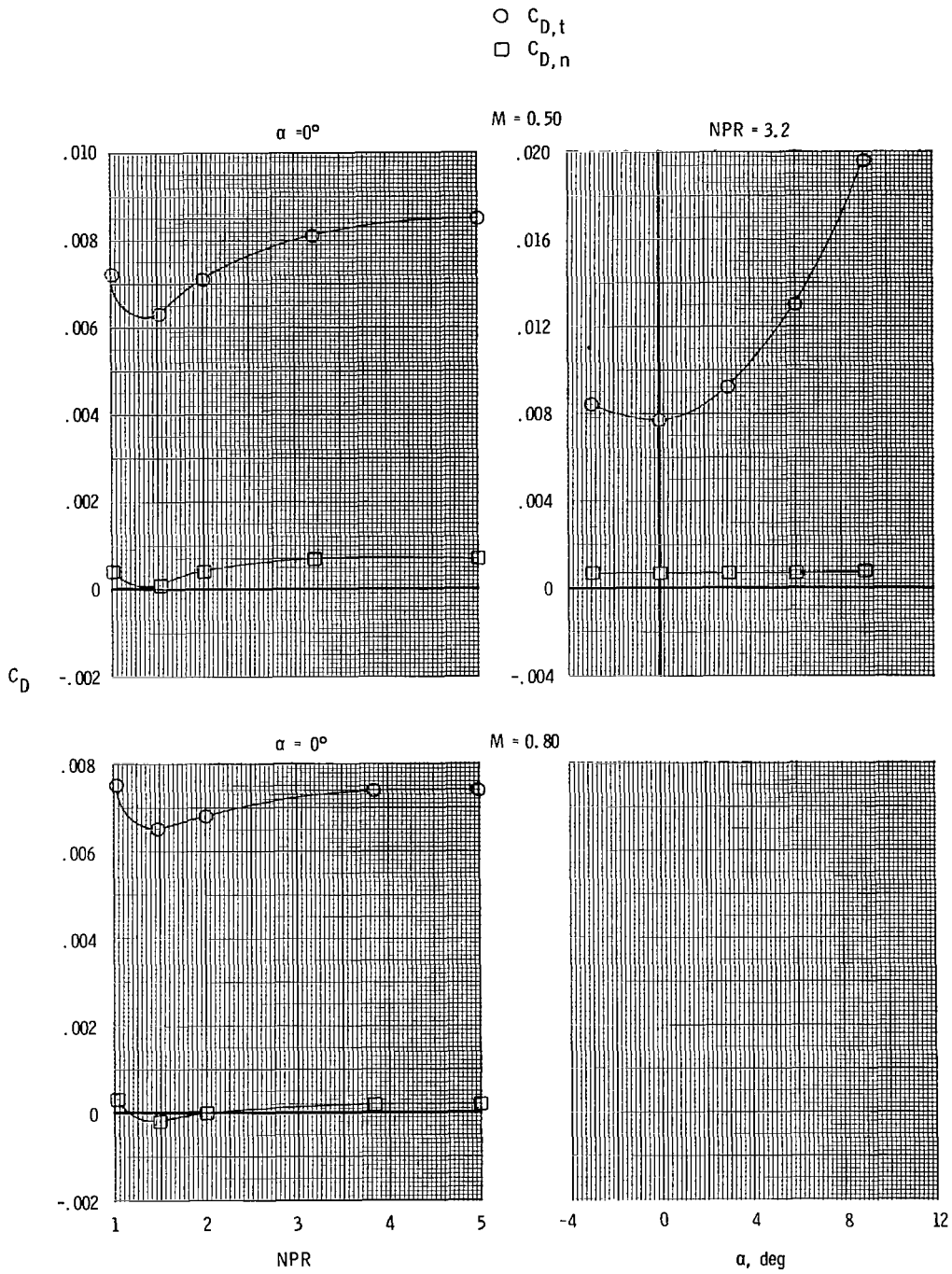
Figure 8.- Continued.

(c) Aft horizontal tails; mid vertical tails.

Figure 8.- Continued.

○ $c_{D,t}$
□ $c_{D,n}$

$\alpha = 0°$ M = 0.85

$\alpha = 0°$ M = 0.90   NPR = 4.2

c_D

NPR

α, deg

(c) Continued.

Figure 8.- Continued.
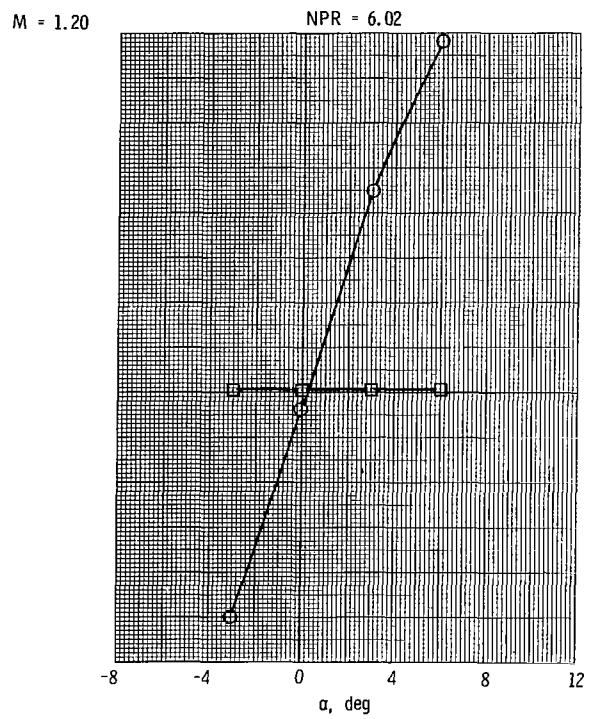
72
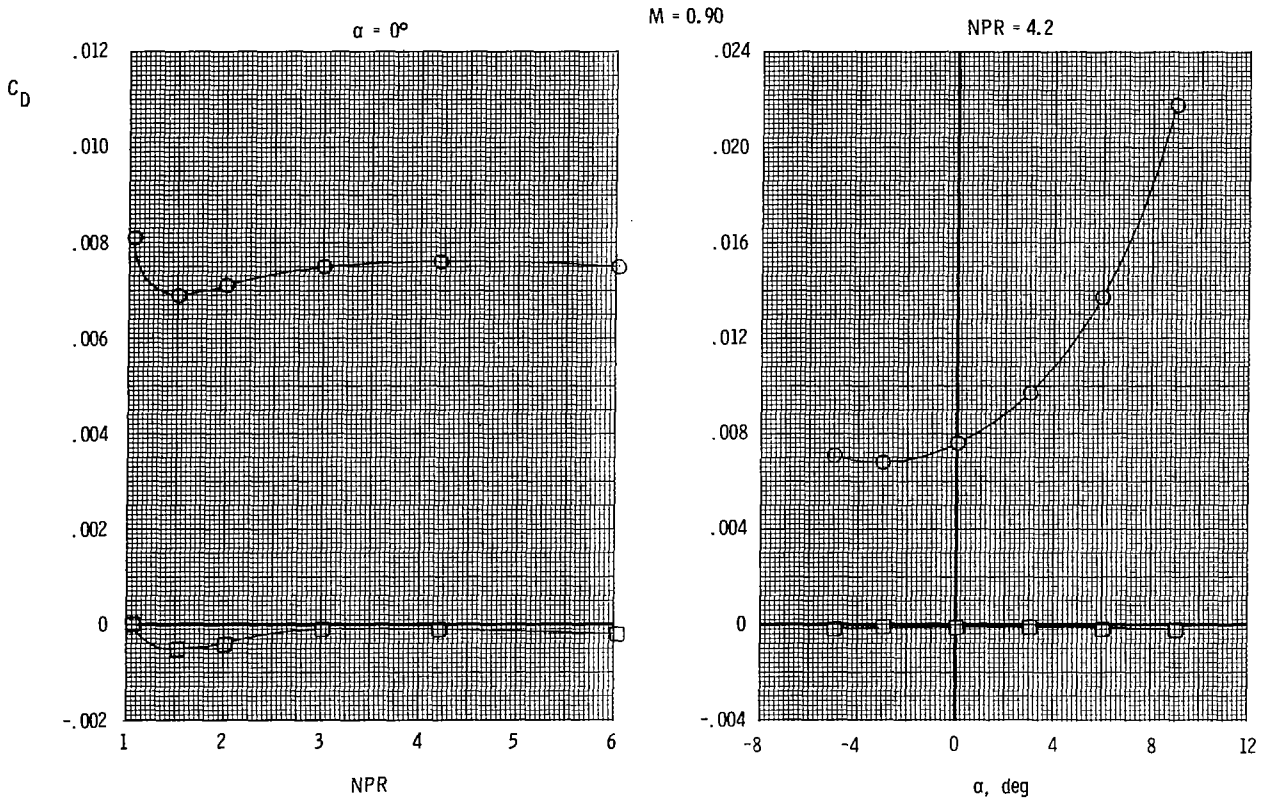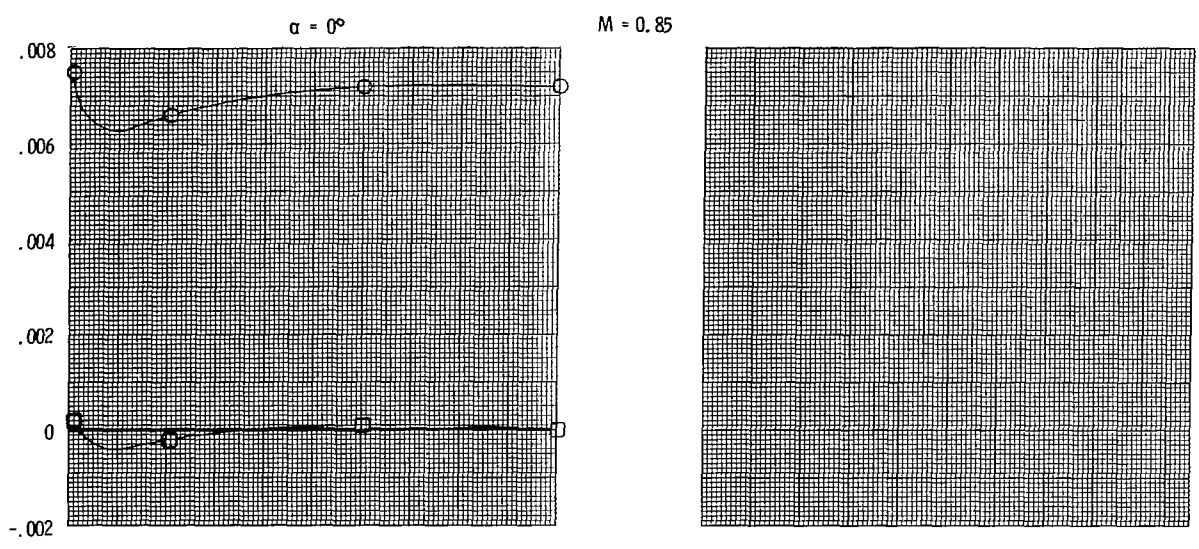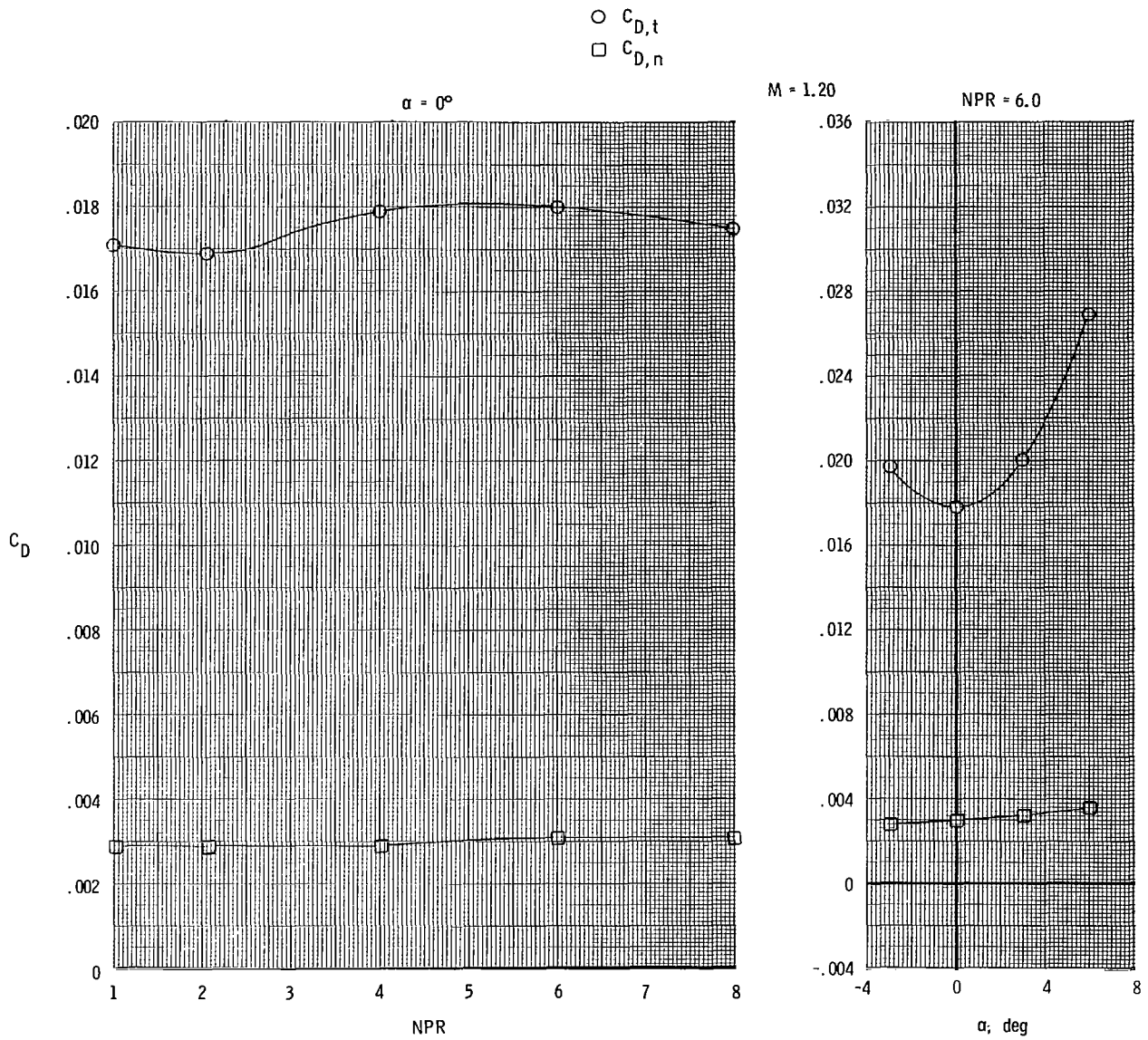
(c) Concluded.

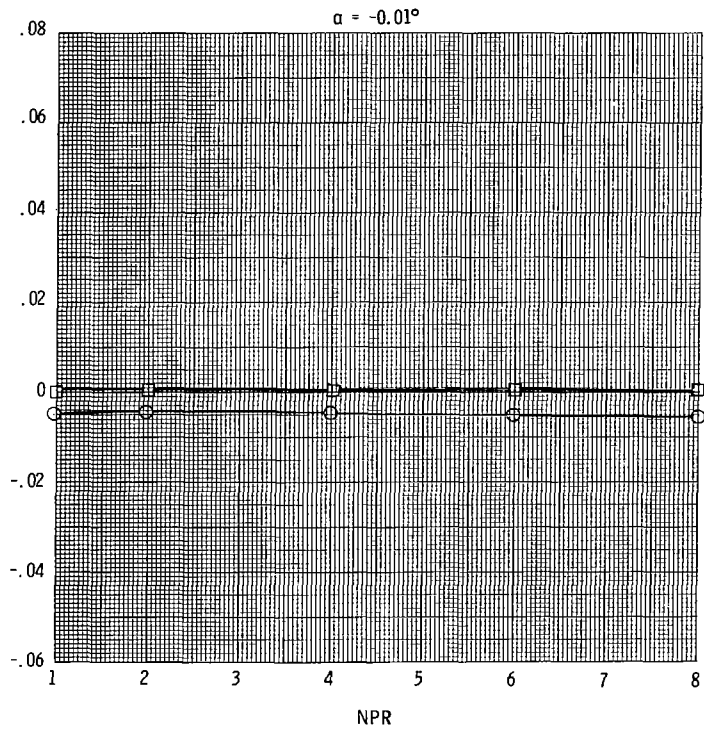Figure 8.- Concluded.
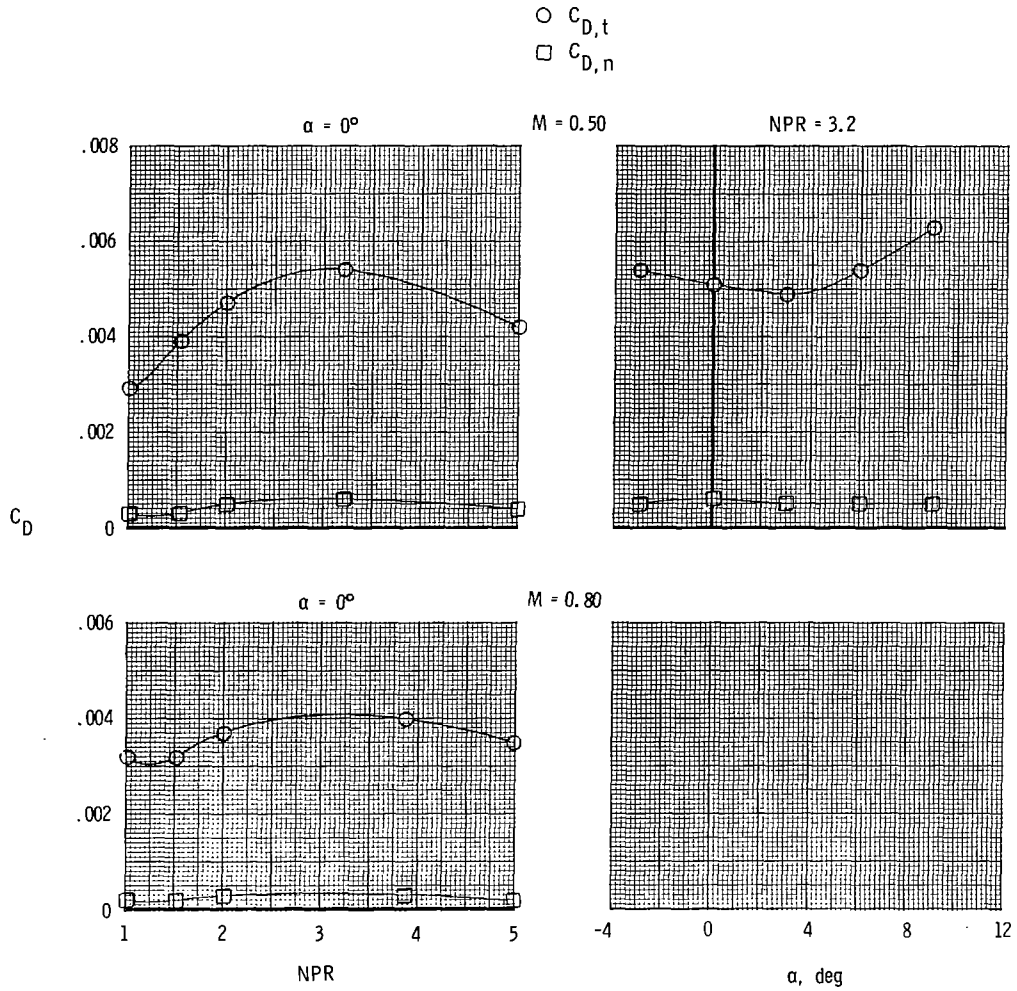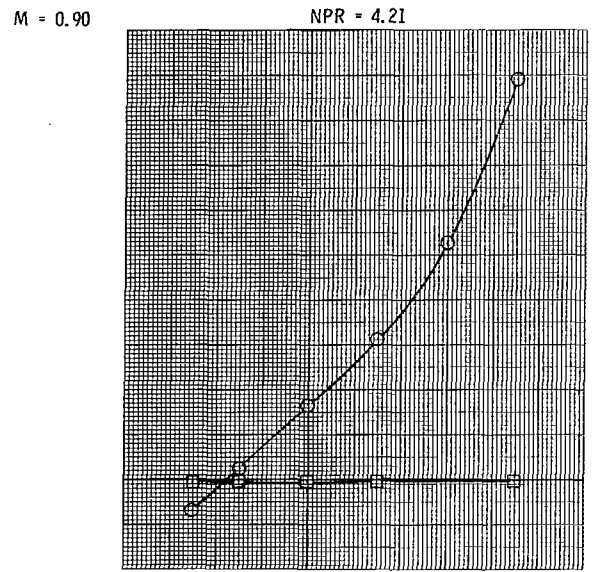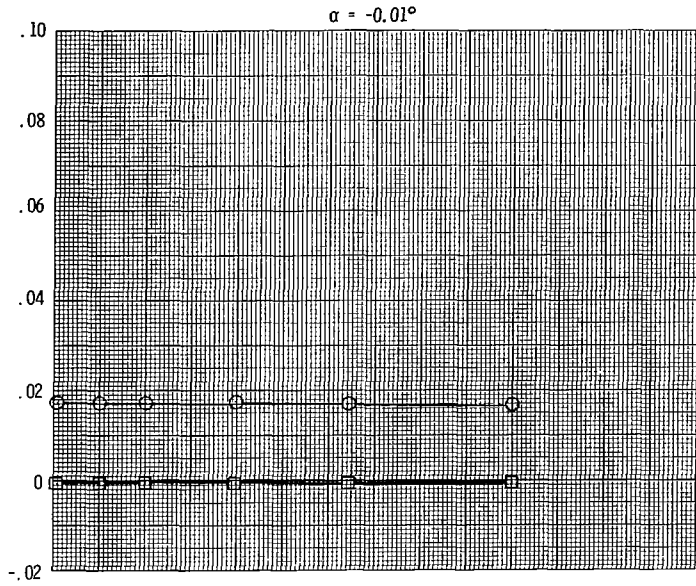
(a) Tails off.

Figure 9.- Variation of total (afterbody + nozzles + tails) and
   nozzle drag coefficients with nozzle pressure ratio and angle
   of attack for short supersonic partial A/B power nozzle.
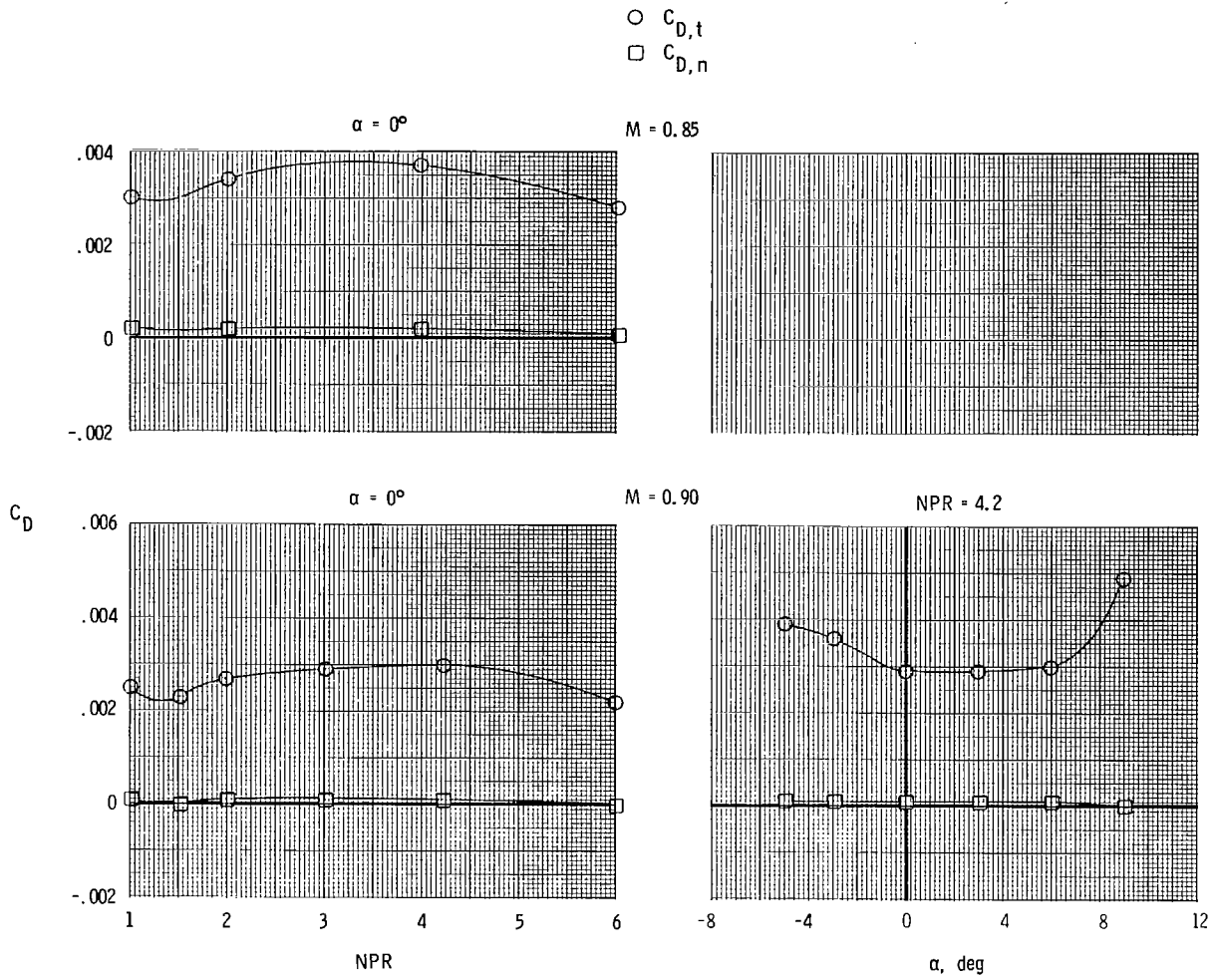
(a) Continued.

Figure 9.- Continued.
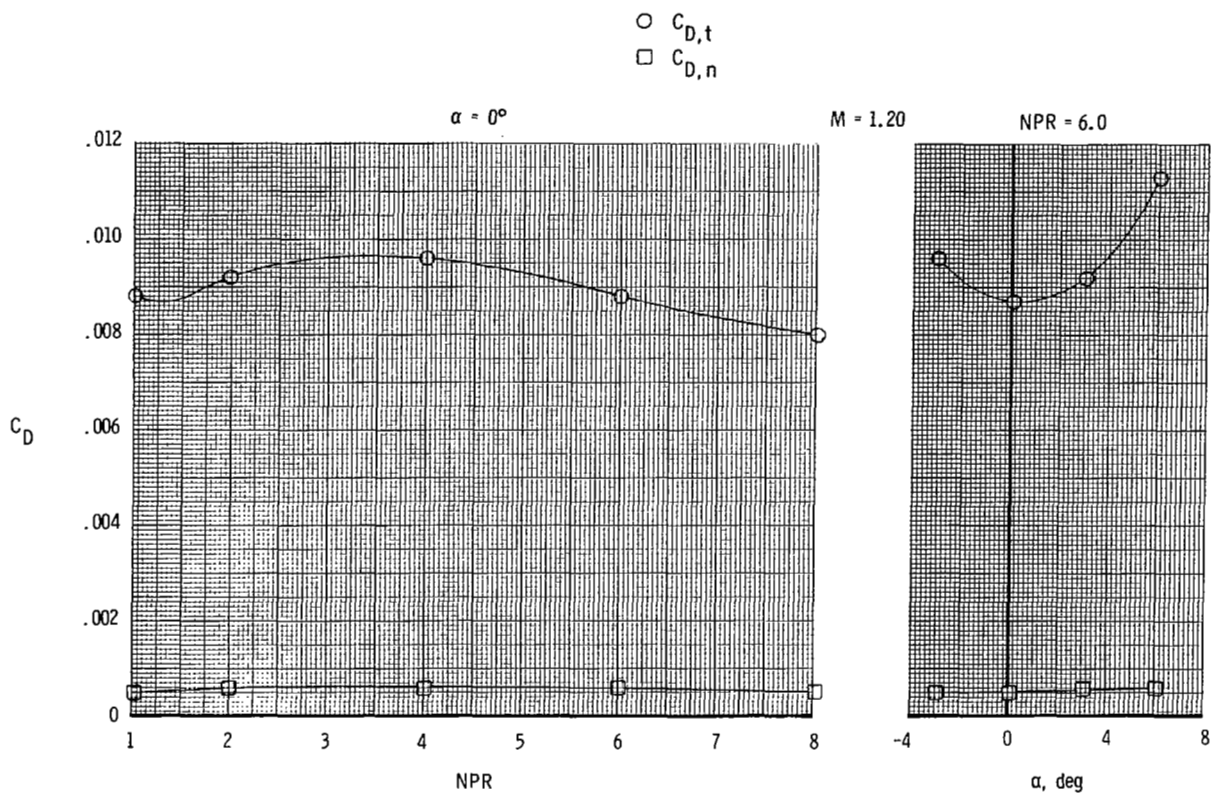
(a) Concluded.
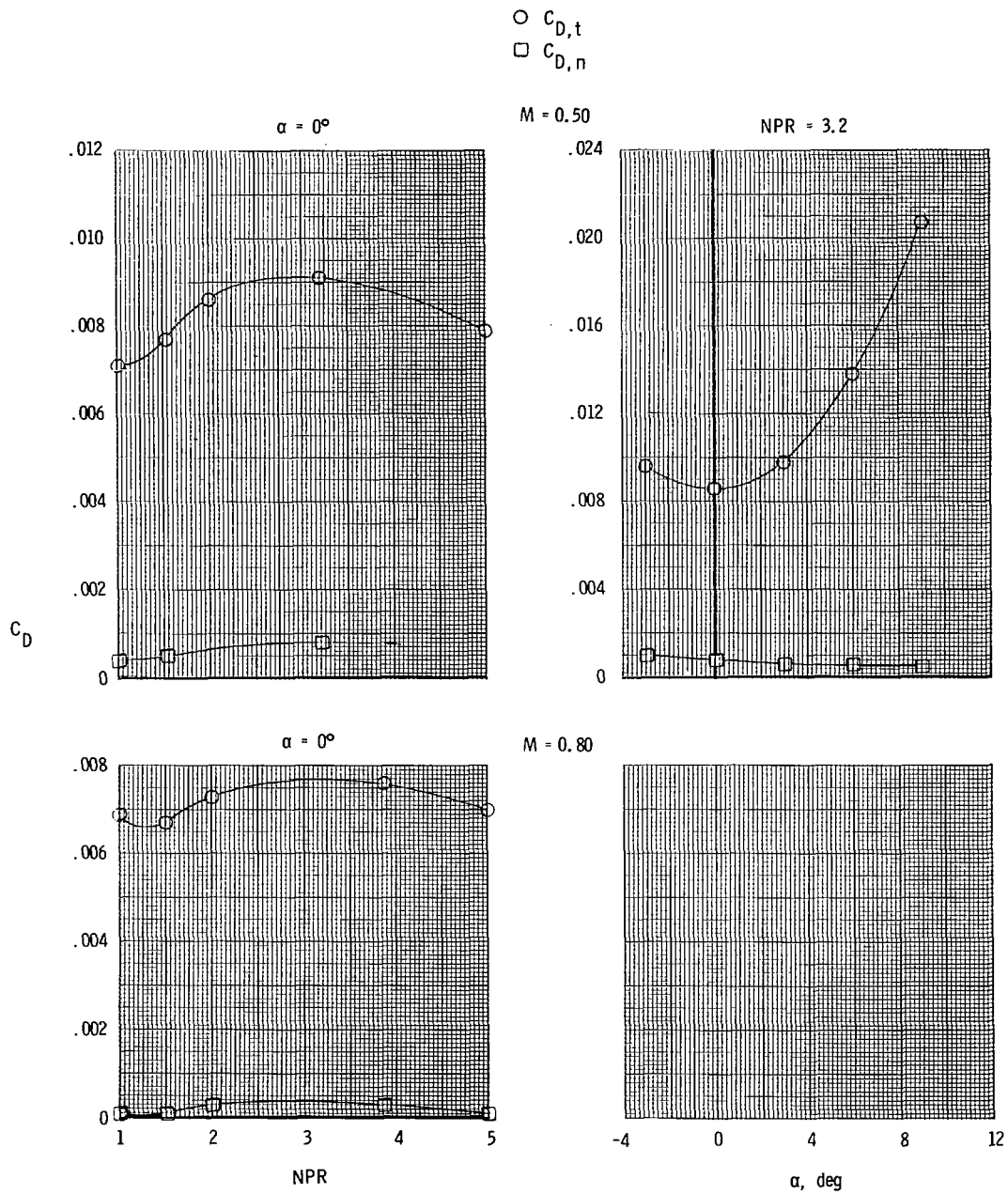
Figure 9.- Continued.

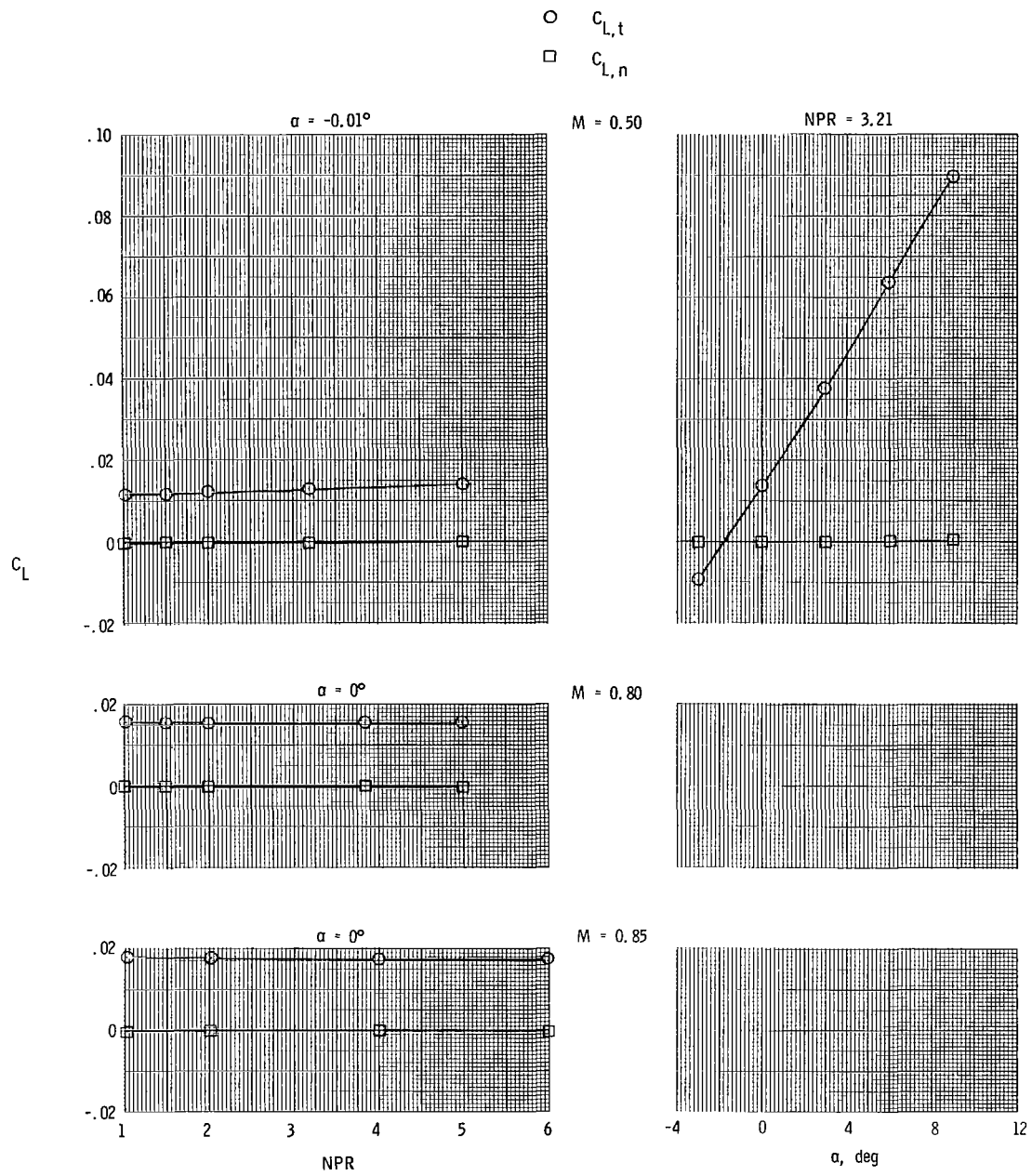(b) Mid horizontal tails; mid vertical tails.
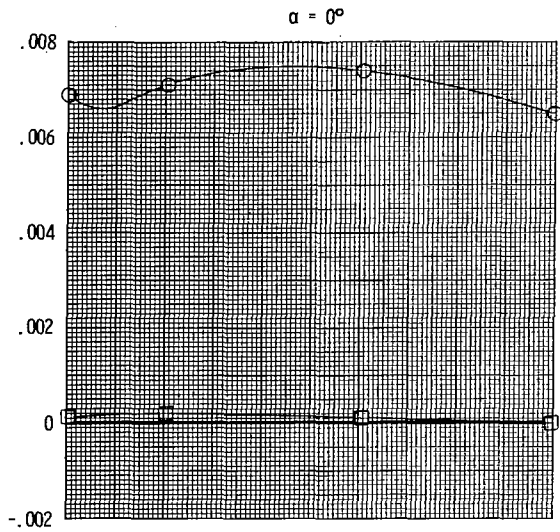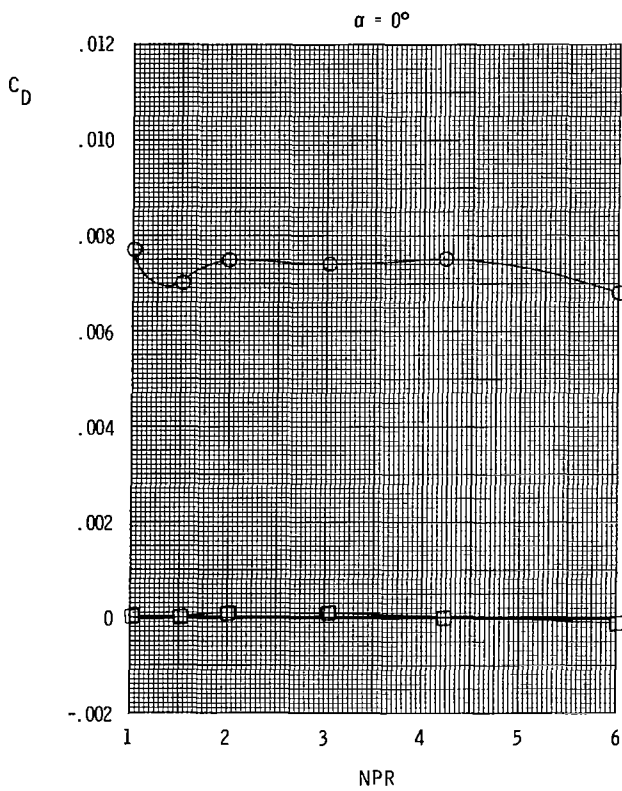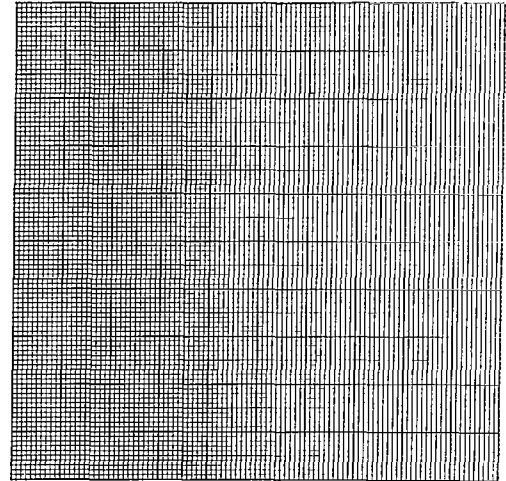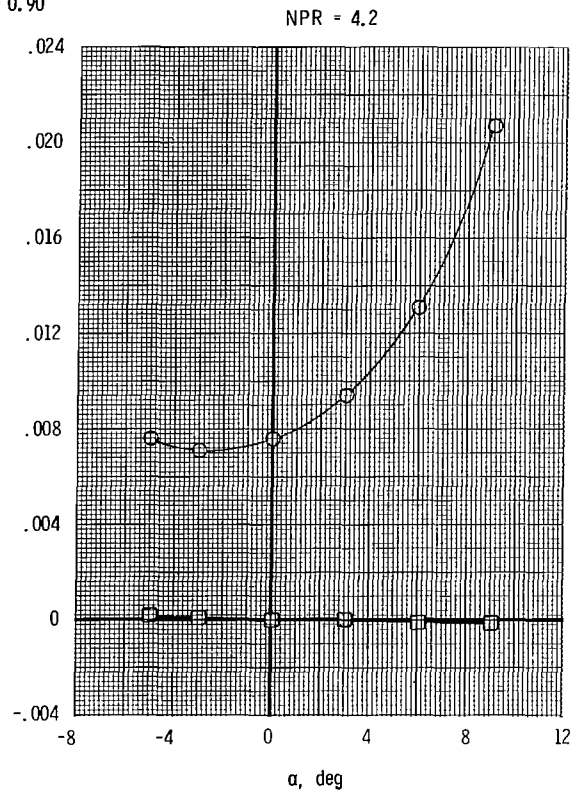
Figure 9.- Continued.

(b) Continued.
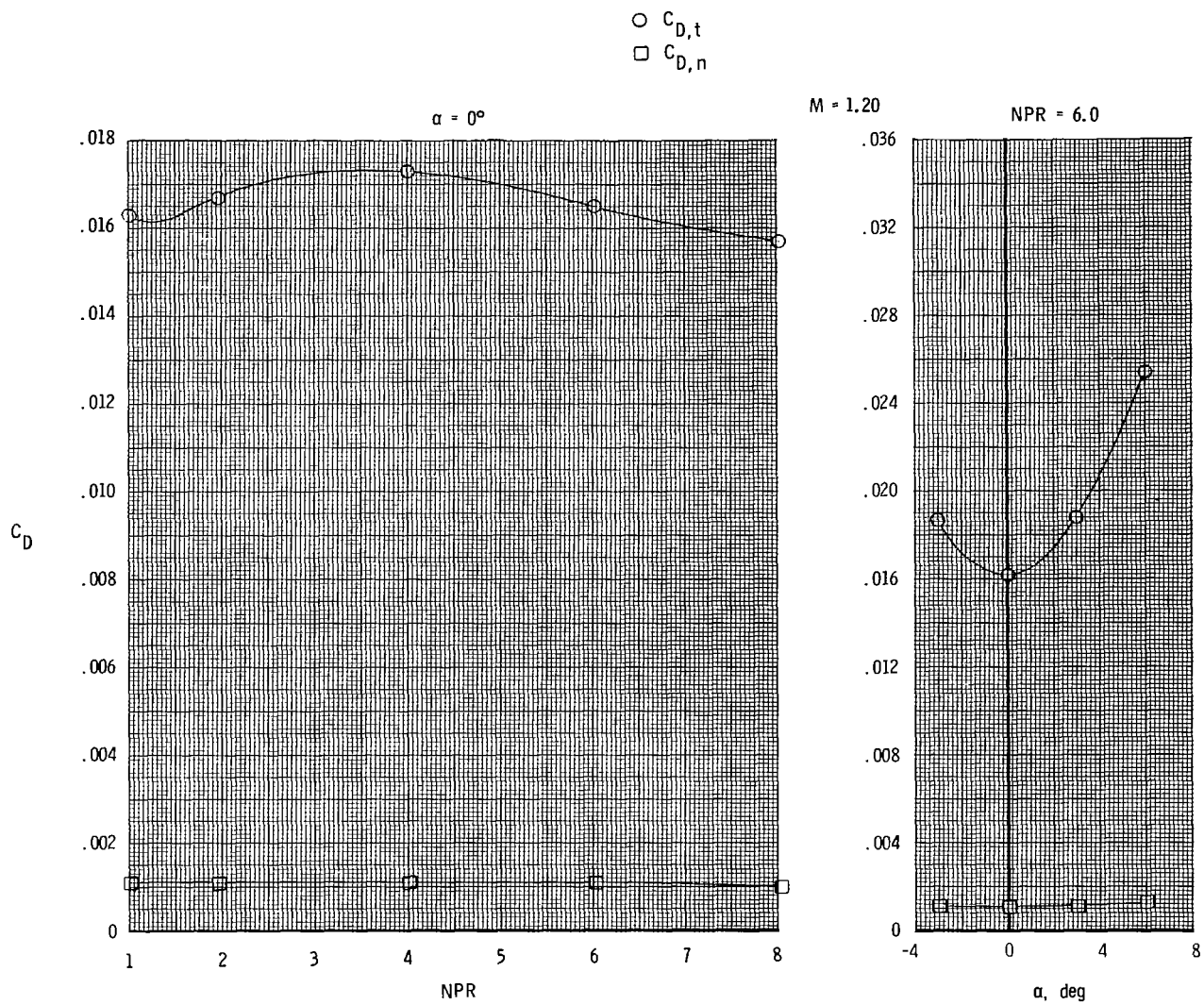
Figure 9.- Continued.

(b) Concluded.
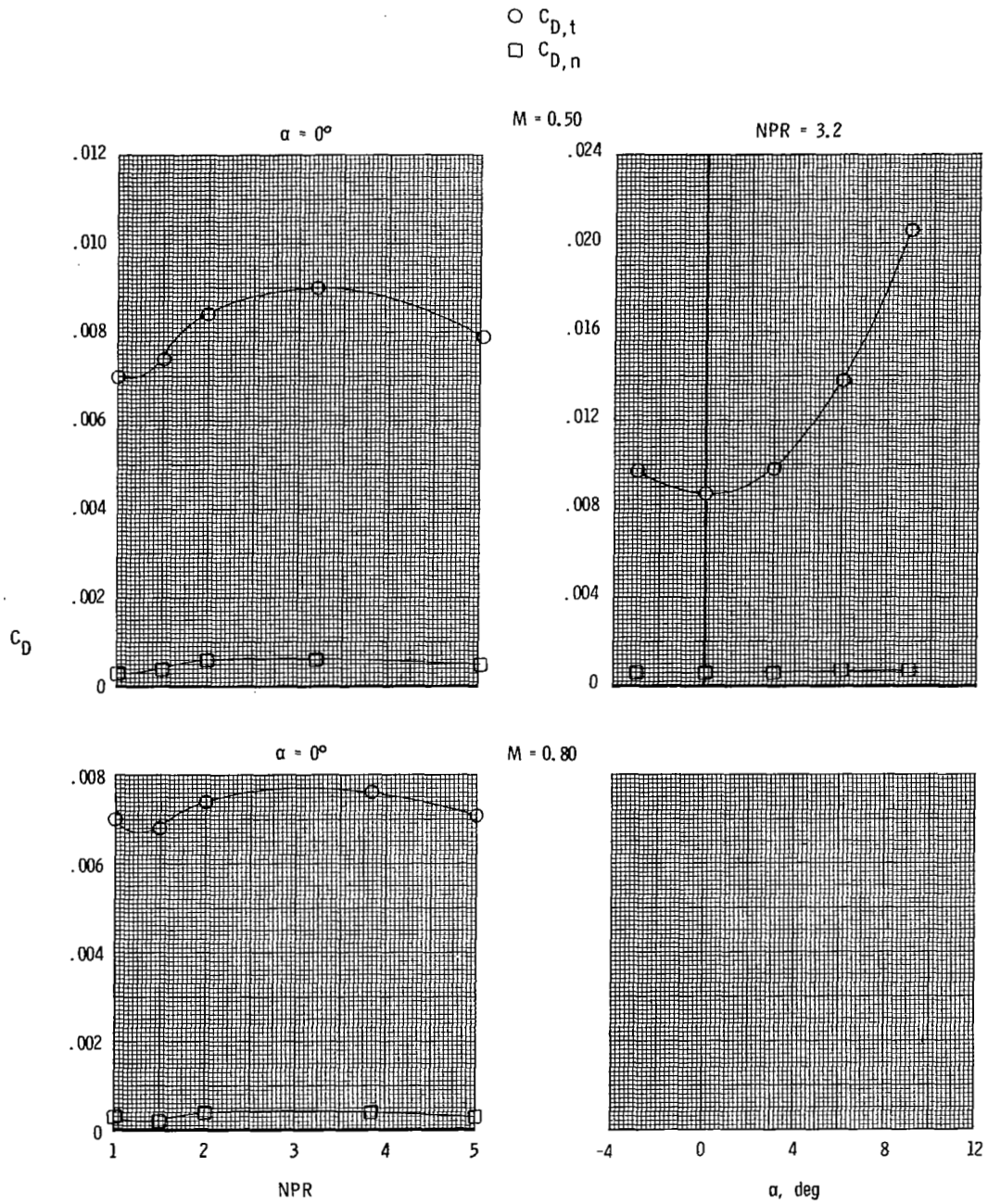
Figure 9.- Continued.

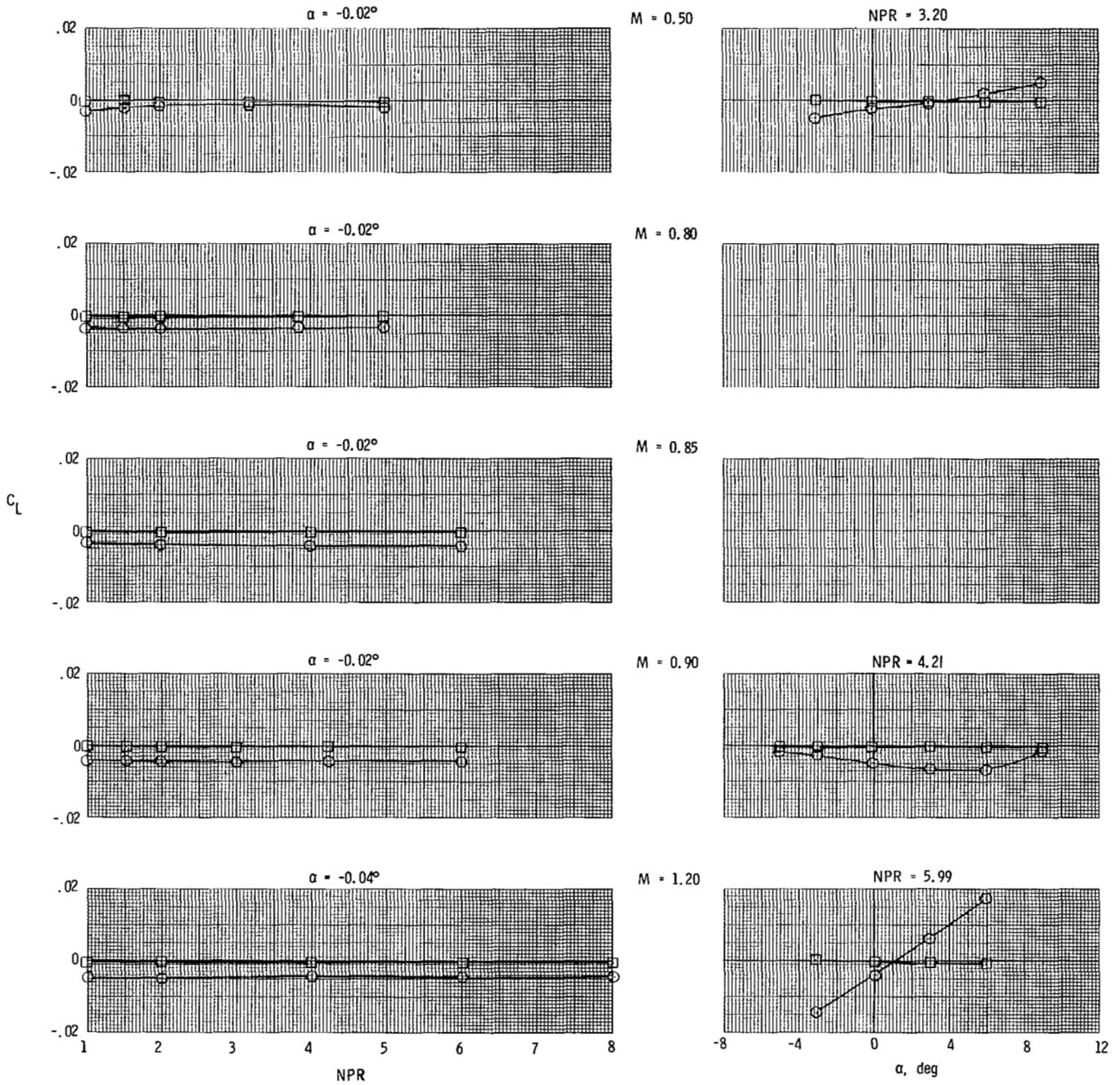(c) Aft horizontal tails; mid vertical tails.
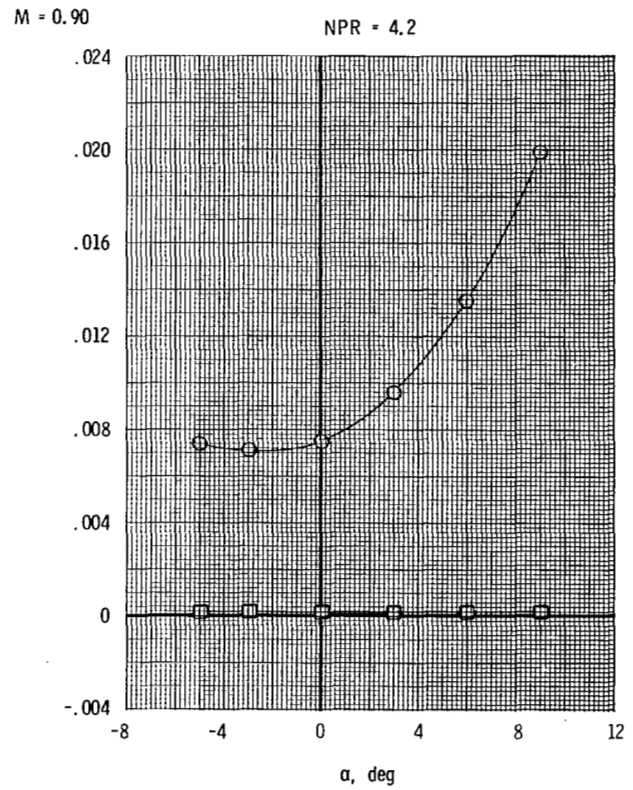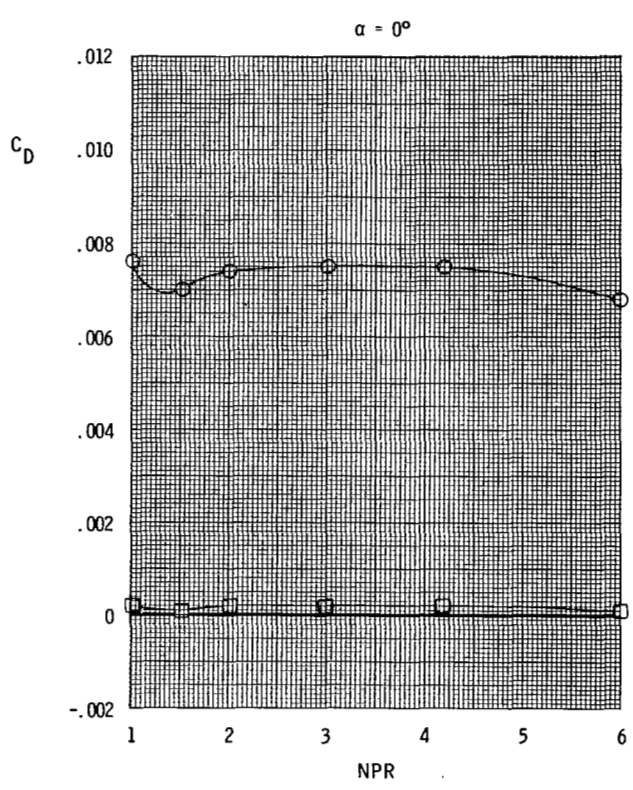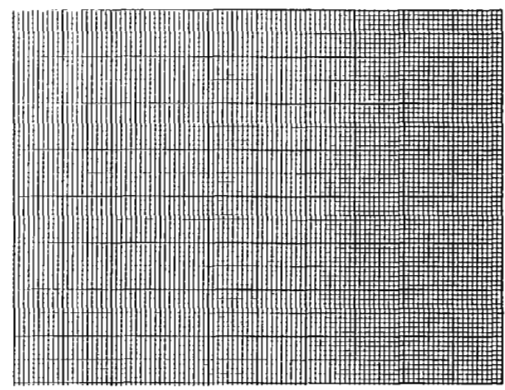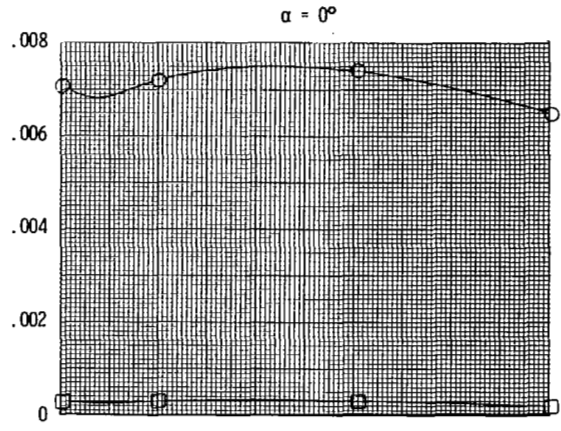
Figure 9.- Continued.

(c) Continued.
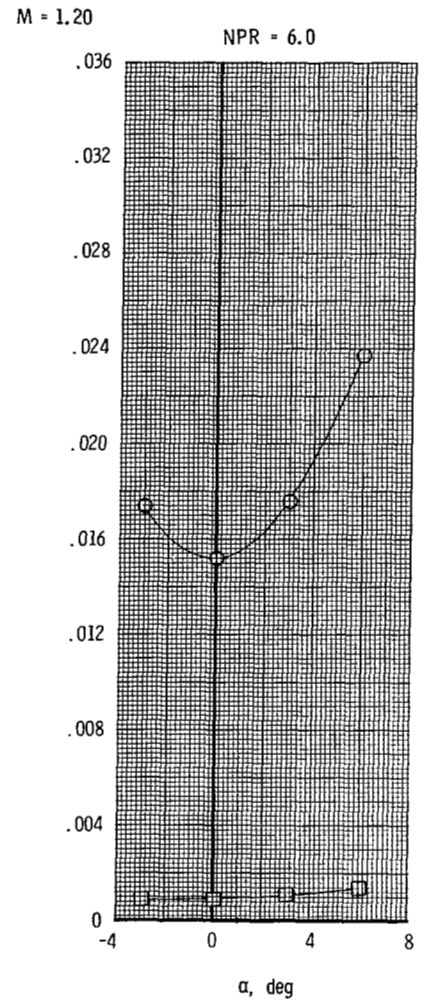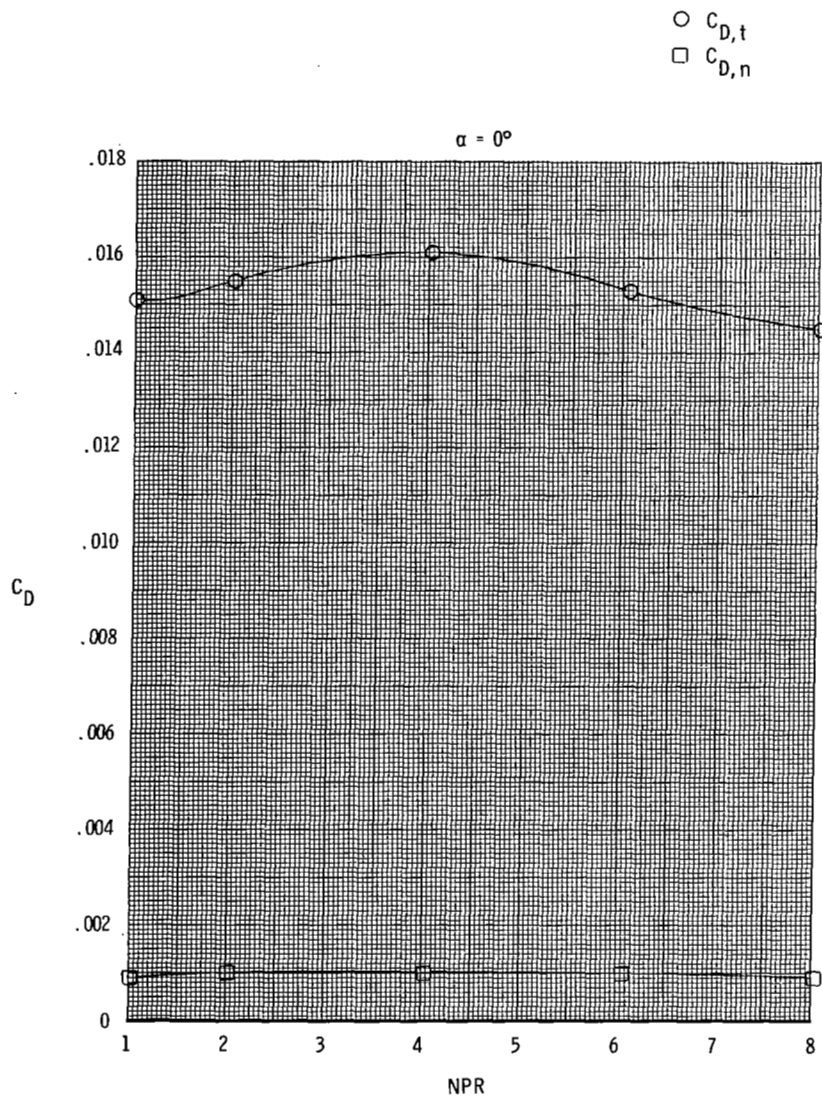
Figure 9.- Continued.

(c) Concluded.

Figure 9.- Concluded.
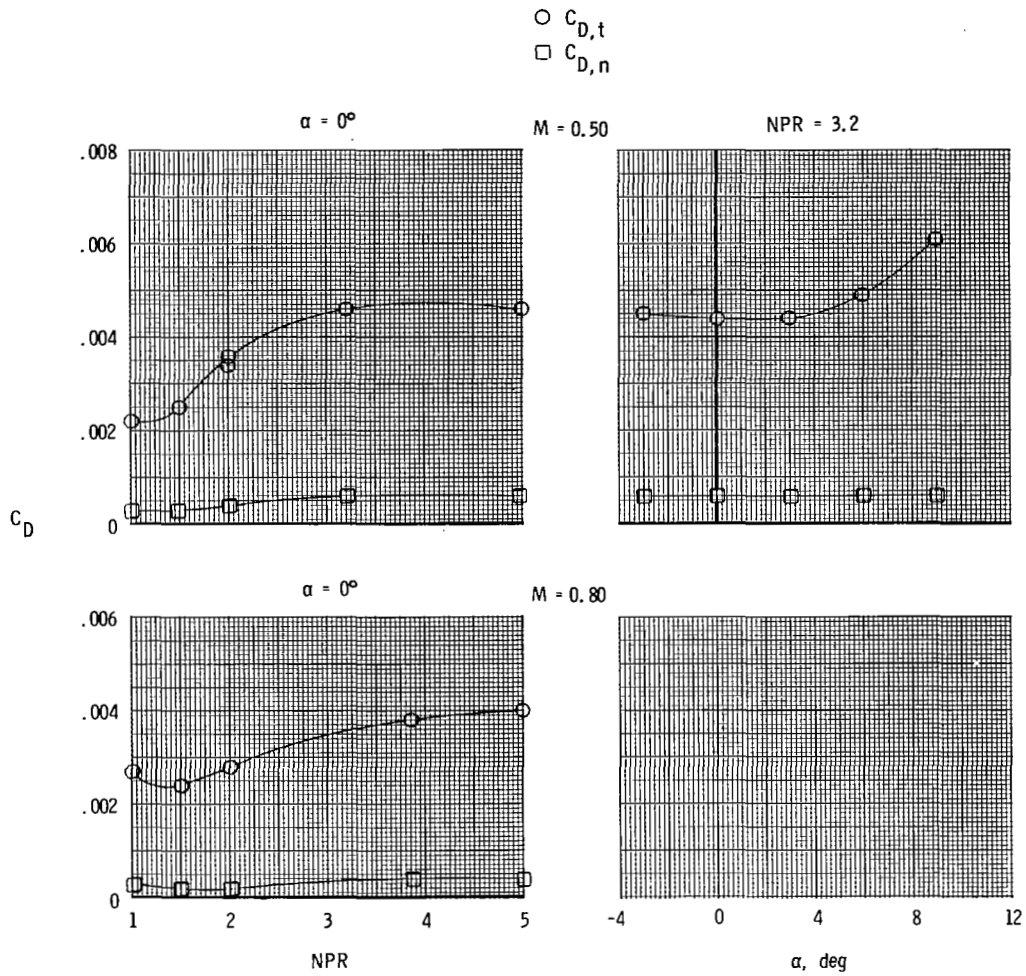
(a) Tails off.

Figure 10.- Variation of total (afterbody + nozzles + tails) and nozzle drag coefficients with nozzle pressure ratio and angle of attack for long supersonic partial A/B power nozzles.
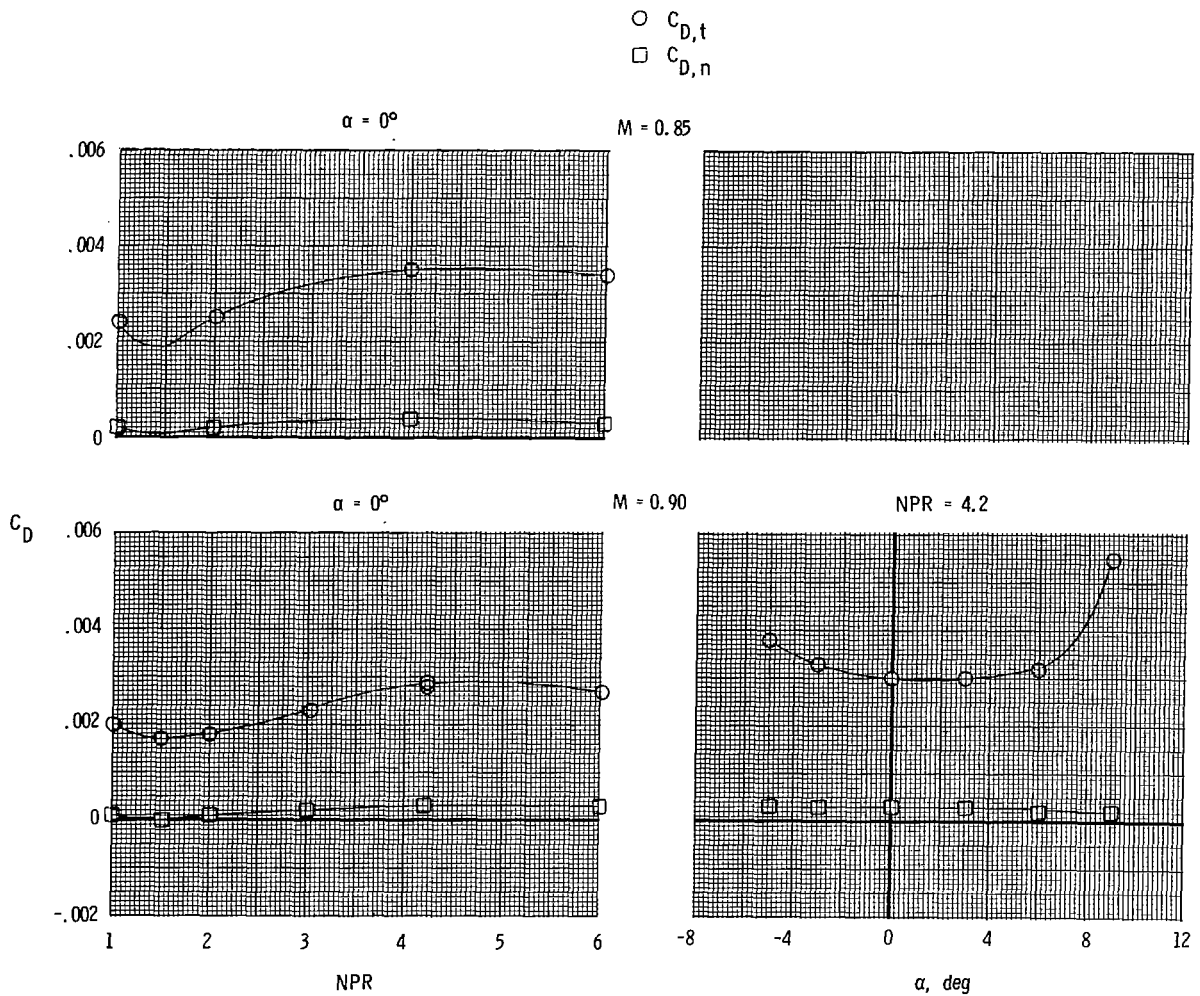
(a) Continued.

Figure 10.- Continued.
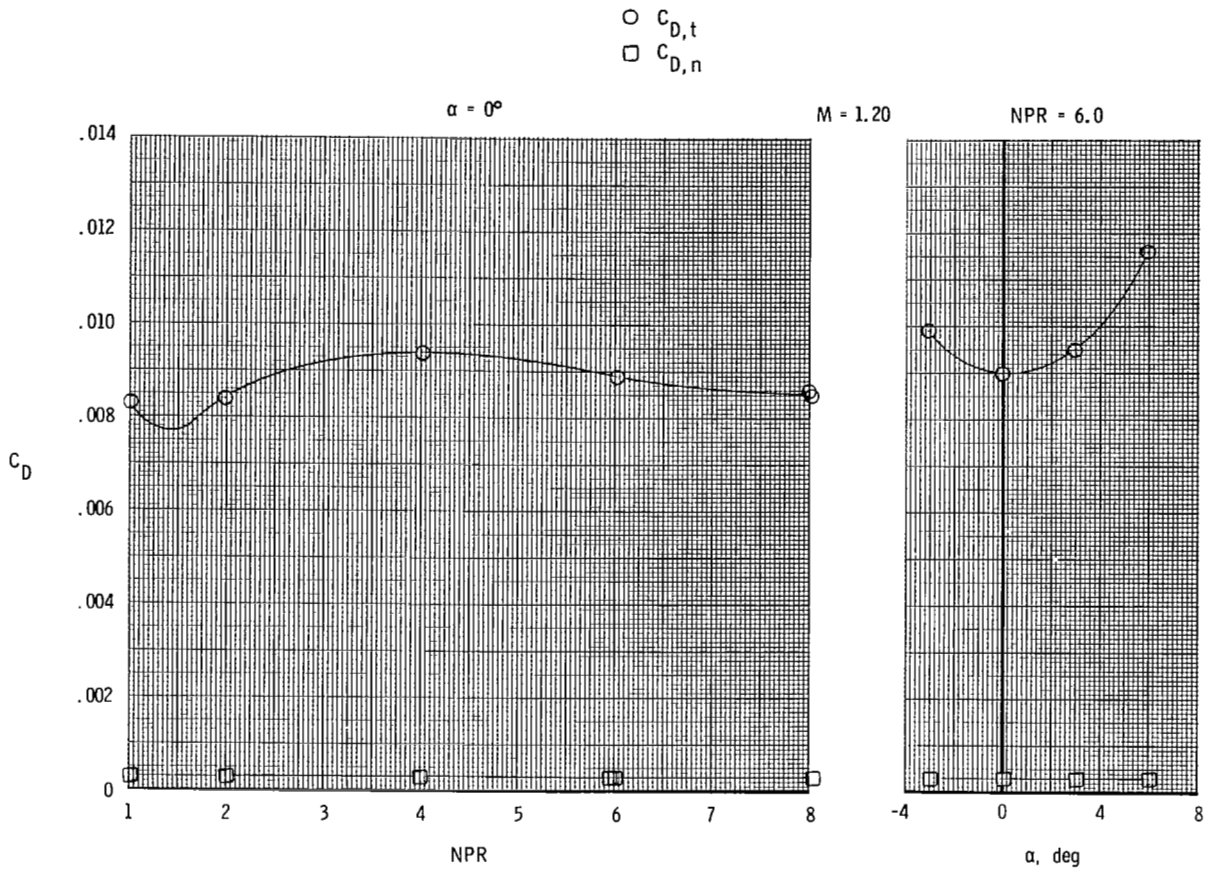
(a) Concluded.
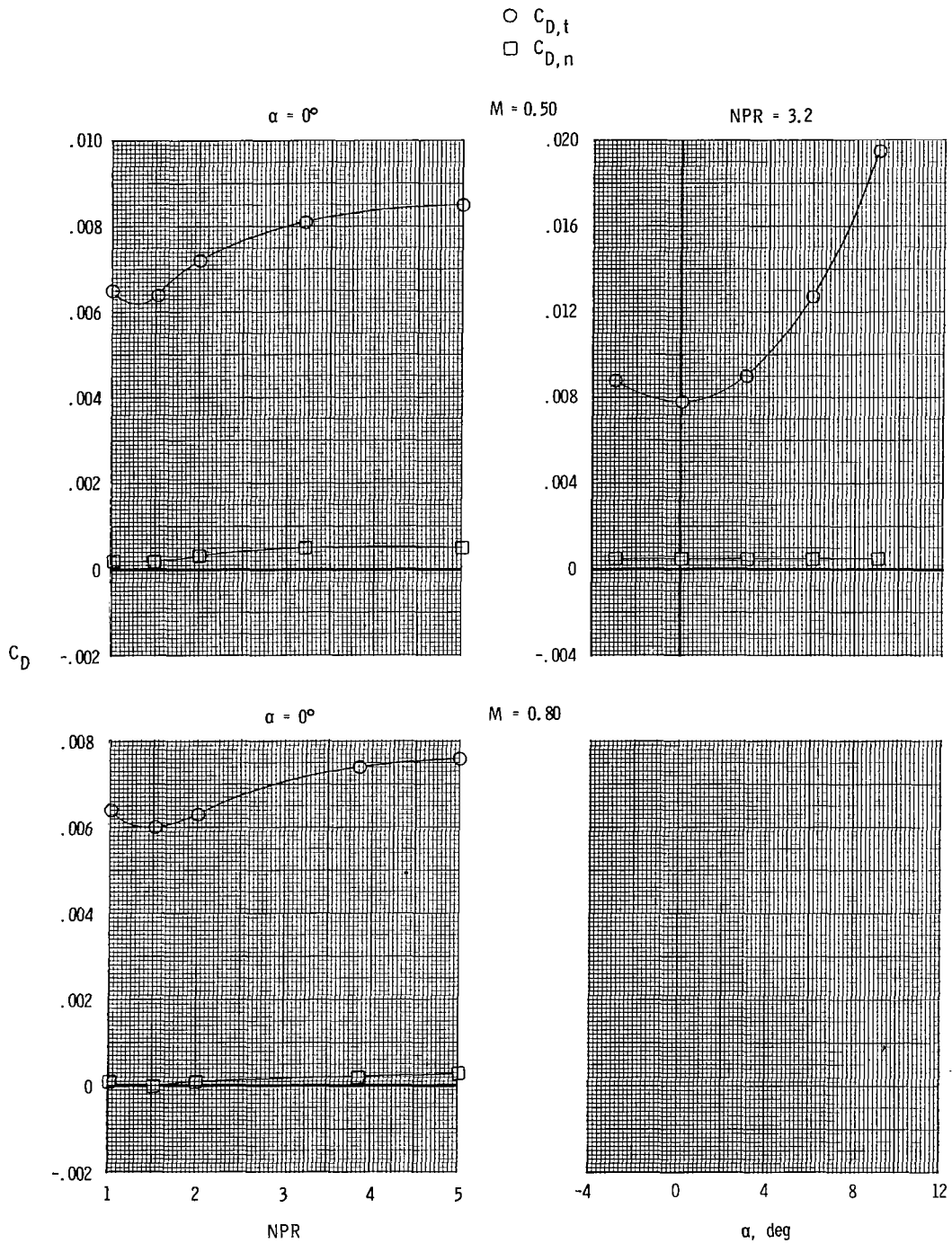
Figure 10.- Continued.

(b) Mid horizontal tails; mid vertical tails.
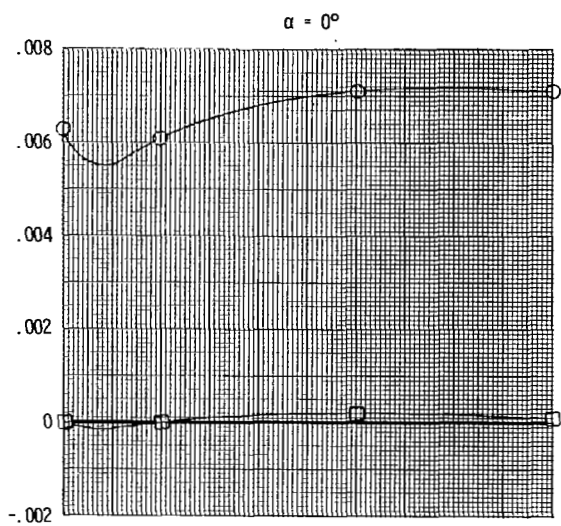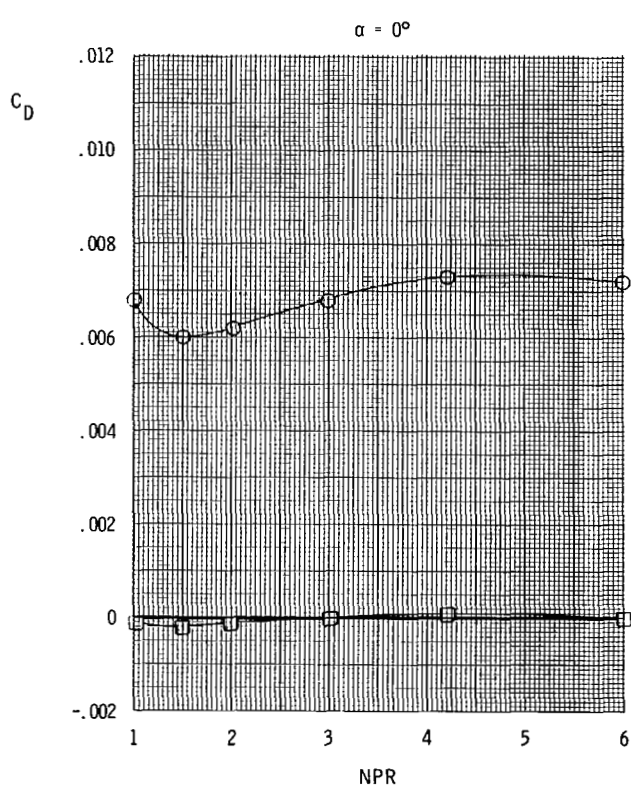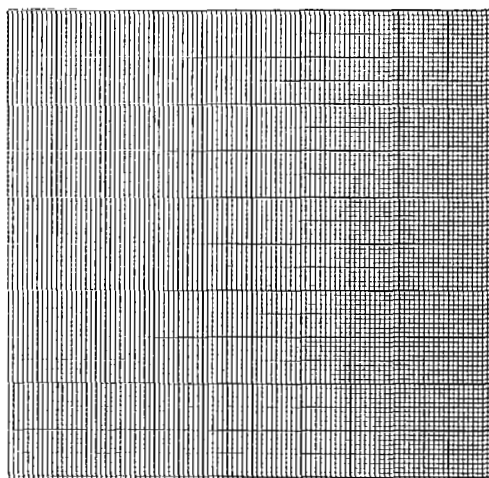
Figure 10.- Continued.
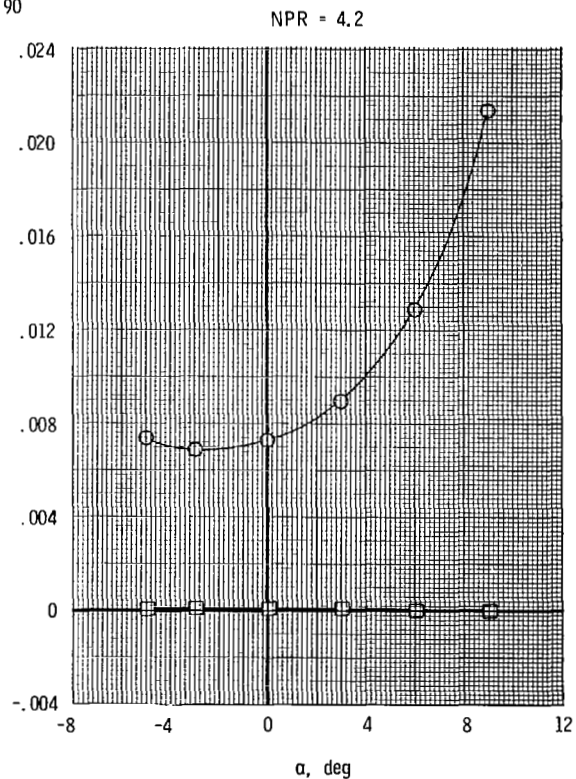
(b) Continued.

Figure 10.- Continued.
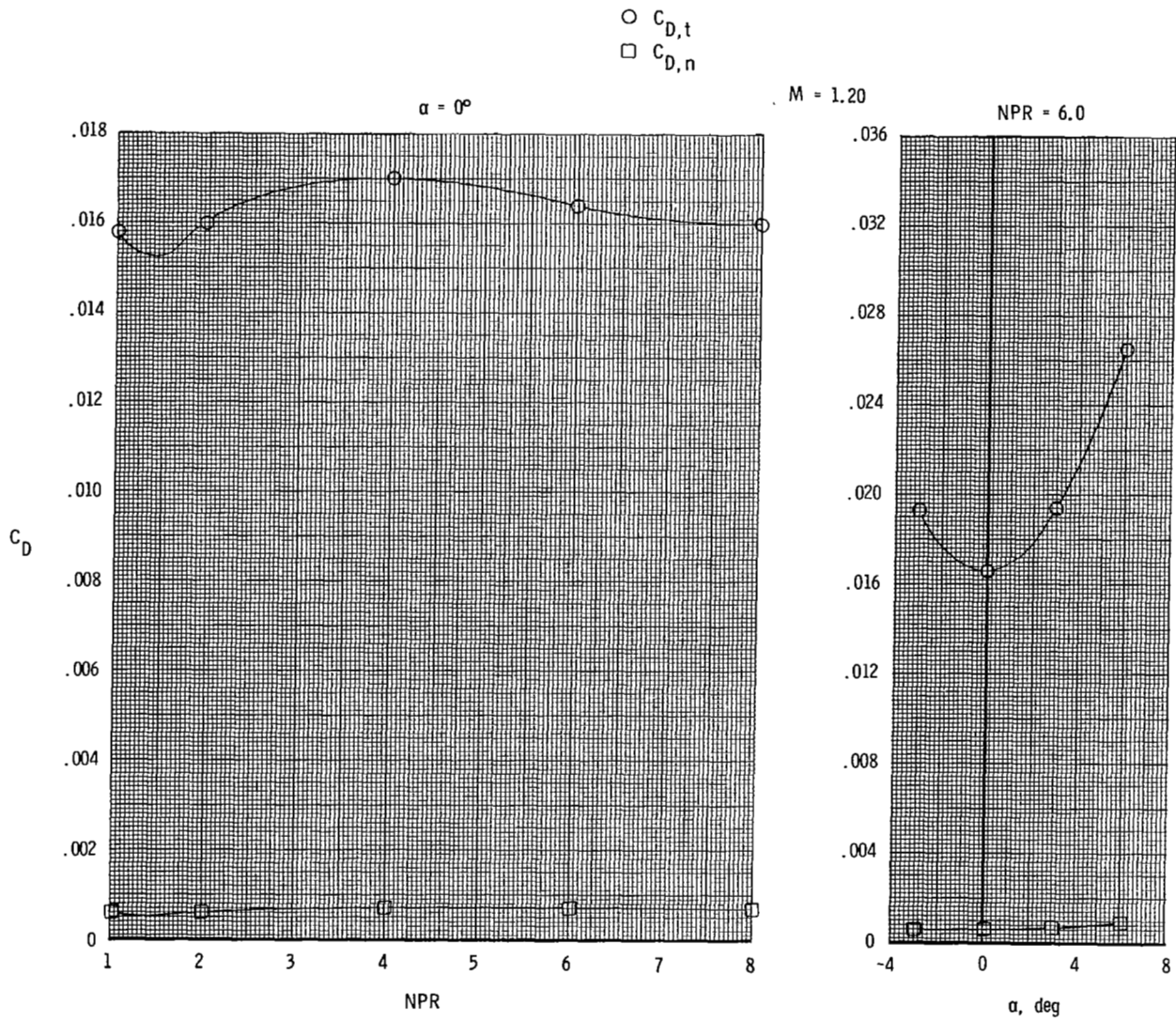
(b) Concluded.
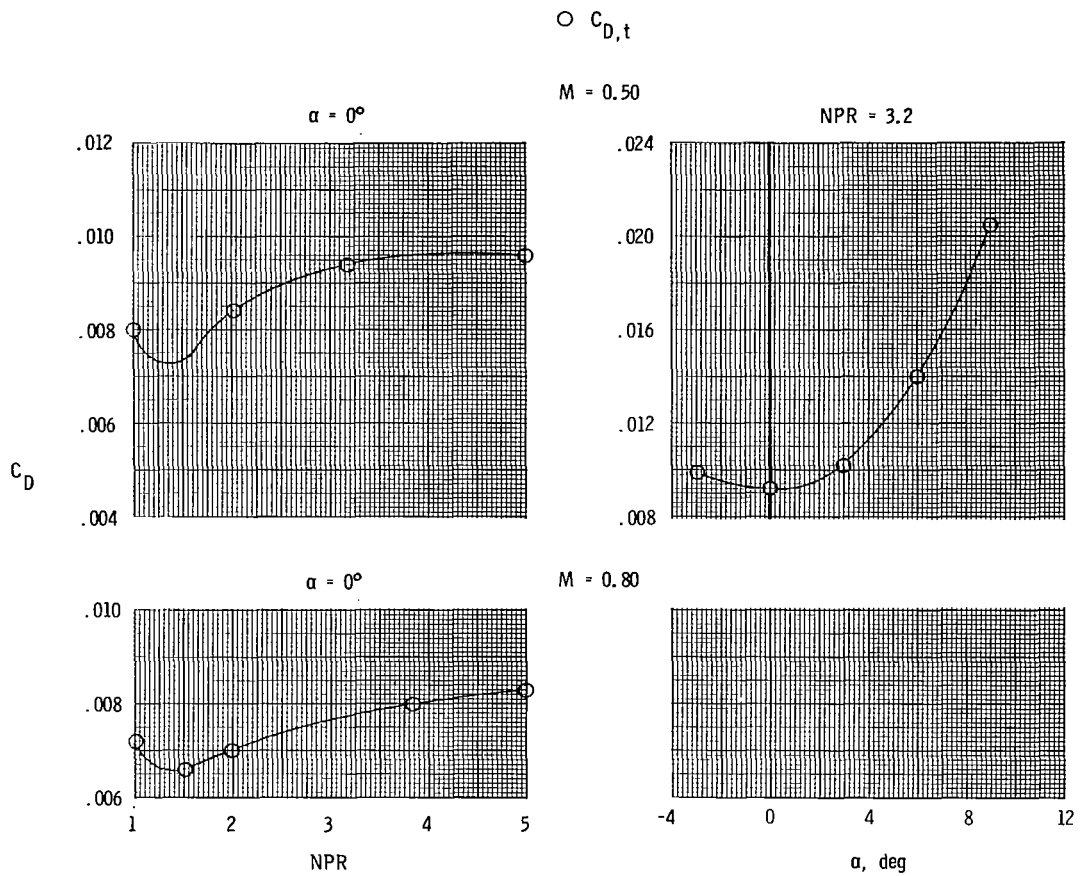
Figure 10.- Continued.

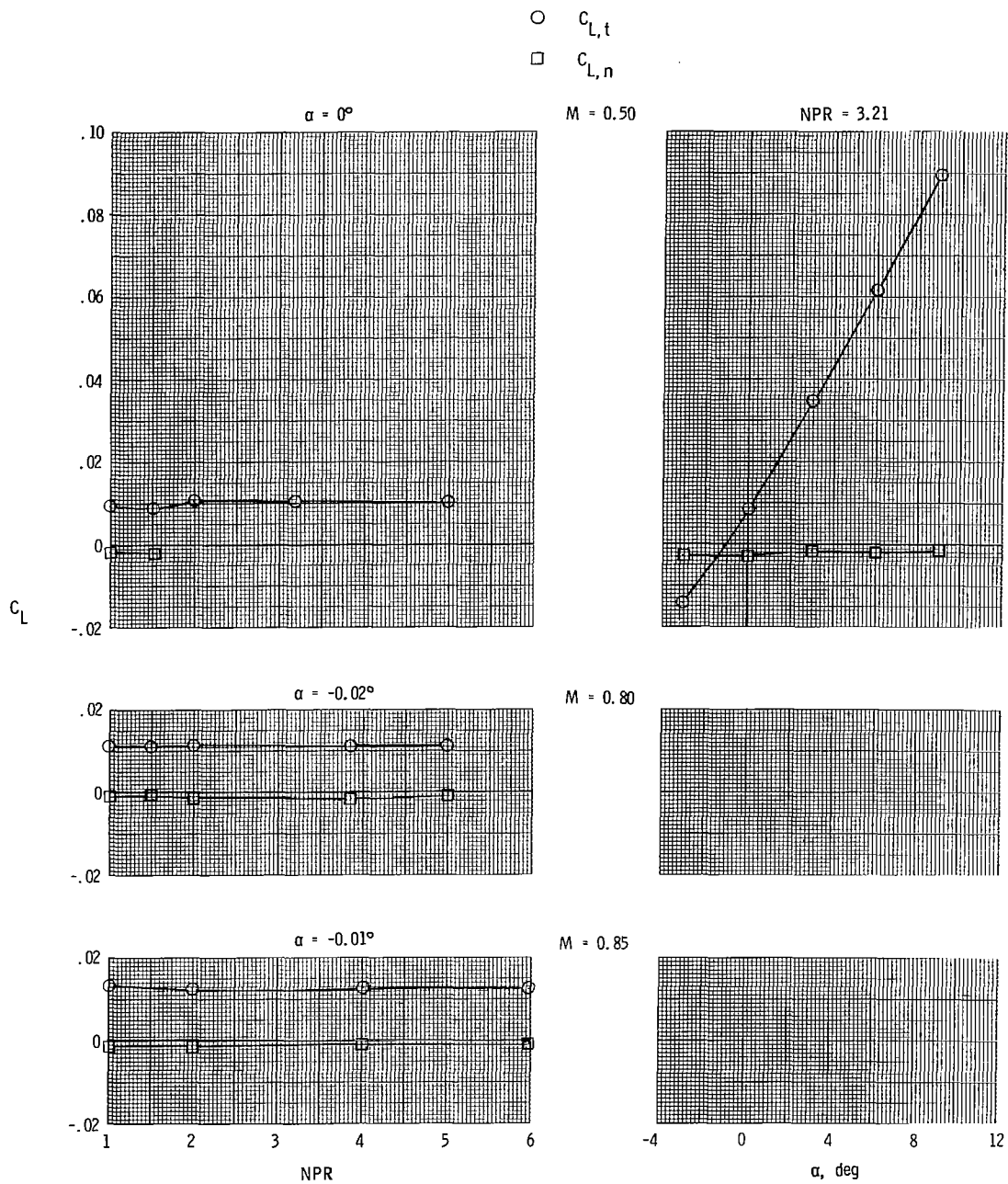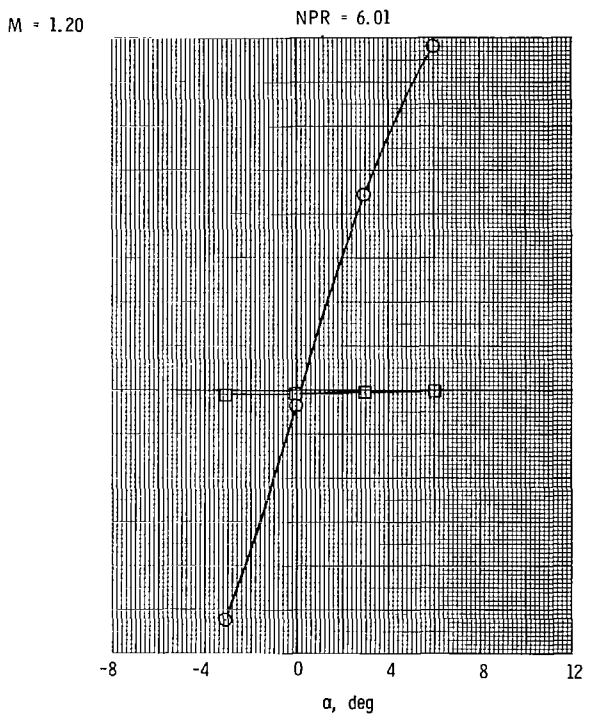(c) Aft horizontal tails; mid vertical tails.

Figure 10.- Continued.
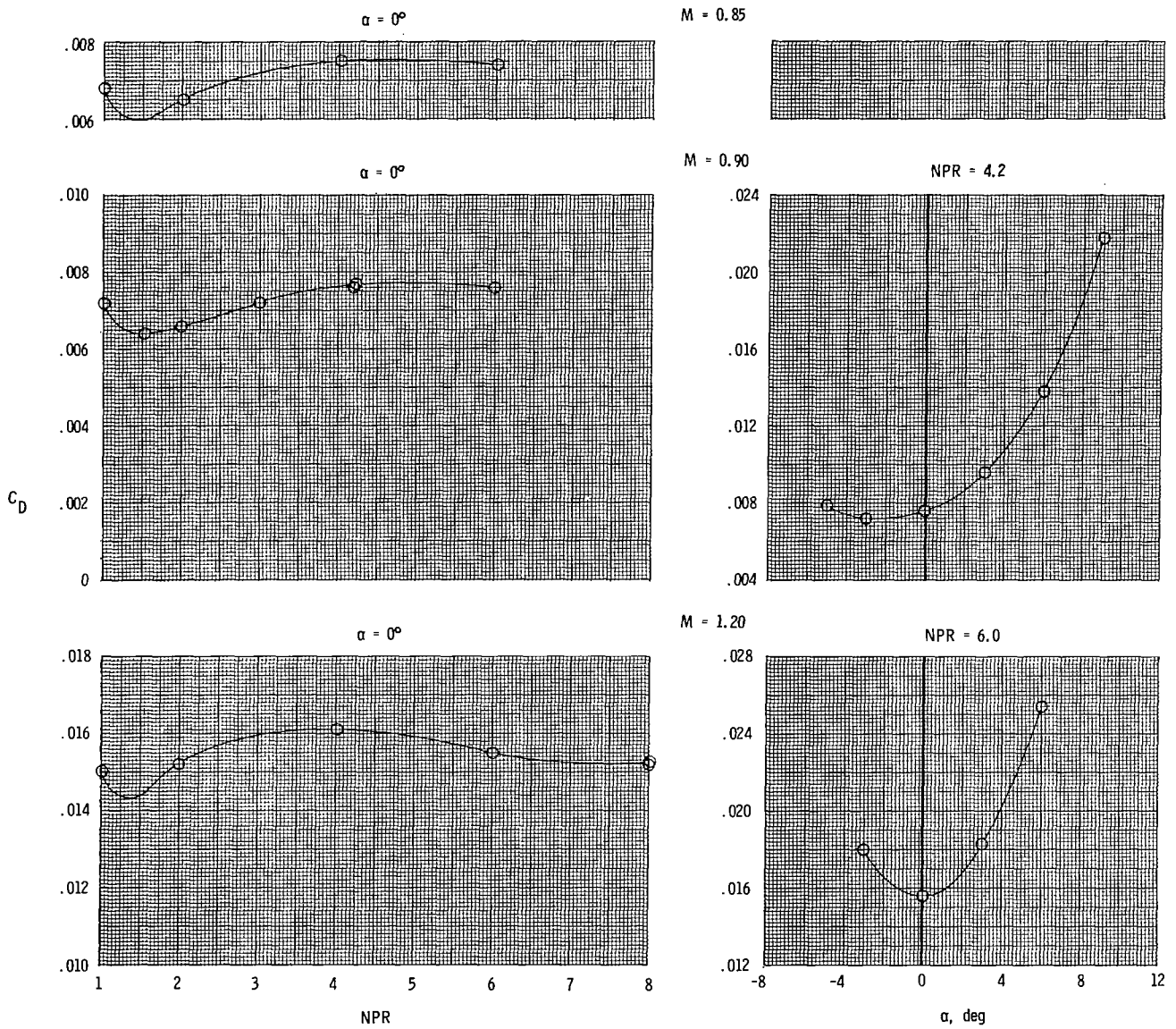
(c) Concluded.

Figure 10.- Concluded.

(a) Tails off.
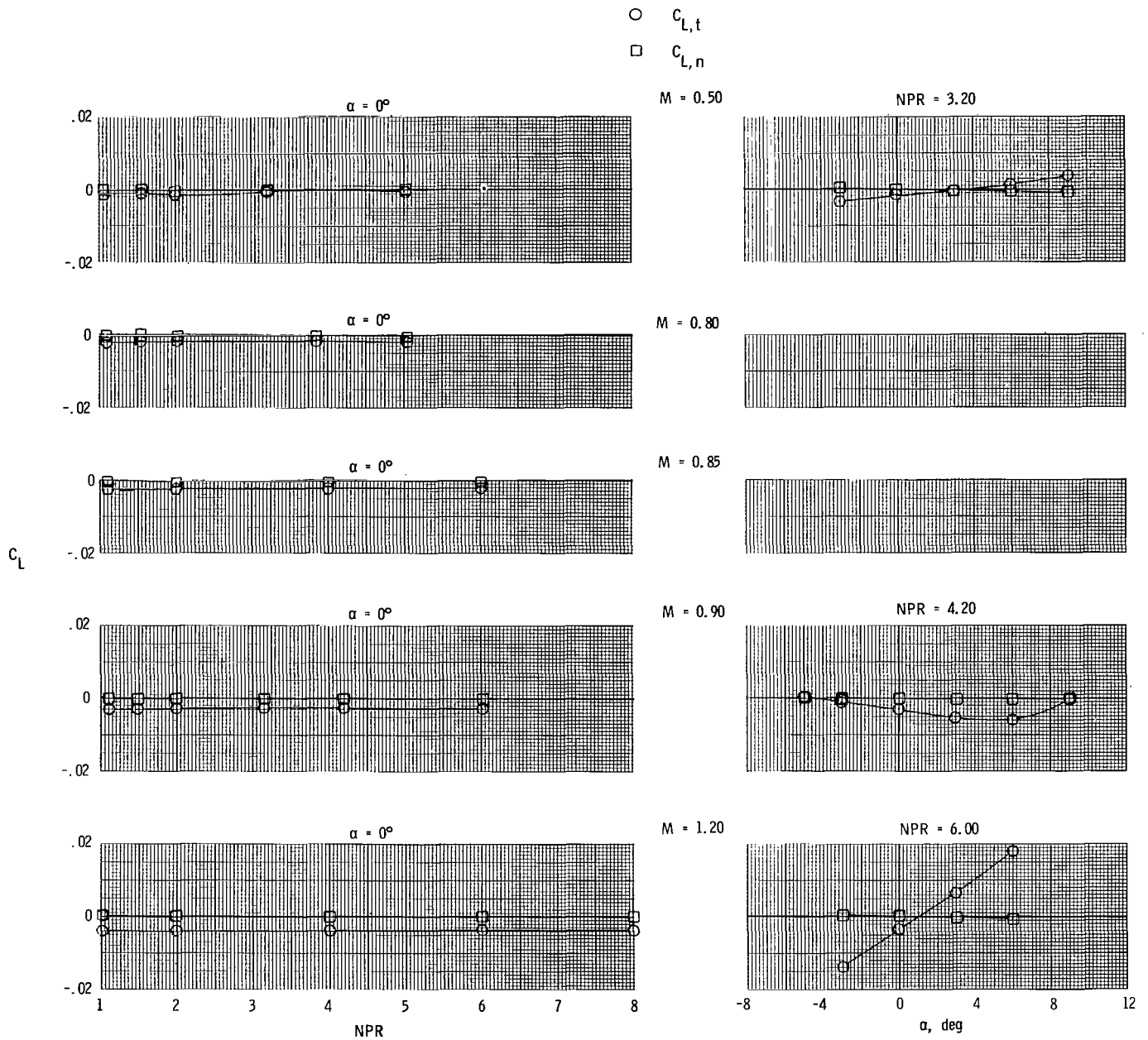
Figure 11.- Variation of total (afterbody + nozzles + tails) and nozzle lift coefficient with nozzle pressure ratio and angle of attack for short subsonic dry power nozzles.
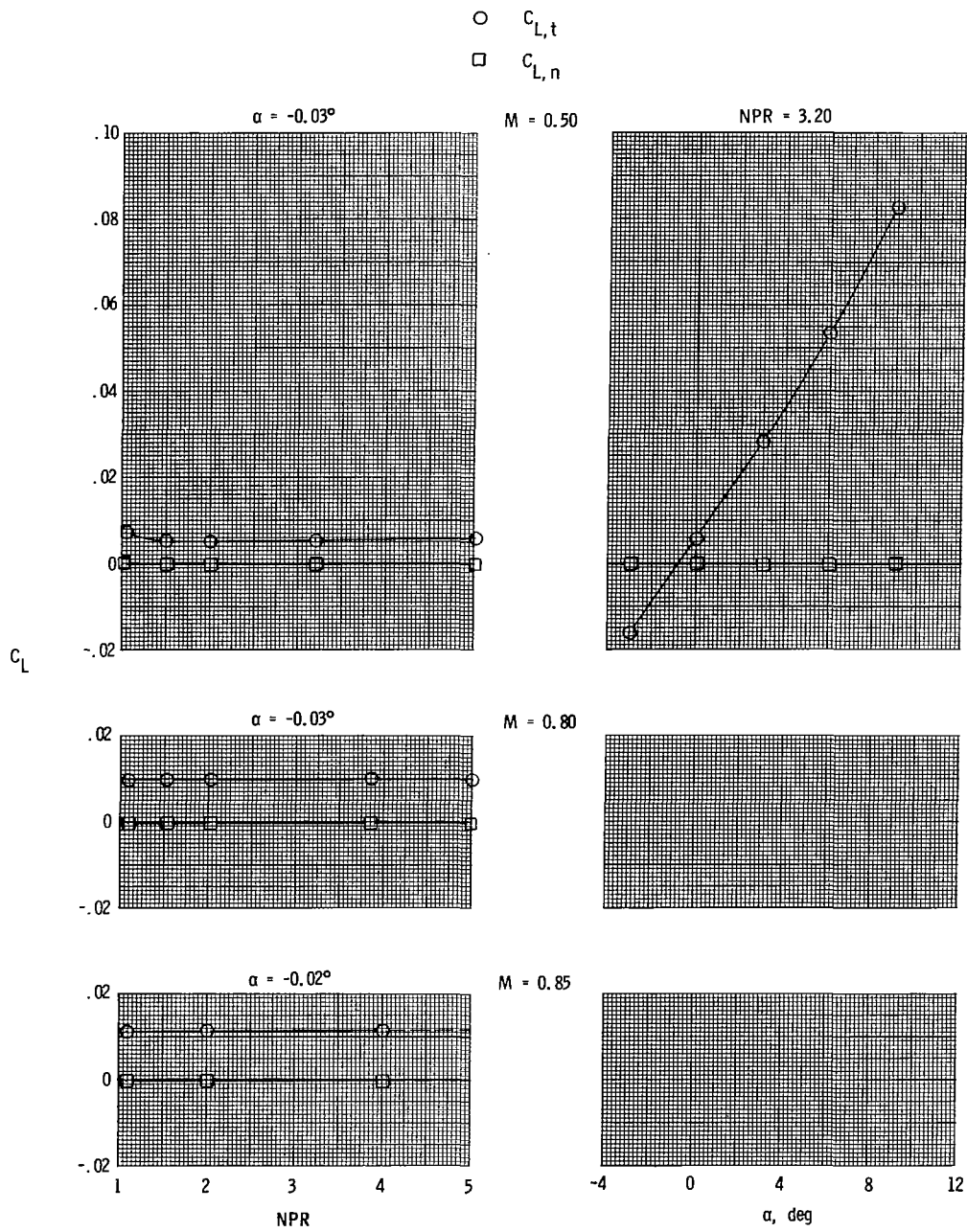
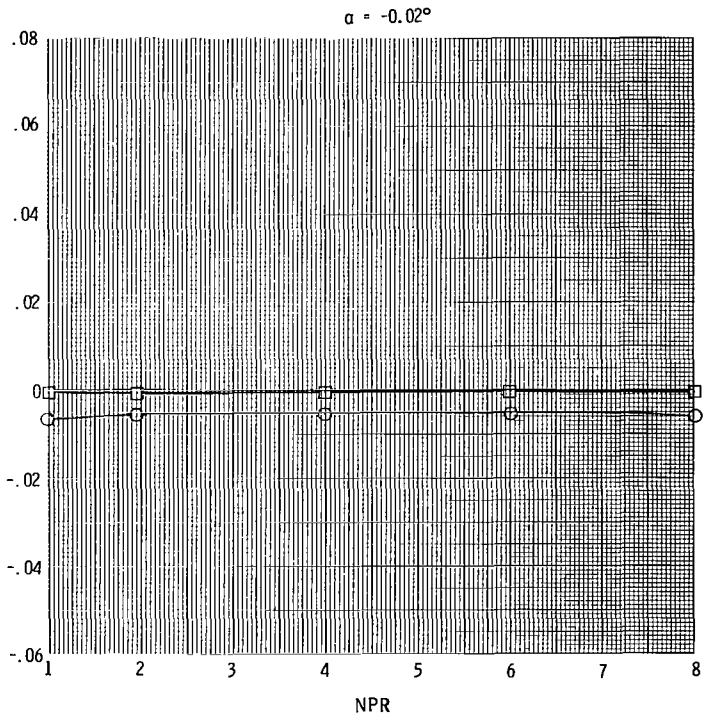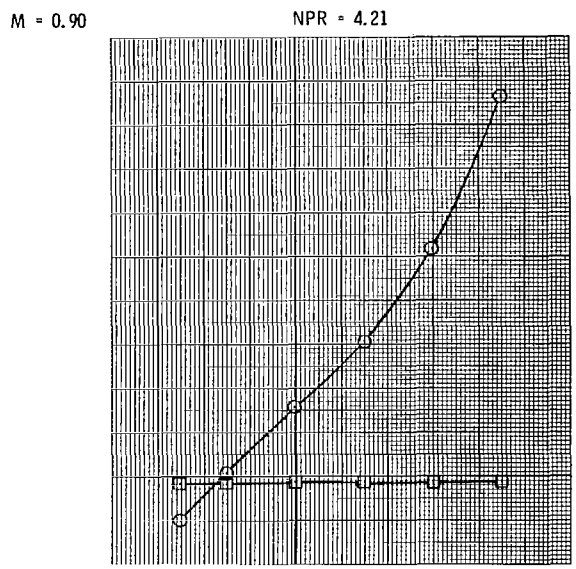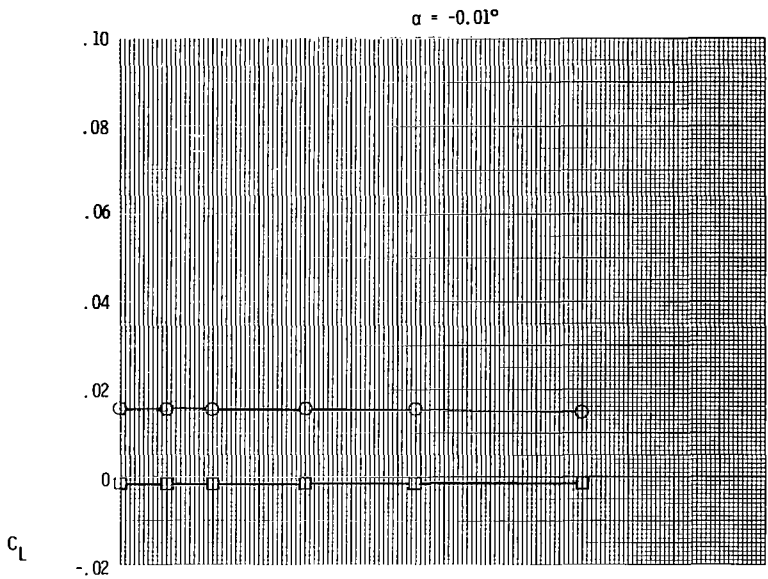(b) Mid horizontal tails; forward vertical tails.
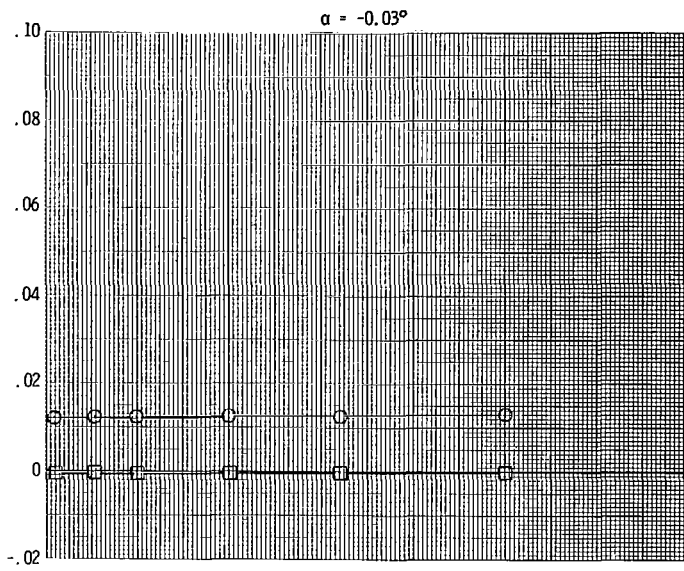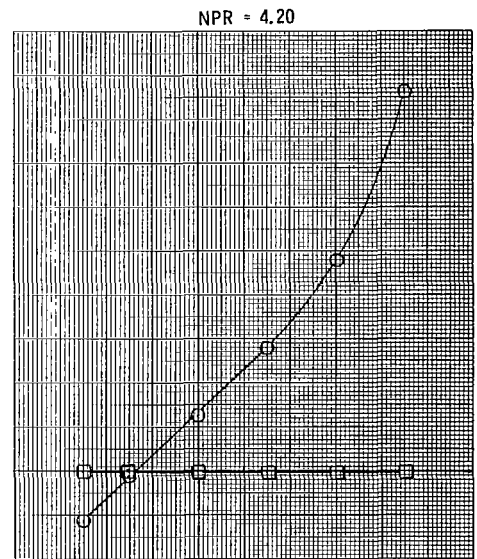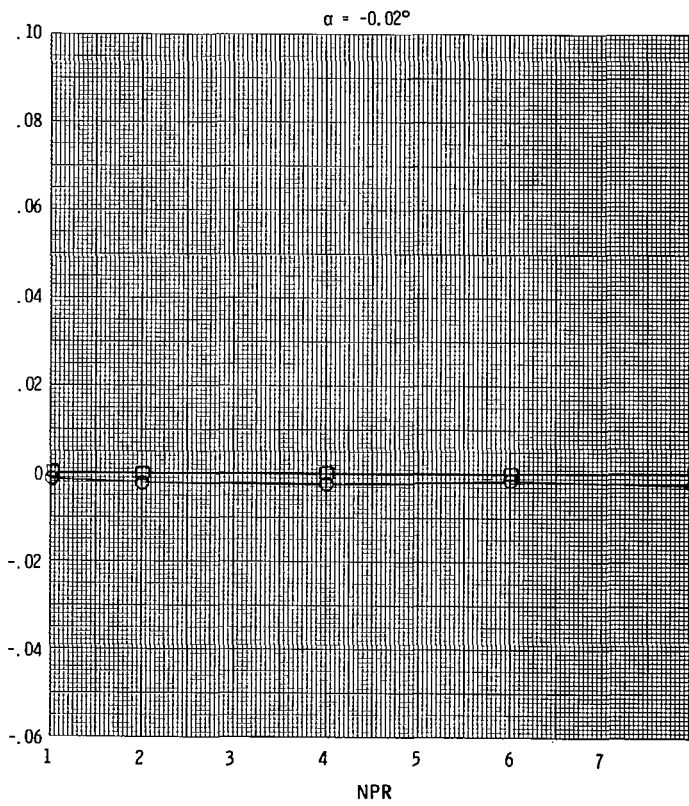
Figure 11.- Continued.
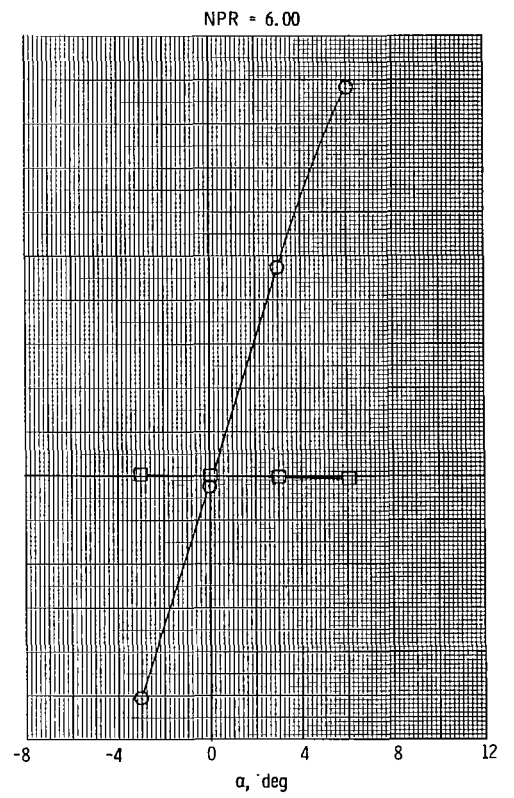
(b) Concluded.
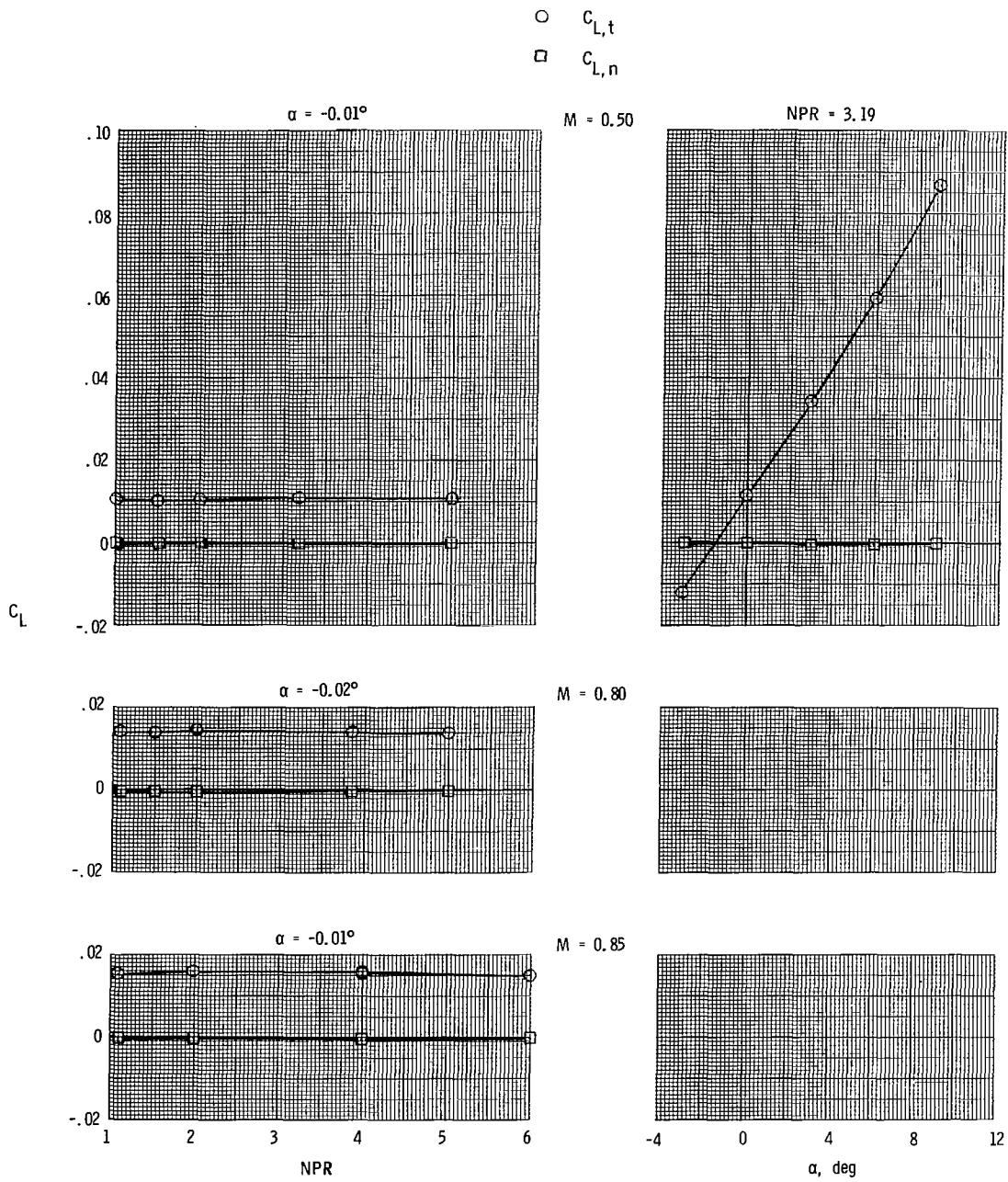
Figure 11.- Continued.

(c) Mid horizontal tails; mid vertical tails.

Figure 11.- Continued.
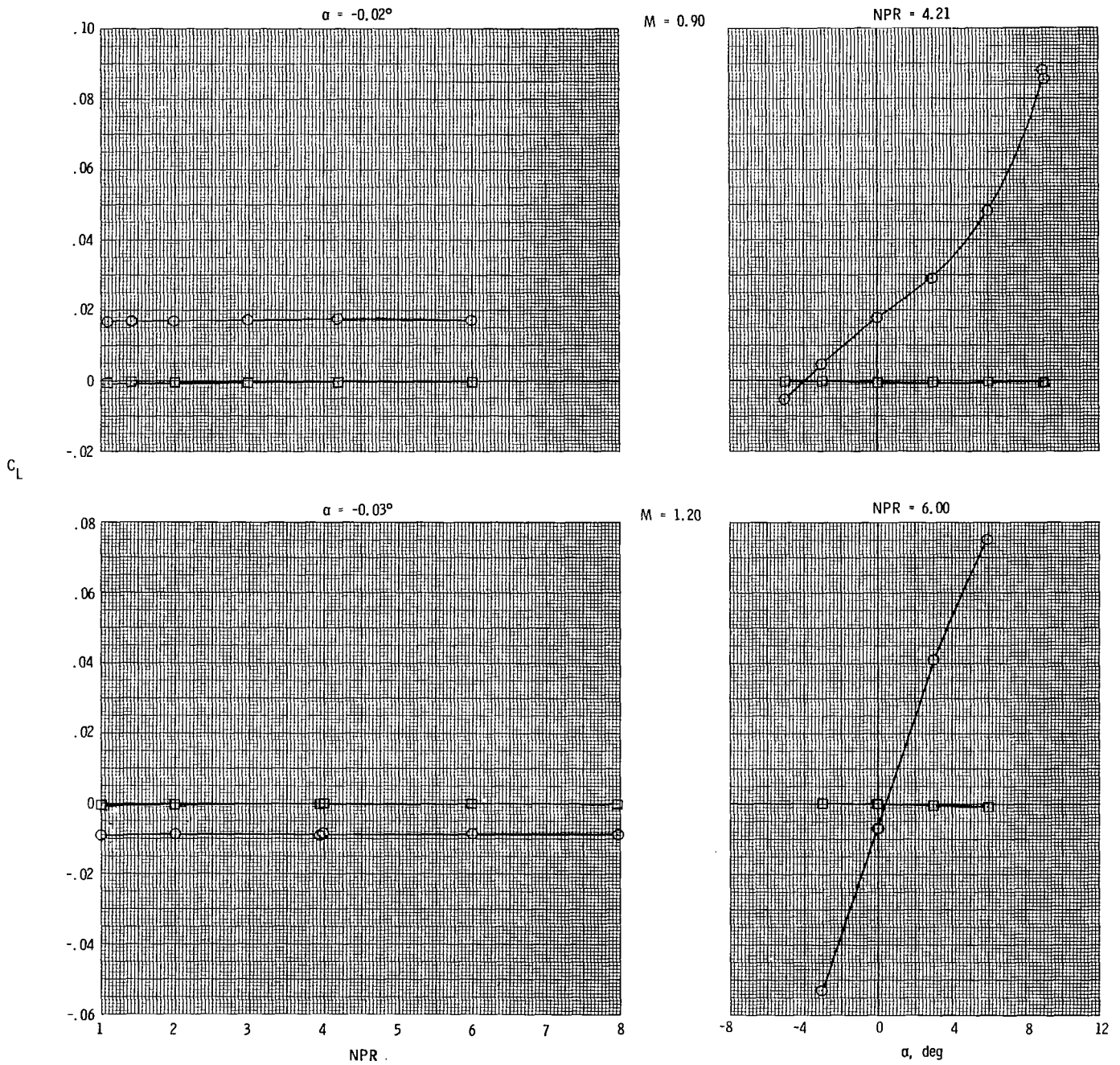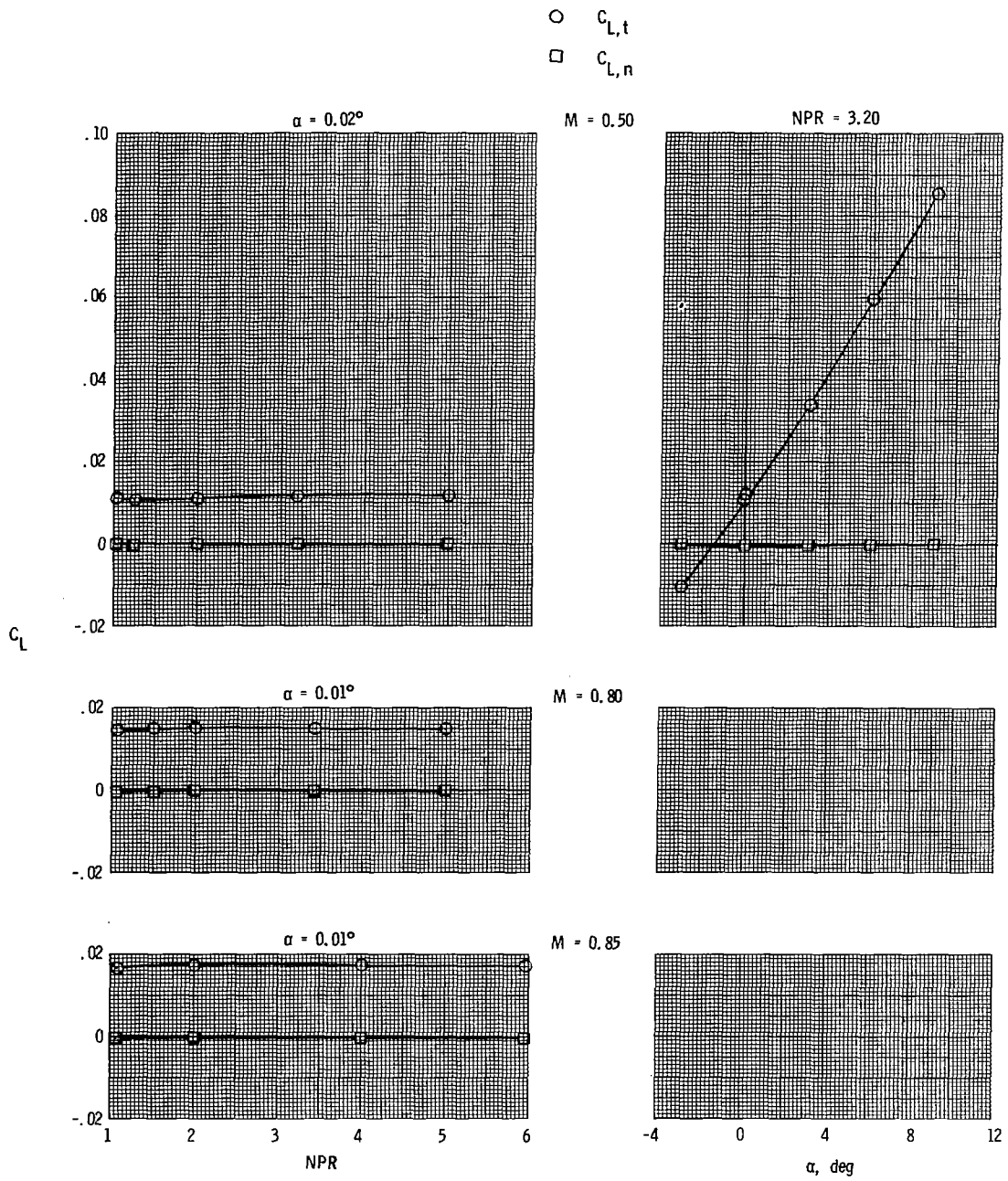
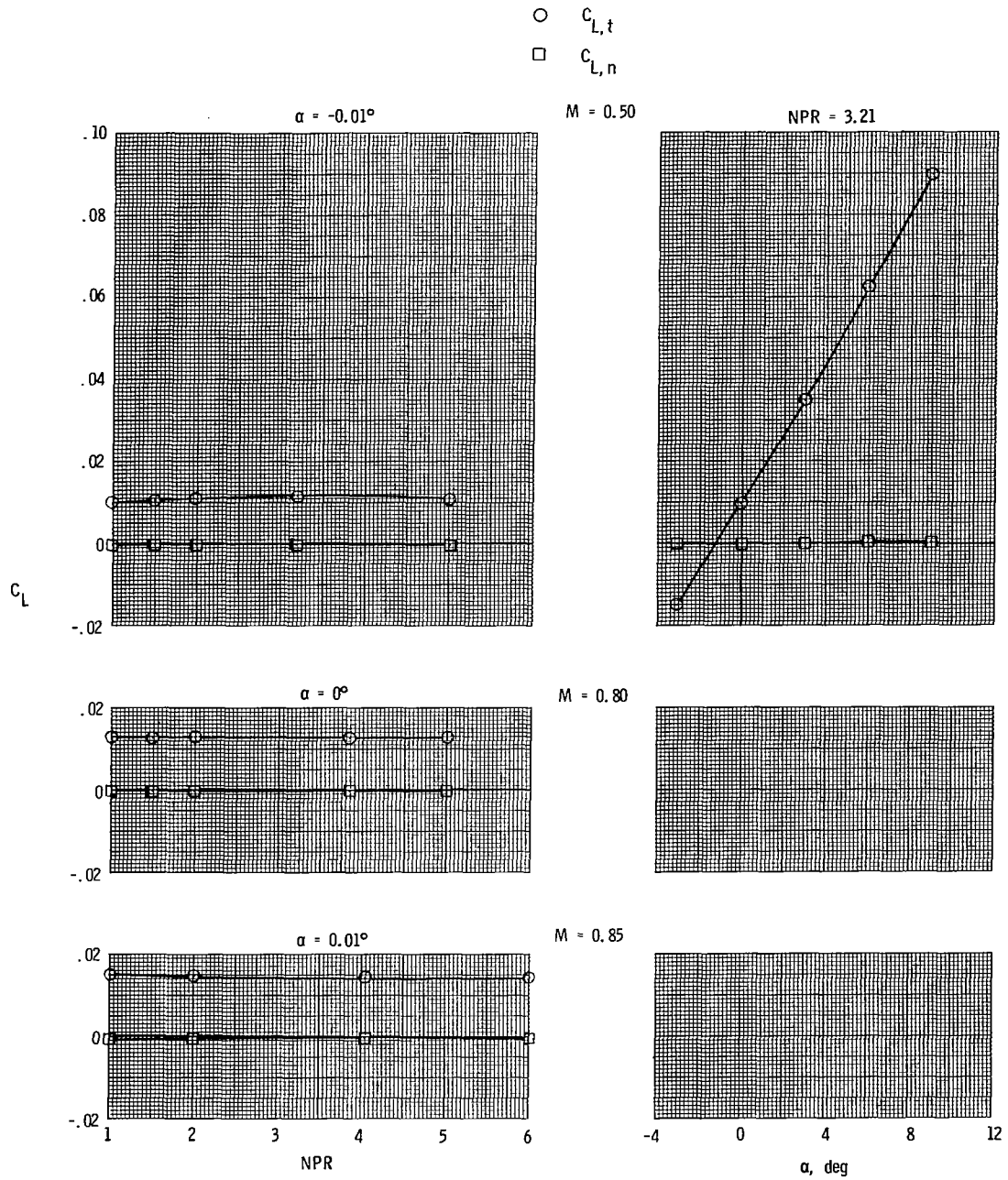(c) Concluded.

Figure 11.- Continued.

(d) Aft horizontal tails; mid vertical tails.

Figure 11.- Continued.
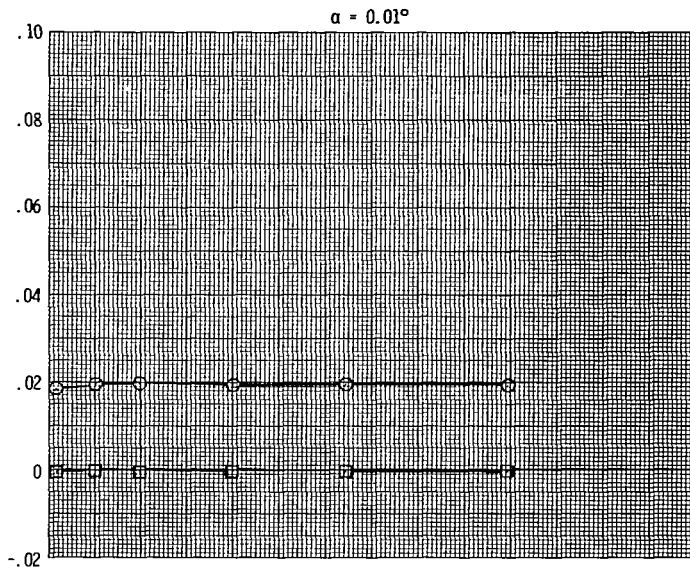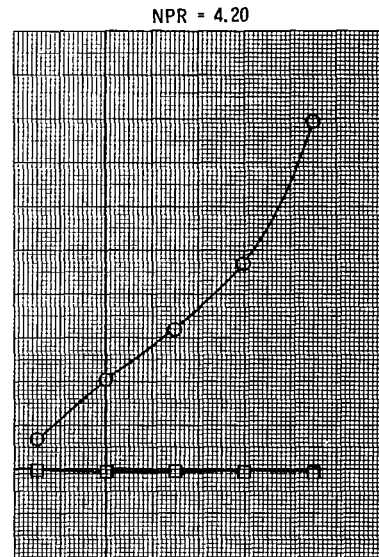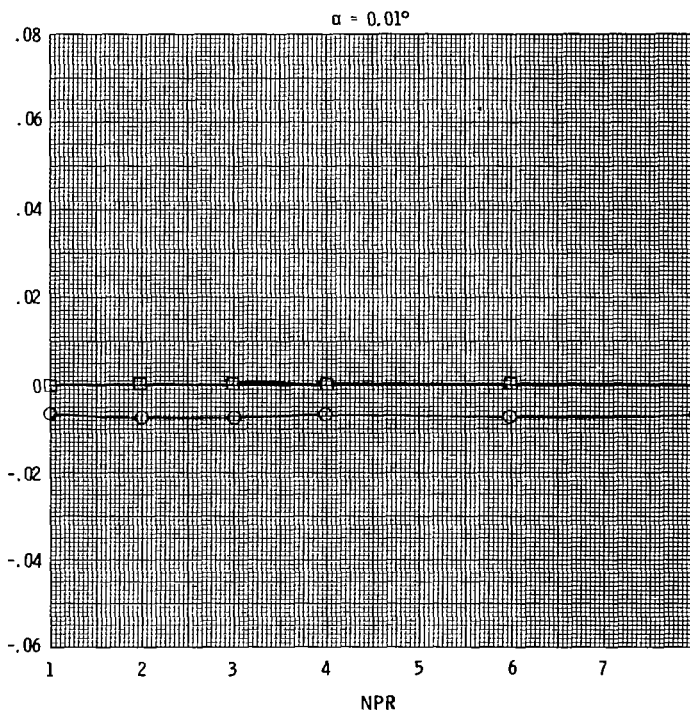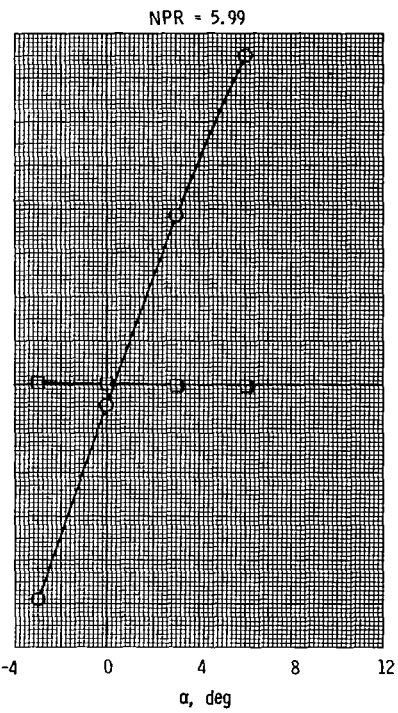
(d) Concluded.

Figure 11.- Concluded.
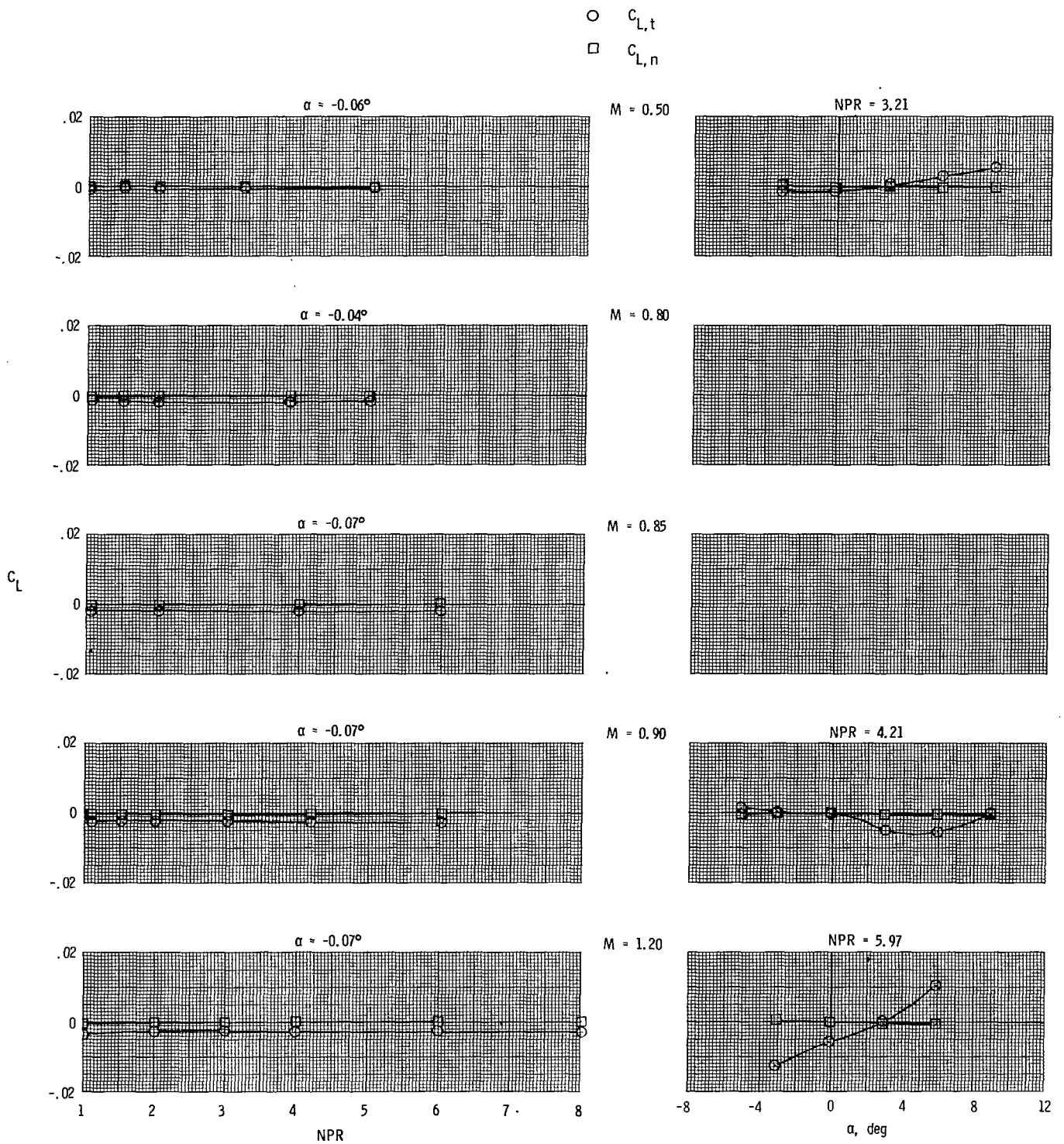
(a) Tails off.

Figure 12.- Variation of total (afterbody + nozzles + tails) and nozzle lift
coefficient with nozzle pressure ratio and angle of attack for long subsonic
dry power nozzles.
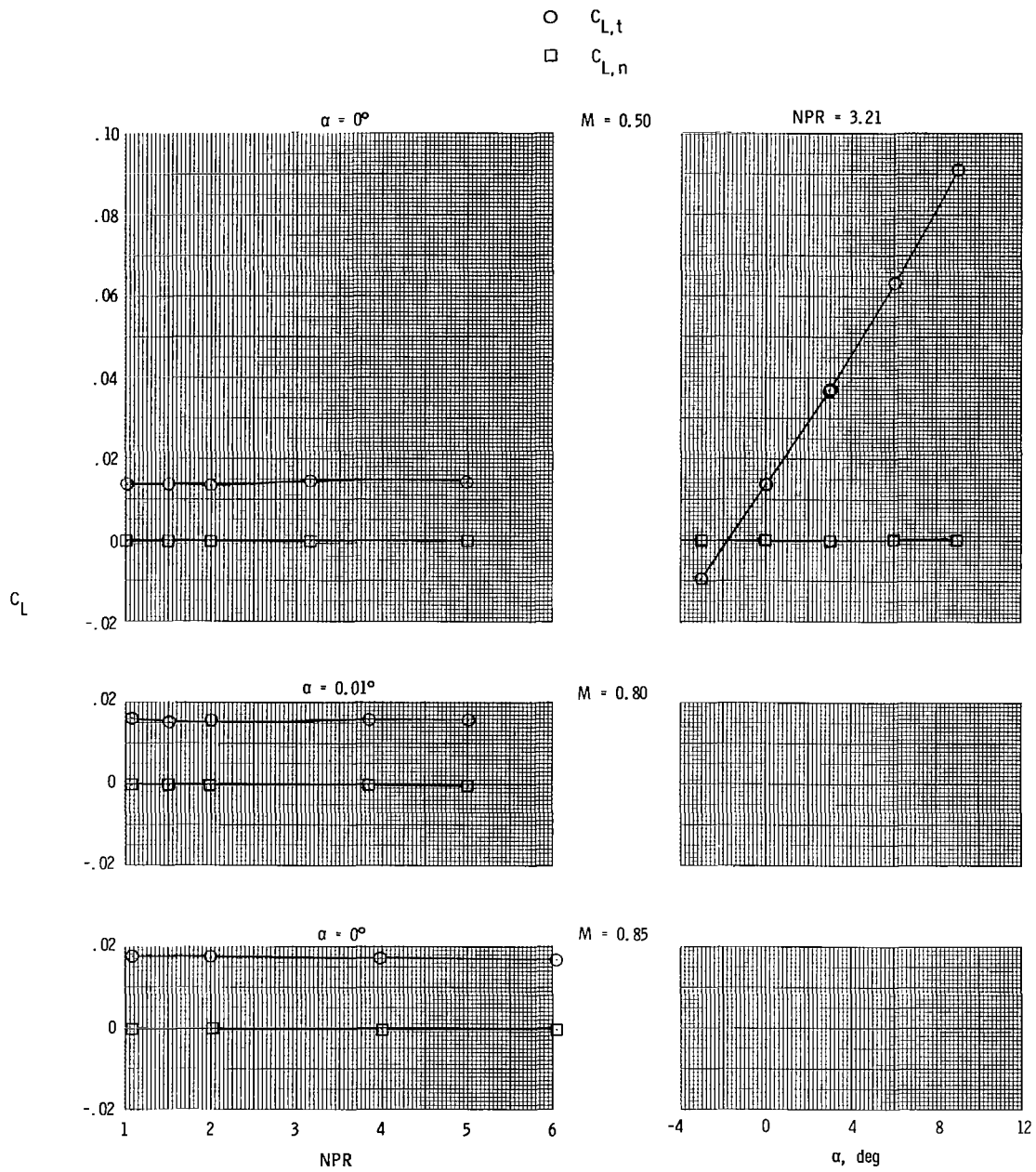
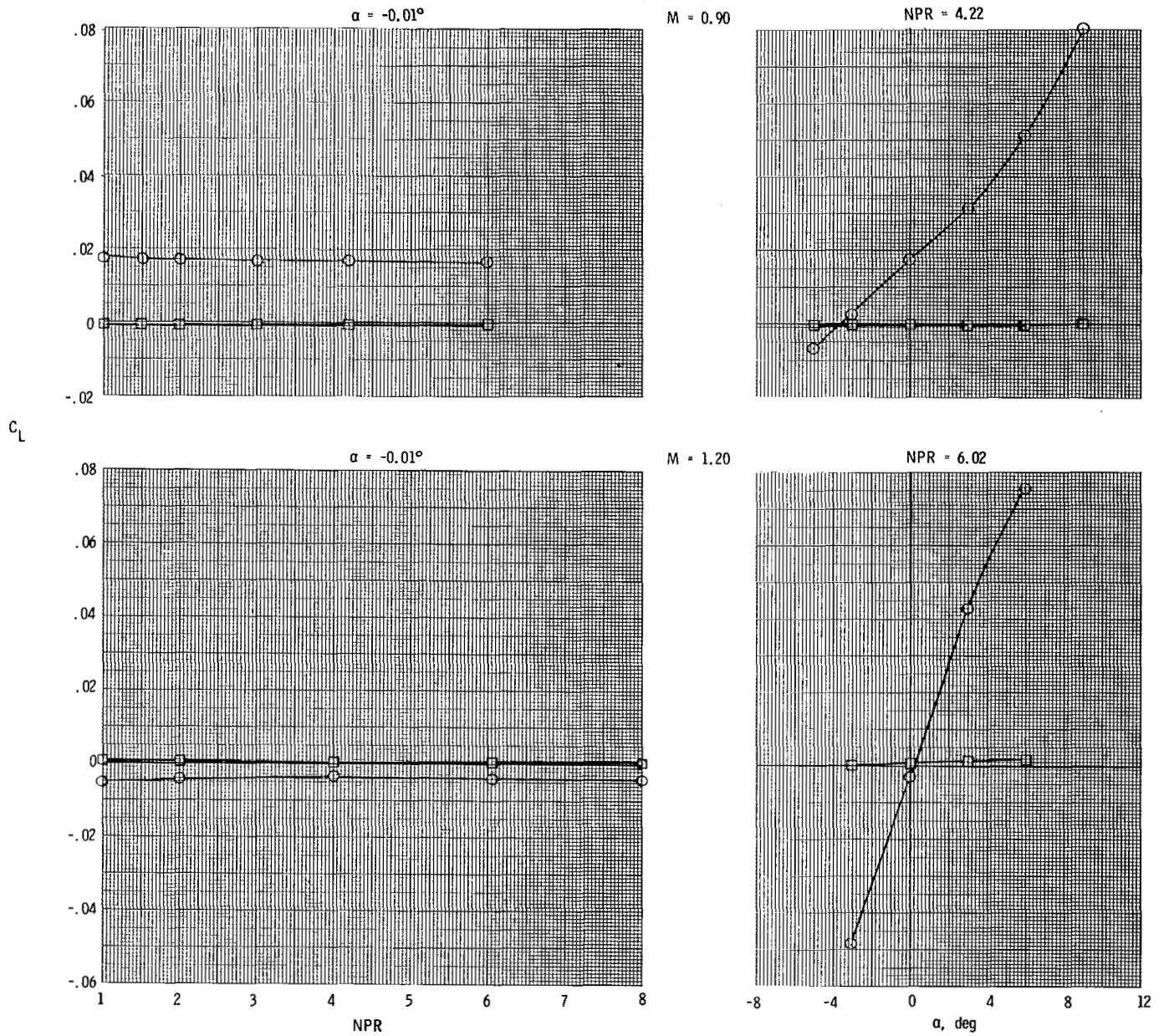(b) Mid horizontal tails; mid vertical tails.

Figure 12.- Continued.
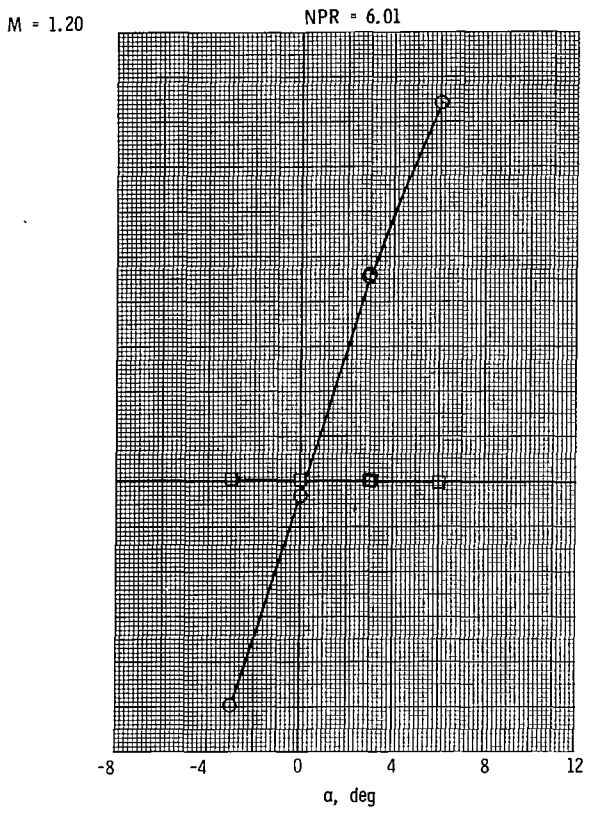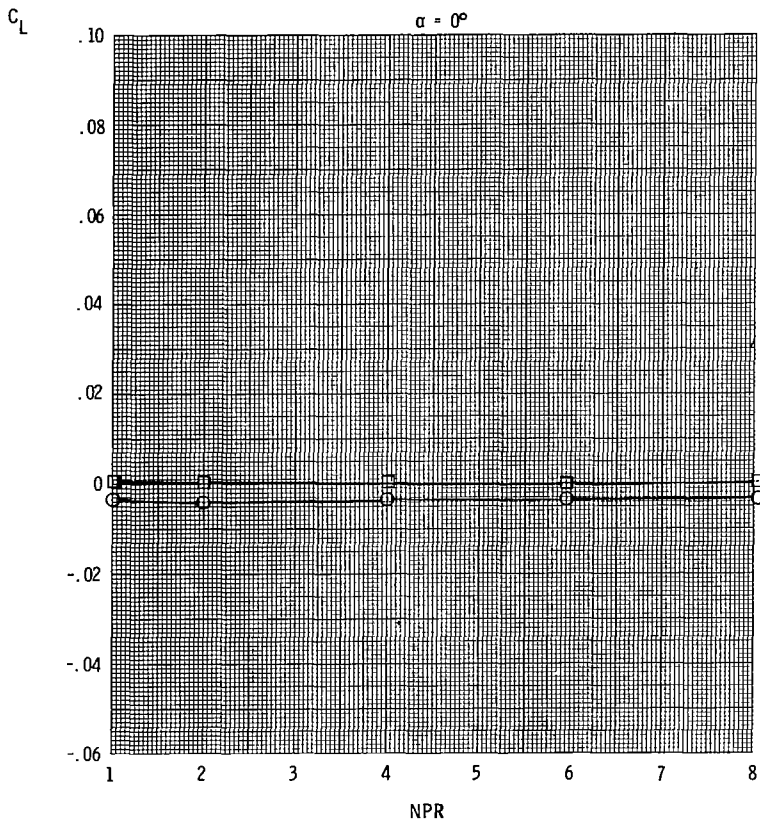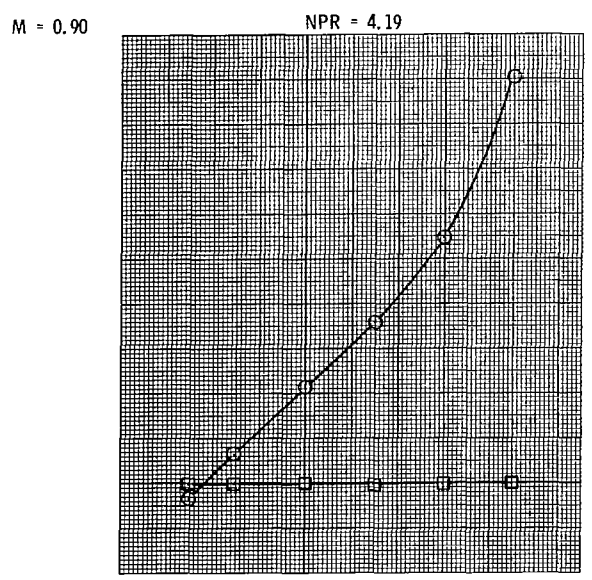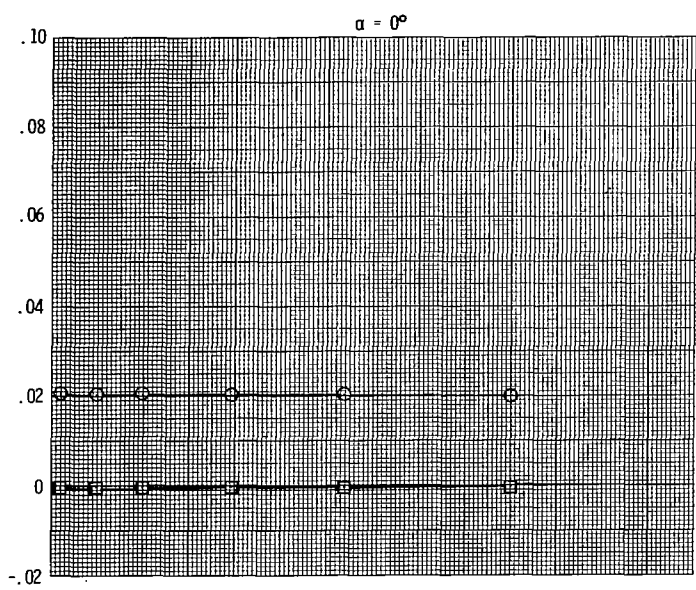
(b) Concluded.

Figure 12.- Continued.
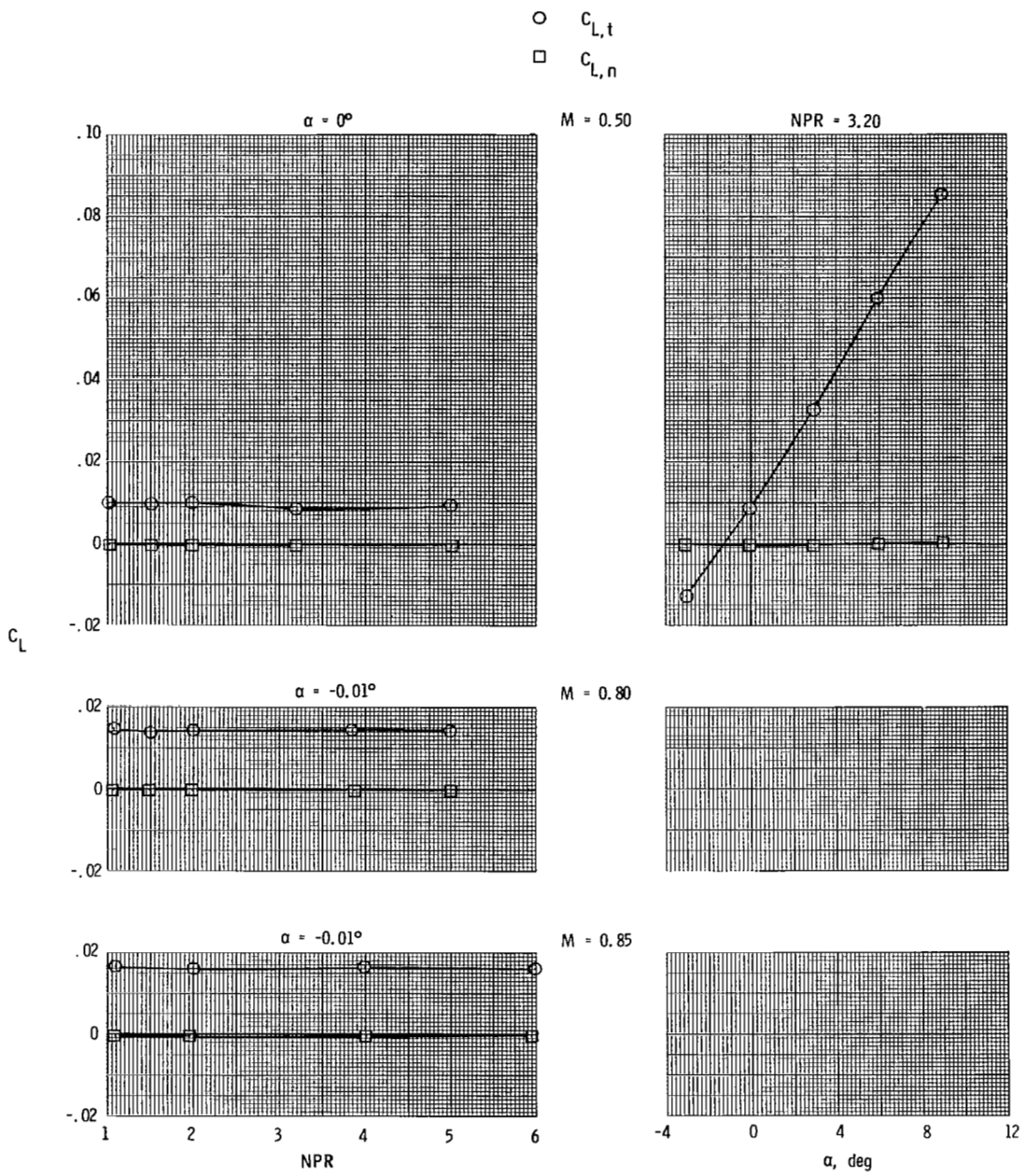
(c) Aft horizontal tails; mid vertical tails.

Figure 12.- Continued.
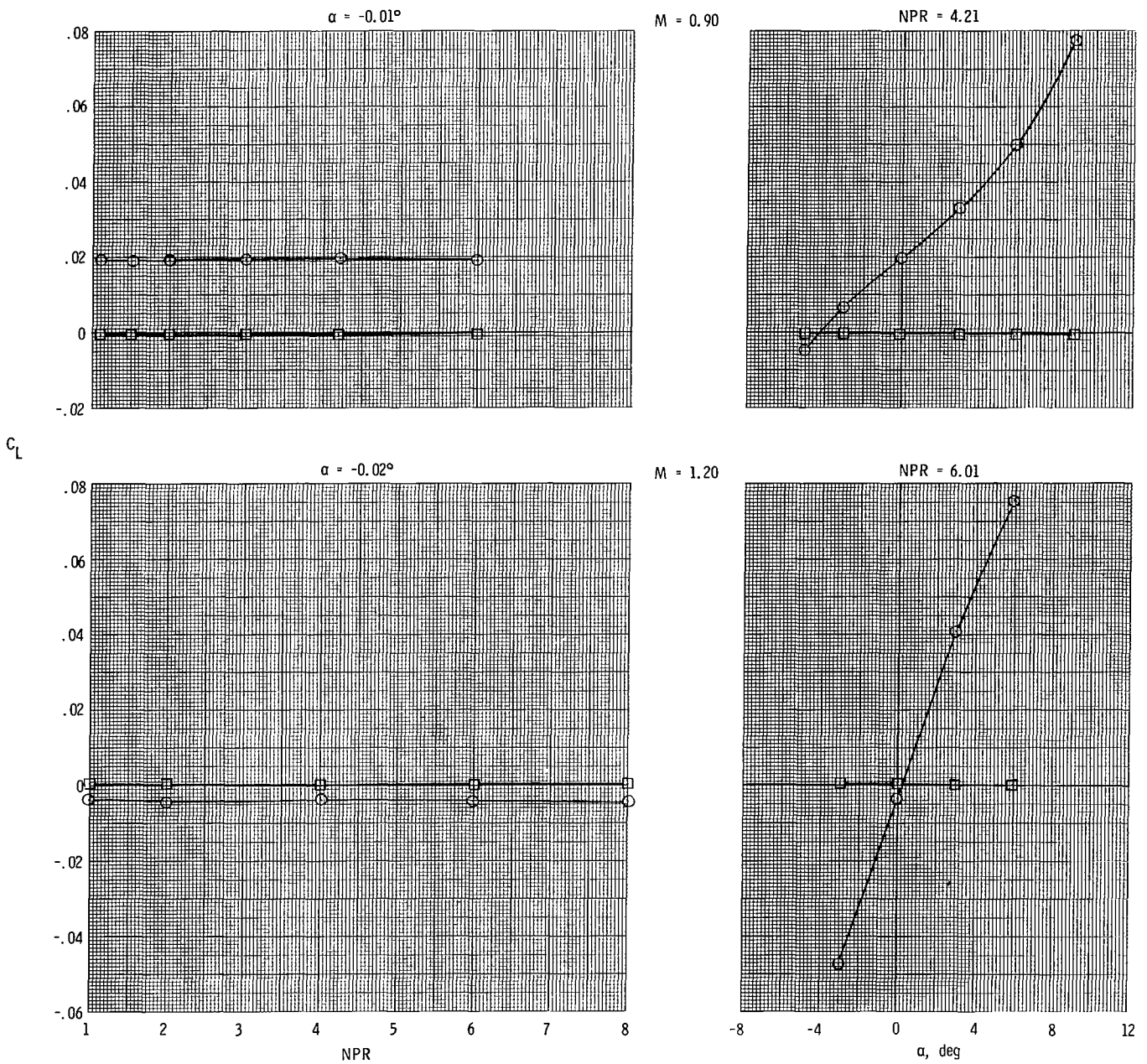
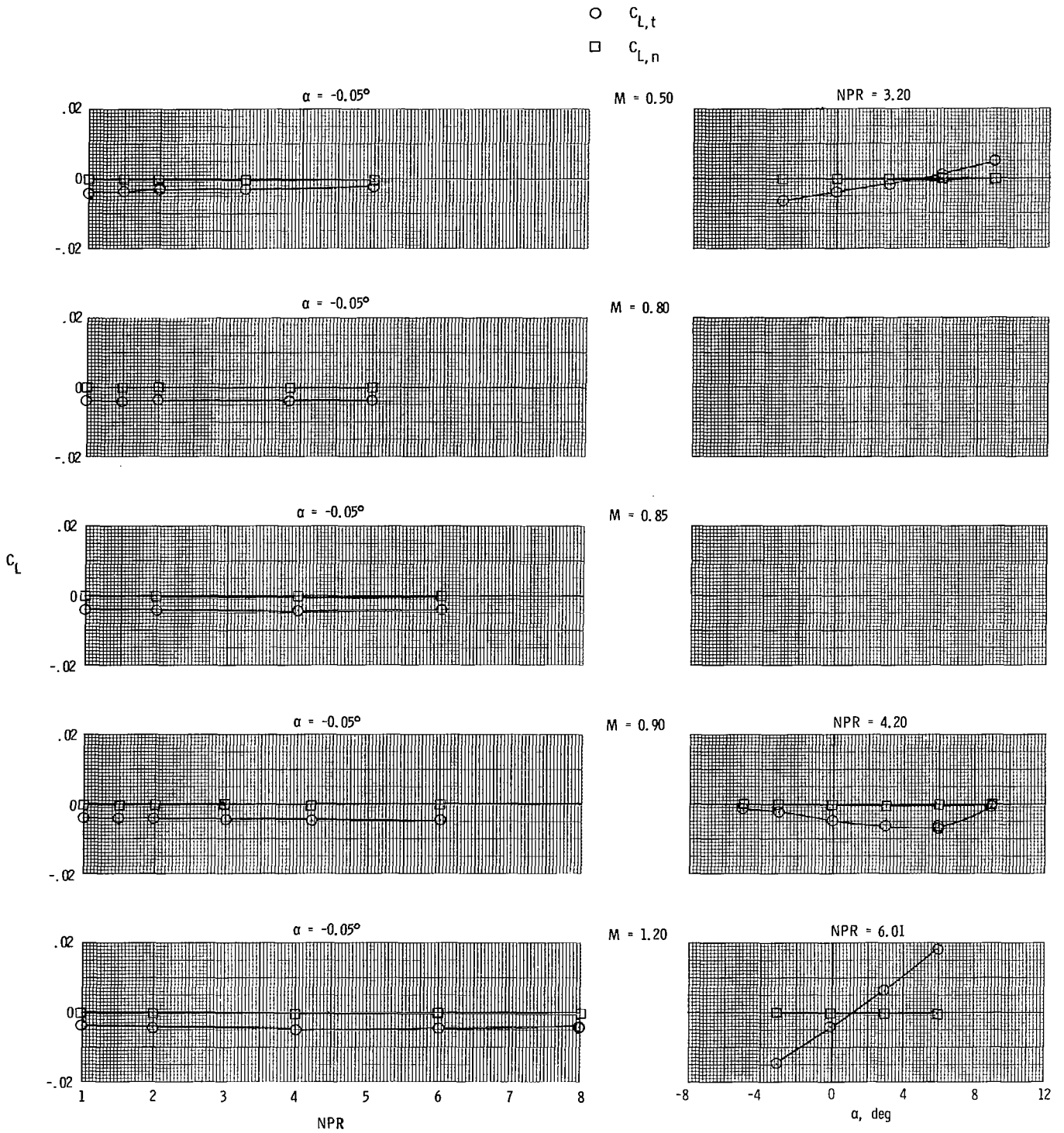(c) Concluded.

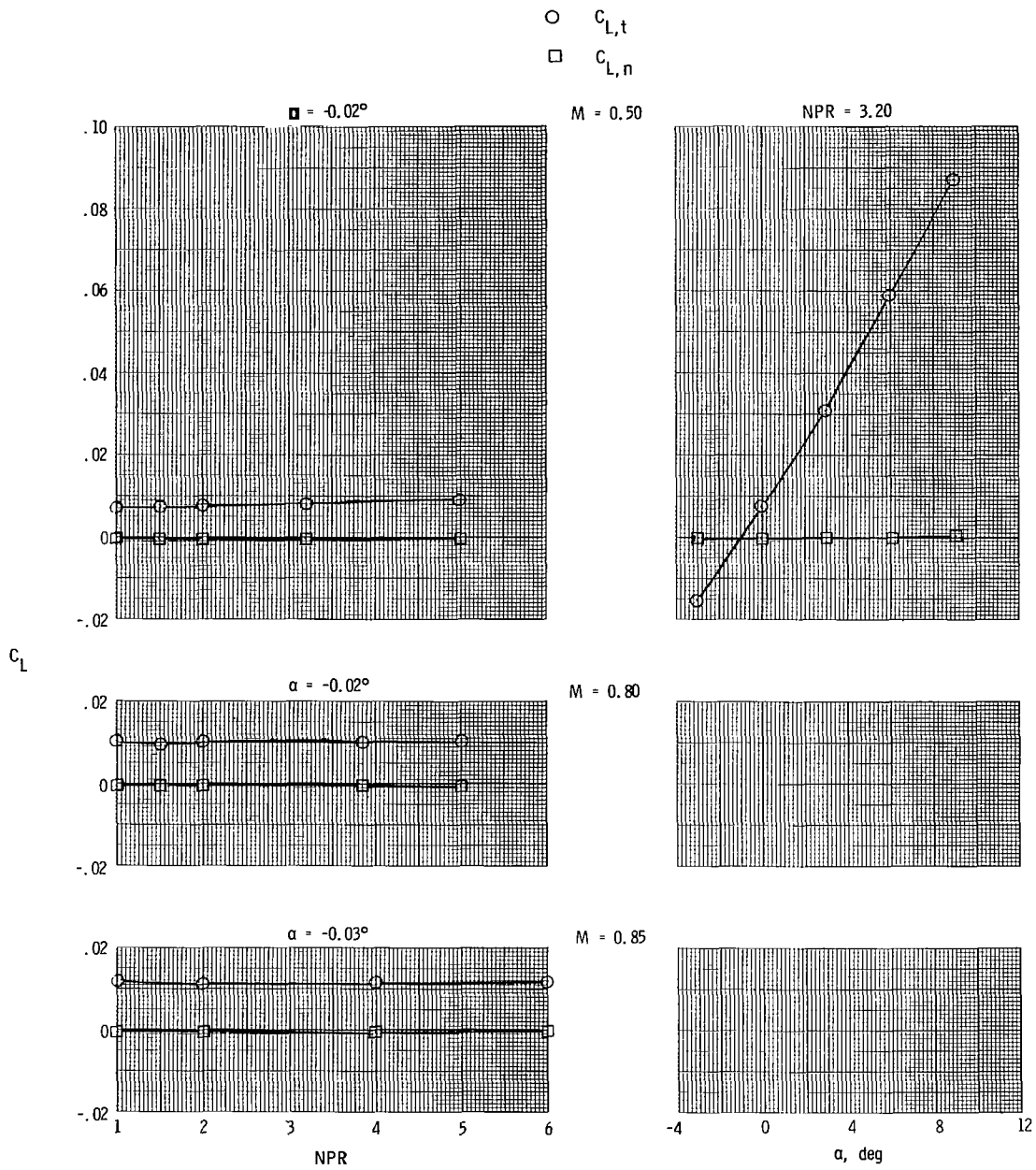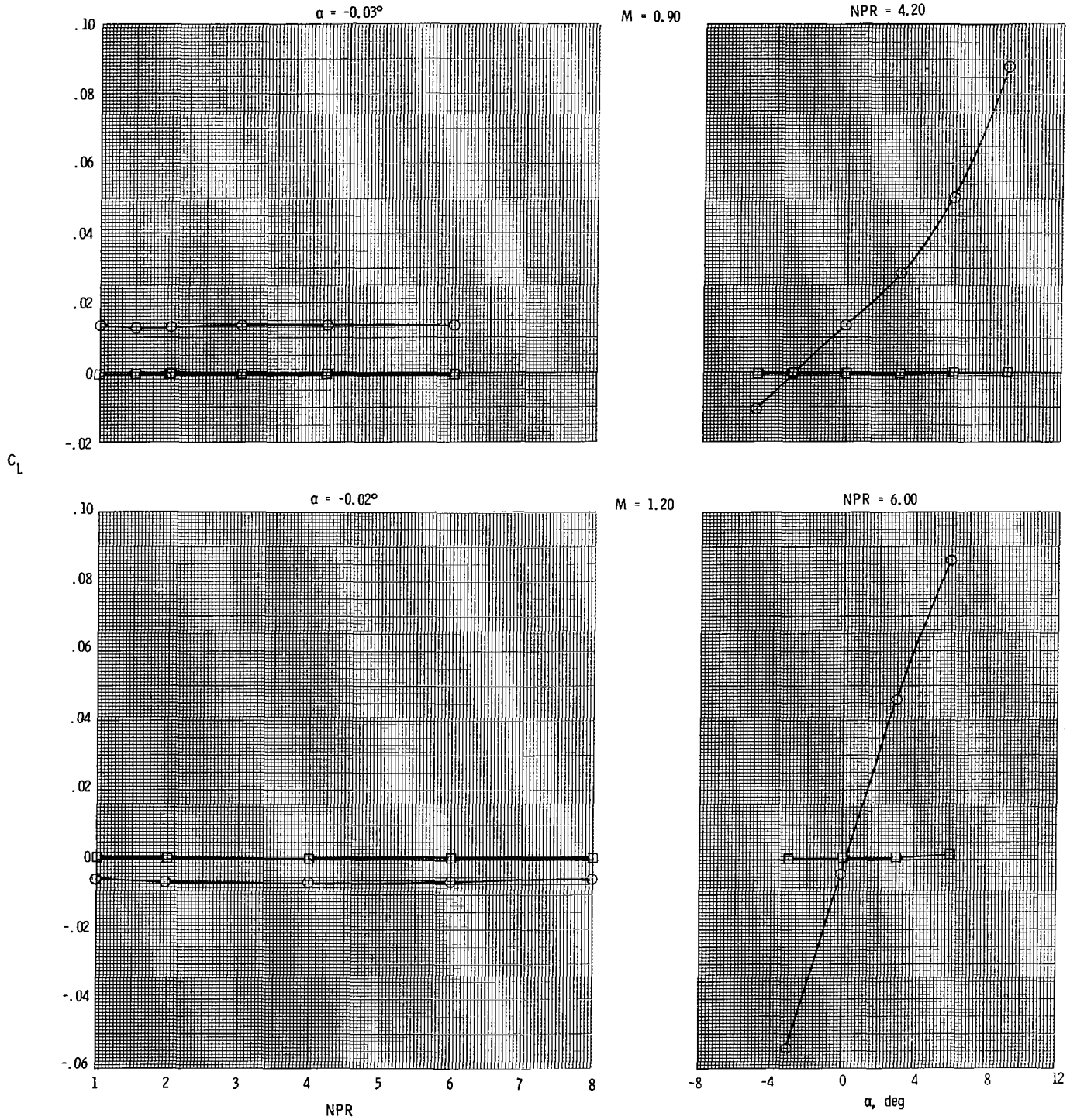Figure 12.- Concluded.
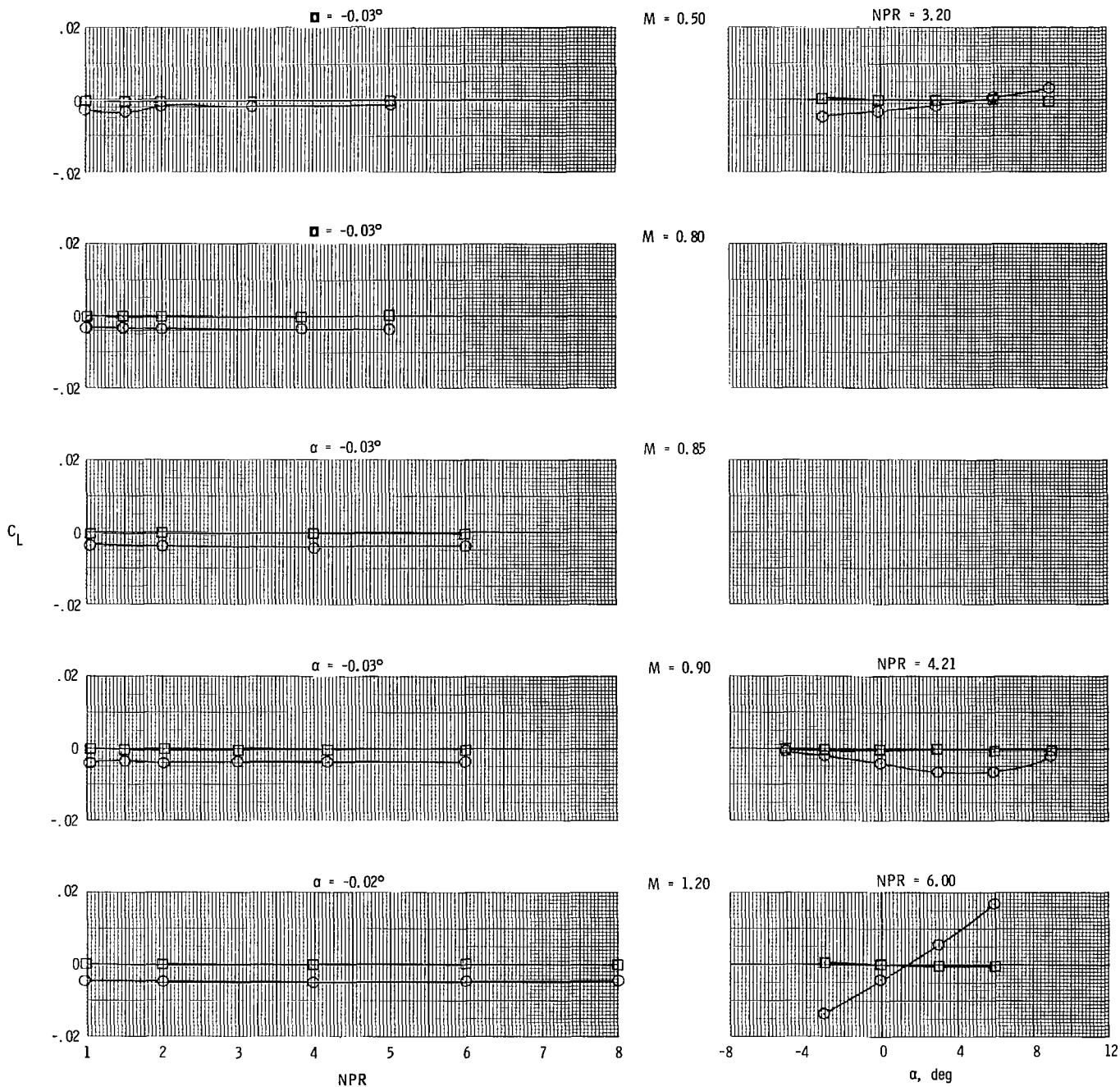
(a) Tails off.

Figure 13.- Variation of total (afterbody + nozzles + tails) and nozzle lift coefficient with nozzle pressure ratio and angle of attack for short supersonic dry power nozzles.
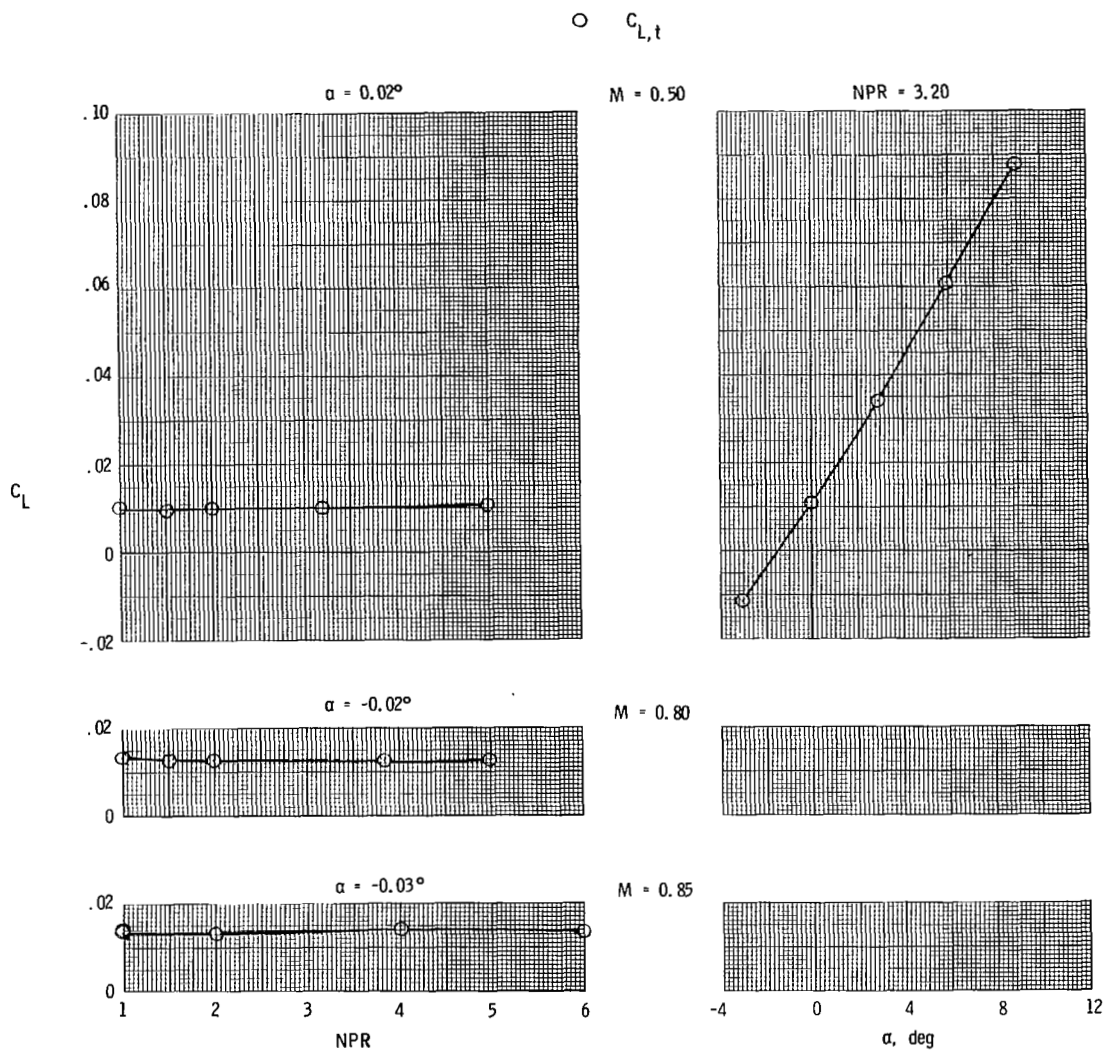
(b) Mid horizontal tails; forward vertical tails.

Figure 13.- Continued.
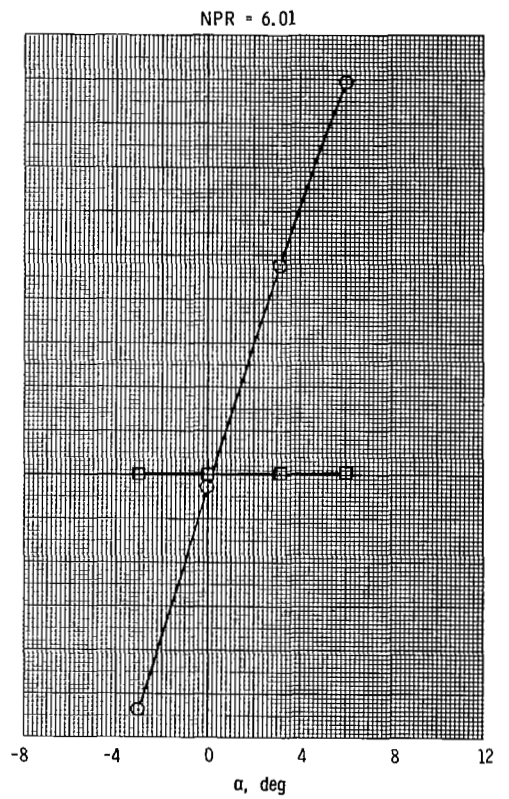
(b) Concluded.

Figure 13.- Continued.

(c) Aft horizontal tails; forward vertical tails.

Figure 13.- Continued.
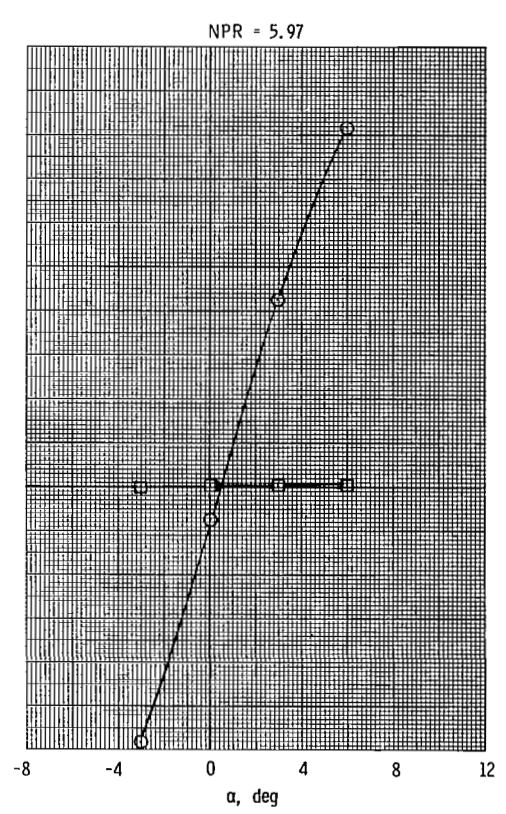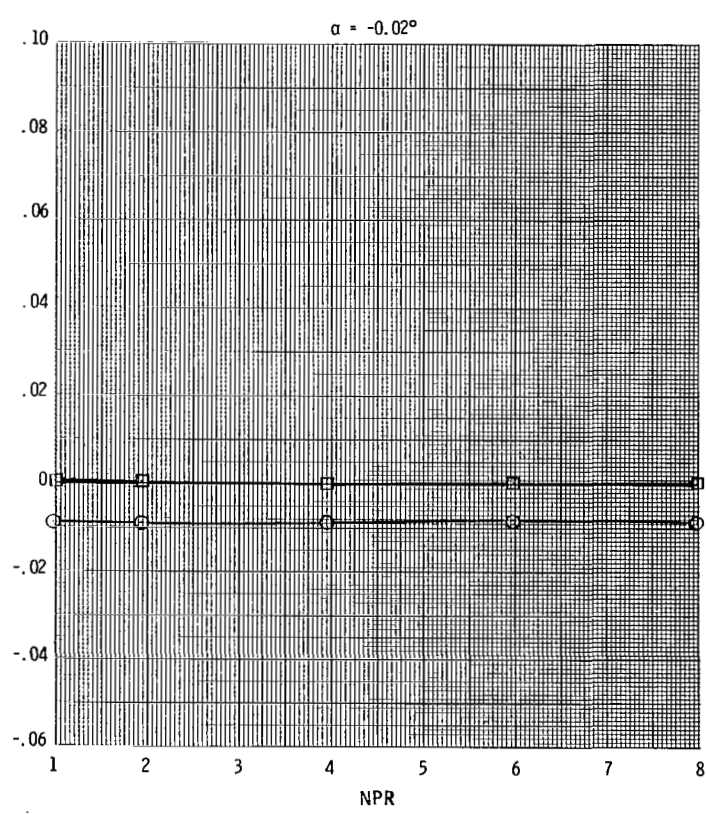
(c) Concluded.
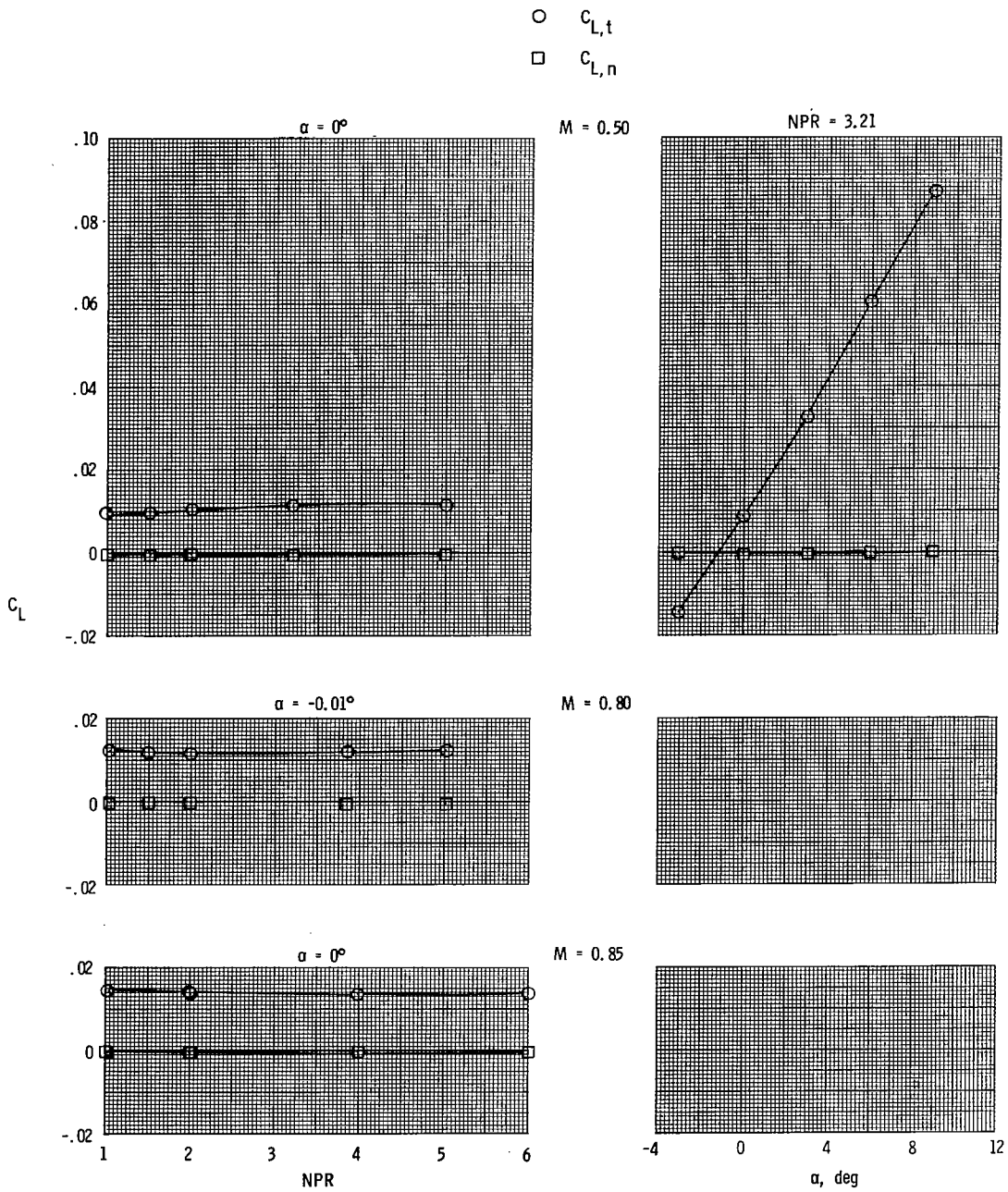
Figure 13.- Continued.

(d) Mid horizontal tails; mid vertical tails.

Figure 13.- Continued.
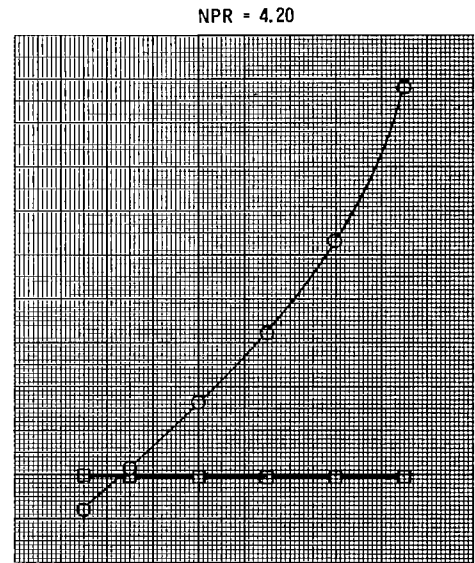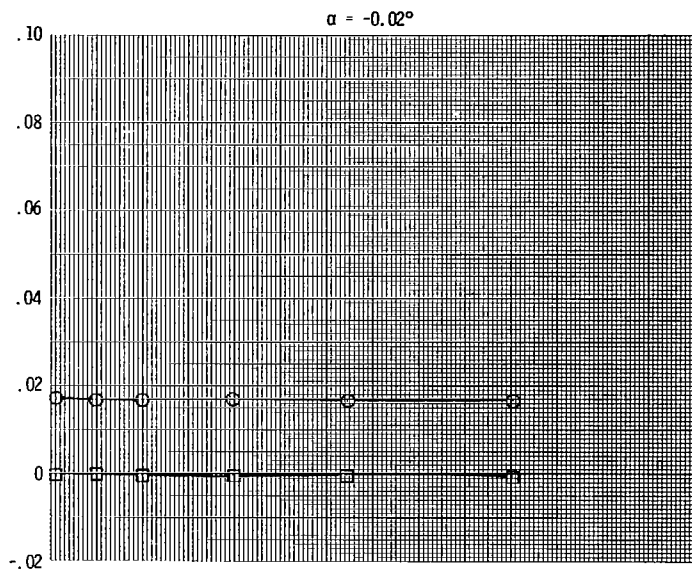
(d) Concluded.
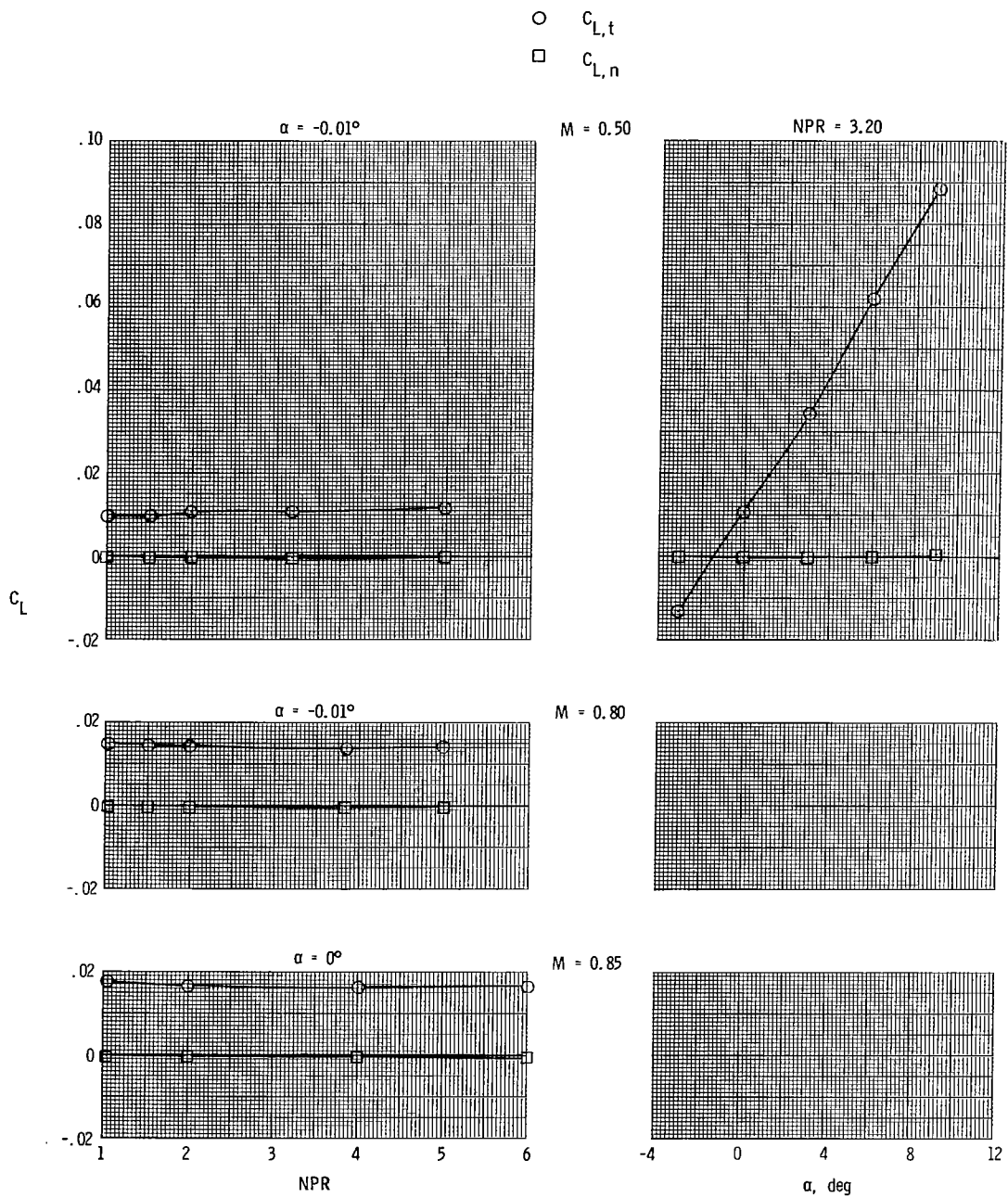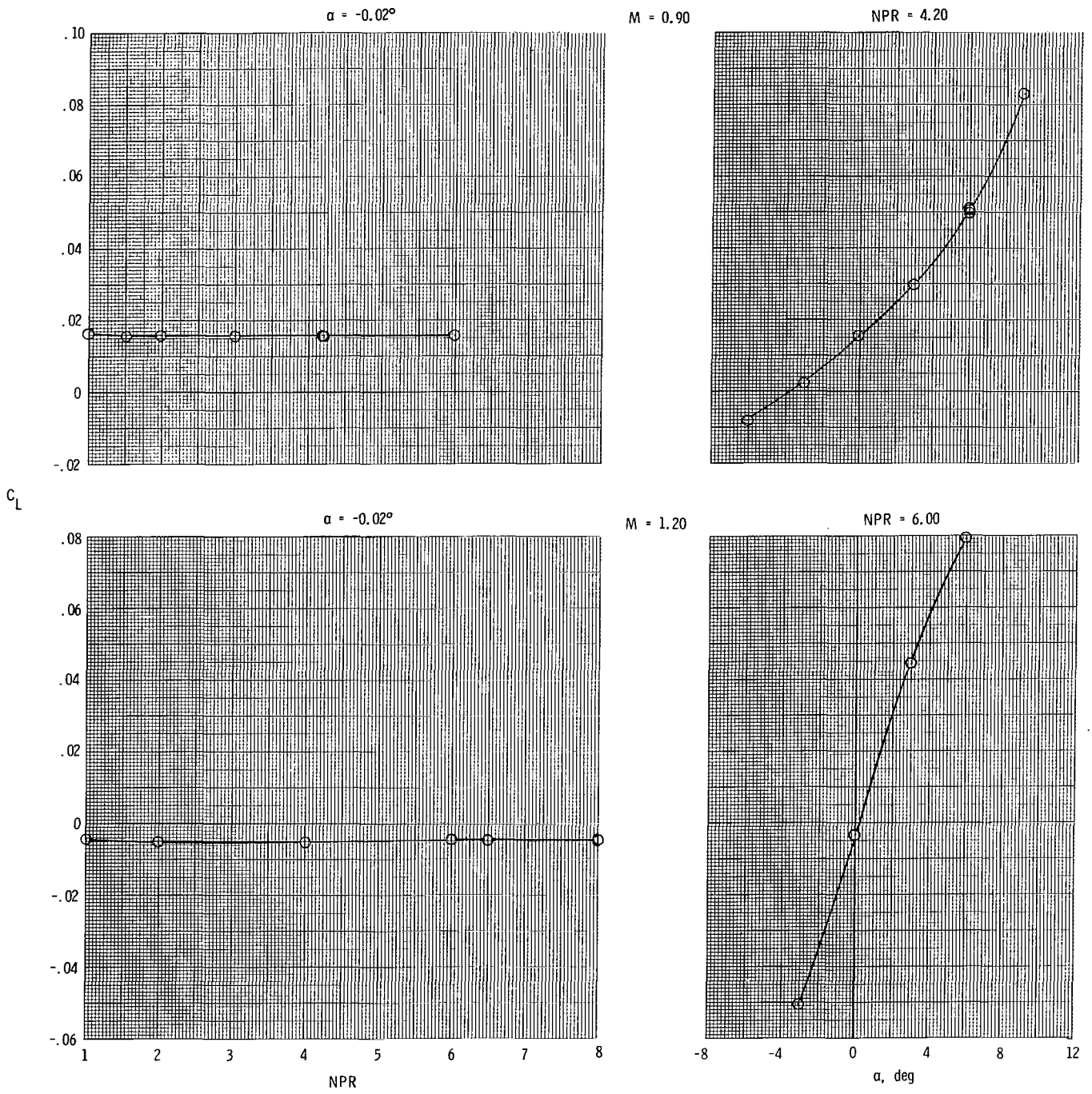
Figure 13.- Continued.

(e) Aft horizontal tails; mid vertical tails.

Figure 13.- Continued.
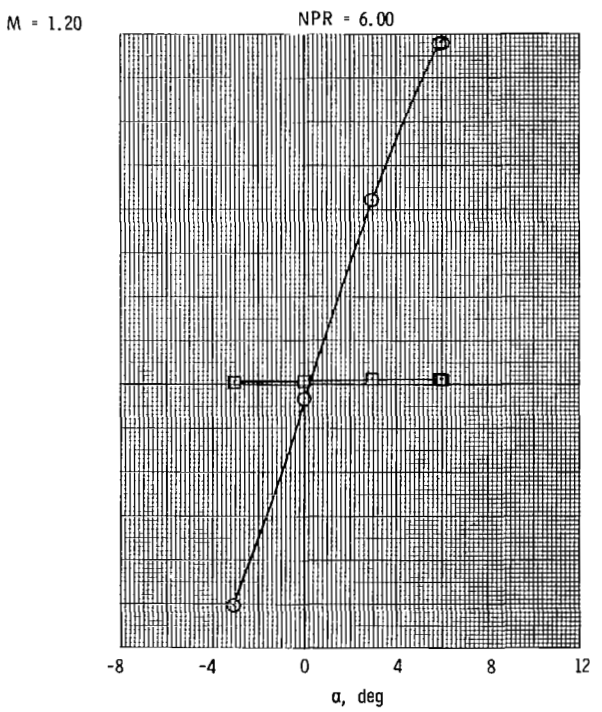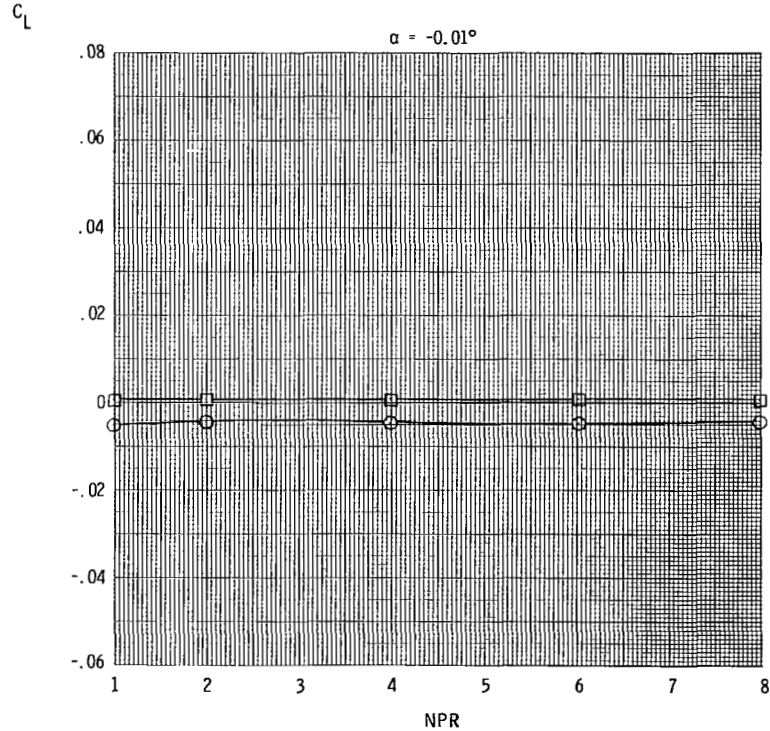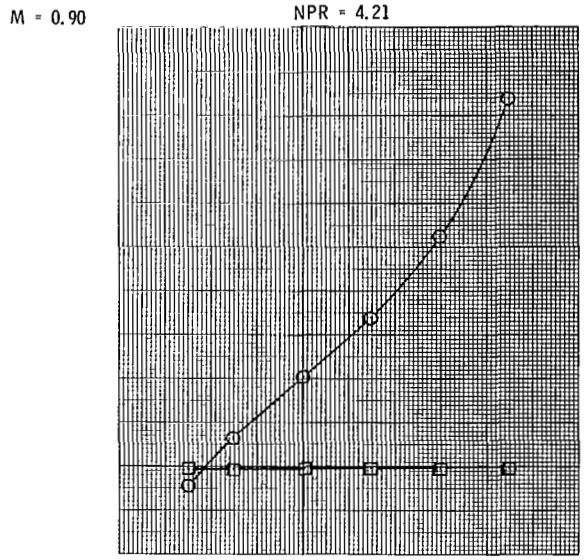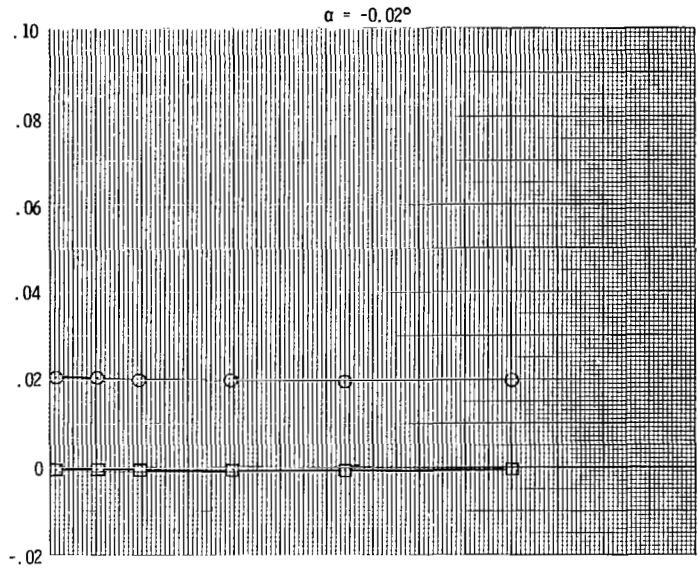
(e) Concluded.

Figure 13.- Concluded.

(a) Tails off.

Figure 14.- Variation of total (afterbody + nozzles + tails) and nozzle lift coefficient with nozzle pressure ratio and angle of attack for long supersonic dry power nozzles.

(b) Mid horizontal tails; mid vertical tails.

Figure 14.- Continued.

(b) Concluded.

Figure 14.- Continued.

(c) Aft horizontal tails; mid vertical tails.
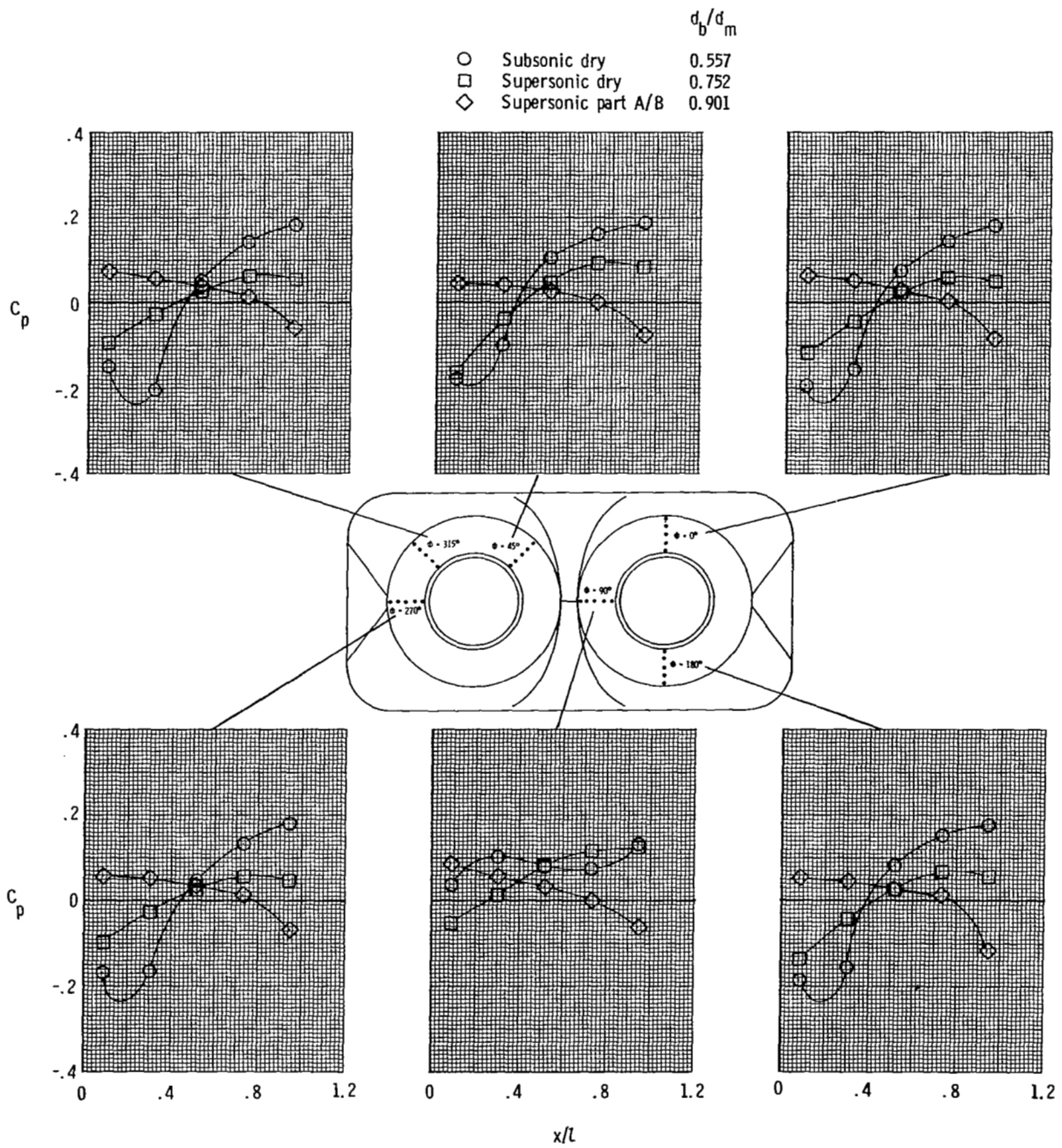
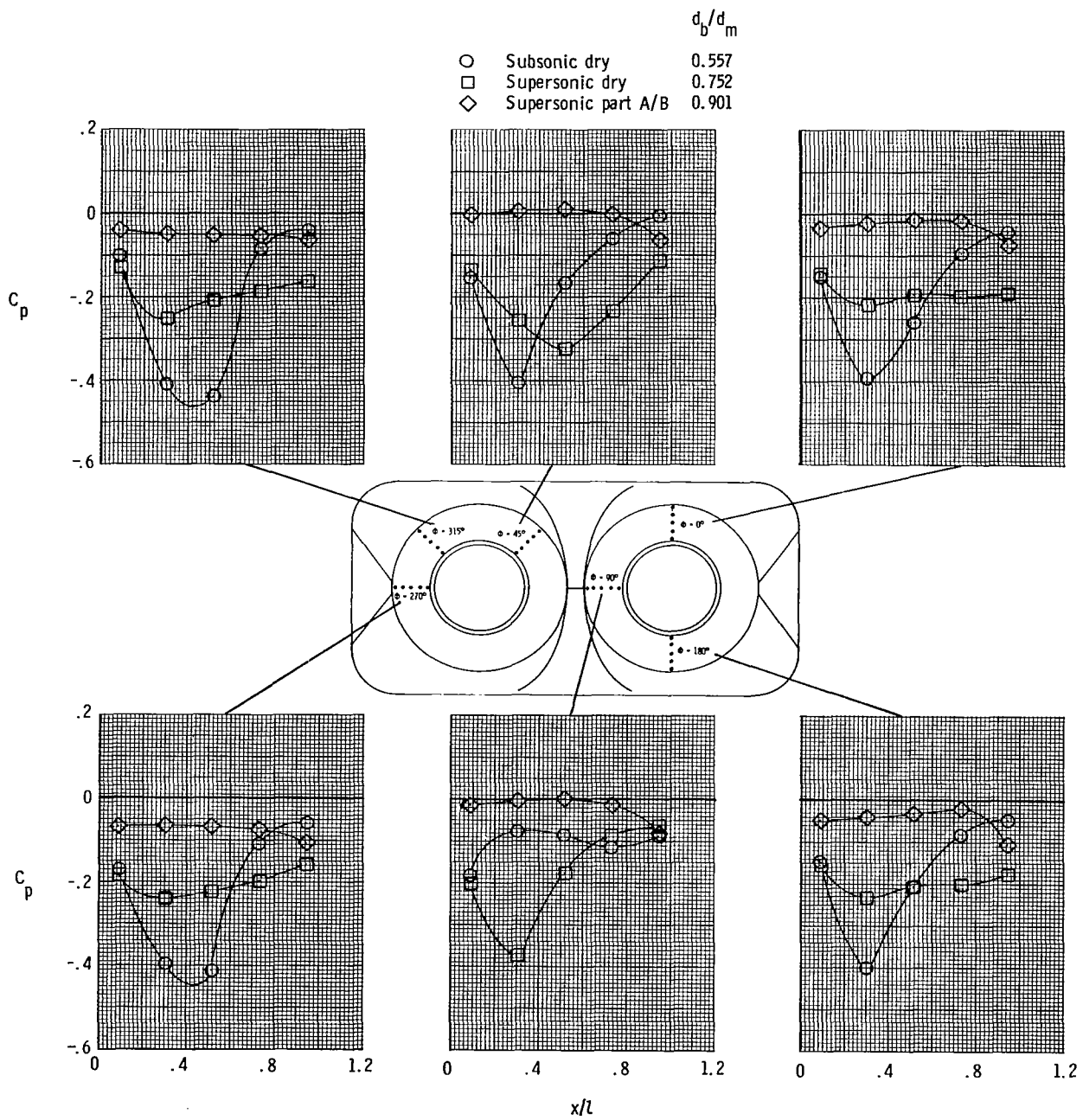Figure 14.- Continued.
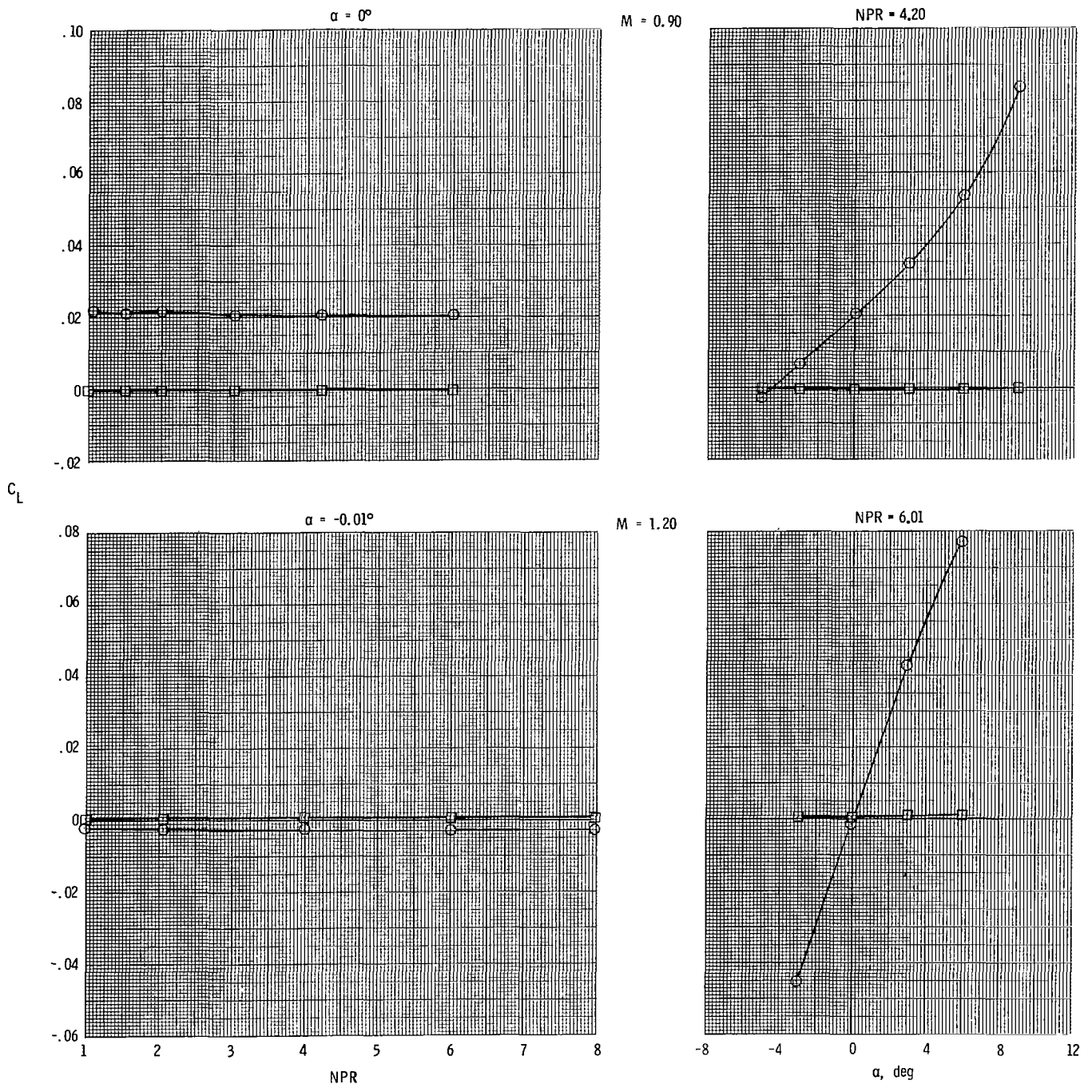
(c) Concluded.

Figure 14.- Concluded.

(a) Tails off.

Figure 15.- Variation of total (afterbody + nozzles + tails) and nozzle lift
coefficient with nozzle pressure ratio and angle of attack for short supersonic
partial A/B power nozzles.

117

(b) Mid horizontal tails; mid vertical tails.

Figure 15.- Continued.

○ $C_{L,t}$

□ $C_{L,n}$

$\alpha = -0.01°$ M = 0.90   NPR = 4.21

$\alpha = -0.02°$ M = 1.20   NPR = 6.01

C_L

NPR

α, deg

(b) Concluded.

Figure 15.- Continued.

(c) Aft horizontal tails; mid vertical tails.

Figure 15.- Continued.

(c) Concluded.

Figure 15.- Concluded.

(a) Tails off.

Figure 16.- Variation of total (afterbody + nozzles + tails) and nozzle lift
coefficient with nozzle pressure ratio and angle of attack for long supersonic
partial A/B power nozzle.

(b) Mid horizontal tails; mid vertical tails.

Figure 16.- Continued.

(b) Concluded.

Figure 16.- Continued.

(c) Aft horizontal tails; mid vertical tails.

Figure 16.- Continued.

$$\bigcirc \quad C_{L,t}$$

(c) Concluded.

Figure 16.- Concluded.
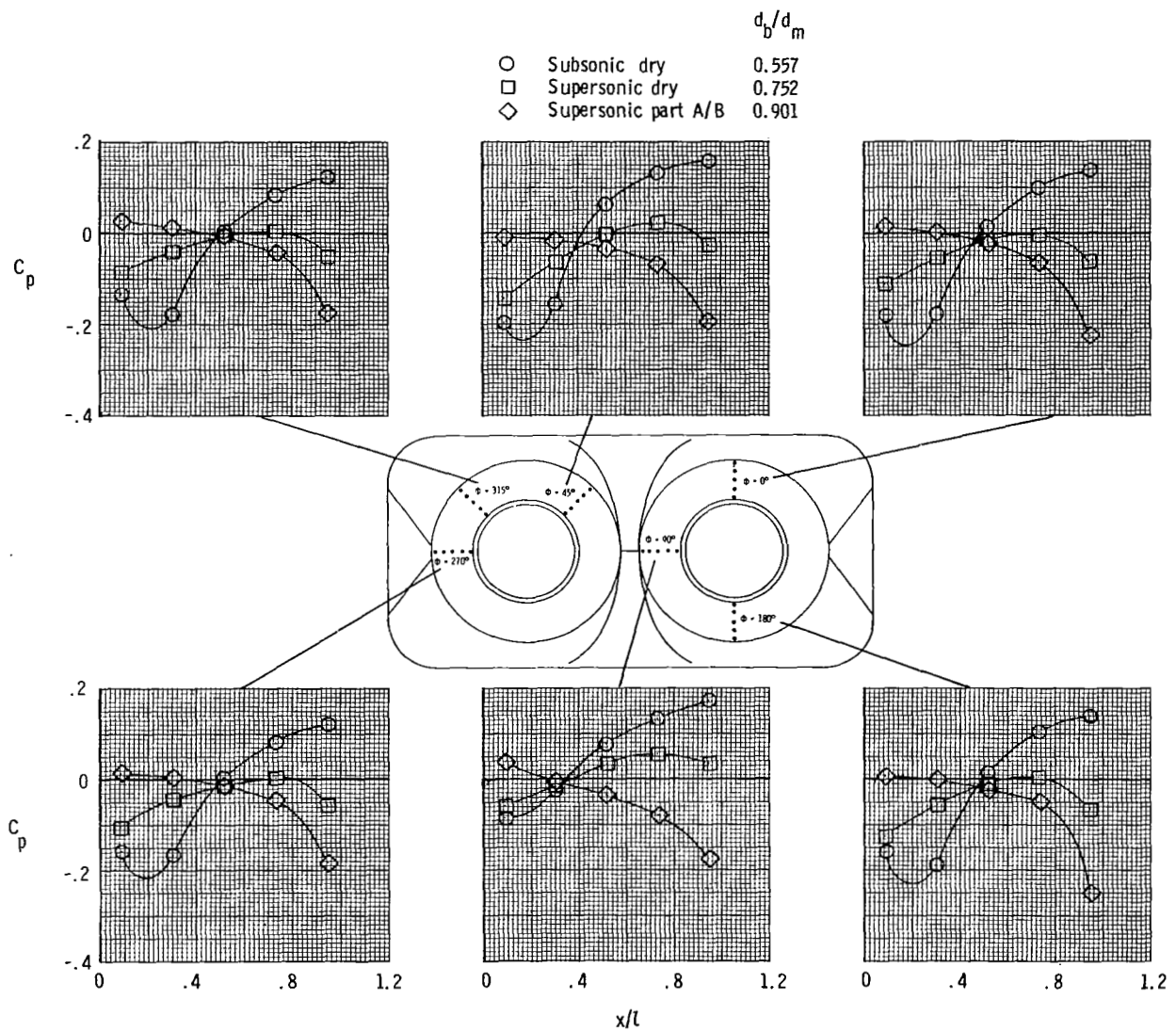
(a)   M = 0.50;   NPR = 3.20.

Figure 17.- Effect of nozzle closure (d_b/d_m) on nozzle pressure distributions for short nozzles and tails off.

d_b/d_m

○	Subsonic dry	0.557
□	Supersonic dry	0.752
◇	Supersonic part A/B	0.901

(b)   M = 0.90;   NPR = 4.20.

Figure 17.- Continued.

d_b/d_m

○ Subsonic dry 0.557
□ Supersonic dry 0.752
◇ Supersonic part A/B 0.901

C_p

.2

0

-.2

-.4

-.6

x/l

0 .4 .8 1.2

(c) M = 1.20; NPR = 6.00.

Figure 17.- Concluded.
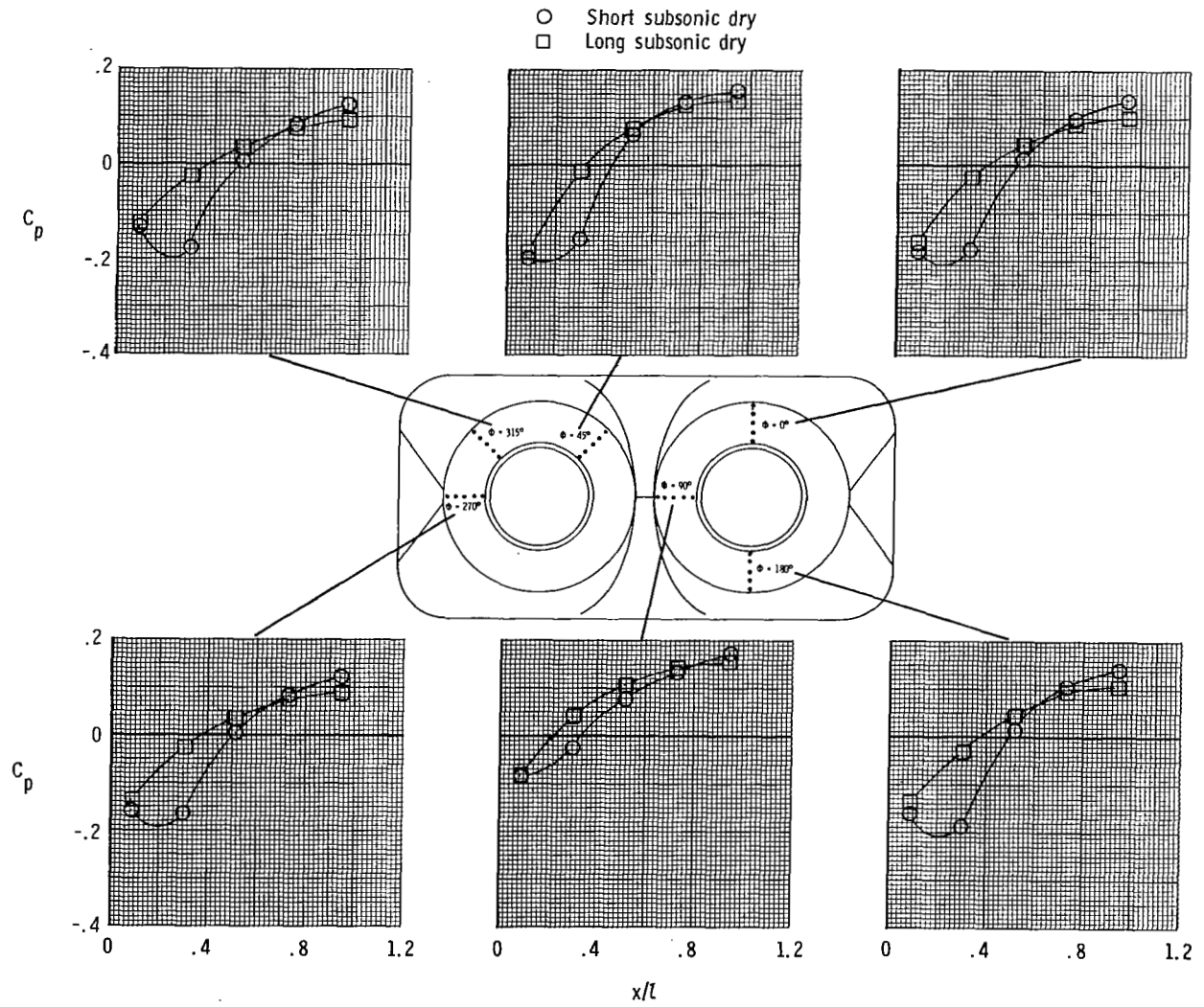
(a) M = 0.50; NPR = 3.20.

Figure 18.- Effect of nozzle length on nozzle pressure distributions for subsonic
dry power nozzles and tails off.
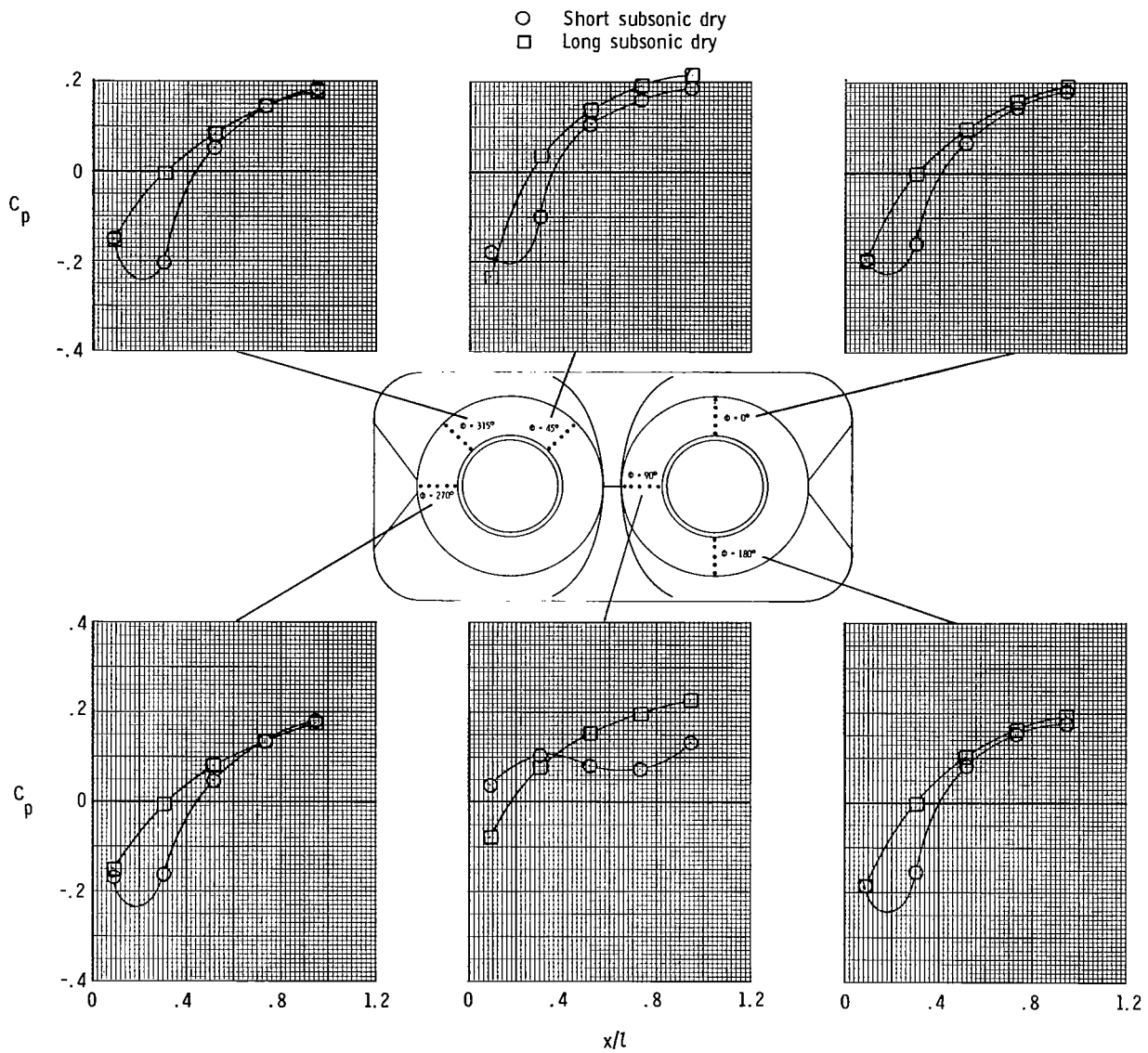
(b)   M = 0.90;   NPR = 4.20.

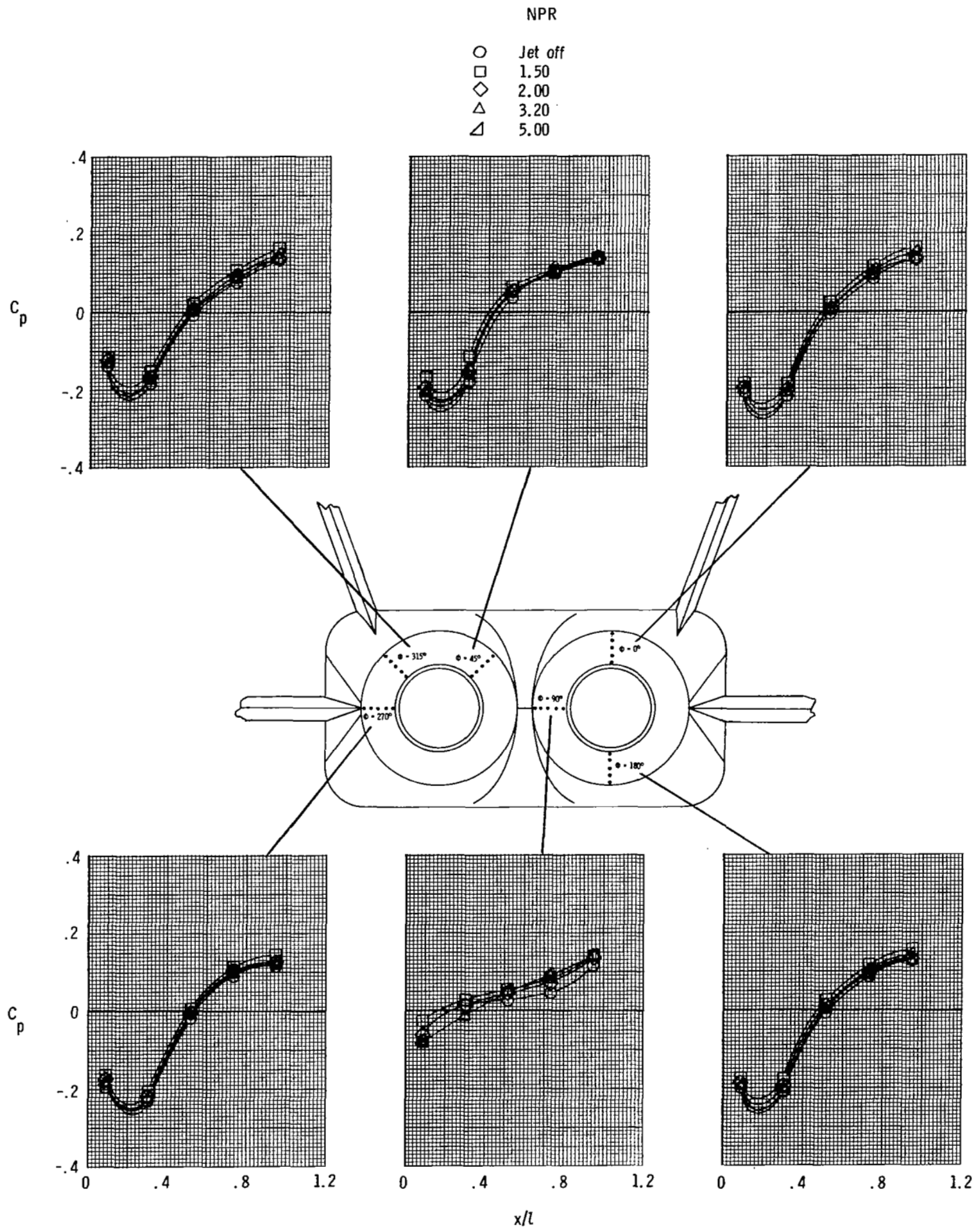Figure 18.- Continued.
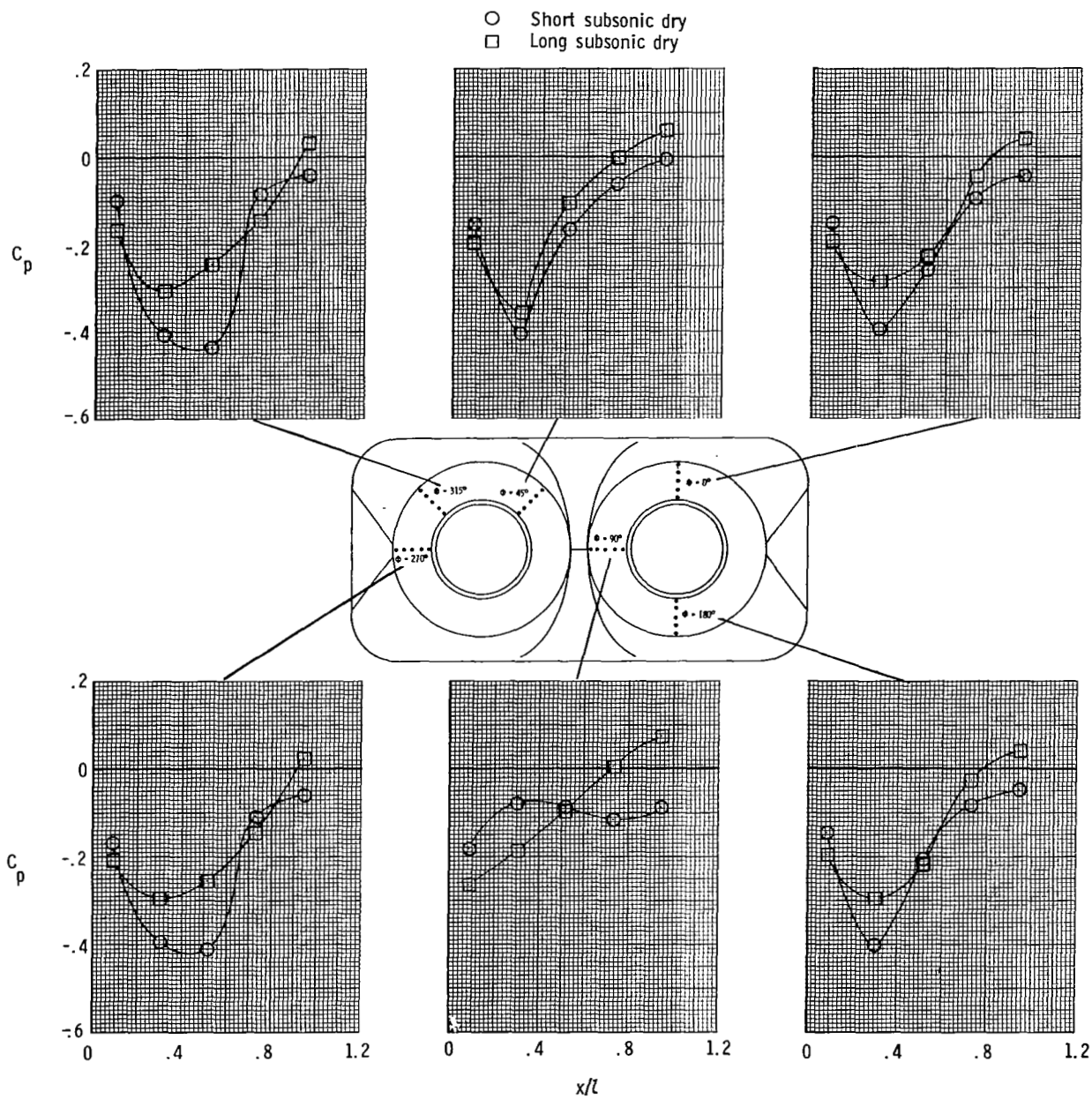
(c) M = 1.20; NPR = 6.00.

Figure 18.- Concluded.

○   Short supersonic part A/B
□   Long supersonic part A/B

(a)   M = 0.50;   NPR = 3.21.
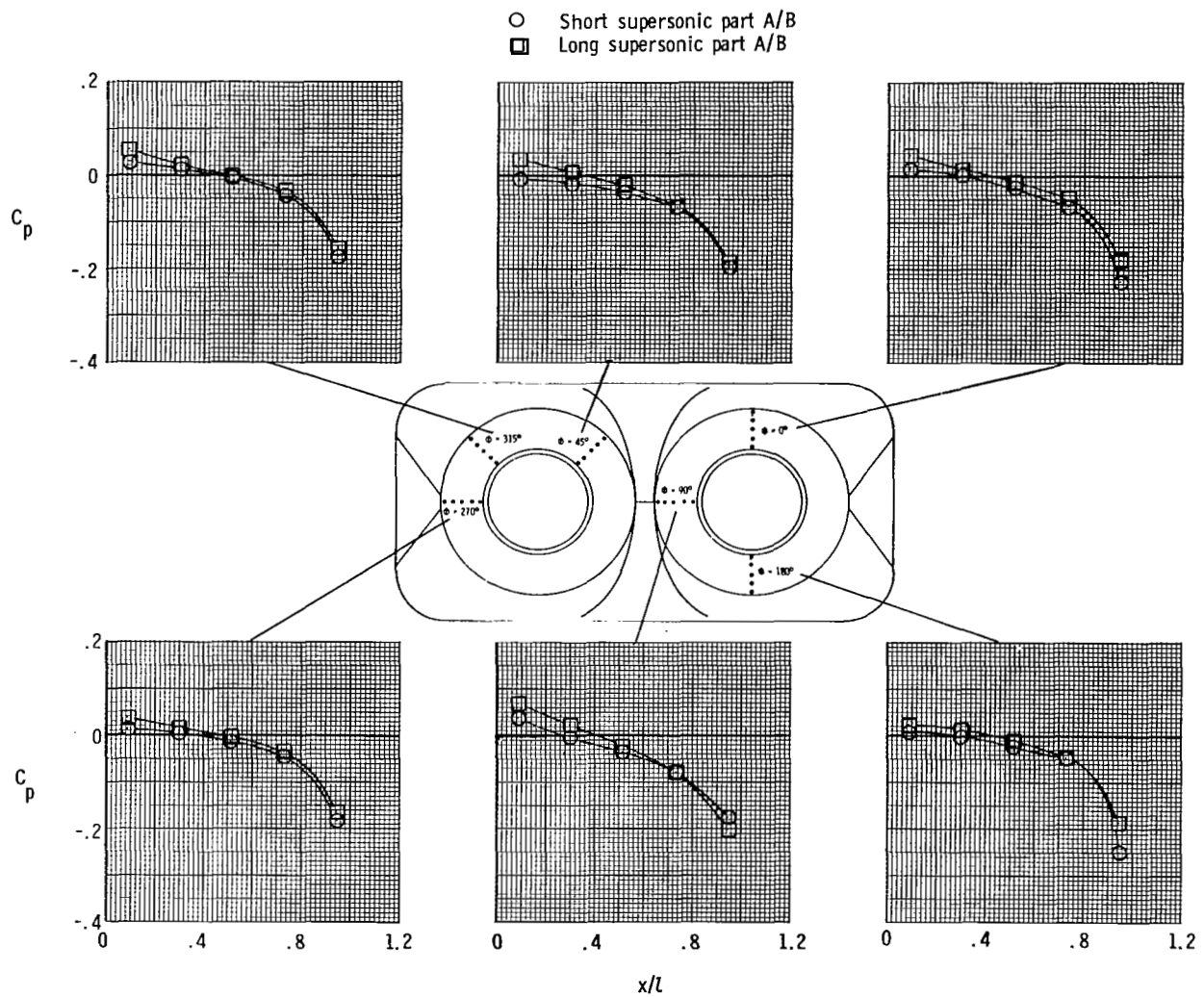
Figure 19.- Effect of nozzle length on nozzle pressure distributions for
supersonic partial A/B power nozzles and tails off.

O   Short supersonic part A/B
▣   Long supersonic part A/B
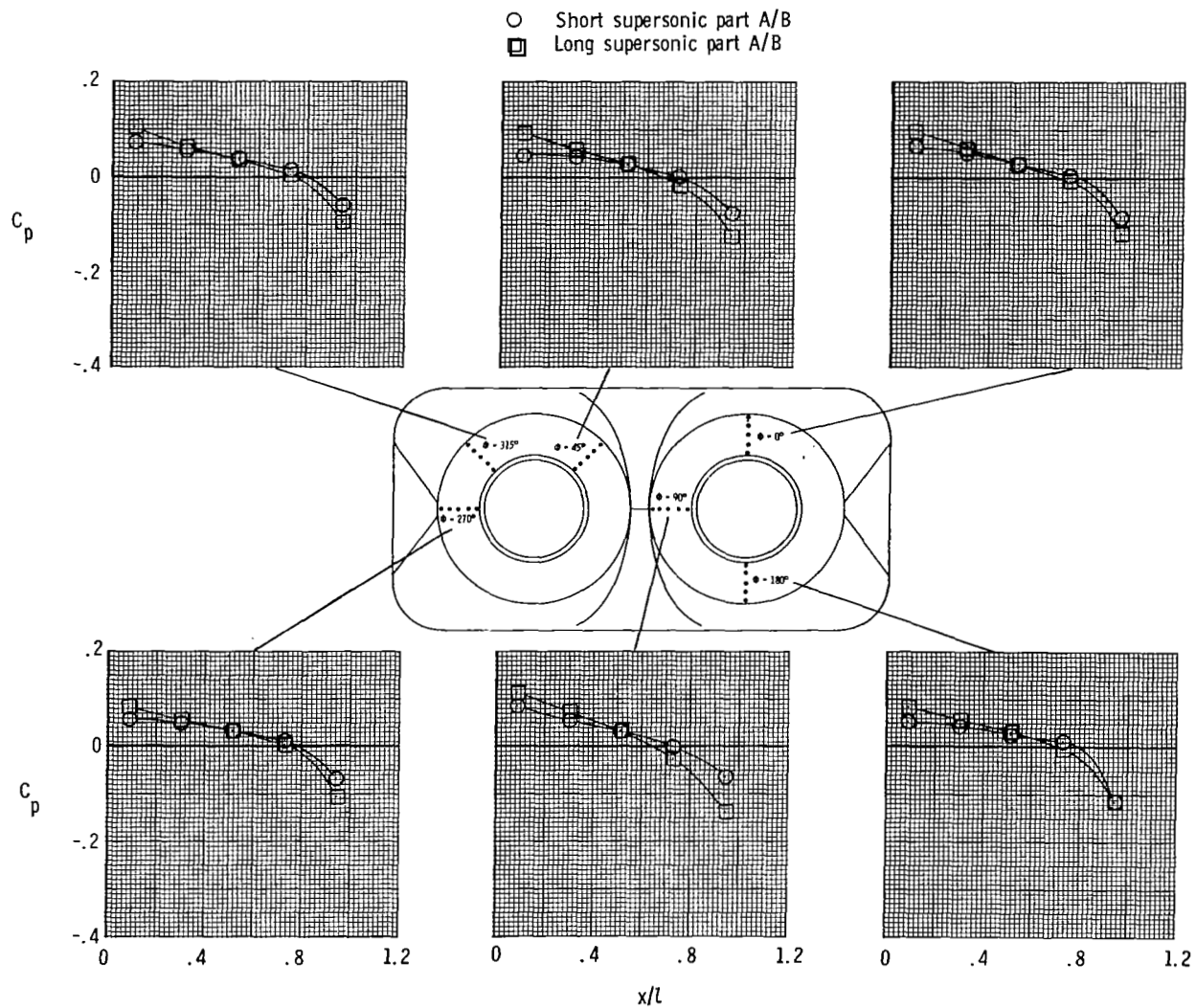
(b)   M = 0.90;   NPR = 4.21.

Figure 19.- Continued.
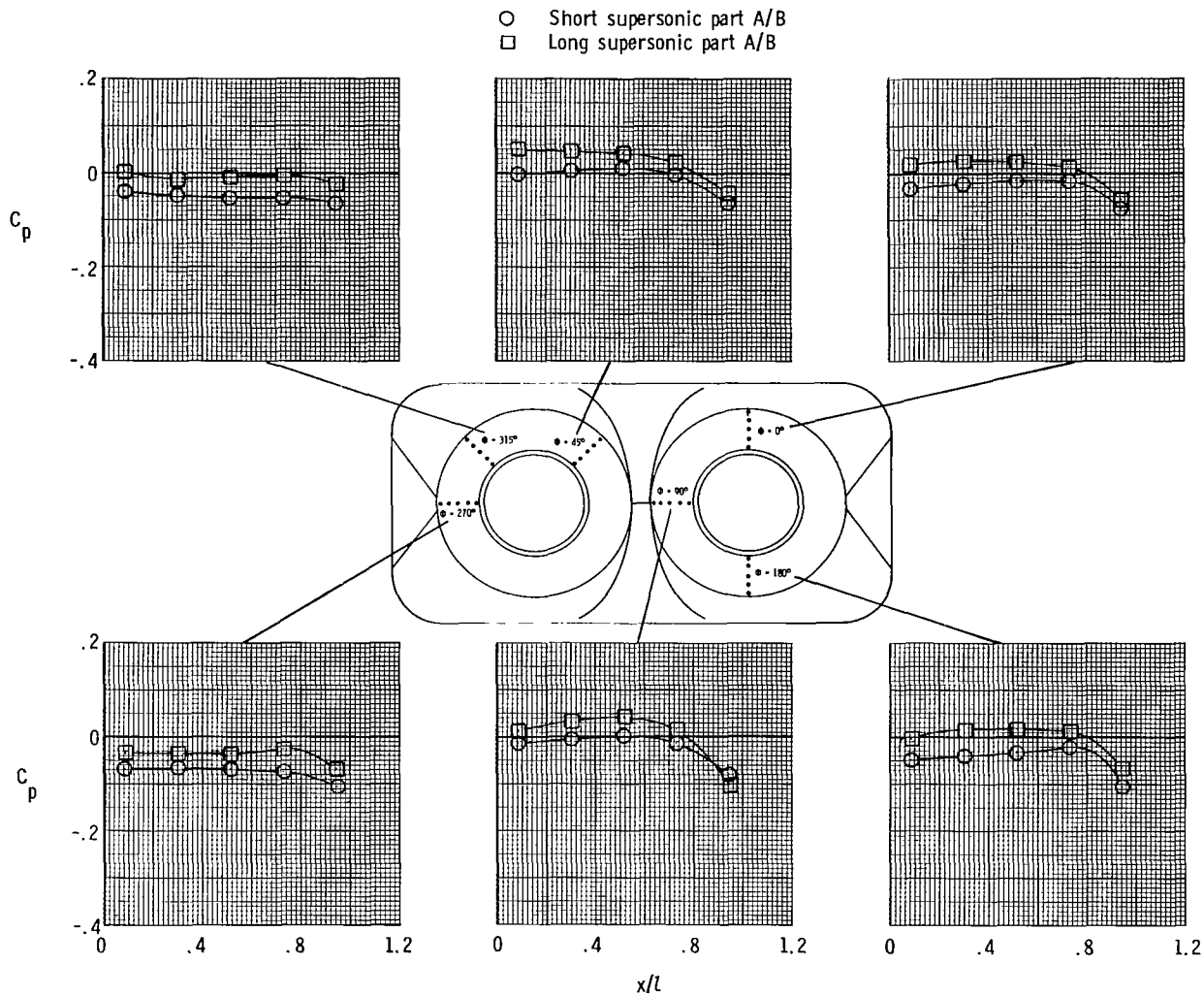
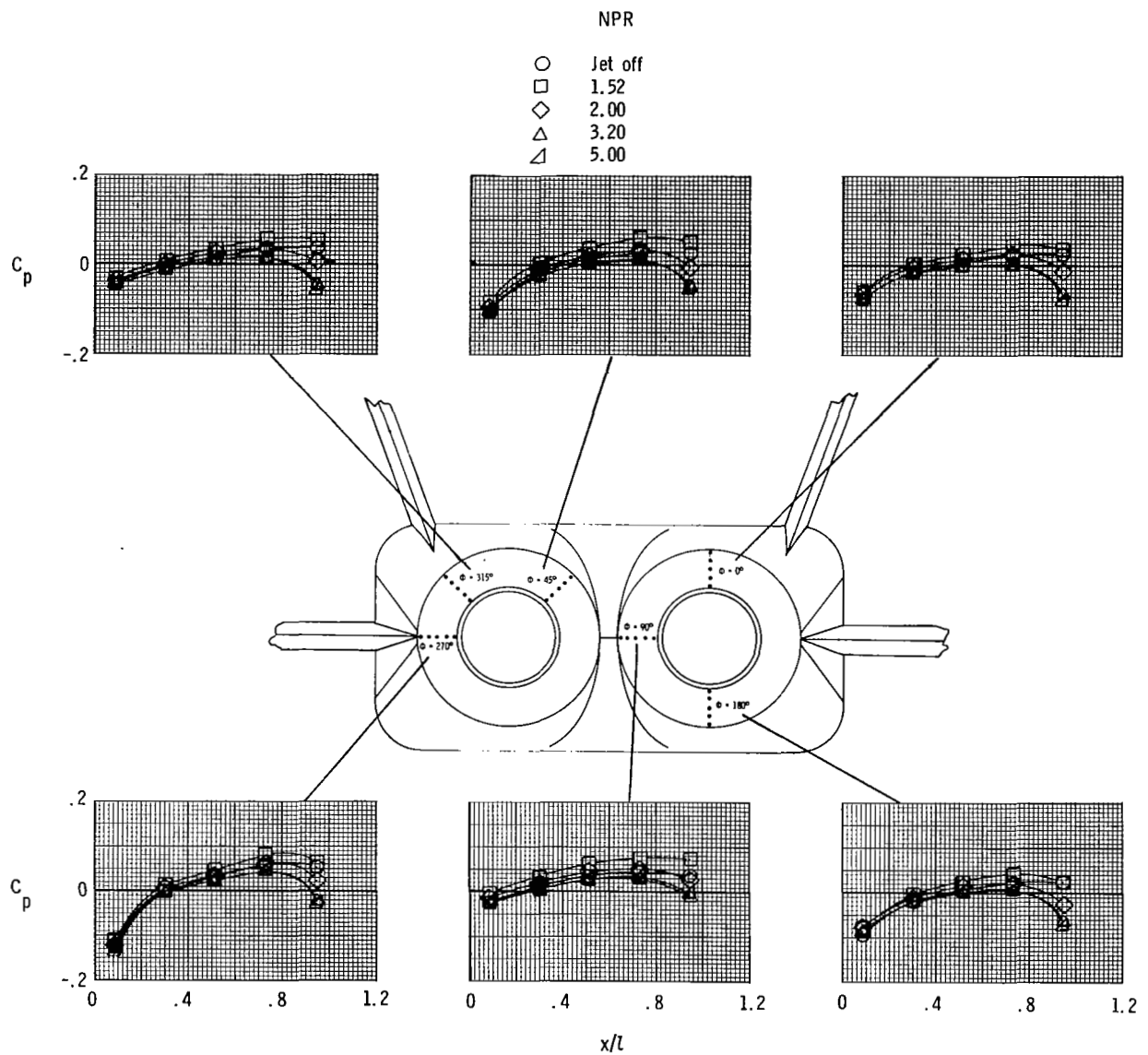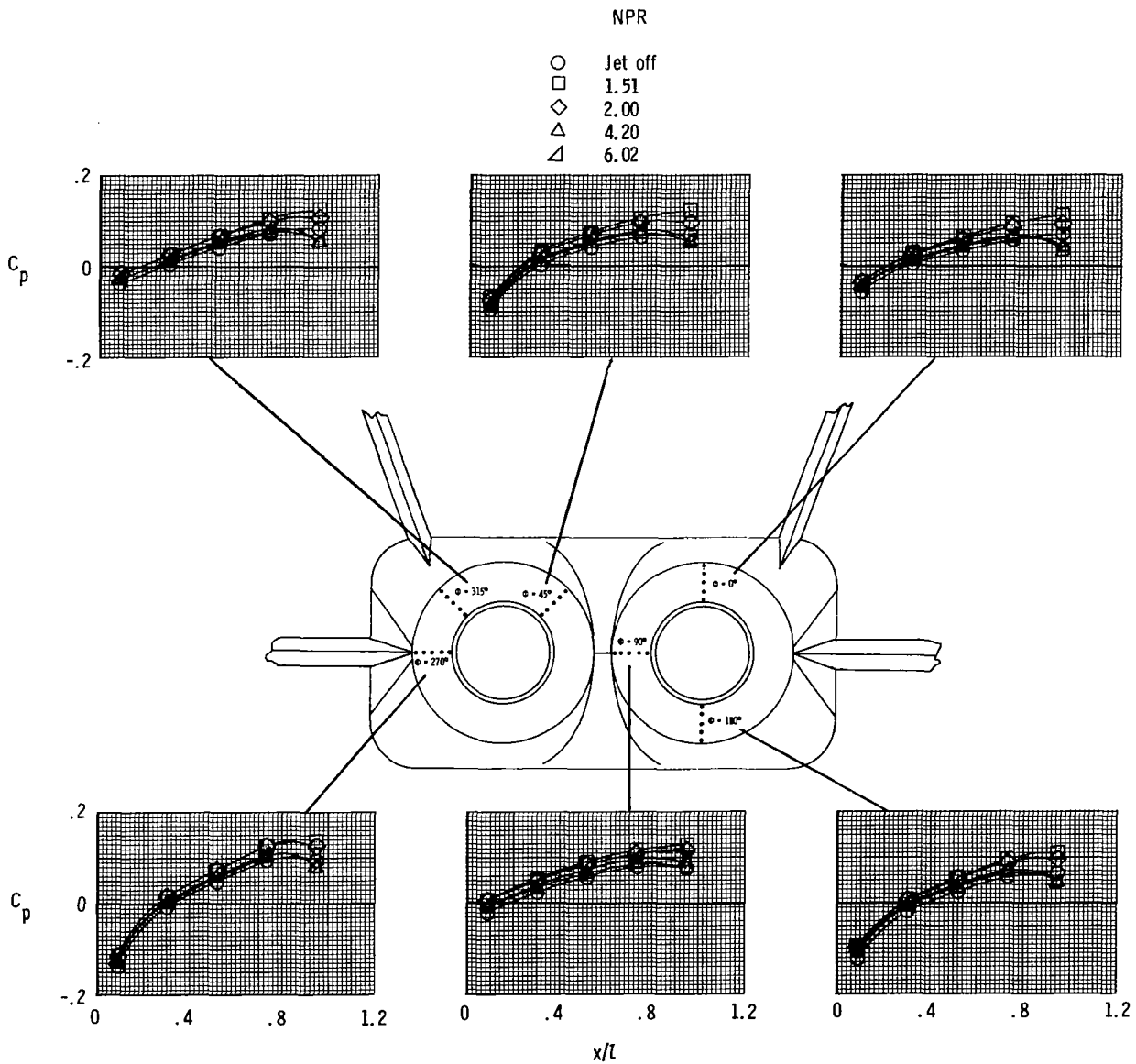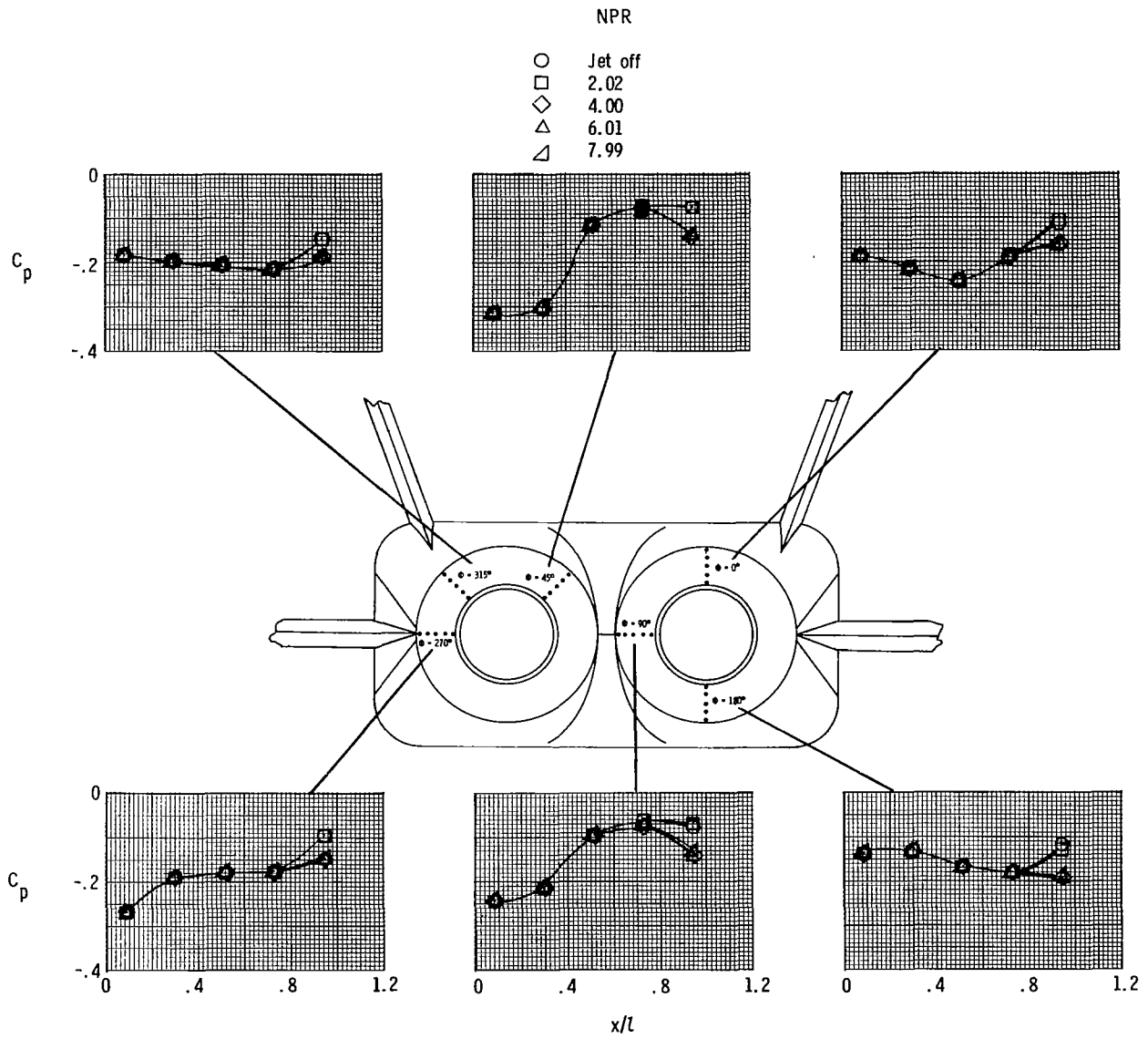(c)   M = 1.20;   NPR = 6.00.

Figure 19.- Concluded.

(a) M = 0.50.

Figure 20.- Effect of nozzle pressure ratio on nozzle pressure distributions for short subsonic dry power nozzles and aft horizontal tails, mid vertical tails.
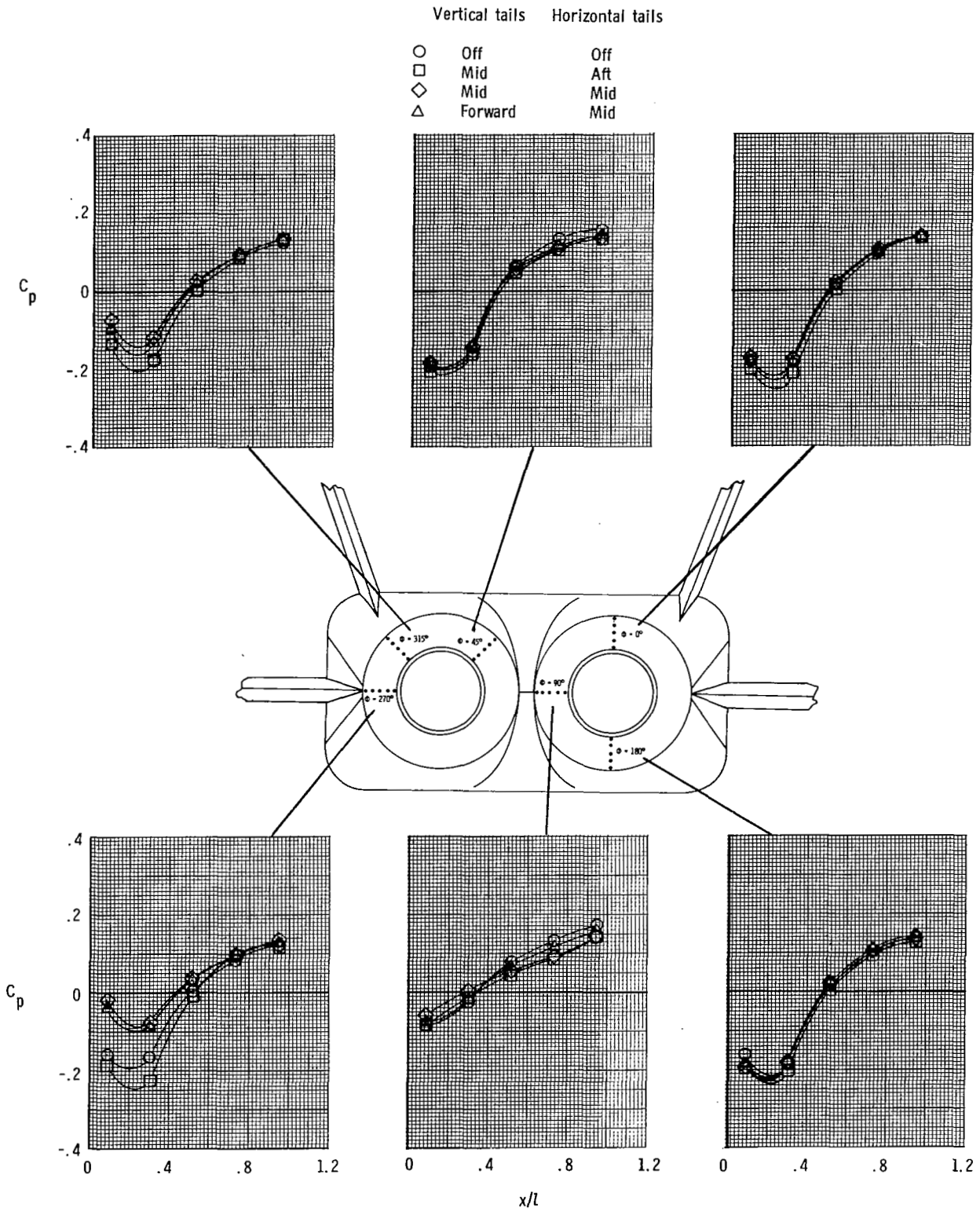
(b)   M = 0.90.

Figure 20.- Continued.

NPR

○   Jet off
□   1.99
◇   4.00
△   5.98
◁   8.04
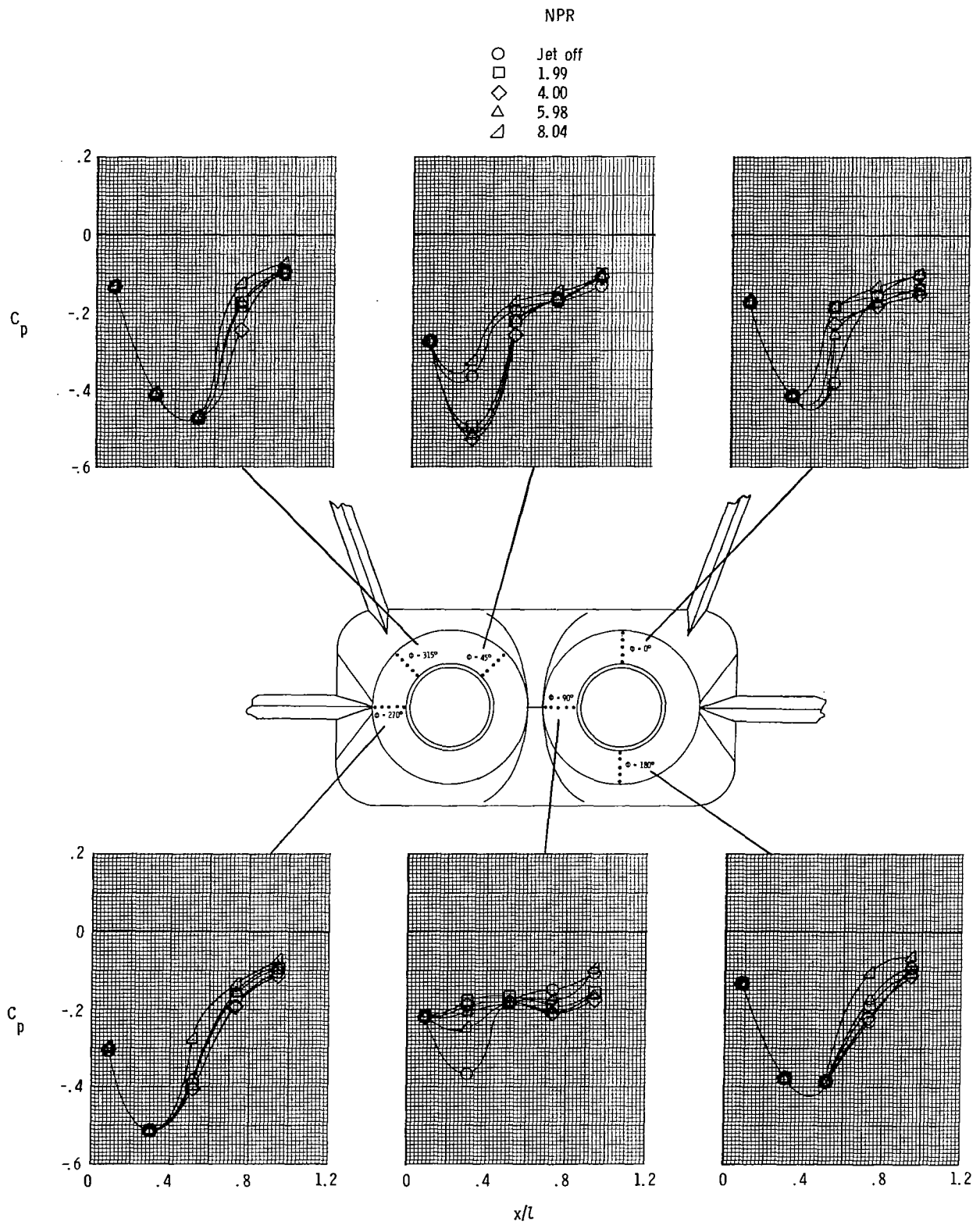
(c)   M = 1.20.

Figure 20.- Concluded.

(a) M = 0.50.

Figure 21.- Effect of nozzle pressure ratio on nozzle pressure distributions for long supersonic dry power nozzles and aft horizontal tails, mid vertical tails.
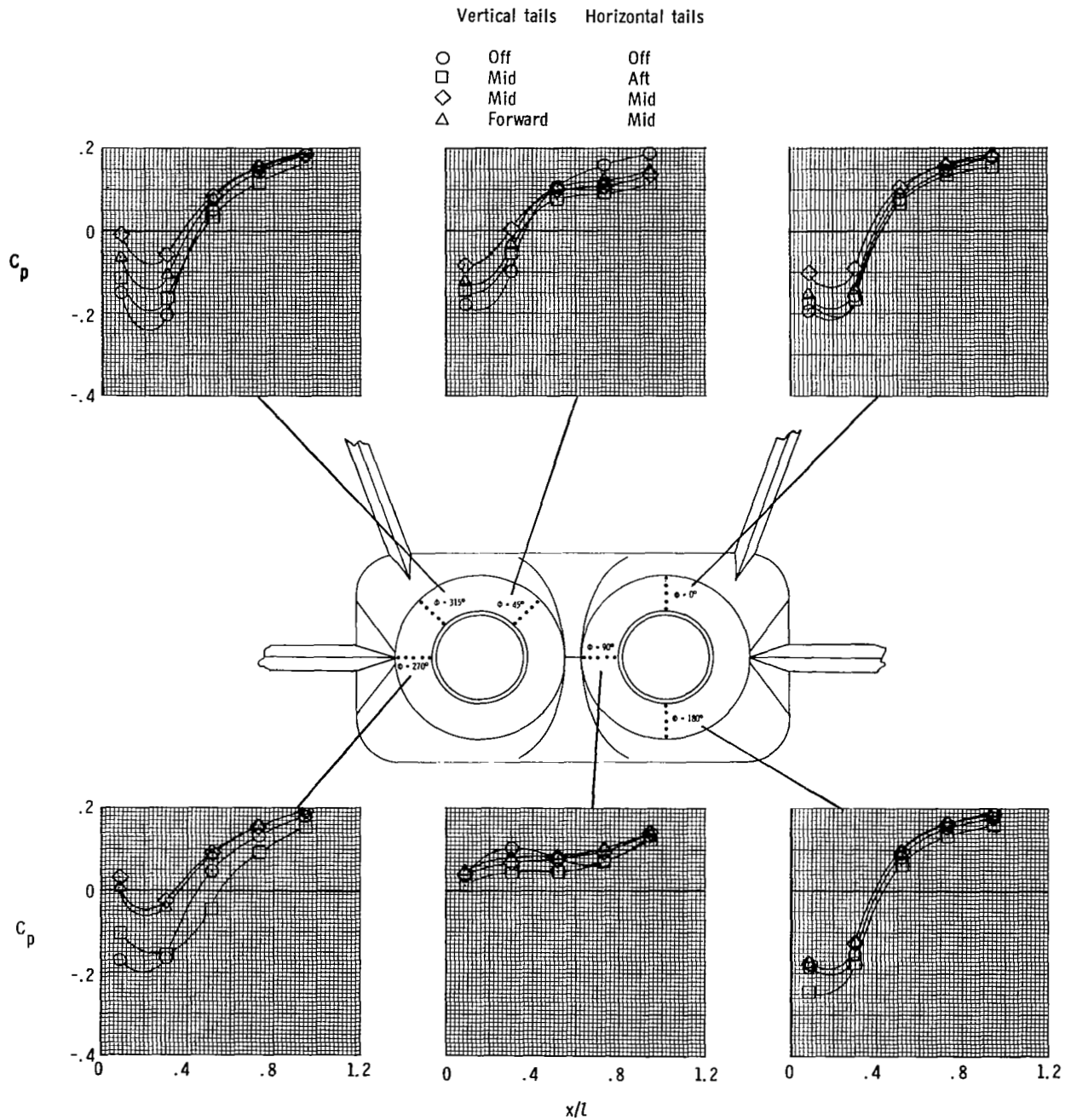
(b)   M = 0.90.

Figure 21.- Continued.

(c)   M = 1.20.

Figure 21.- Concluded.

Vertical tails Horizontal tails

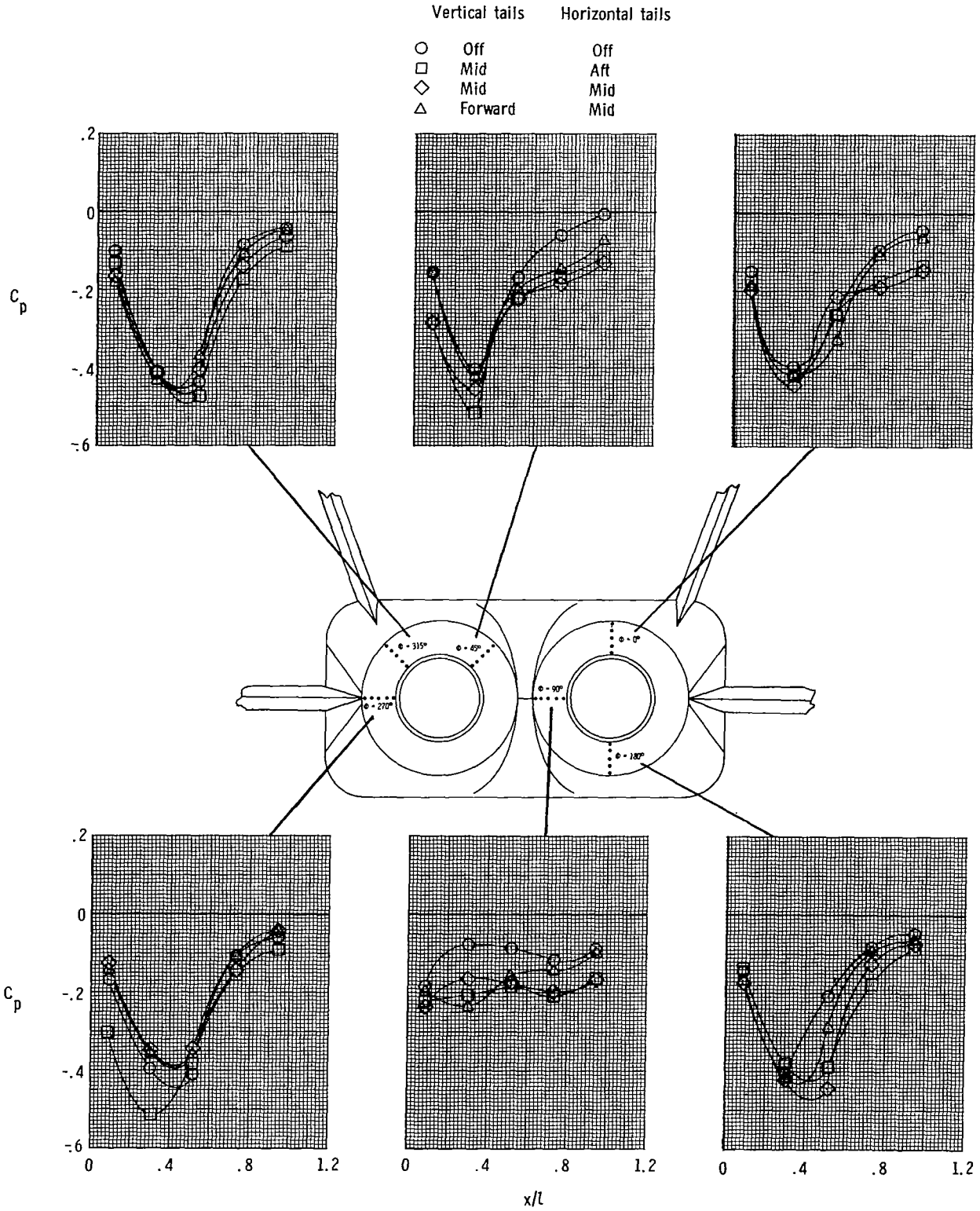|		
○	Off	Off
□	Mid	Aft
◇	Mid	Mid
△	Forward	Mid

(a)   M = 0.50;   NPR = 3.20.

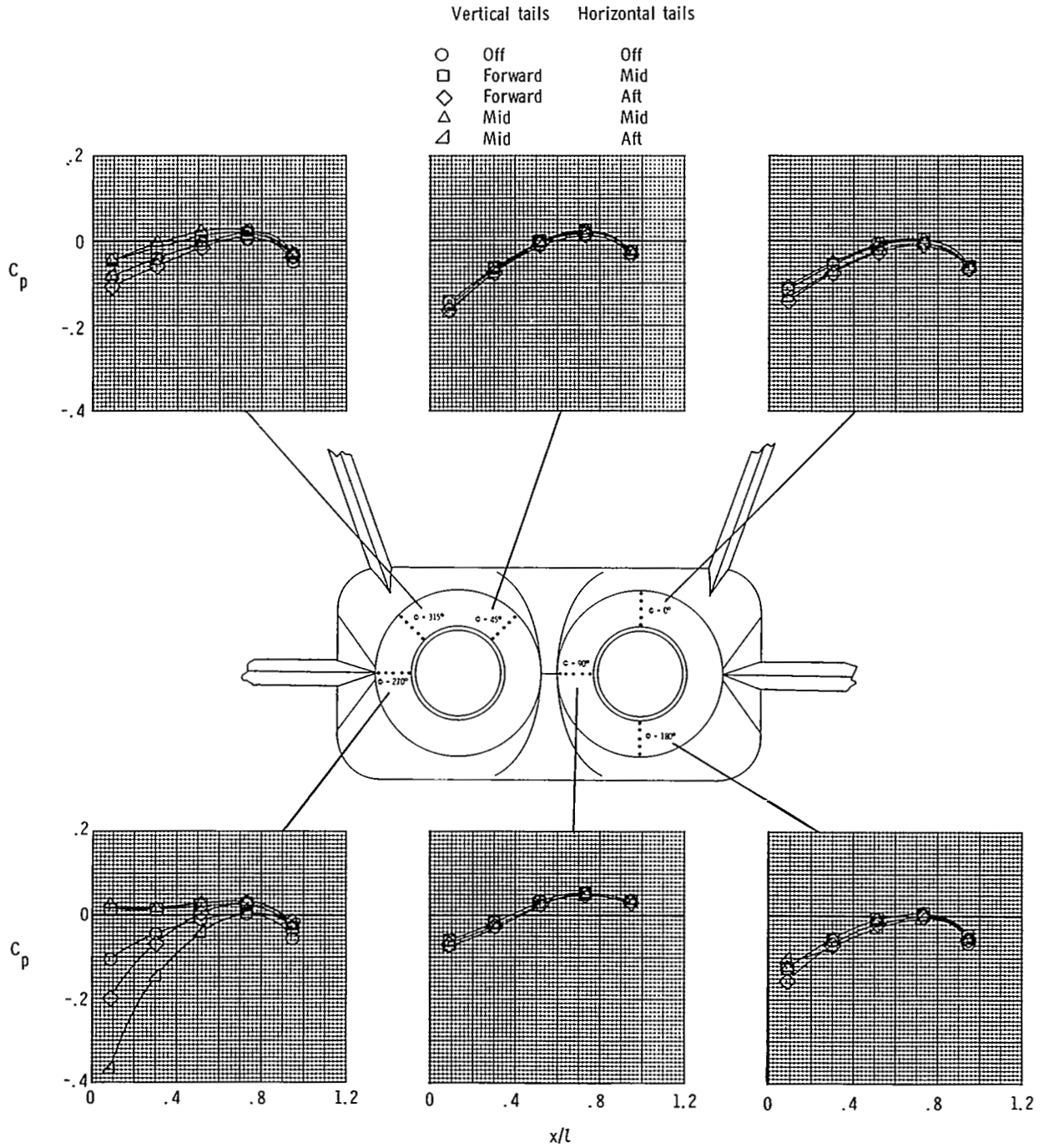Figure 22.- Effect of empennage arrangement on nozzle pressure distributions for short subsonic dry power nozzles.

c_p

c_p
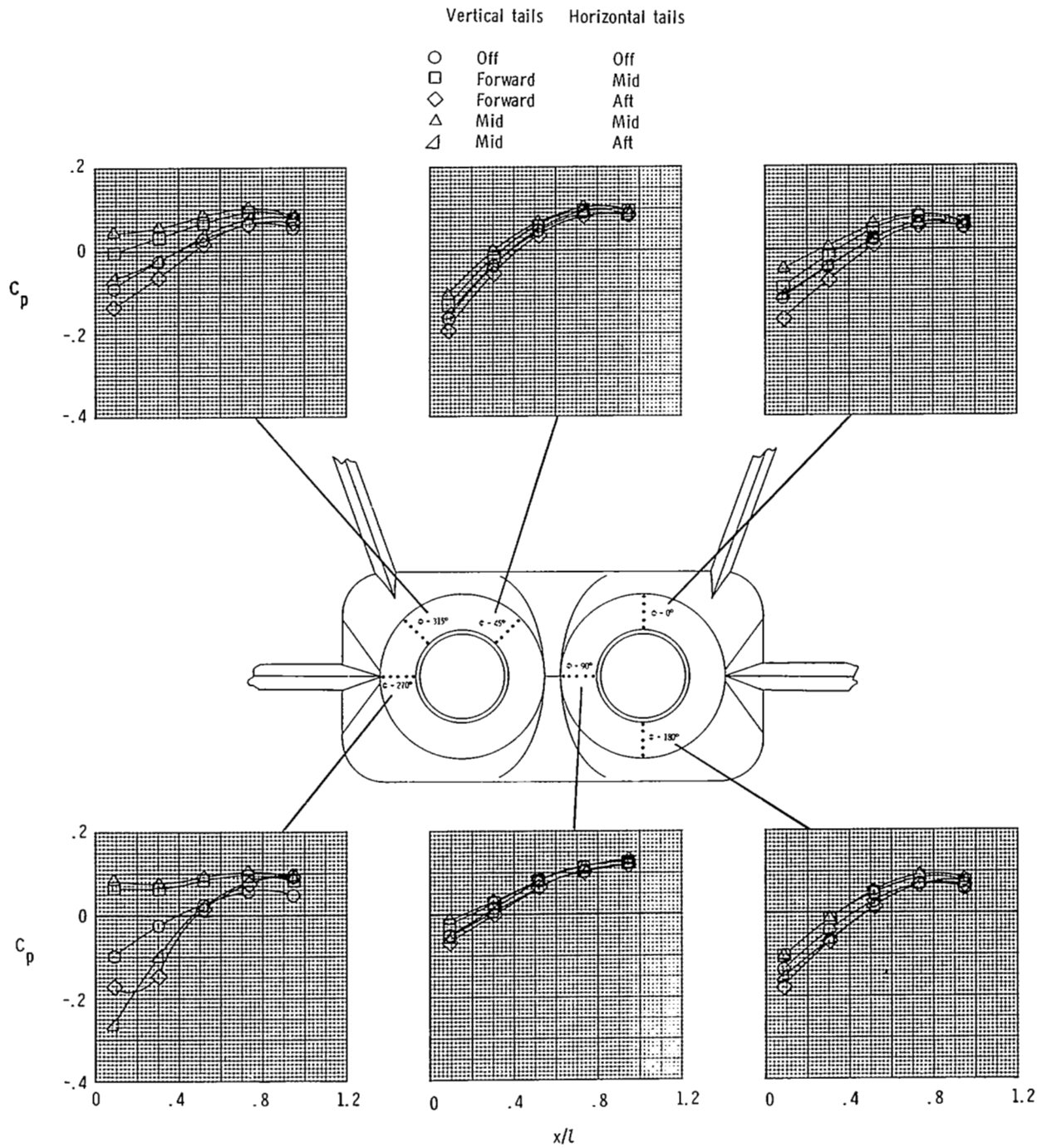
x/l

(b)   M = 0.90;   NPR = 4.20.

Figure 22.- Continued.

Vertical tails   Horizontal tails

○   Off   Off
□   Mid   Aft
◇   Mid   Mid
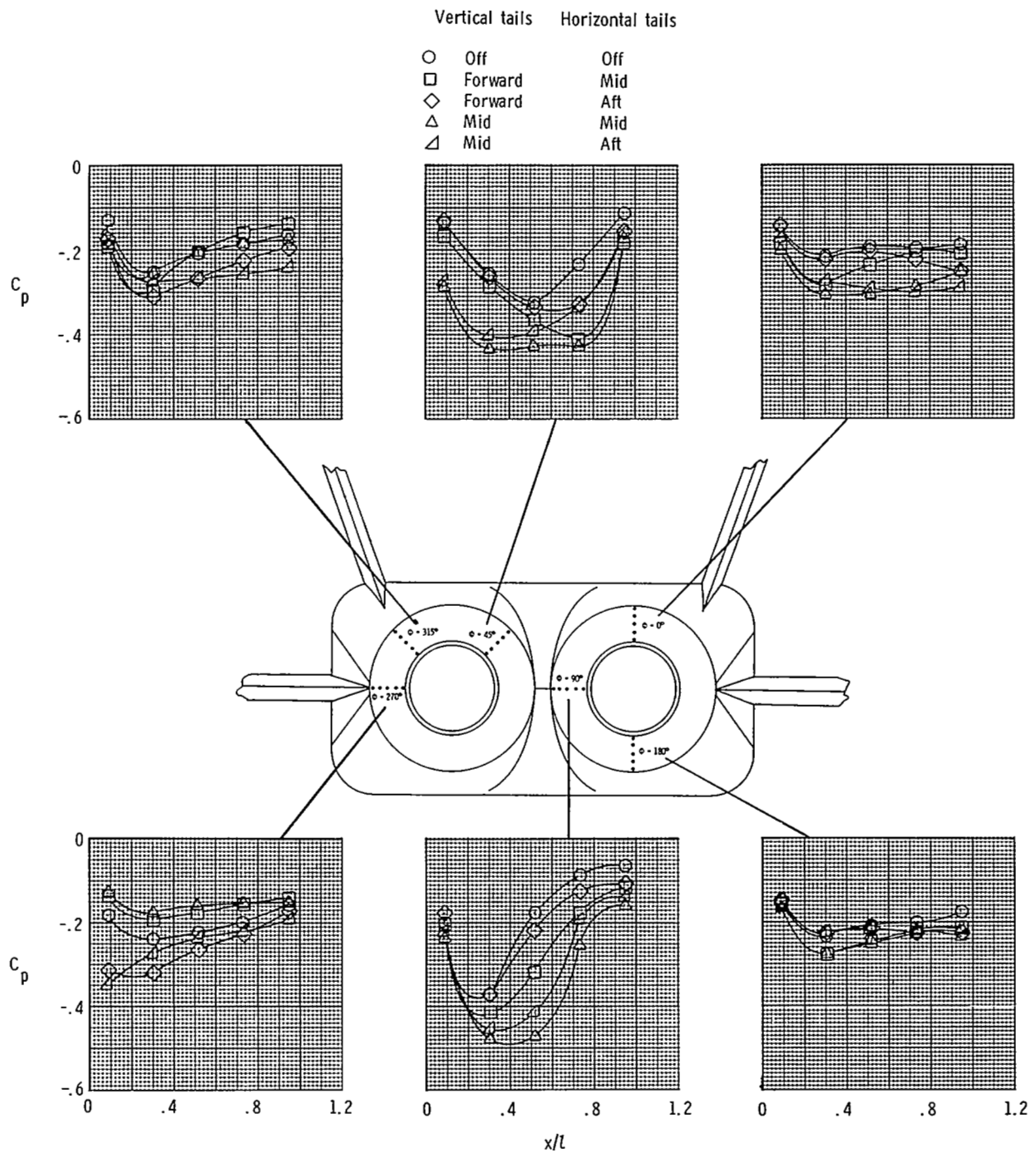△   Forward   Mid

(c)   M = 1.20;   NPR = 5.99.

Figure 22.- Concluded.

Figure 23.- Effect of empennage arrangement on nozzle pressure distributions for short supersonic dry power nozzles.

145

Vertical tails | Horizontal tails

○	Off	Off
□	Forward	Mid
◇	Forward	Aft
△	Mid	Mid
◿	Mid	Aft

C_p

.2

0

-.2

-.4

C_p

.2

0

-.2

-.4

0   .4   .8   1.2

0   .4   .8   1.2

0   .4   .8   1.2

x/l

(b)   M = 0.90;   NPR = 4.20.

Figure 23.- Continued.

146

Vertical tails   Horizontal tails

	Vertical tails	Horizontal tails
○	Off	Off
□	Forward	Mid
◇	Forward	Aft
△	Mid	Mid
◹	Mid	Aft

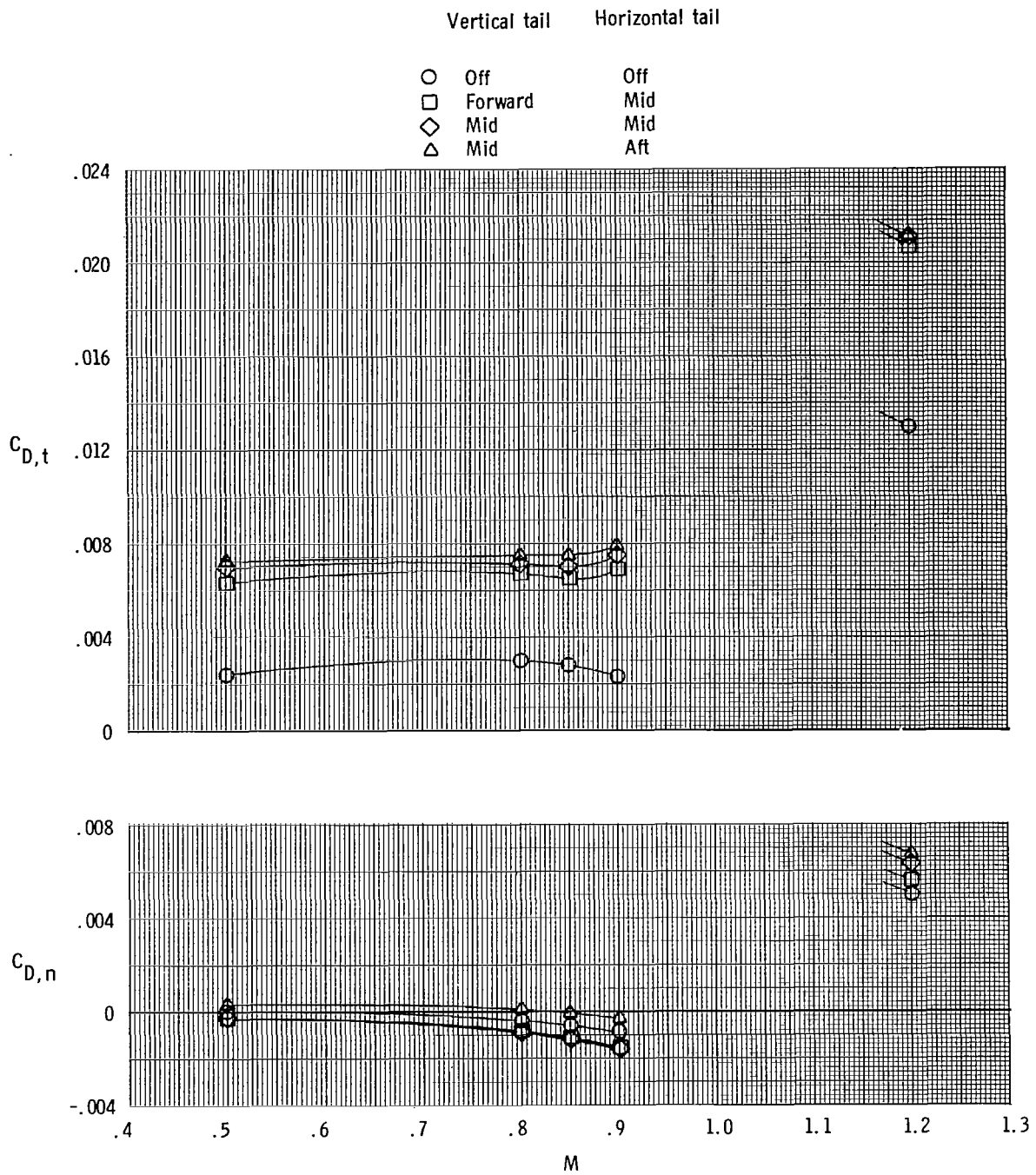(c)   M = 1.20;   NPR = 6.00.

Figure 23.- Concluded.
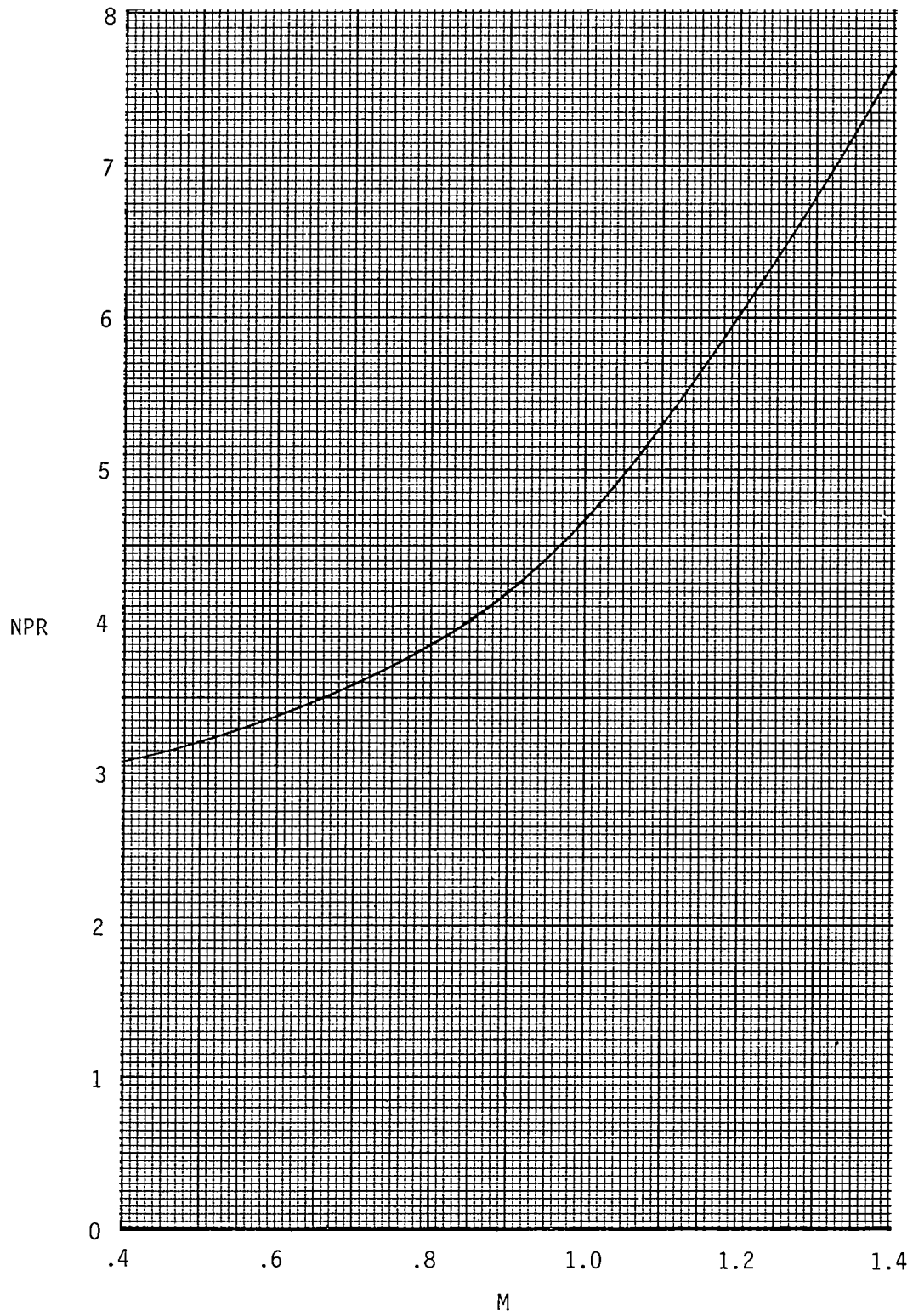
Figure 24.- Typical nozzle pressure ratio schedule for a turbofan engine.

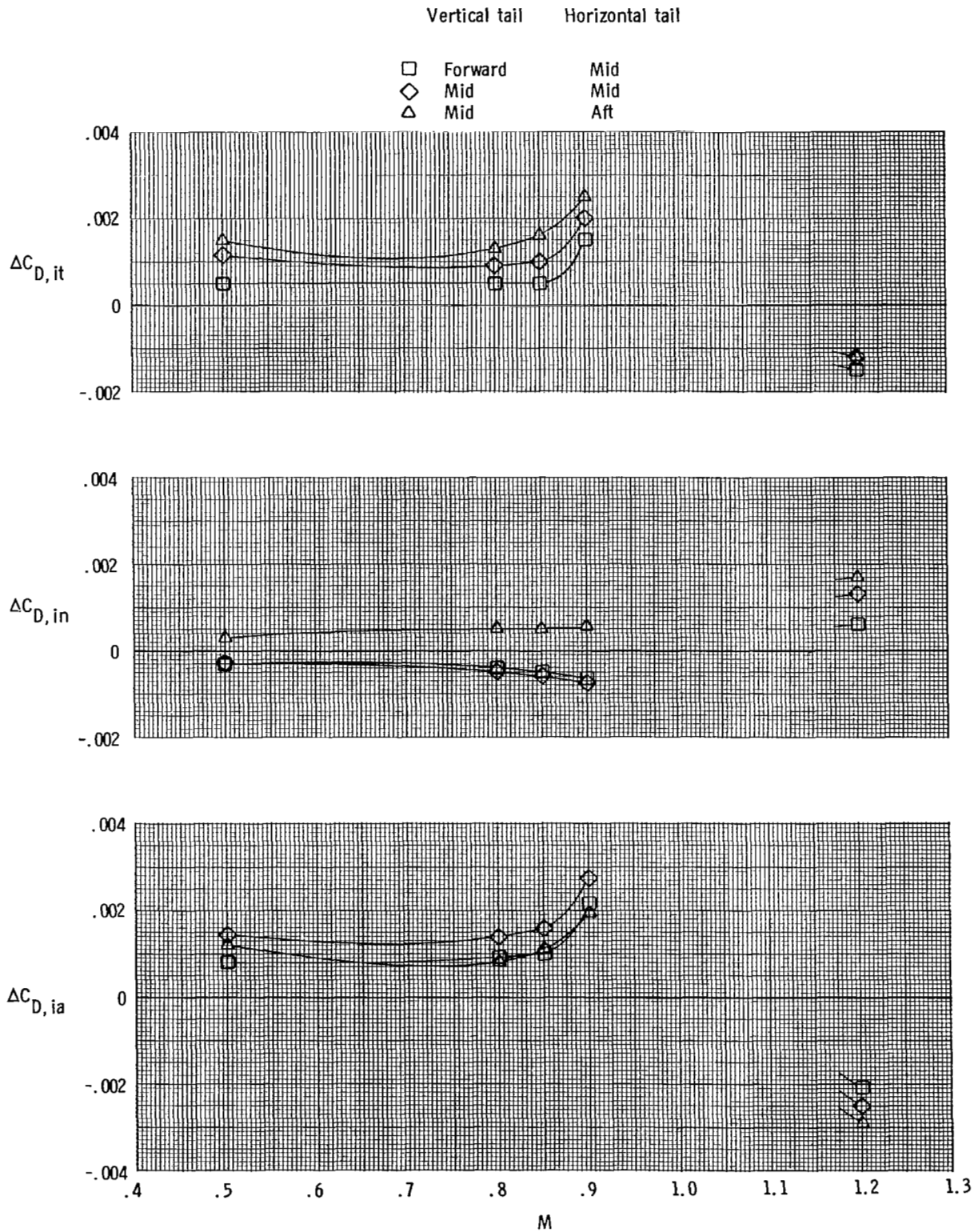(a) Total and nozzle drag coefficients.

Figure 25.- Effect of empennage arrangement on variation of aft-end drag
coefficient components with Mach number for scheduled nozzle pressure
ratios for short subsonic dry power nozzles.

Vertical tail   Horizontal tail

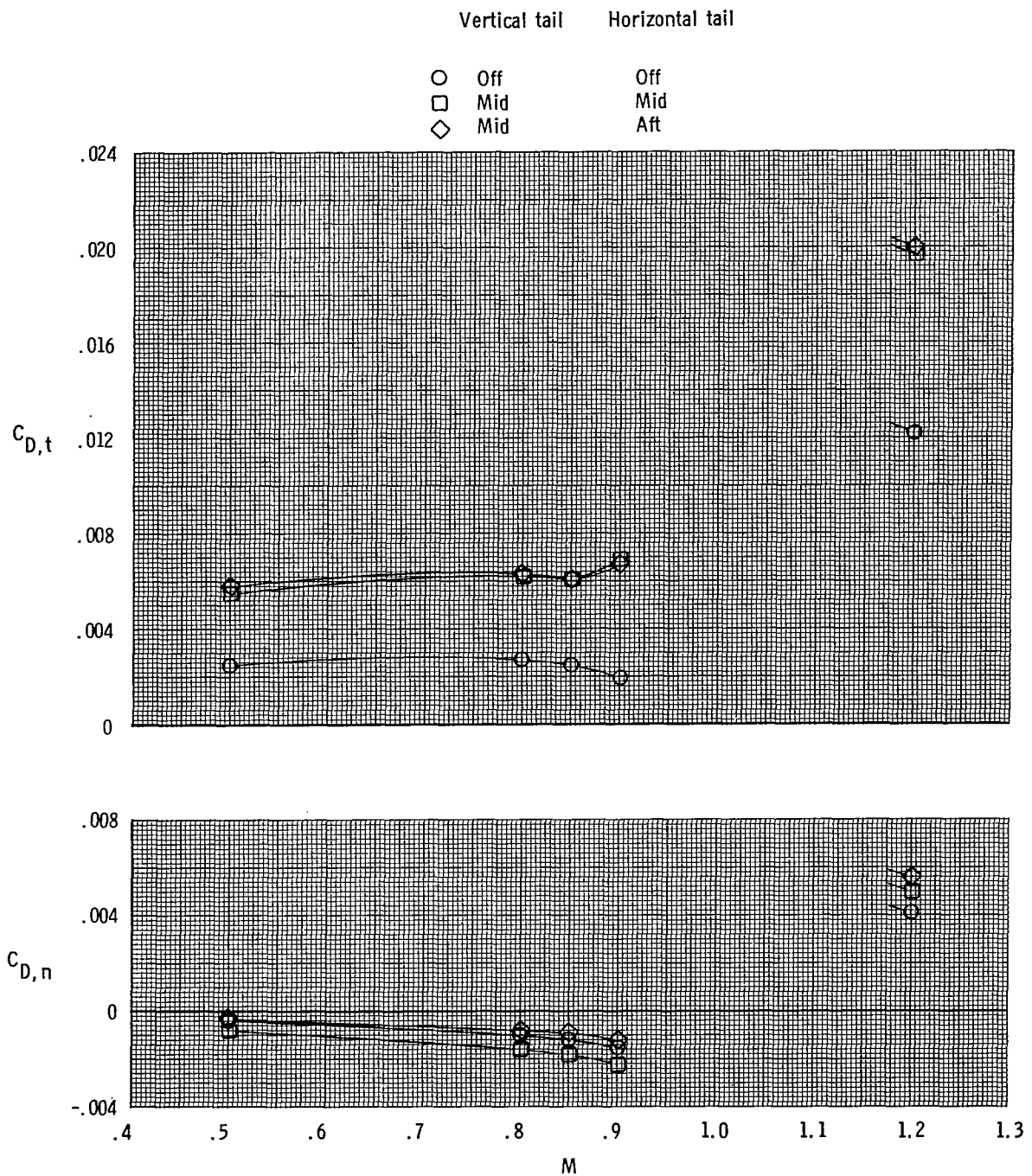|		
○	Off	Off
□	Forward	Mid
◇	Mid	Mid
△	Mid	Aft
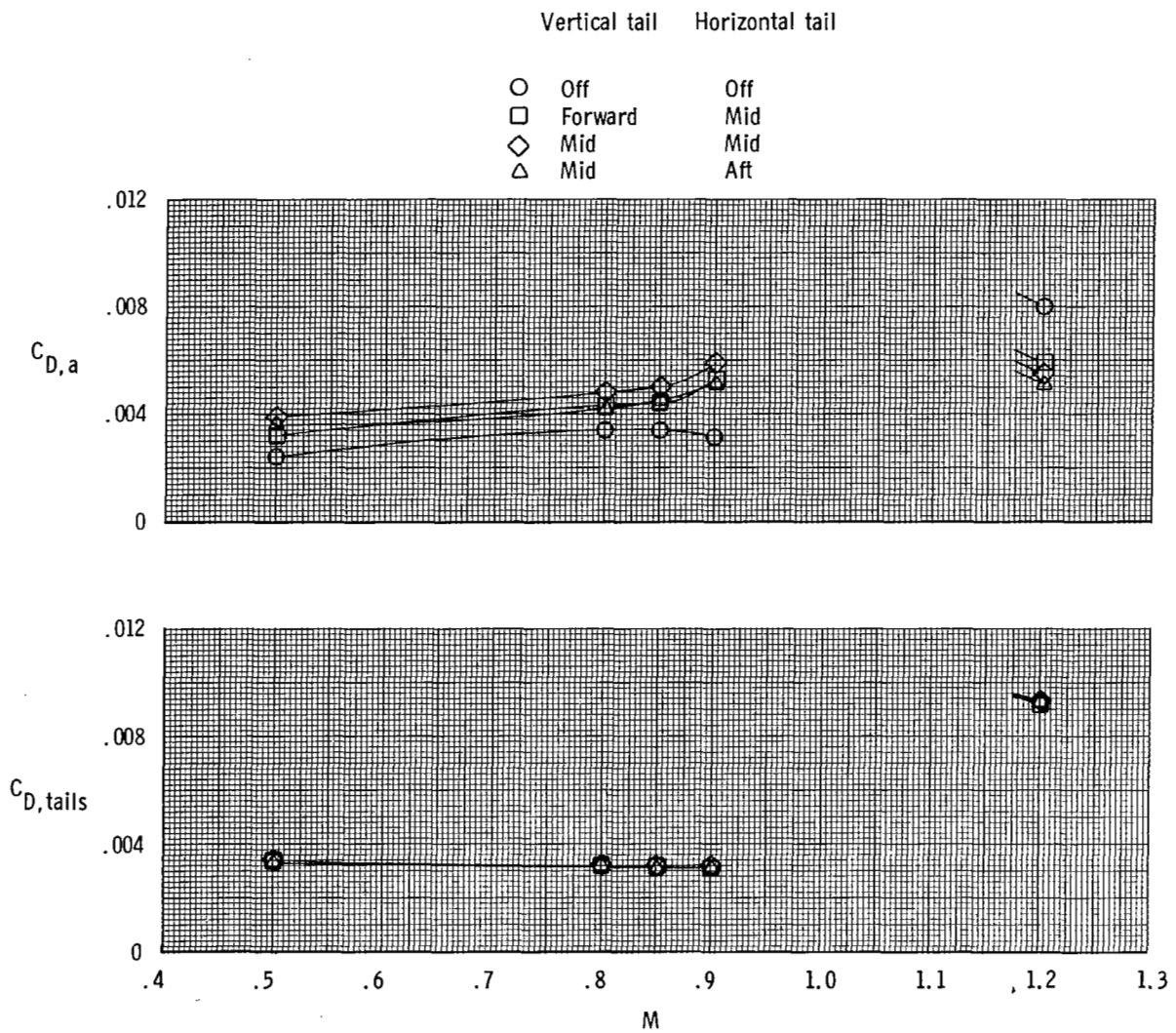
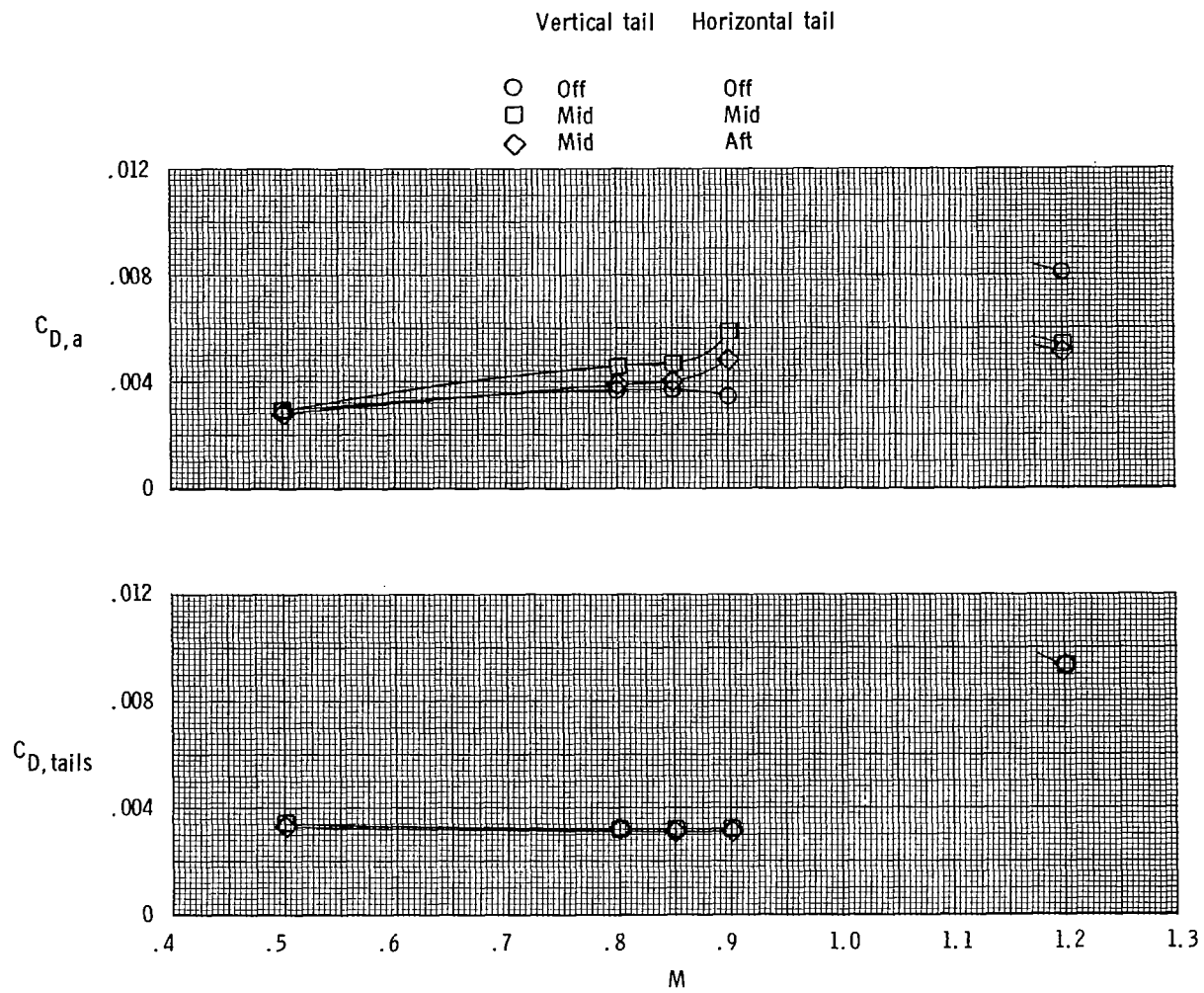(b) Afterbody and tail drag coefficients.

Figure 25.- Continued.

(c) Empennage interference-drag coefficient increments.
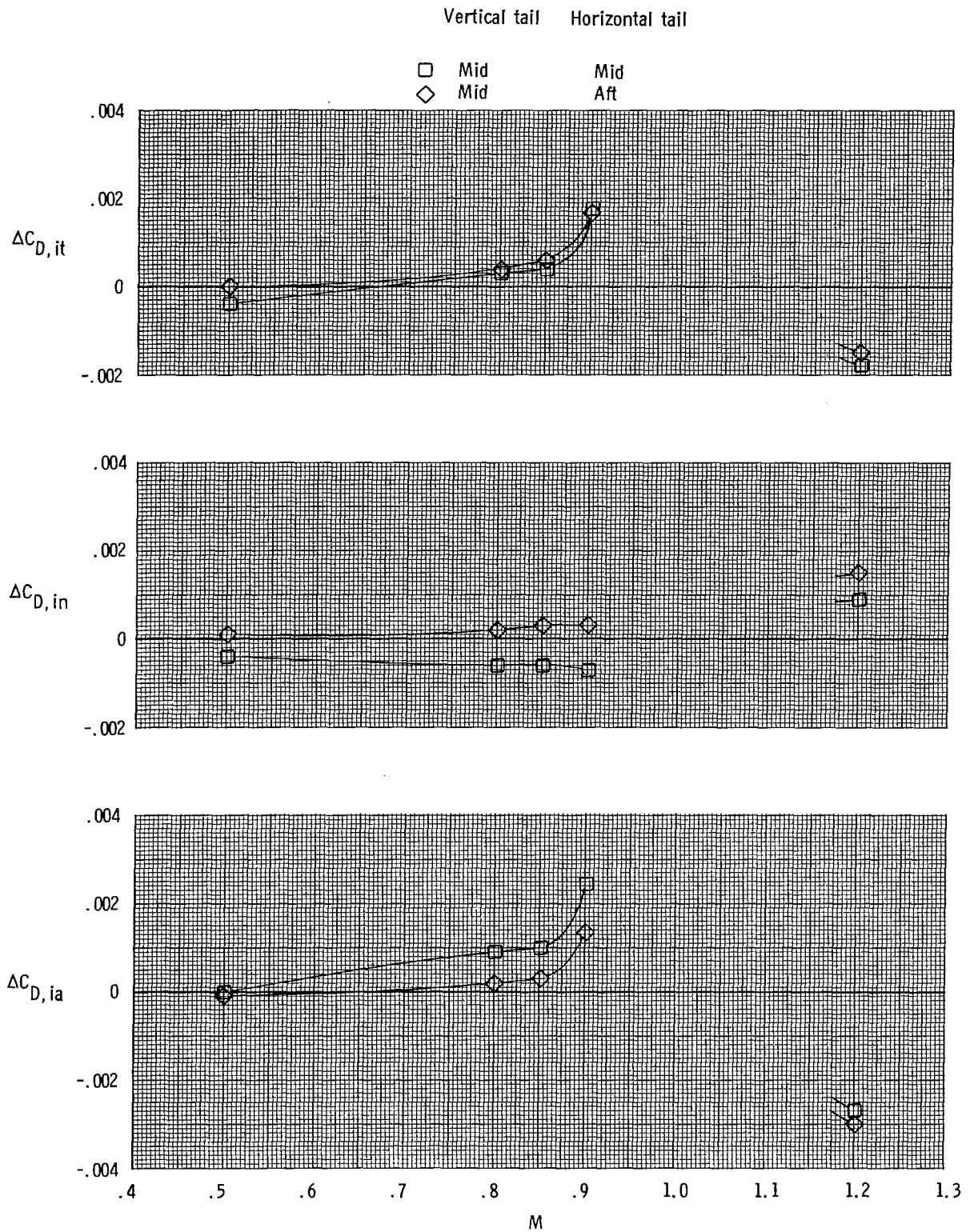
Figure 25.- Concluded.

(a) Total and nozzle drag coefficients.

Figure 26.- Effect of empennage arrangement on variation of aft-end drag coefficient components with Mach number for scheduled nozzle pressure ratios for long subsonic dry power nozzles.
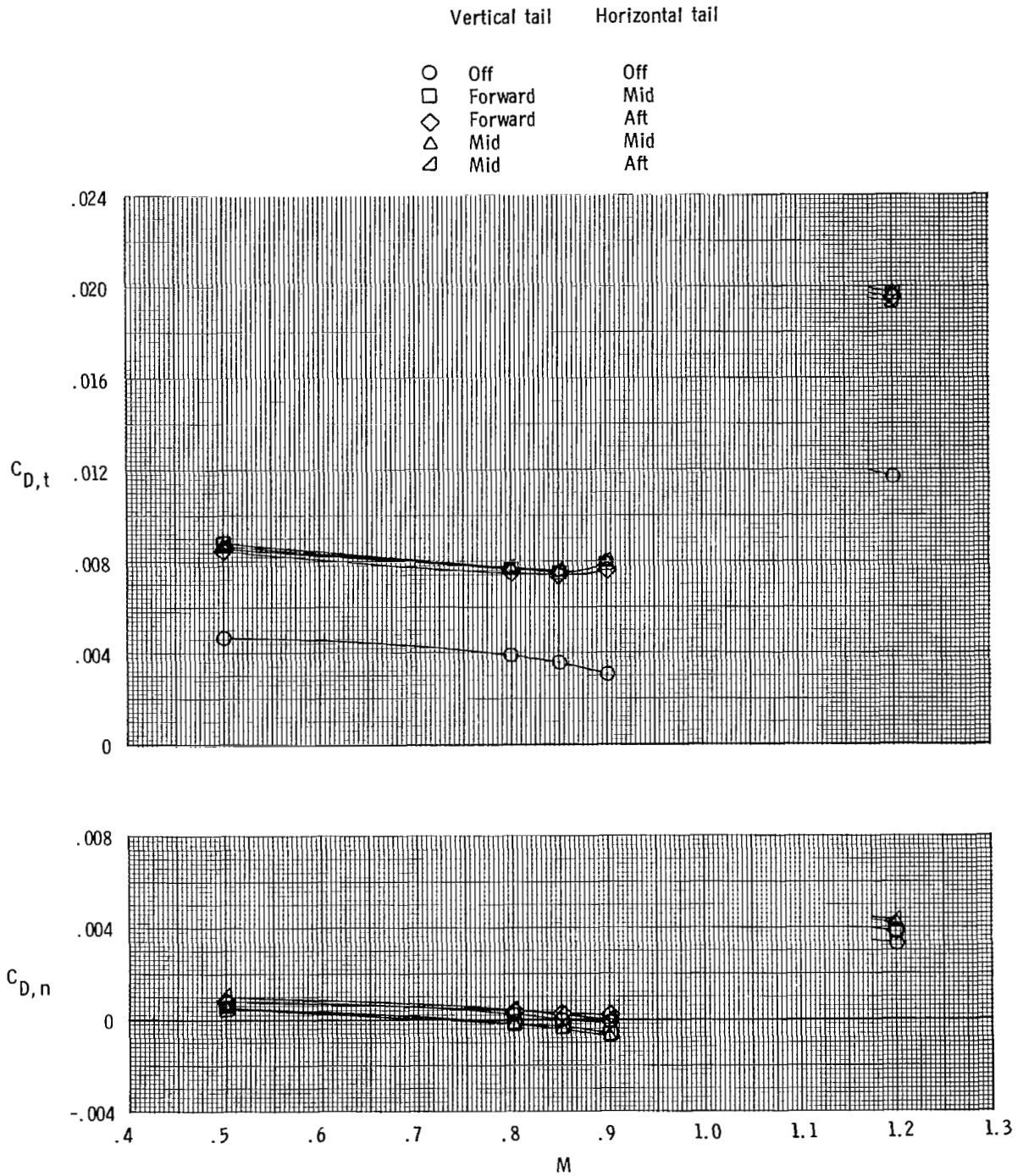
(b) Afterbody and tail drag coefficients.
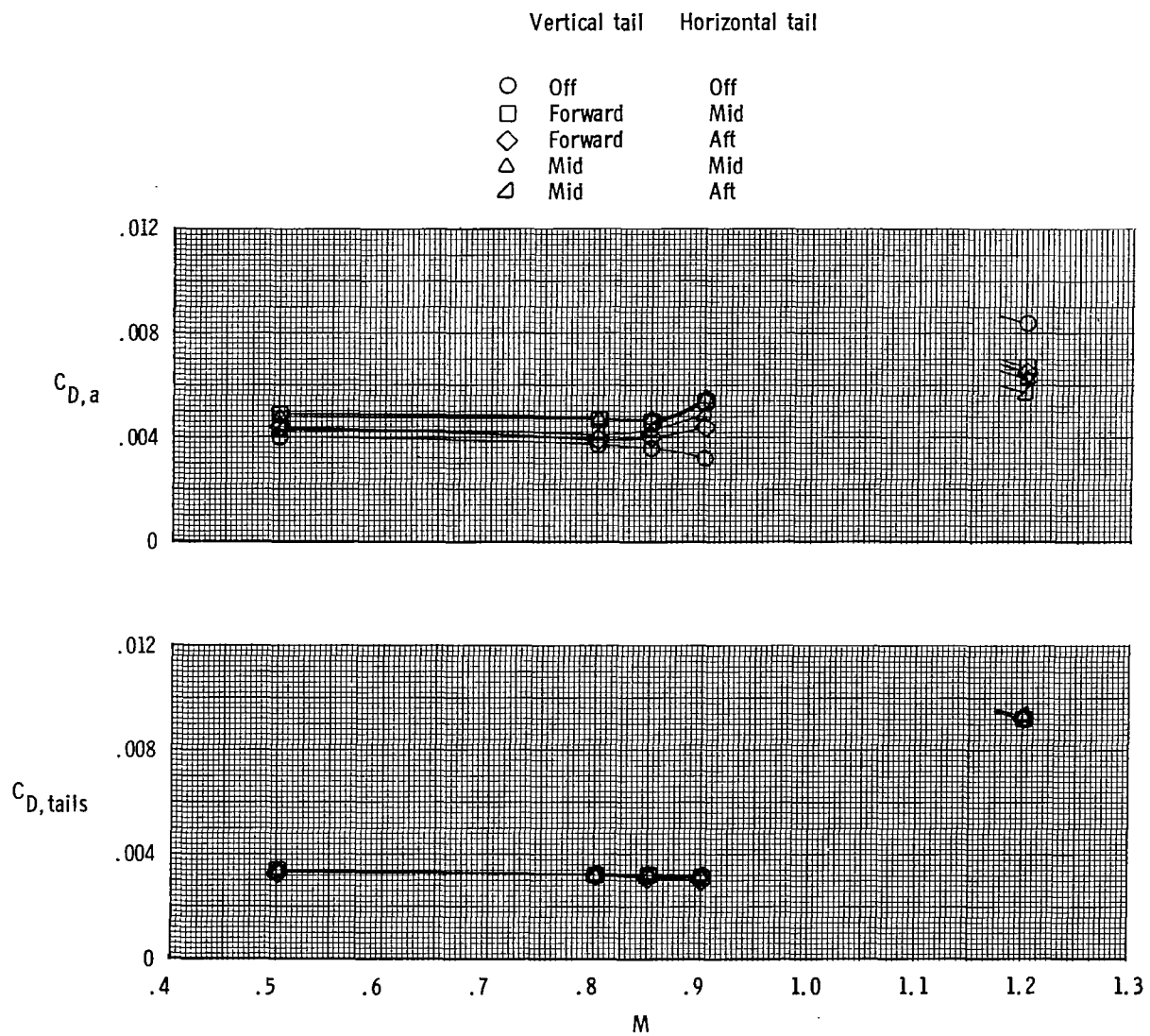
Figure 26.- Continued.

(c) Empennage interference-drag coefficient increments.

Figure 26.- Concluded.

Vertical tail   Horizontal tail

○   Off   Off
□   Forward   Mid
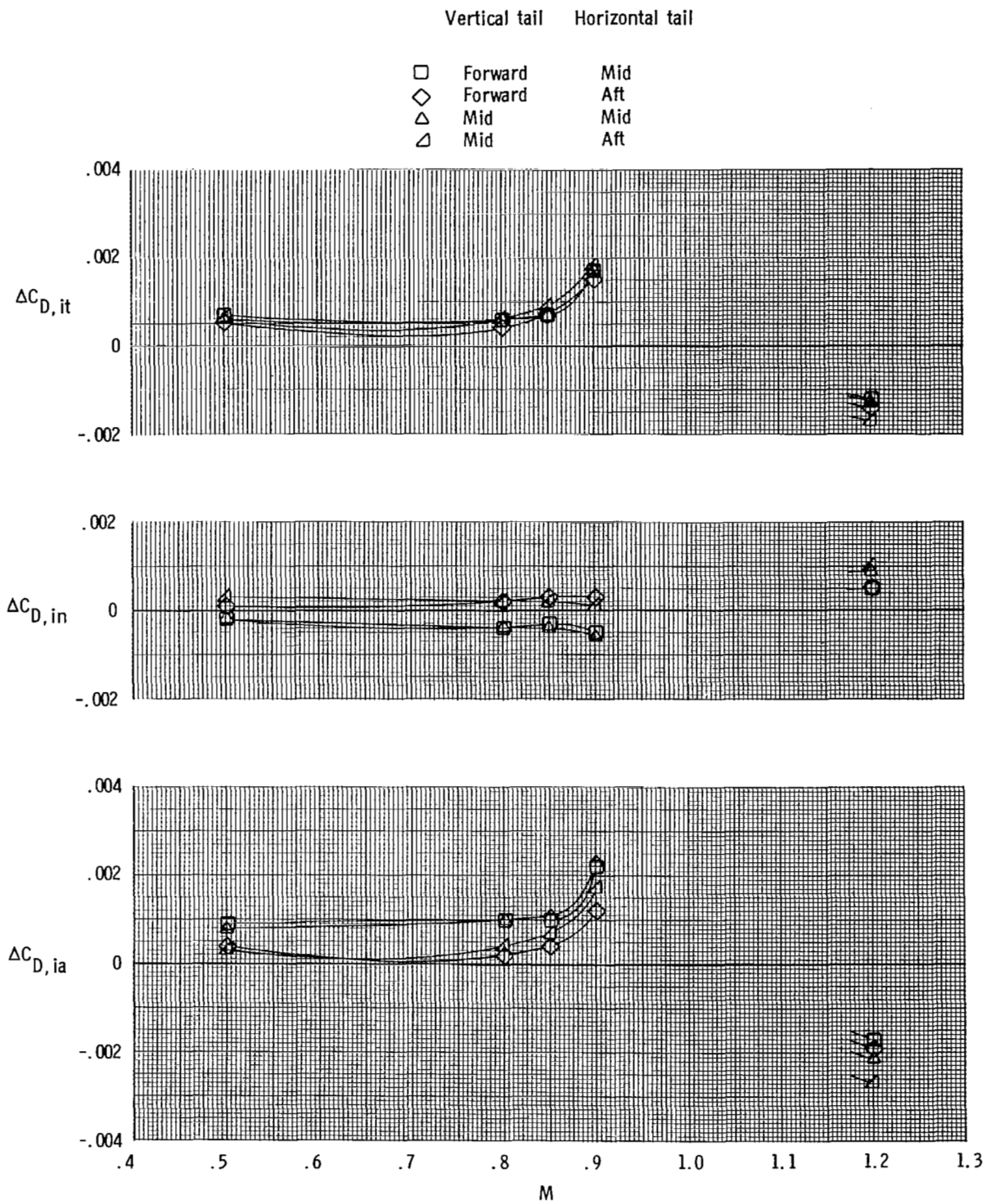◇   Forward   Aft
△   Mid   Mid
◁   Mid   Aft

(a) Total and nozzle drag coefficients.

Figure 27.- Effect of empennage arrangement on variation of aft-end drag
   coefficient components with Mach number for scheduled nozzle pressure
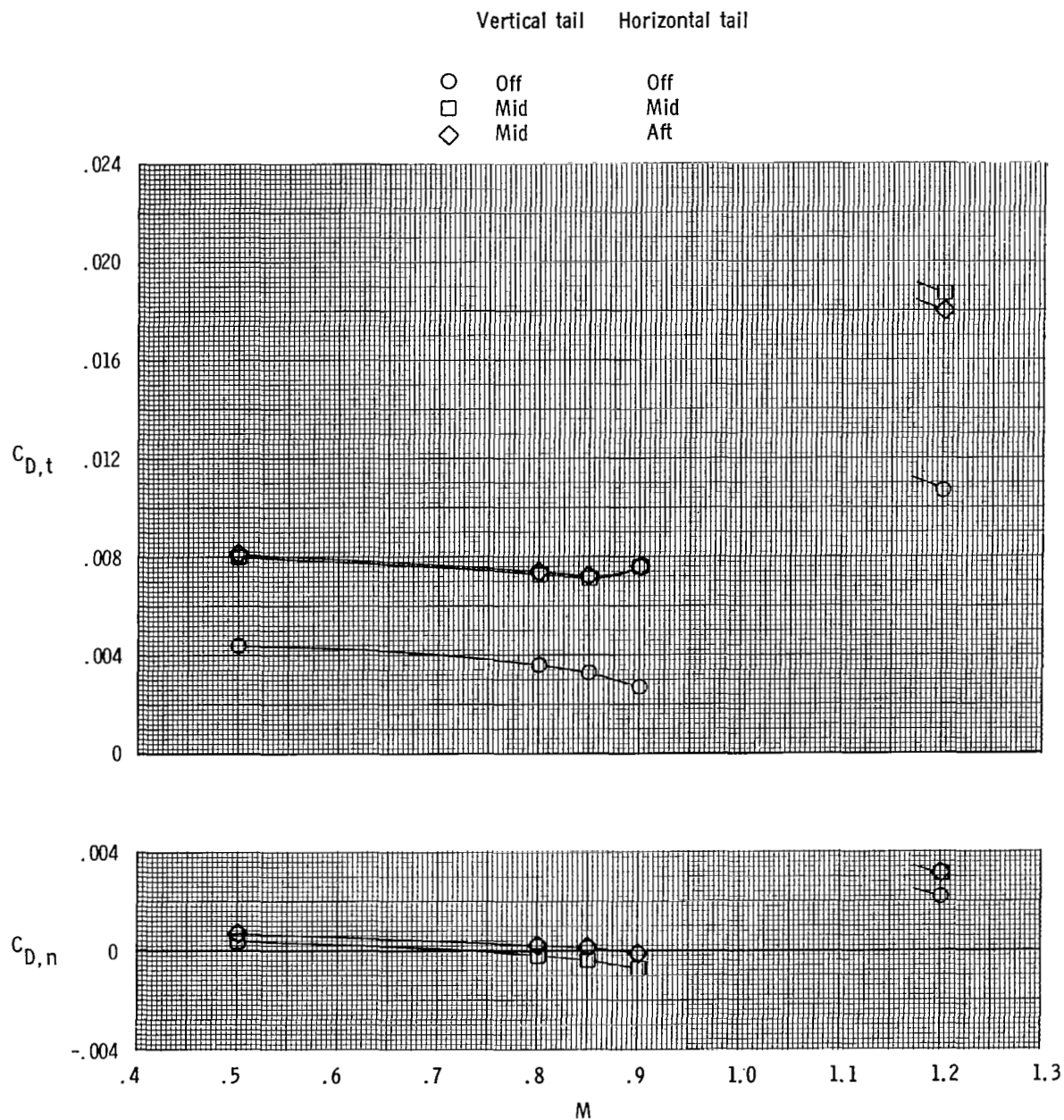   ratios for short supersonic dry power nozzles.

(b) Afterbody and tail drag coefficients.

Figure 27.- Continued.

Vertical tail   Horizontal tail

☐   Forward   Mid
◇   Forward   Aft
△   Mid   Mid
◿   Mid   Aft

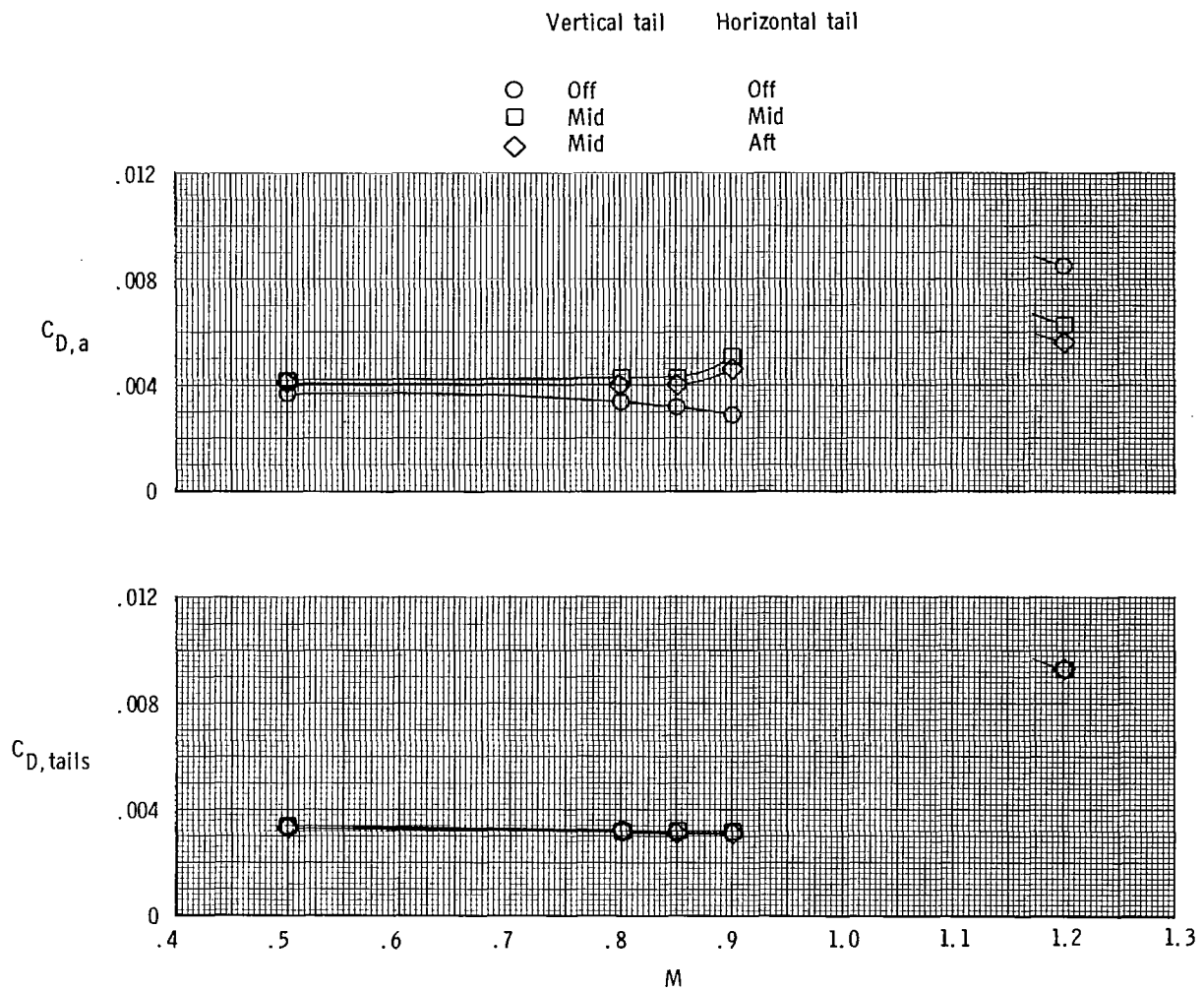(c) Empennage interference-drag coefficient increments.

Figure 27.- Concluded.
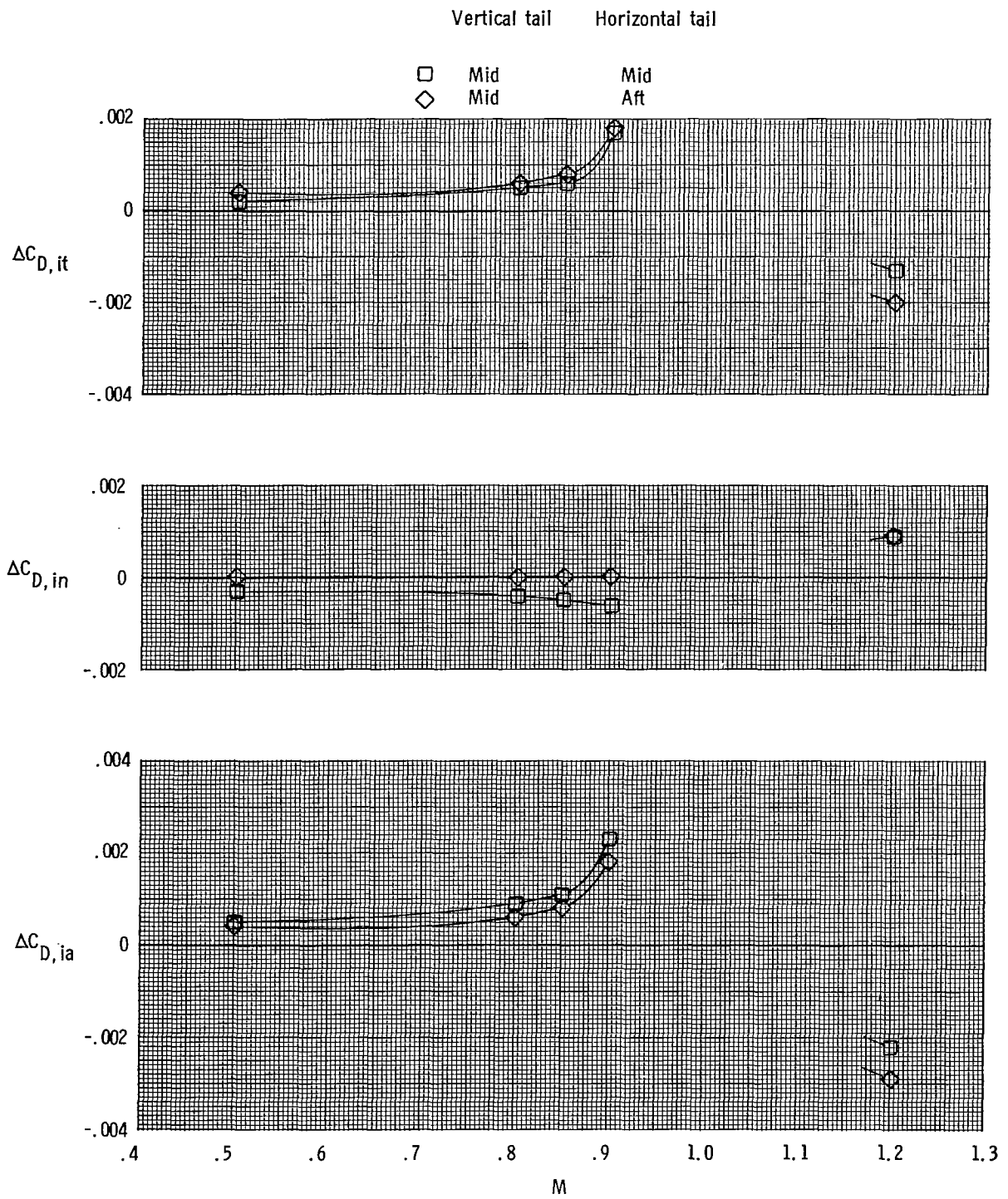
(a) Total and nozzle drag coefficients.

Figure 28.- Effect of empennage arrangement on variation of aft-end drag coefficient components with Mach number for scheduled nozzle pressure ratios for long supersonic dry power nozzles.
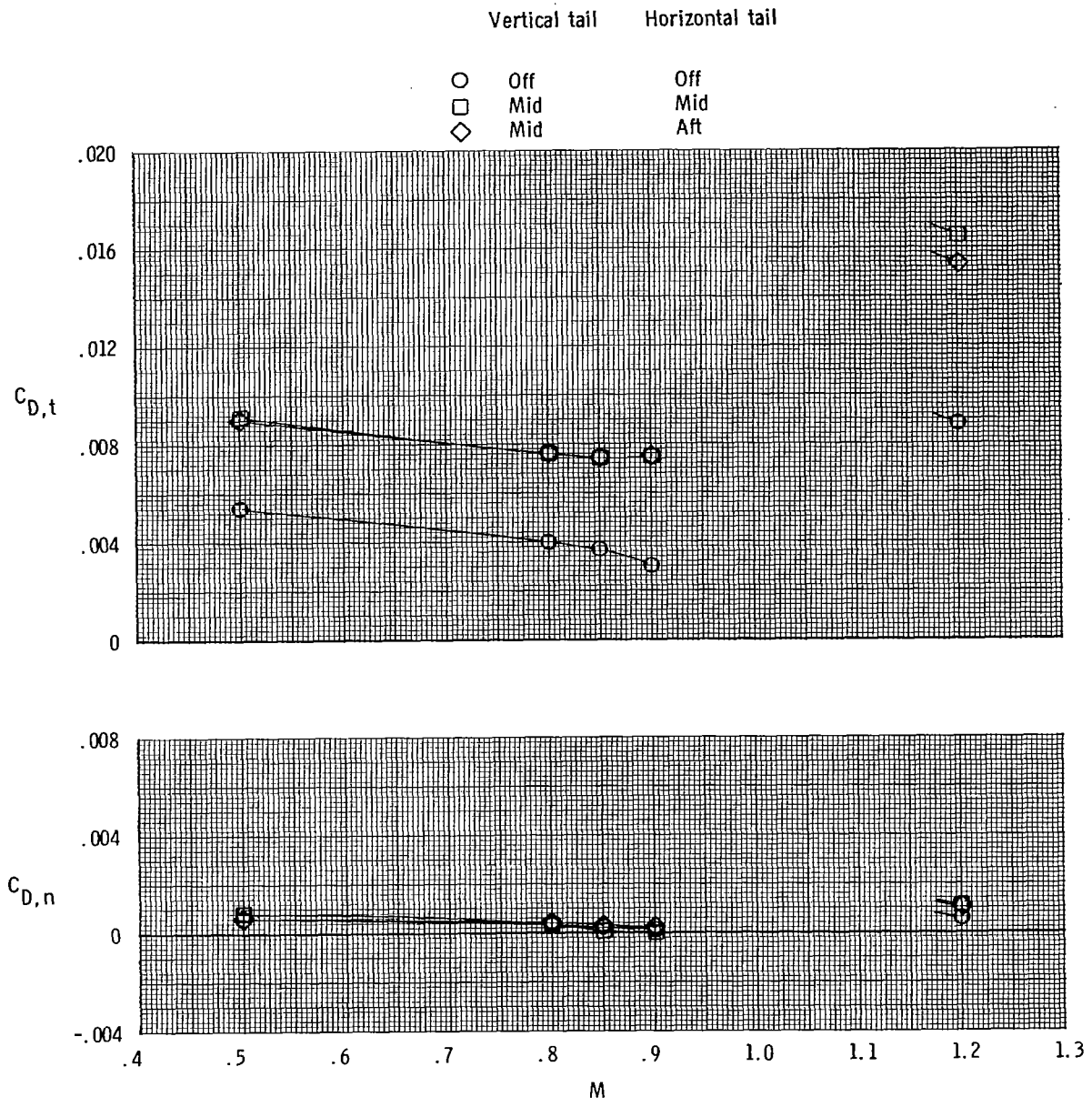
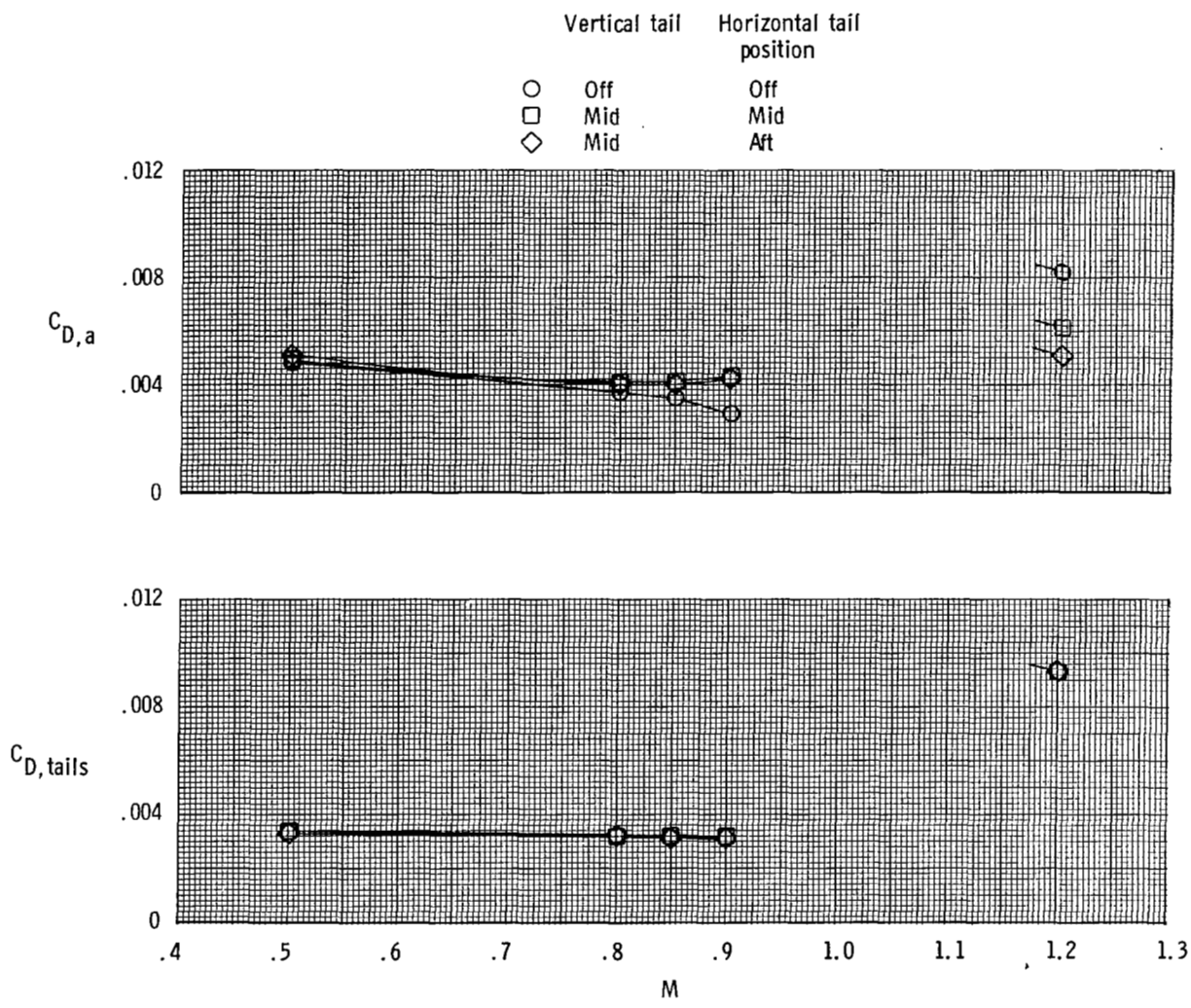(b) Afterbody and tail drag coefficients.

Figure 28.- Continued.

(c) Empennage interference-drag coefficient increments.

Figure 28.- Concluded.

Vertical tail   Horizontal tail

○   Off   Off
□   Mid   Mid
◇   Mid   Aft

$C_{D,t}$

.020

.016

.012

.008

.004

0

$C_{D,n}$

.008

.004

0

-.004

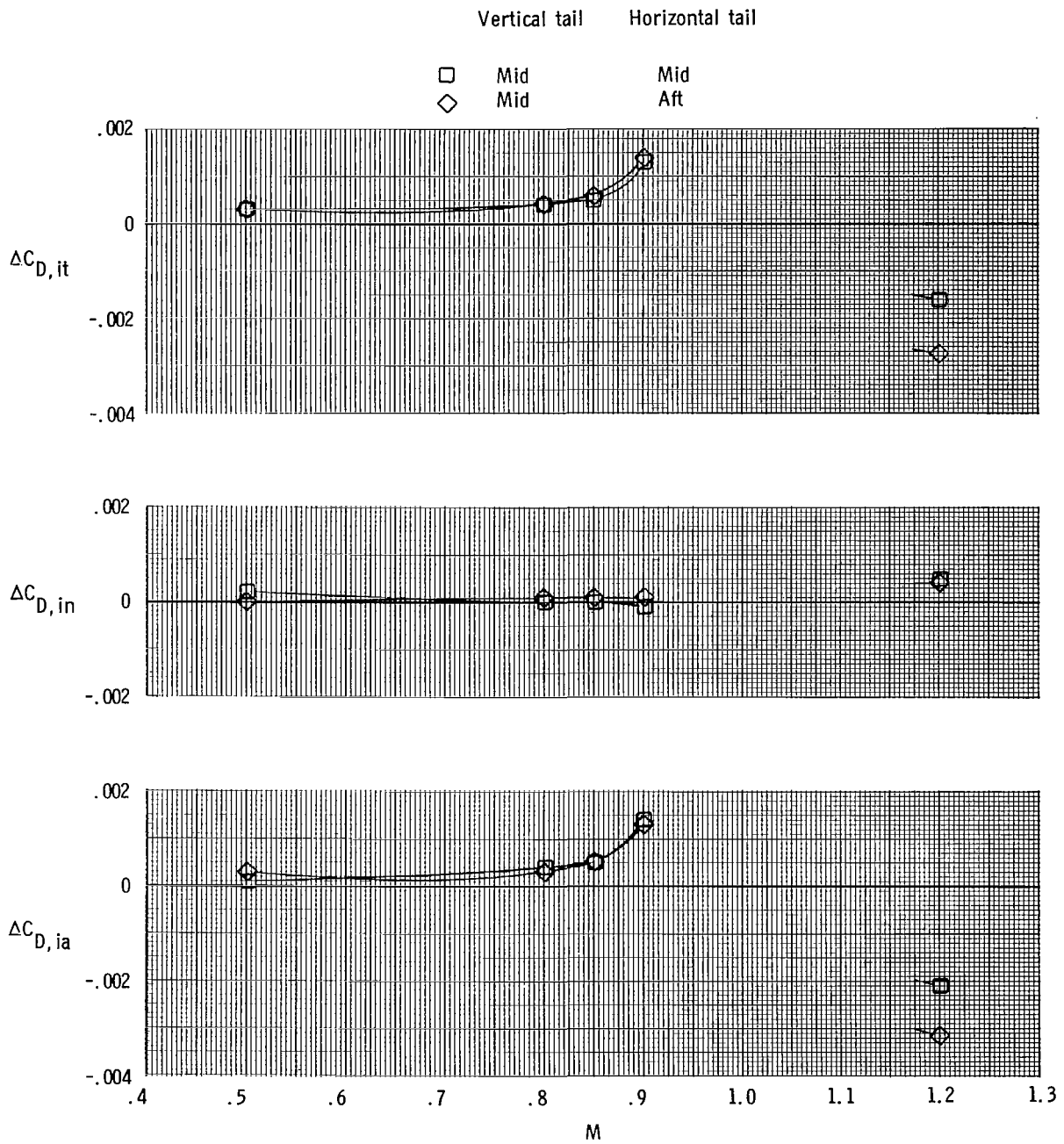.4   .5   .6   .7   .8   .9   1.0   1.1   1.2   1.3

M

(a) Total and nozzle drag coefficients.

Figure 29.- Effect of empennage arrangement on variation of aft-end drag
coefficient components with Mach number for scheduled nozzle pressure
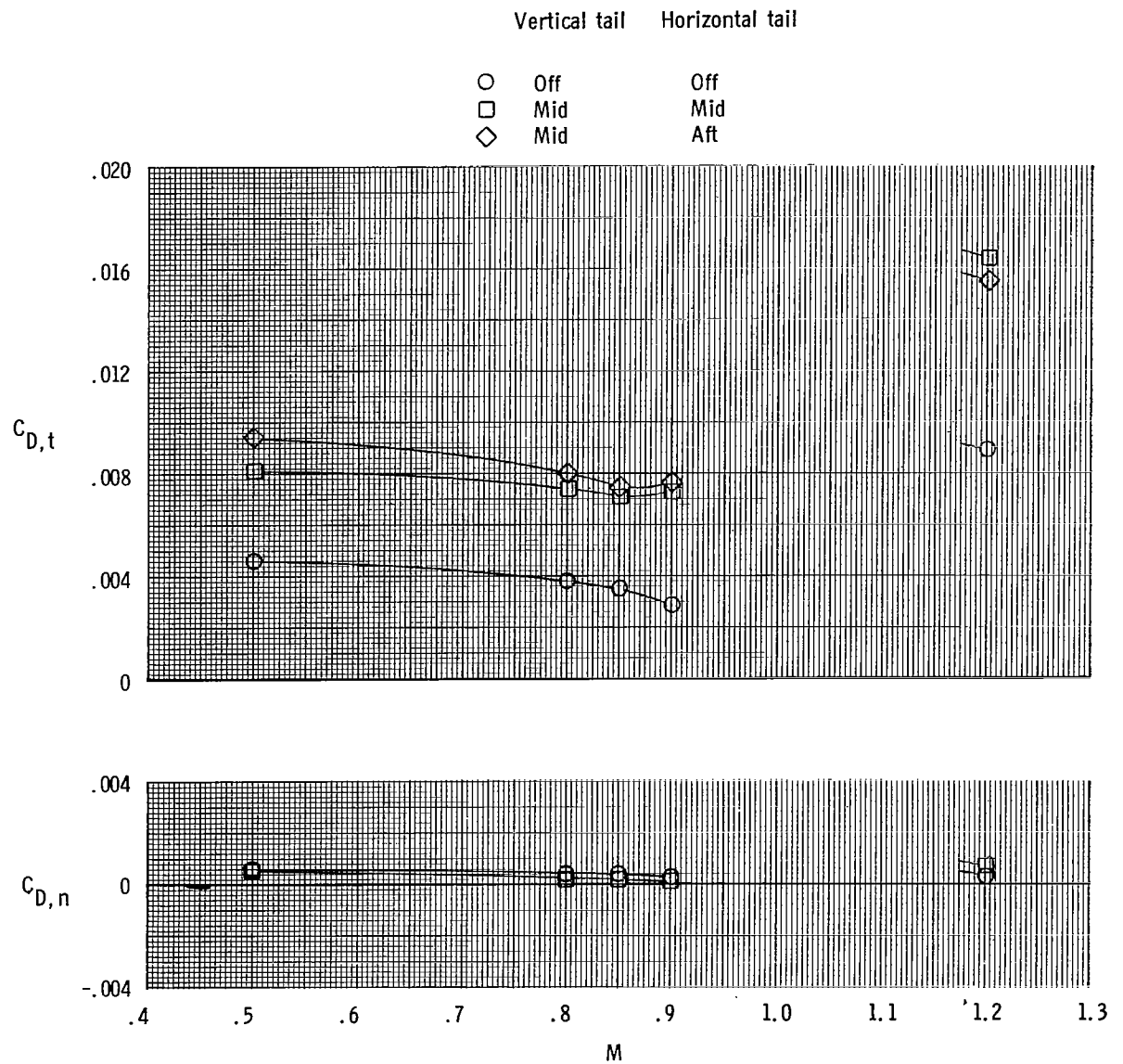ratios for short supersonic partial A/B power nozzles.

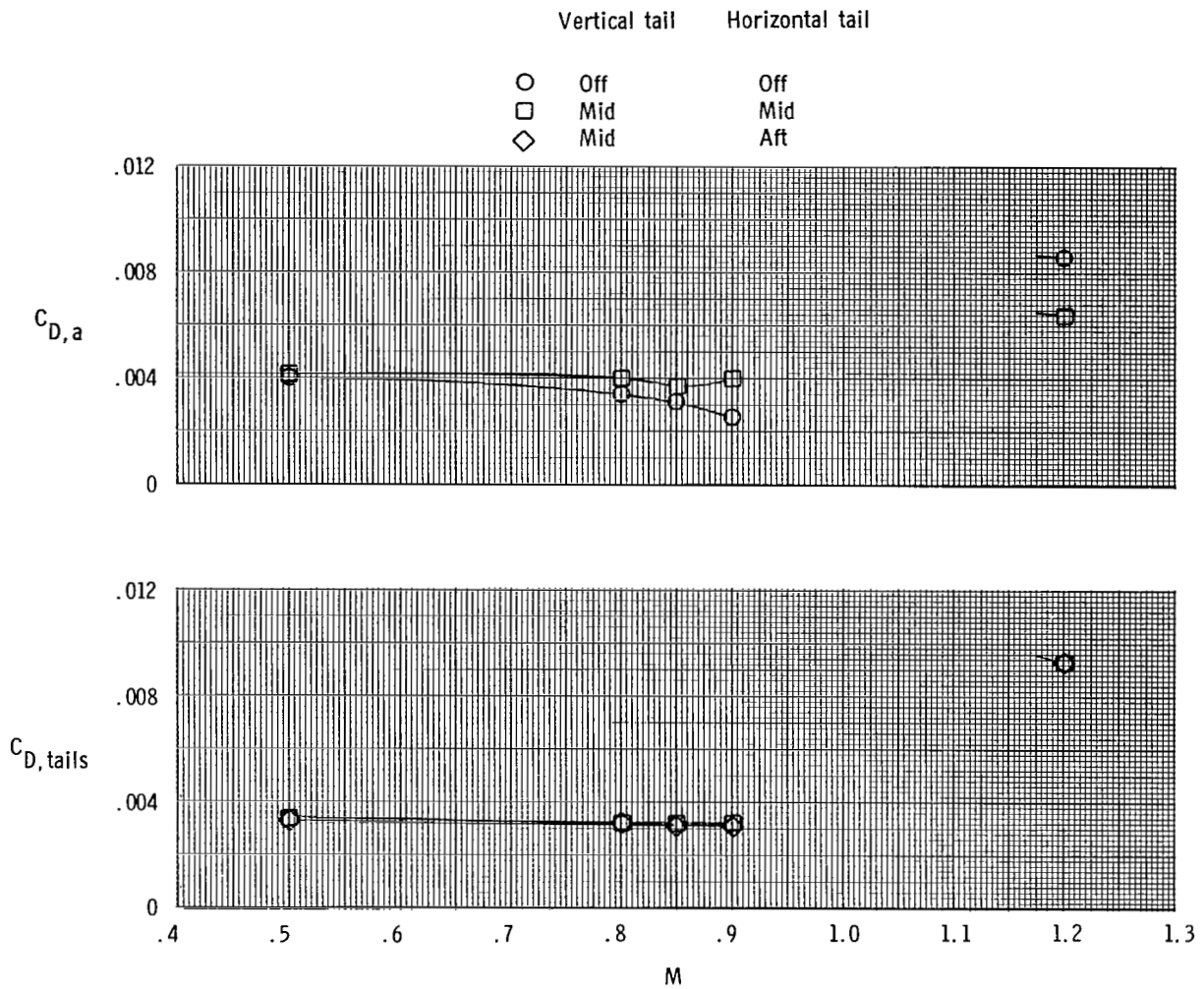(b) Afterbody and tail drag coefficients.

Figure 29.- Continued.

(c) Empennage interference-drag coefficient increments.
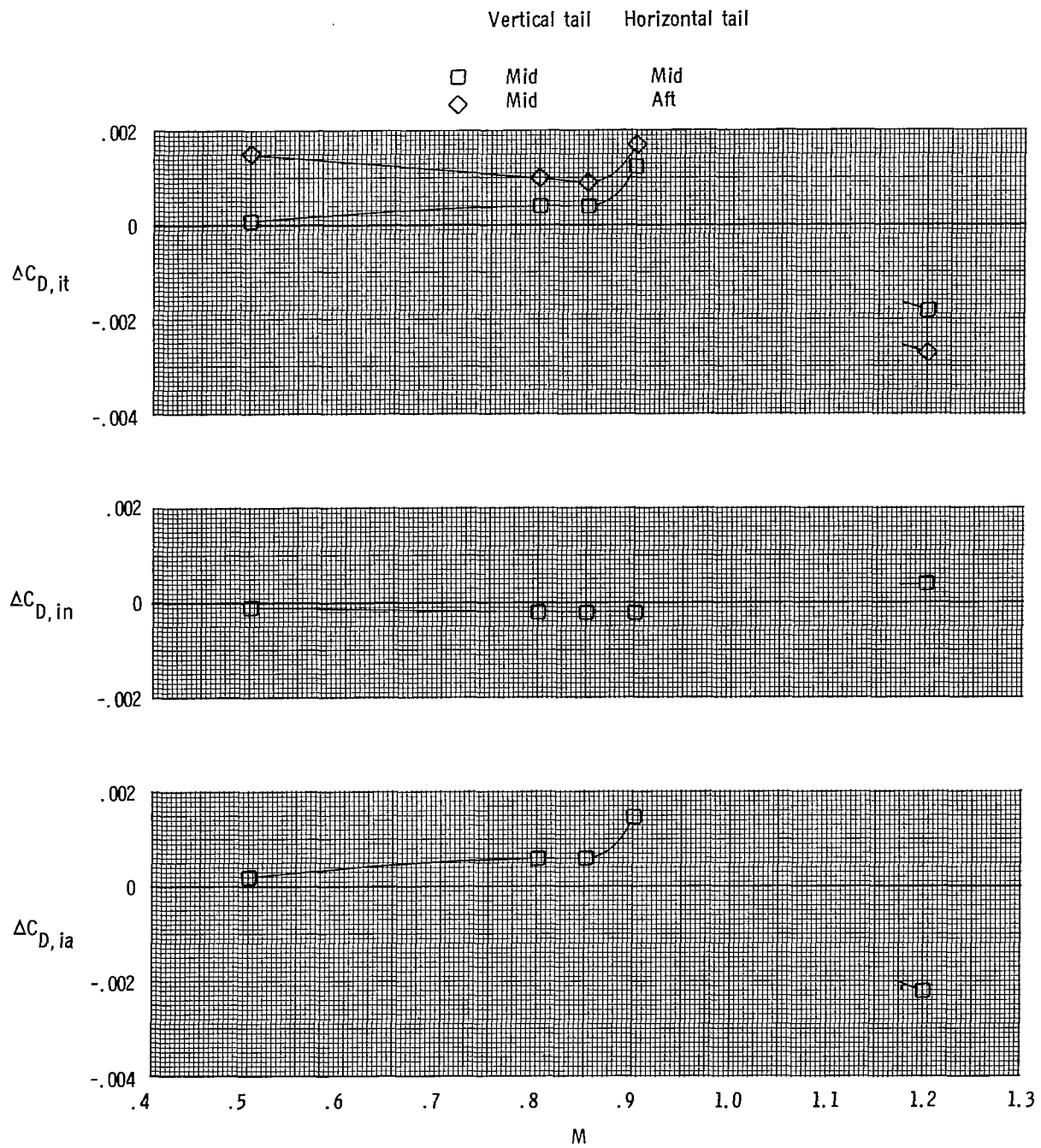
Figure 29.- Concluded.

(a) Total and nozzle drag coefficients.

Figure 30.- Effect of empennage arrangement on variation of aft-end drag
coefficient components with Mach number for scheduled nozzle pressure
ratios for long supersonic partial A/B power nozzles.

Vertical tail   Horizontal tail

○   Off   Off
□   Mid   Mid
◇   Mid   Aft

(b) Afterbody and tail drag coefficients.

Figure 30.- Continued.

Vertical tail   Horizontal tail

□   Mid   Mid
◇   Mid   Aft

$\Delta C_{D,it}$

.002

0

-.002

-.004

$\Delta C_{D,in}$

.002

0

-.002

$\Delta C_{D,ia}$

.002

0

-.002

-.004

.4   .5   .6   .7   .8   .9   1.0   1.1   1.2   1.3

M

(c) Empennage interference-drag coefficient increments.

Figure 30.- Concluded.

(a) Total and nozzle drag coefficients.

Figure 31.- Effect of nozzle length on variation of aft-end drag coefficient
components with Mach number for scheduled nozzle pressure ratios for
subsonic dry power nozzles.

	l/d_m	β, deg	A_e/A_t	d_b/d_m
O	0.831	18.30	1.22	0.557
□	1.124	12.30	1.22	0.557

(b) Afterbody and tail drag coefficients.

Figure 31.- Continued.

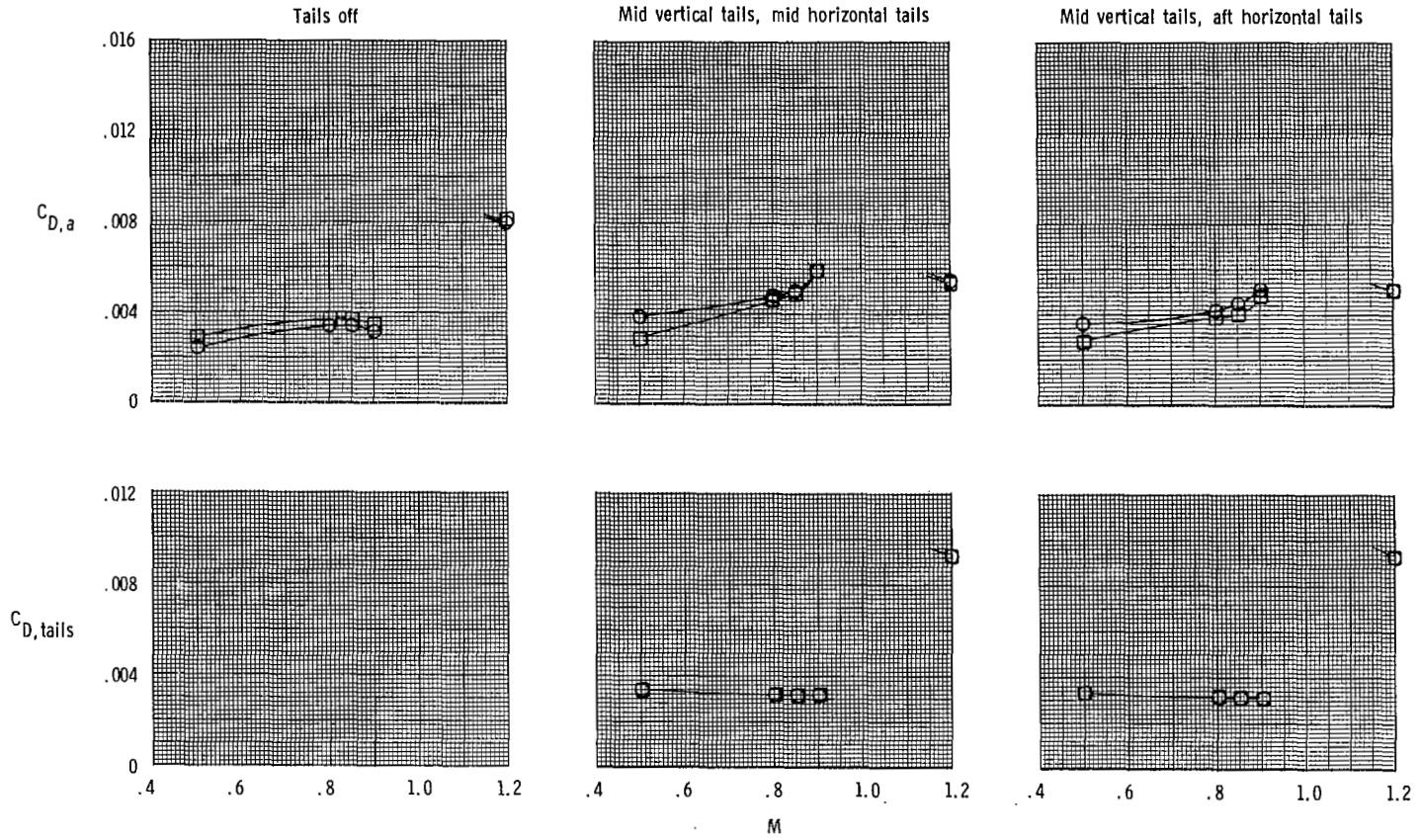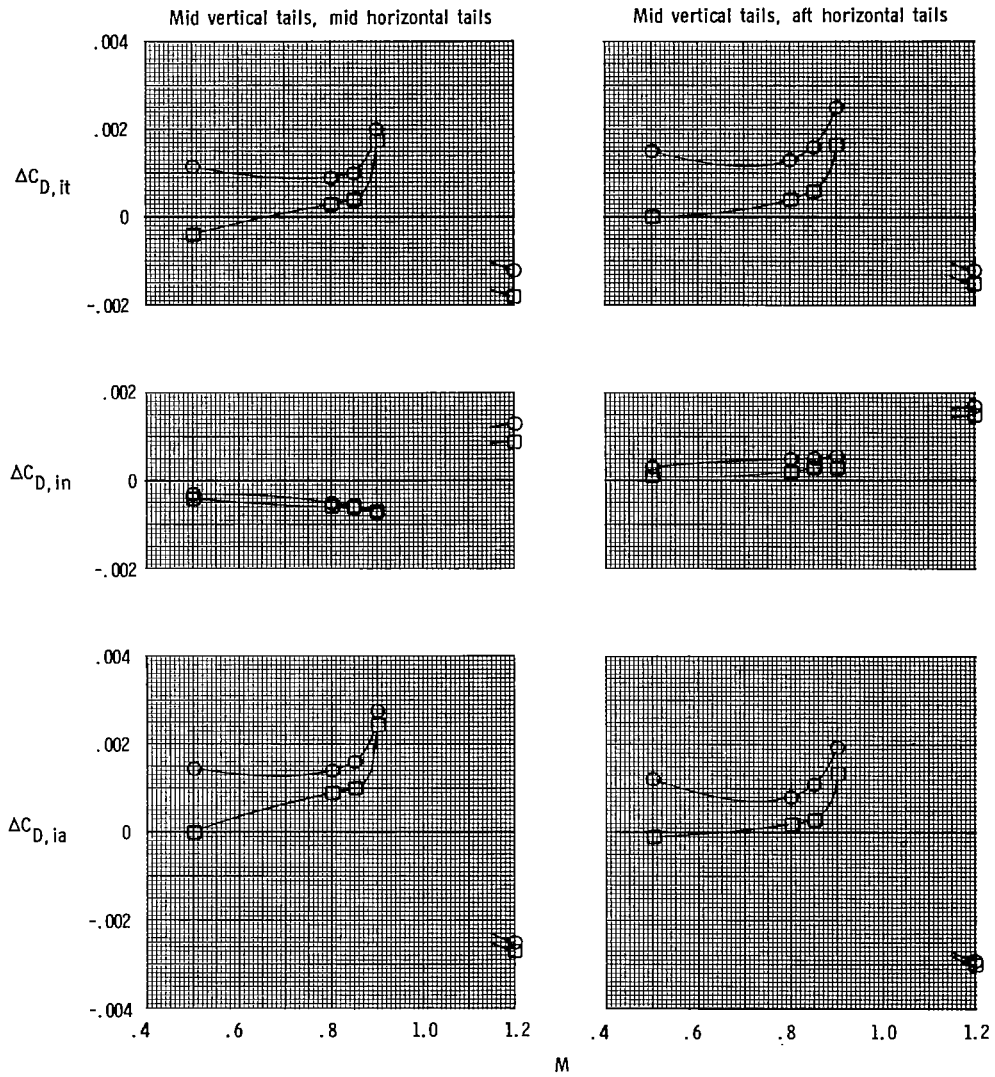(c) Empennage interference-drag coefficient increments.

Figure 31.- Concluded.

	l/d_m	β, deg	A_e/A_t	d_b/d_m
O	0.814	9.65	2.24	0.752
□	1.114	6.72	2.24	0.752
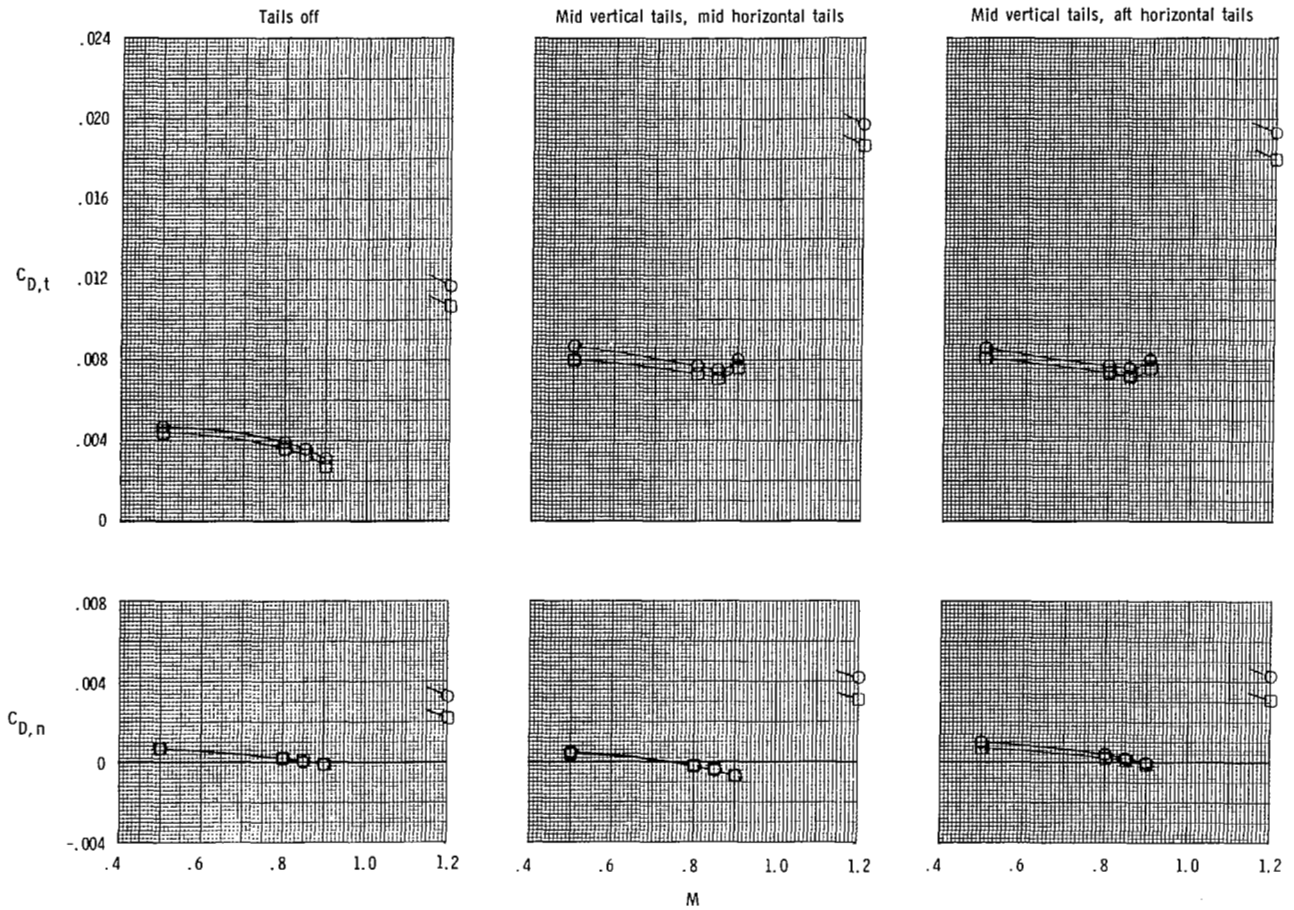
(a) Total and nozzle drag coefficients.

Figure 32.- Effect of nozzle length on variation of aft-end drag coefficient components with Mach number for scheduled nozzle pressure ratios for supersonic dry power nozzles.
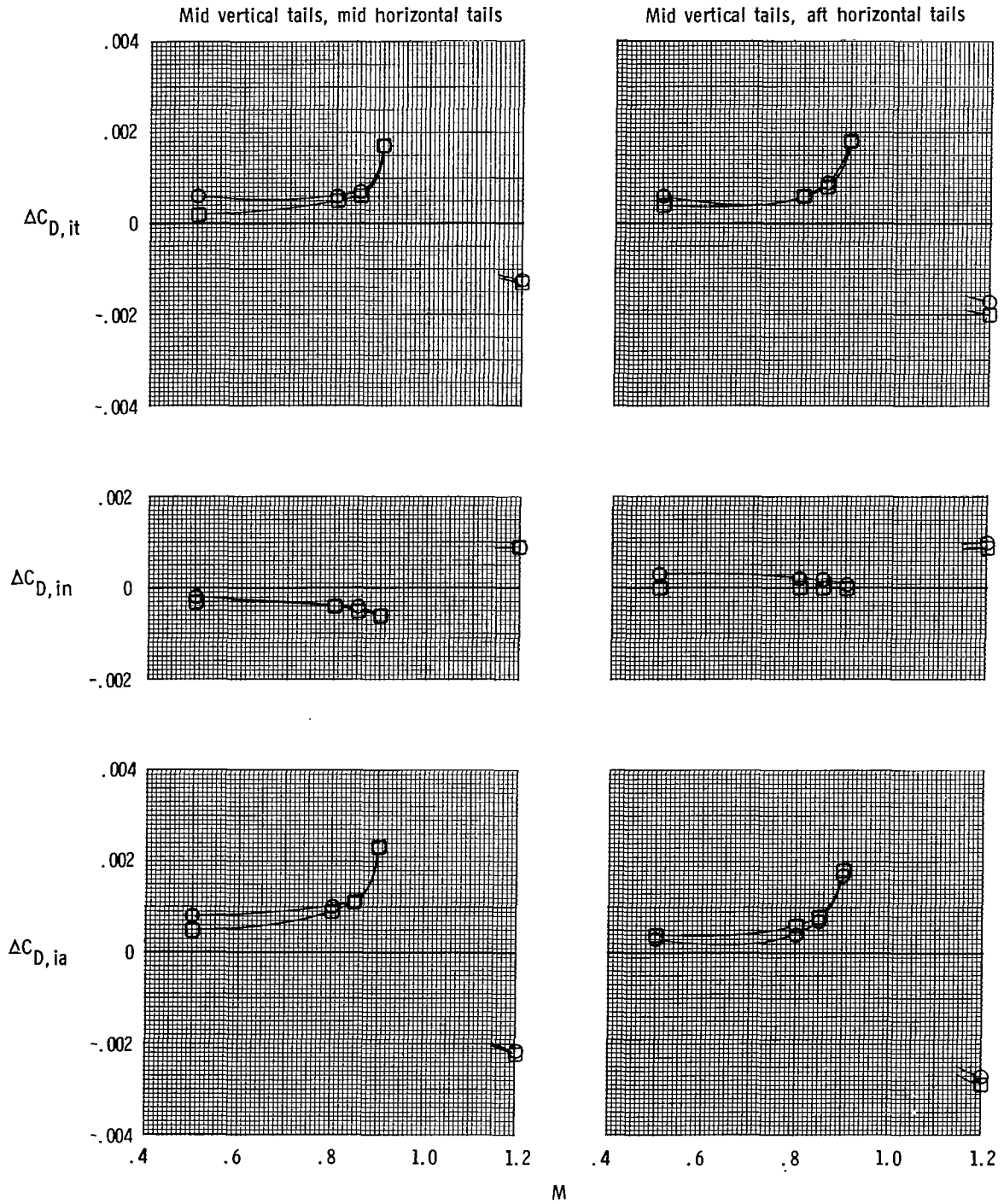
	l/d_m	β, deg	A_e/A_t	d_b/d_m
O	0.814	9.65	2.24	0.752
□	1.114	6.72	2.24	0.752
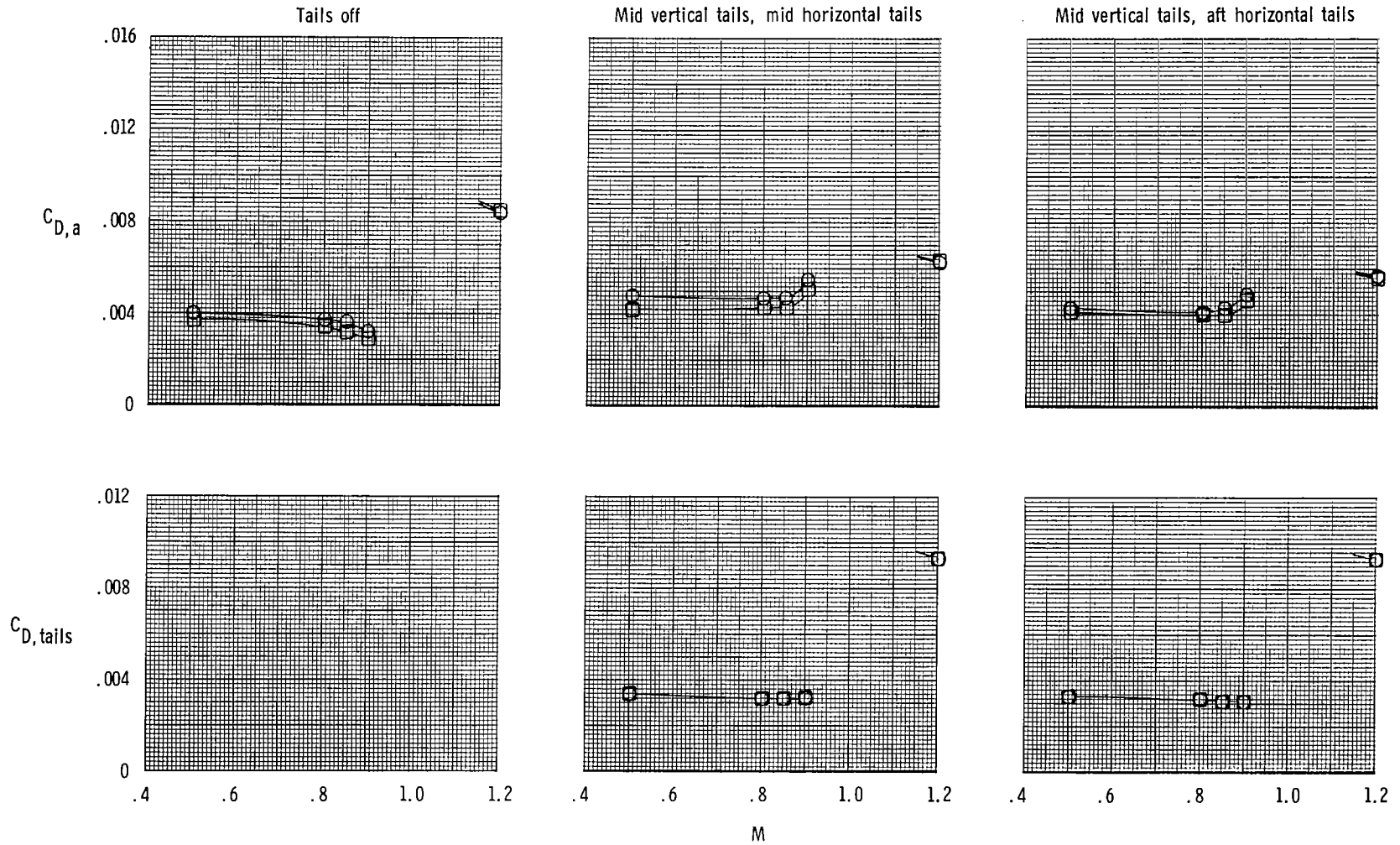
(b) Afterbody and tail drag coefficients.

Figure 32.- Continued.

	l/d_m	β, deg	A_e/A_t	d_b/d_m
O	0.814	9.65	2.24	0.752
□	1.114	6.72	2.24	0.752

(c) Empennage interference-drag coefficient increments.

Figure 32.- Concluded.

	l/d_m	β, deg	A_e/A_t	d_b/d_m
○	0.833	3.57	2.24	0.901
□	1.135	2.57	2.24	0.901

Tails off

Mid vertical tails, mid horizontal tails

Mid vertical tails, aft horizontal tails

$C_{D,t}$

$C_{D,n}$

M
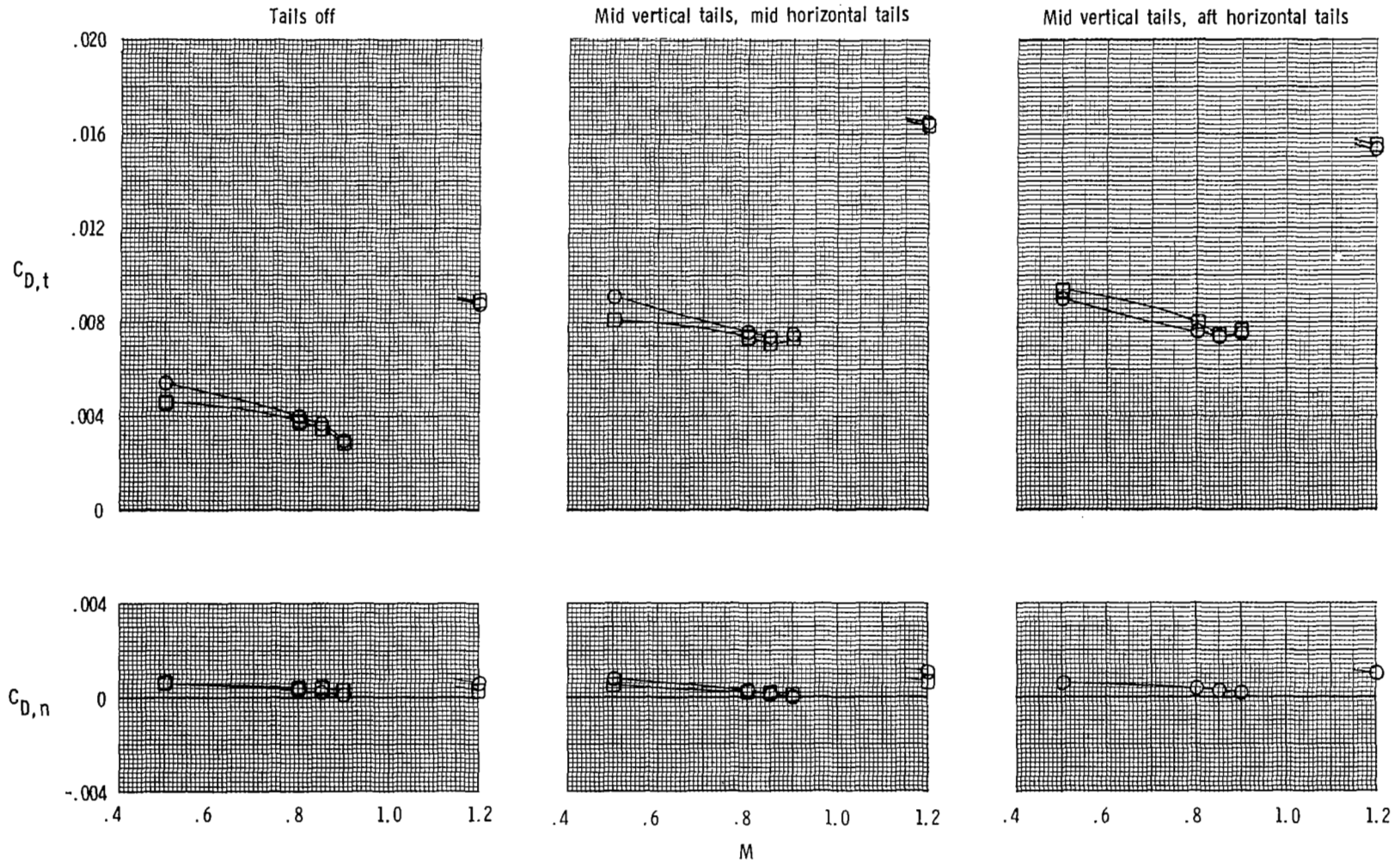
(a) Total and nozzle drag coefficients.

Figure 33.- Effect of nozzle length on variation of aft-end drag coefficient components with Mach number for scheduled nozzle pressure ratios for supersonic partial A/B power nozzles.

	l/d_m	β, deg	A_e/A_t	d_b/d_m
O	0.833	3.57	2.24	0.901
□	1.135	2.57	2.24	0.901

Tails off

Mid vertical tails, mid horizontal tails

Mid vertical tails, aft horizontal tails

.012

.008

$C_{D,a}$

.004

0

.012

.008

$C_{D,tails}$

.004

0

.4   .6   .8   1.0   1.2

.4   .6   .8   1.0   1.2

.4   .6   .8   1.0   1.2

M

(b) Afterbody and tail drag coefficients.

Figure 33.- Continued.

Mid vertical tails, mid horizontal tails   Mid vertical tails, aft horizontal tails

(c) Empennage interference-drag coefficient increments.

Figure 33.- Concluded.

	M	NPR
○	0.50	3.20
□	0.80	3.85
◇	0.85	4.00
△	0.90	4.20
◿	1.20	6.00
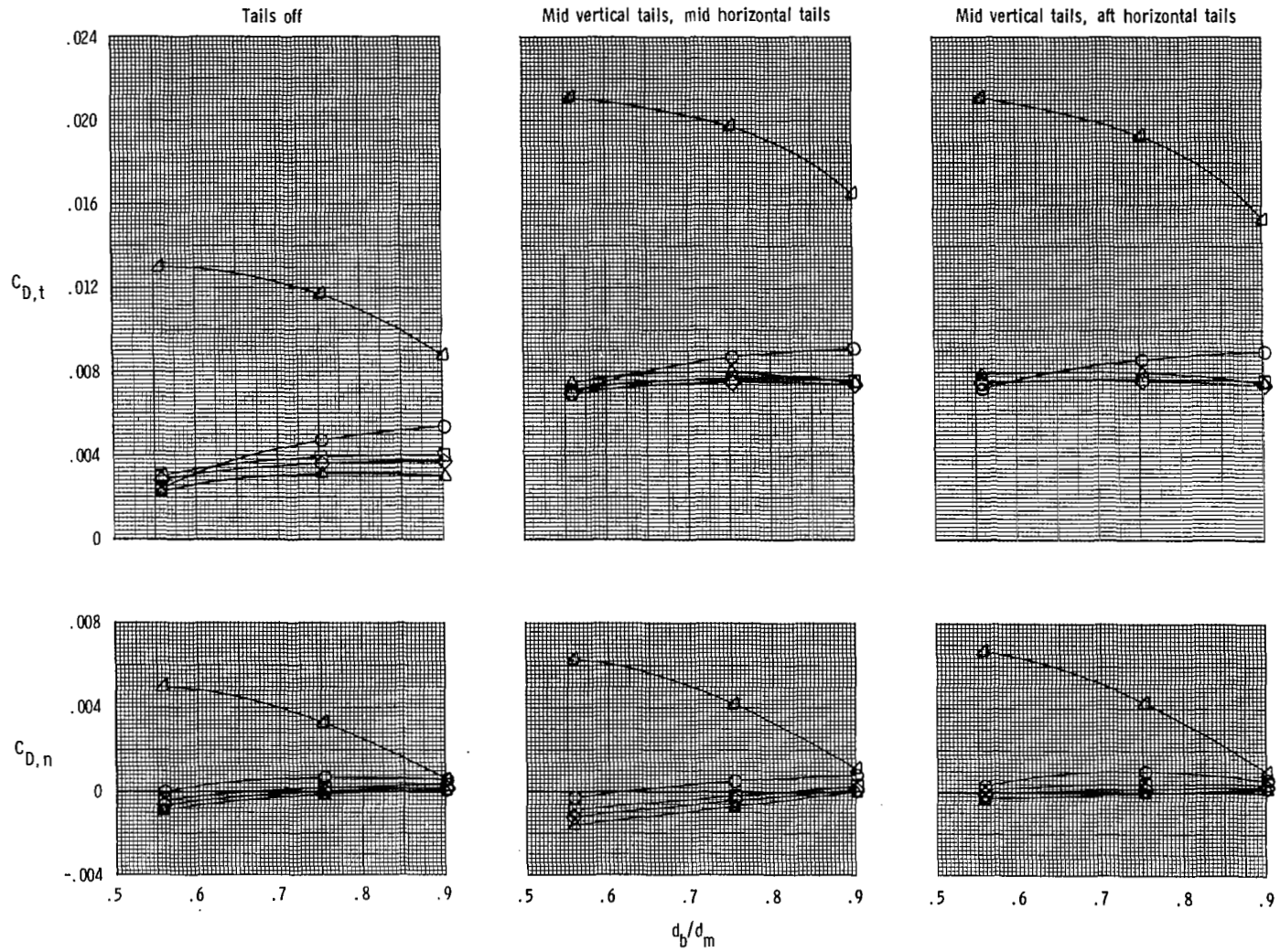
(a) Total and nozzle drag coefficients.

Figure 34.- Effect of nozzle closure on aft-end drag coefficient components for short nozzle.
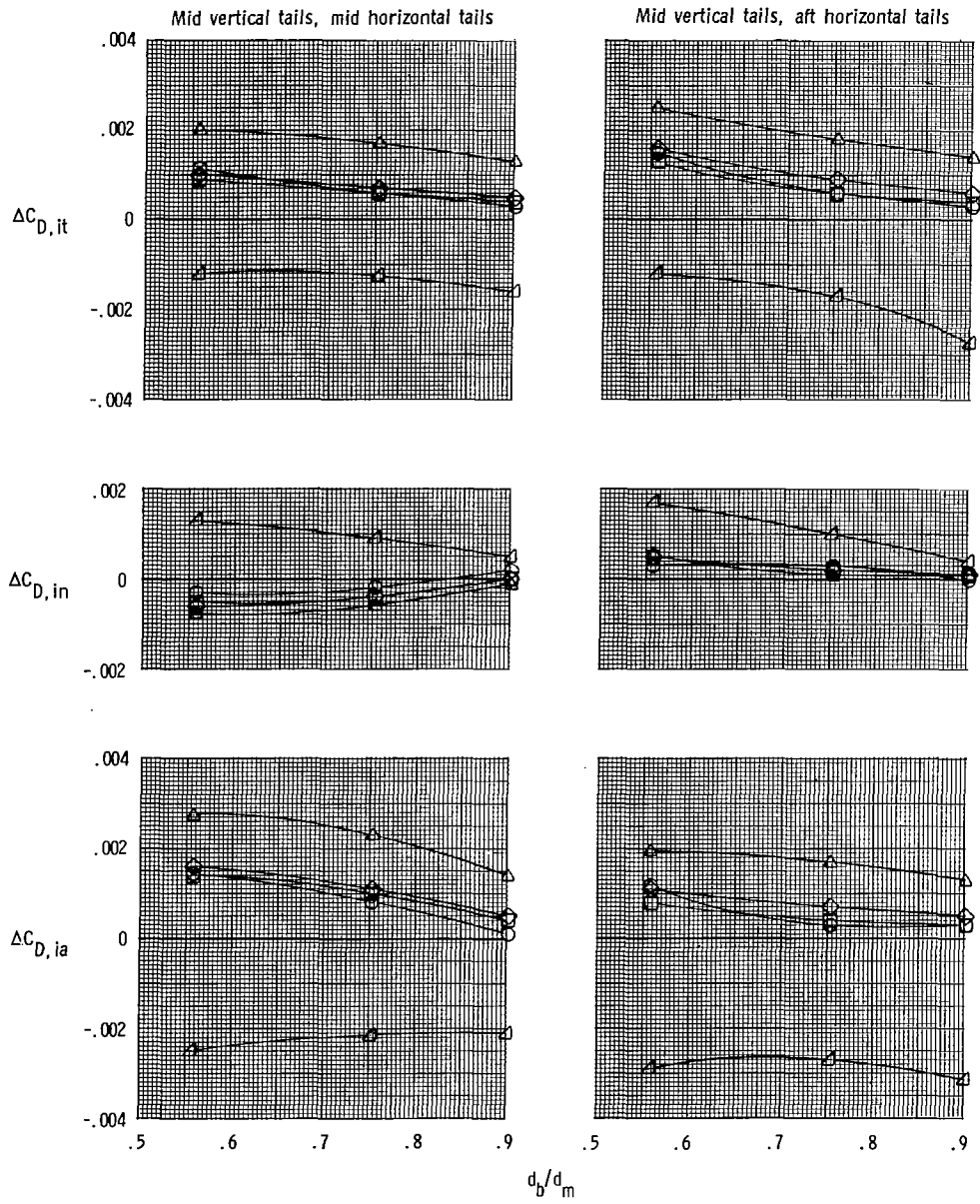
	M	NPR
○	0.50	3.20
□	0.80	3.85
◇	0.85	4.00
△	0.90	4.20
◁	1.20	6.00
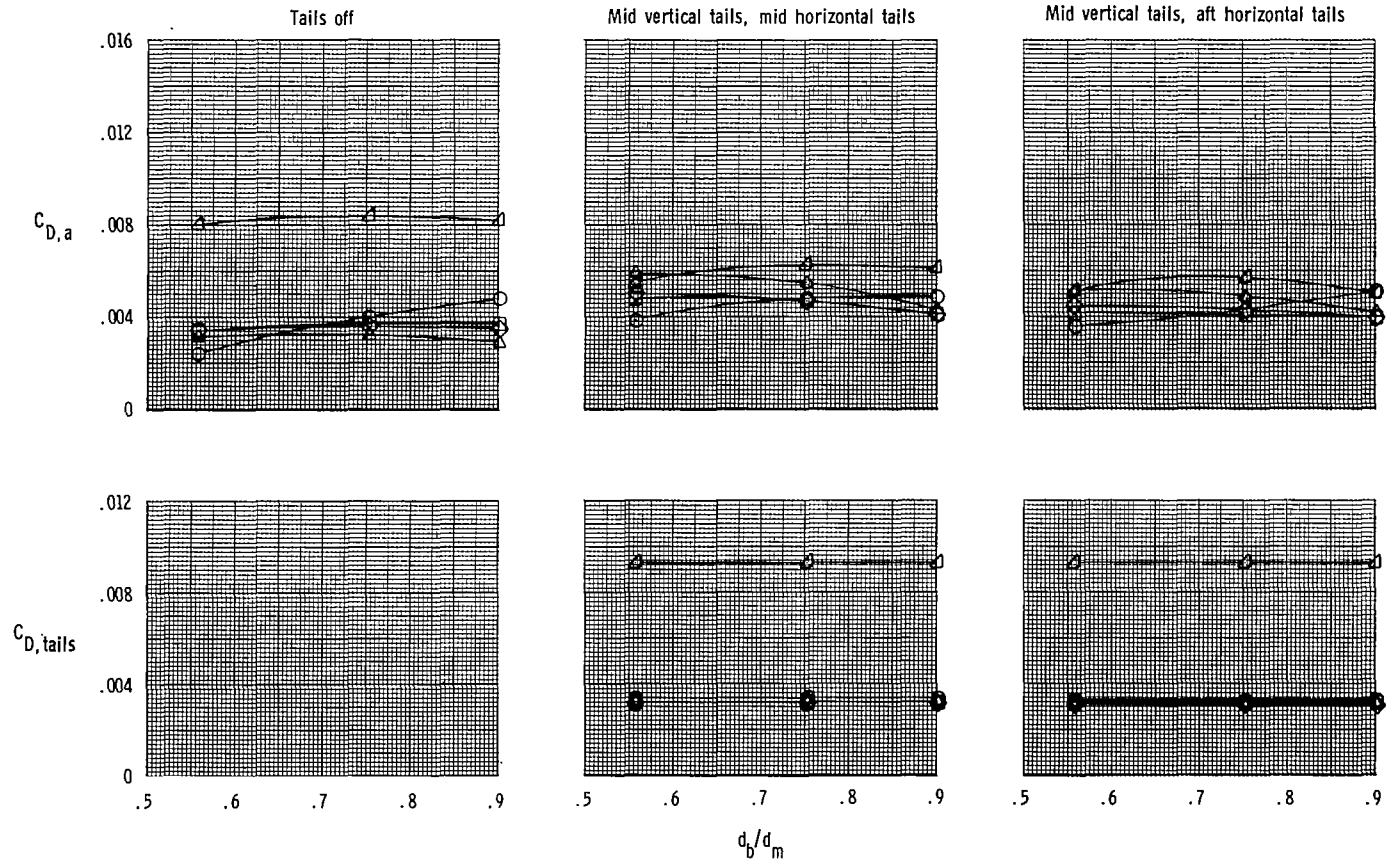
(b) Afterbody and tail drag coefficients.

Figure 34.- Continued.

(c) Empennage interference-drag coefficient increments.

Figure 34.- Concluded.

Figure legend:

	M	NPR
○	0.50	3.20
□	0.80	3.85
◇	0.85	4.00
△	0.90	4.20
◁	1.20	6.00

Tails off   Mid vertical tails, mid horizontal tails   Mid vertical tails, aft horizontal tails

$C_{D,t}$

$C_{D,n}$

d_b/d_m

(a) Total and nozzle drag coefficients.

Figure 35.- Effect of nozzle closure on aft-end drag coefficient components for long nozzle.

	M	NPR
○	0.50	3.20
□	0.80	3.85
◇	0.85	4.00
△	0.90	4.20
◁	1.20	6.00
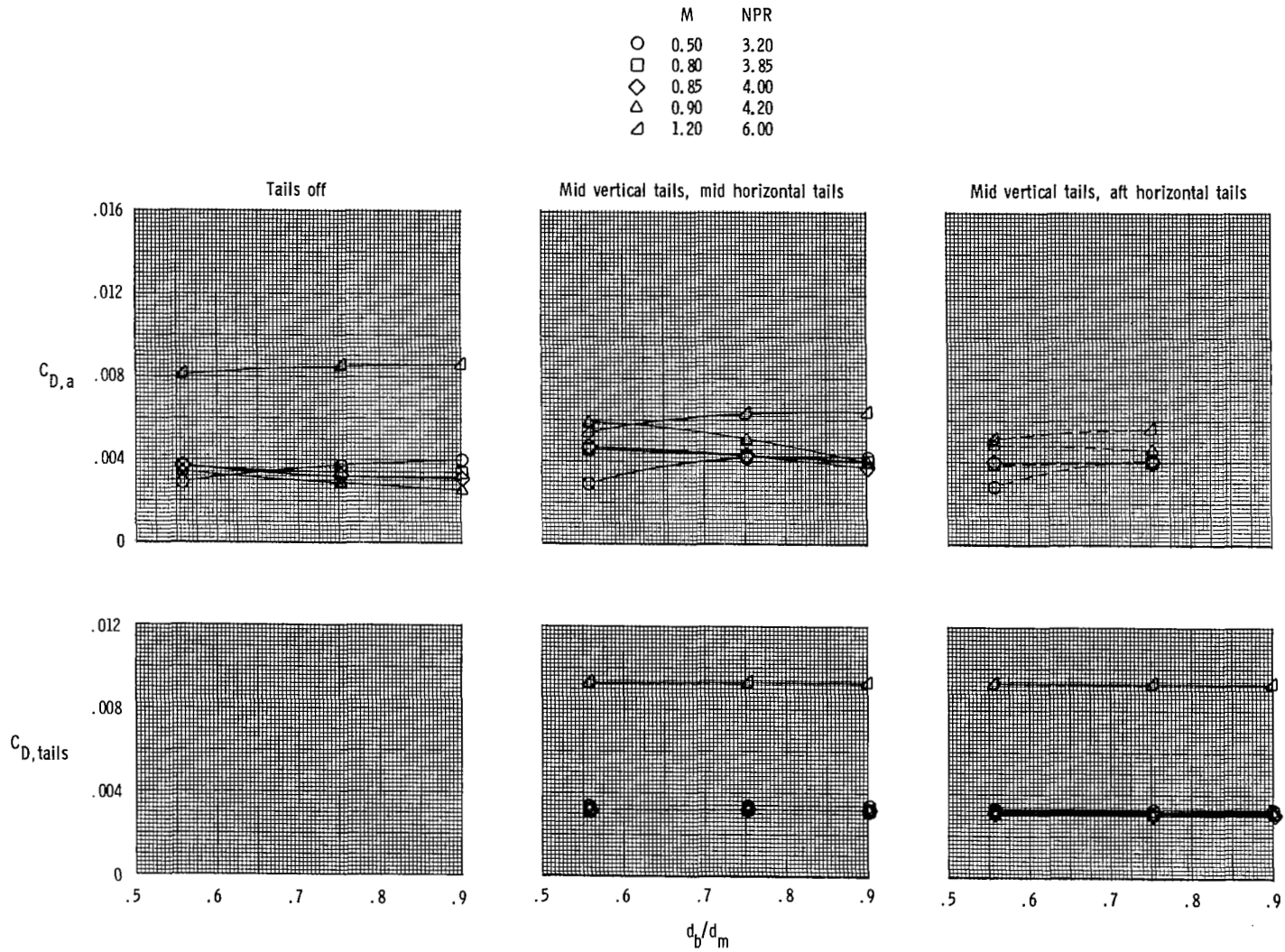
(b) Afterbody and tail drag coefficients.

Figure 35.- Continued.

	M	NPR
O	0.50	3.20
□	0.80	3.85
◇	0.85	4.00
△	0.90	4.20
◁	1.20	6.00

Mid vertical tails, mid horizontal tails   Mid vertical tails, aft horizontal tails

$\Delta C_{D,it}$

$\Delta C_{D,in}$

$\Delta C_{D,ia}$

d_b/d_m
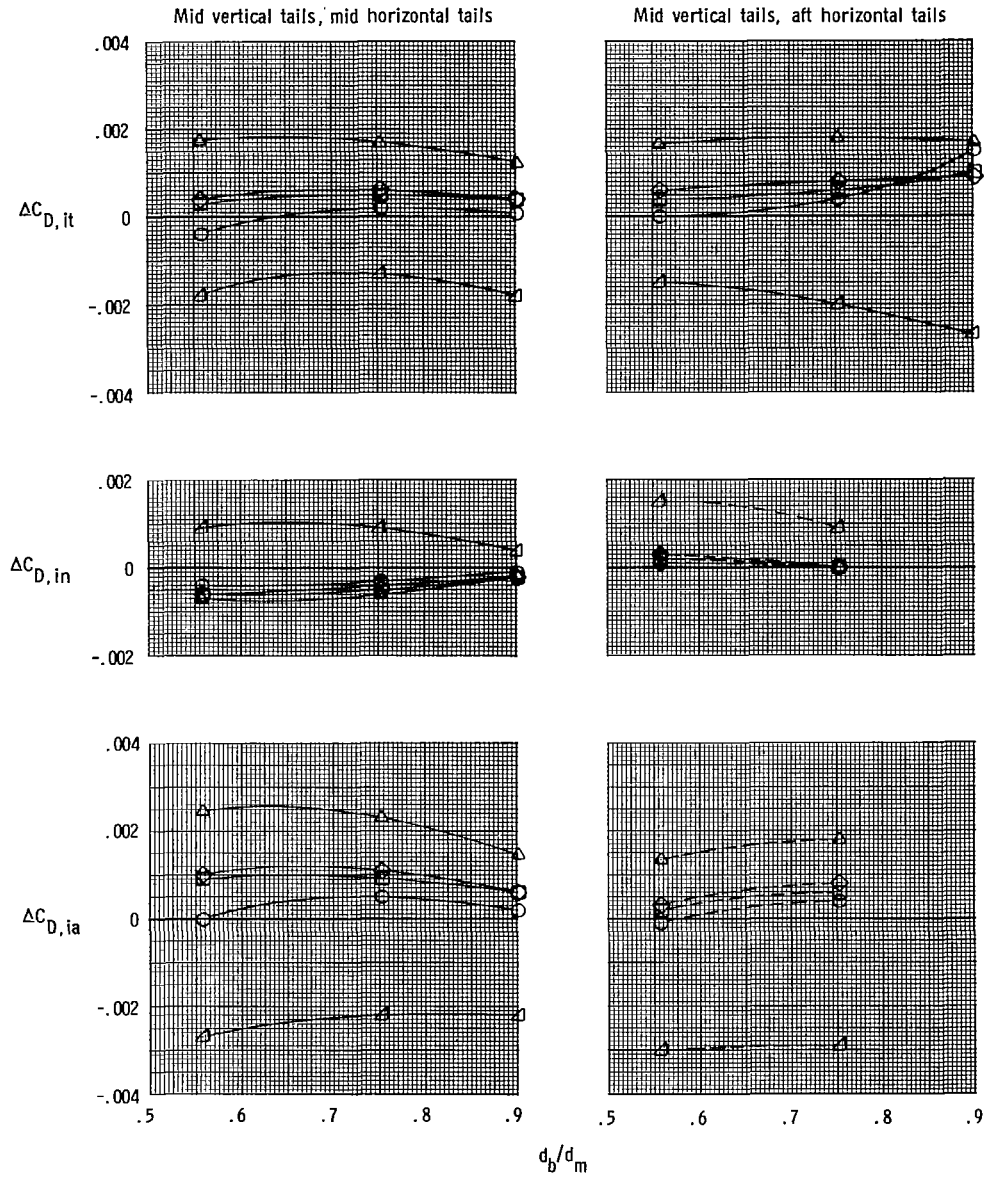
(c) Empennage interference-drag coefficient increments.

Figure 35.- Concluded.

- ────O──── Twin-engine installation
- ─ ─ ─ ─ Single-engine installation (ref. 3)
- ─────── ─ Isolated installation (conf. D-1.22-S of ref. 2)

M = 0.80

M = 0.90

$C_{D,n,one}$

M = 1.20

NPR
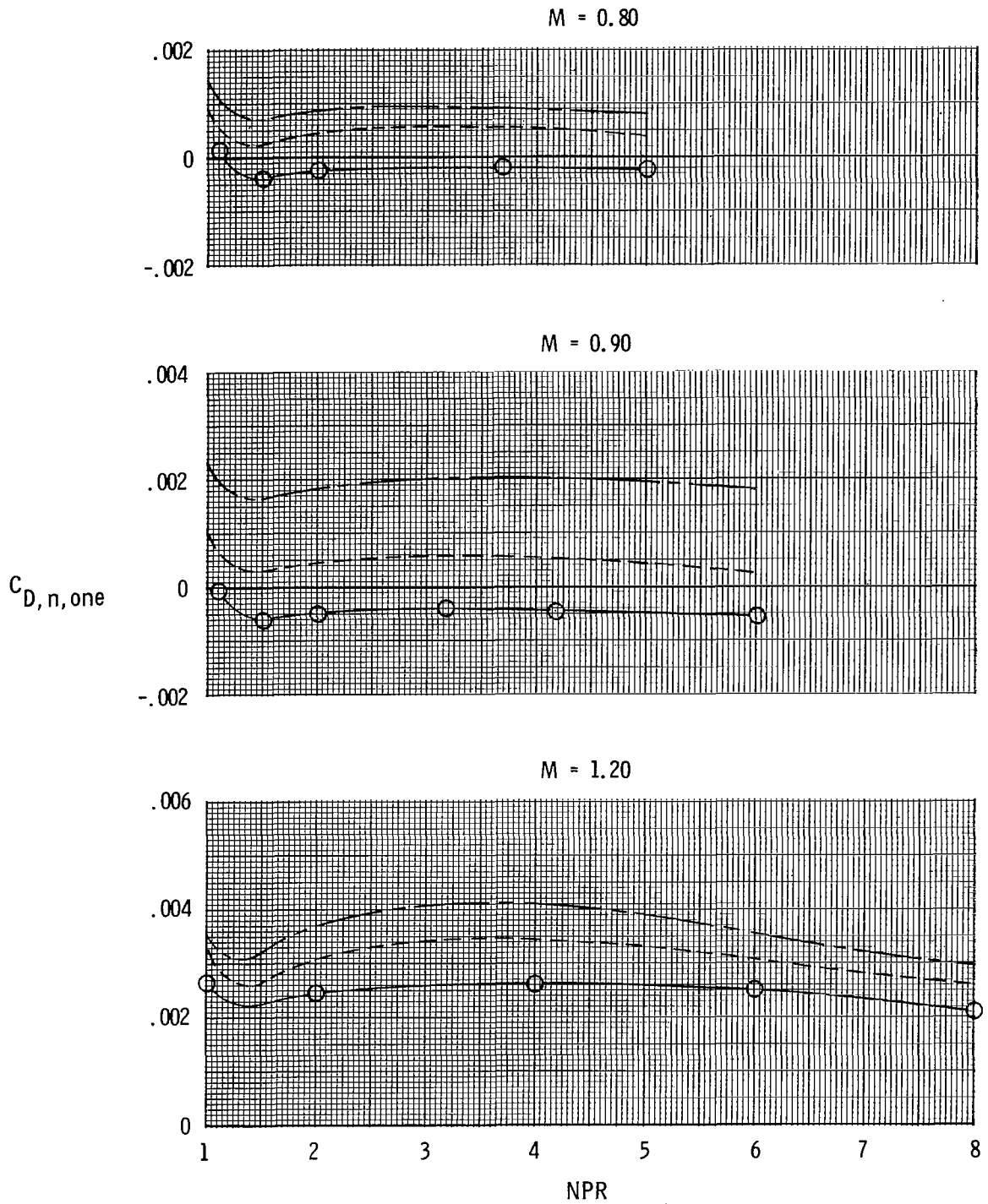
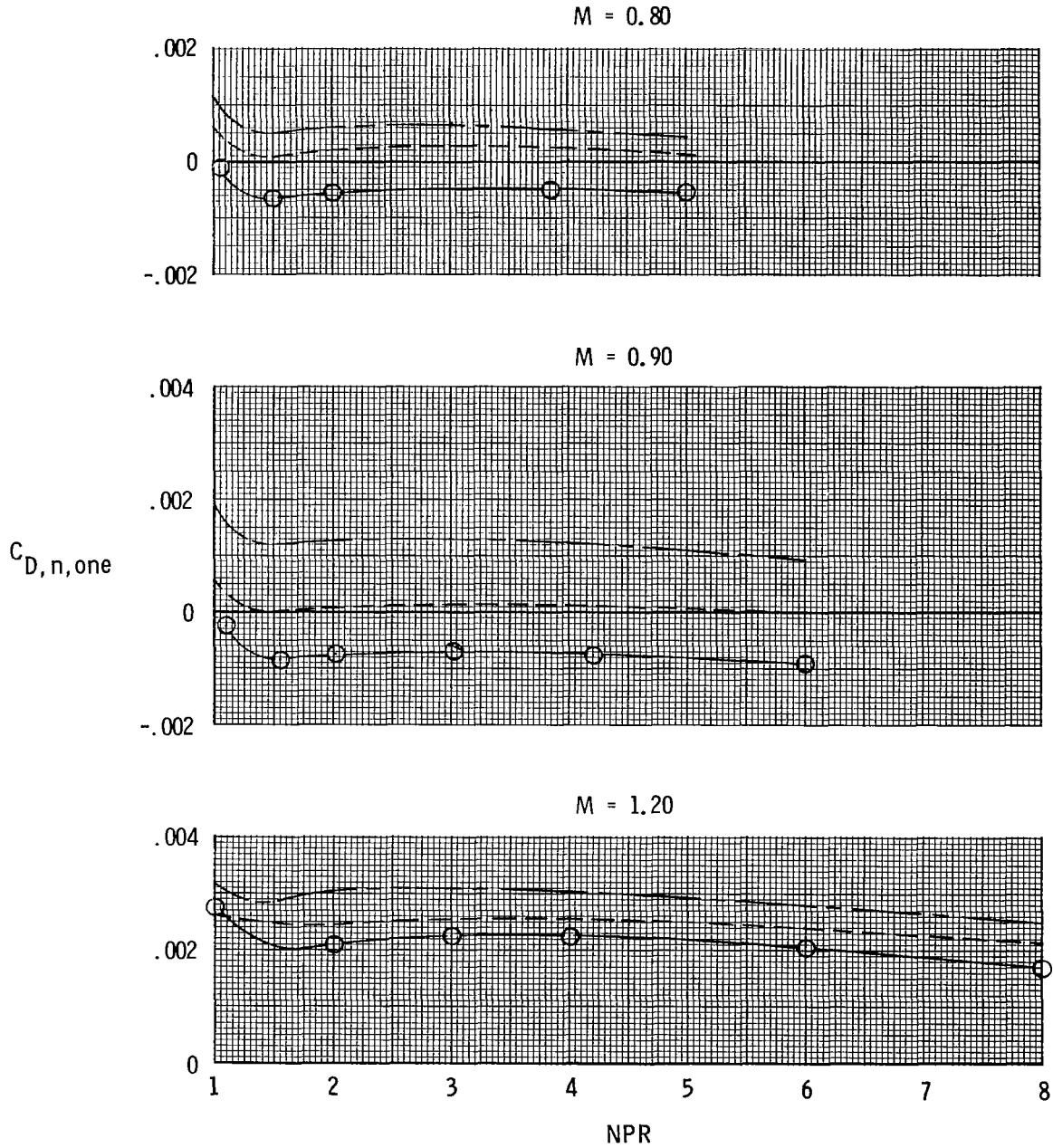(a) Short subsonic (A_e/A_t = 1.22) dry power nozzle.

Figure 36.- Comparison of installed and isolated nozzle drag coefficients.
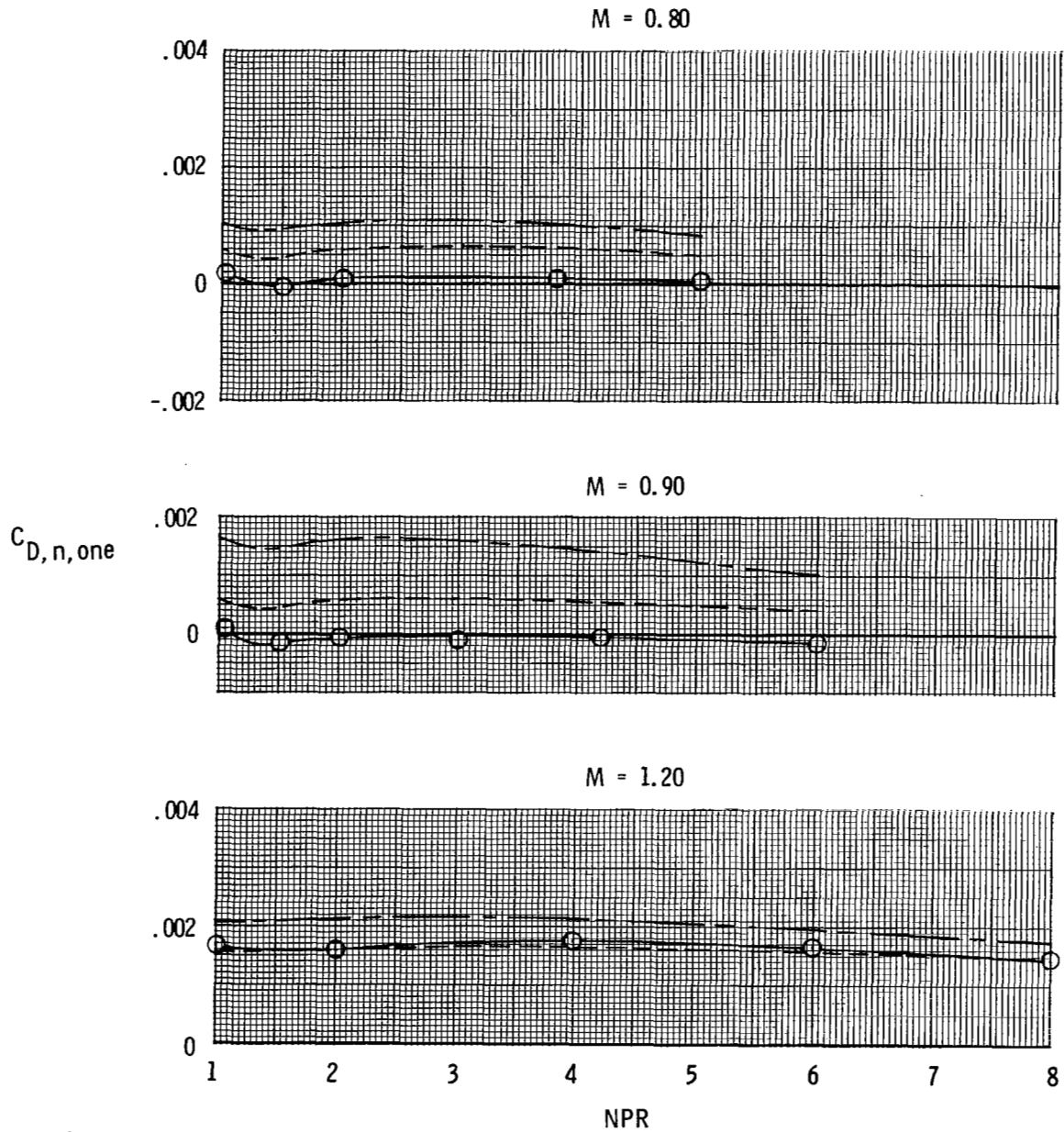Tails off; α = 0°.

Legend:
—○— Twin-engine installation
— — — — Single-engine installation (ref. 3)
————— — Isolated installation (conf. D-1.22-L of ref. 2)

M = 0.80

M = 0.90

$c_{D,n,one}$

M = 1.20

NPR

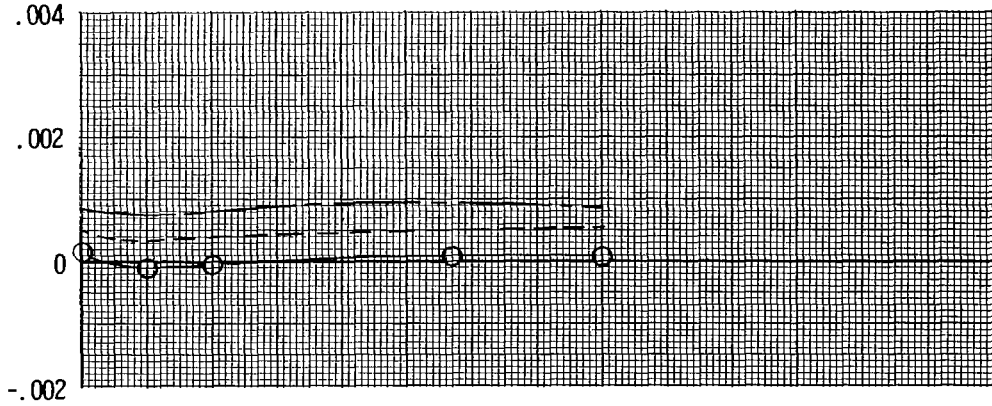(b) Long subsonic (A_e/A_t = 1.22) dry power nozzle.

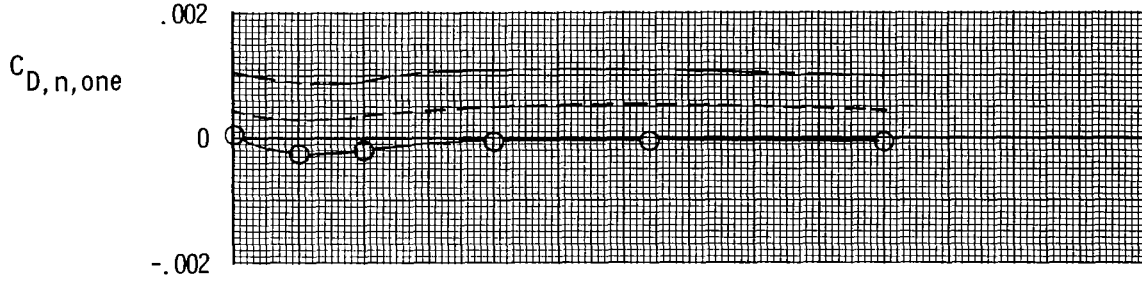Figure 36.- Continued.

(c) Short supersonic (A_e/A_t = 2.24) dry power nozzle.

Figure 36.- Continued.

Twin-engine installation
Single-engine installation (ref. 3)
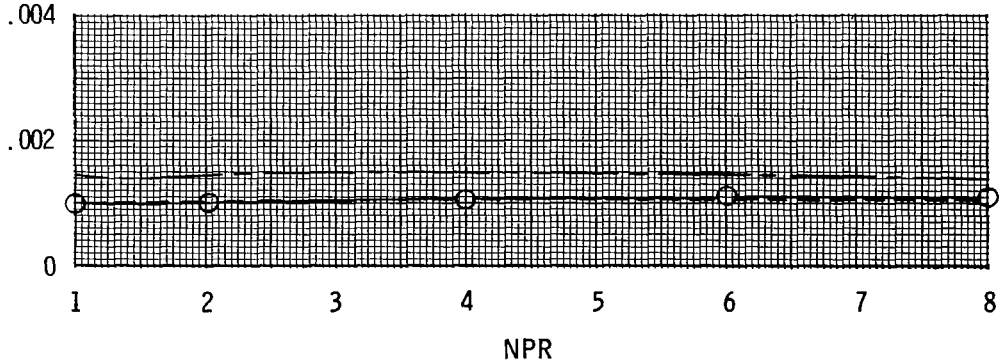Isolated installation (conf. D-2.24-L of ref. 2)

M = 0.80

M = 0.90

M = 1.20

$C_{D,n,one}$

NPR

(d) Long supersonic (A_e/A_t = 2.24) dry power nozzle.

Figure 36.- Continued.

Twin-engine installation

Single-engine installation (ref. 3)

Isolated installation (conf. P-2.24-S of ref. 2)

M = 0.80

M = 0.90

$C_{D,n,one}$
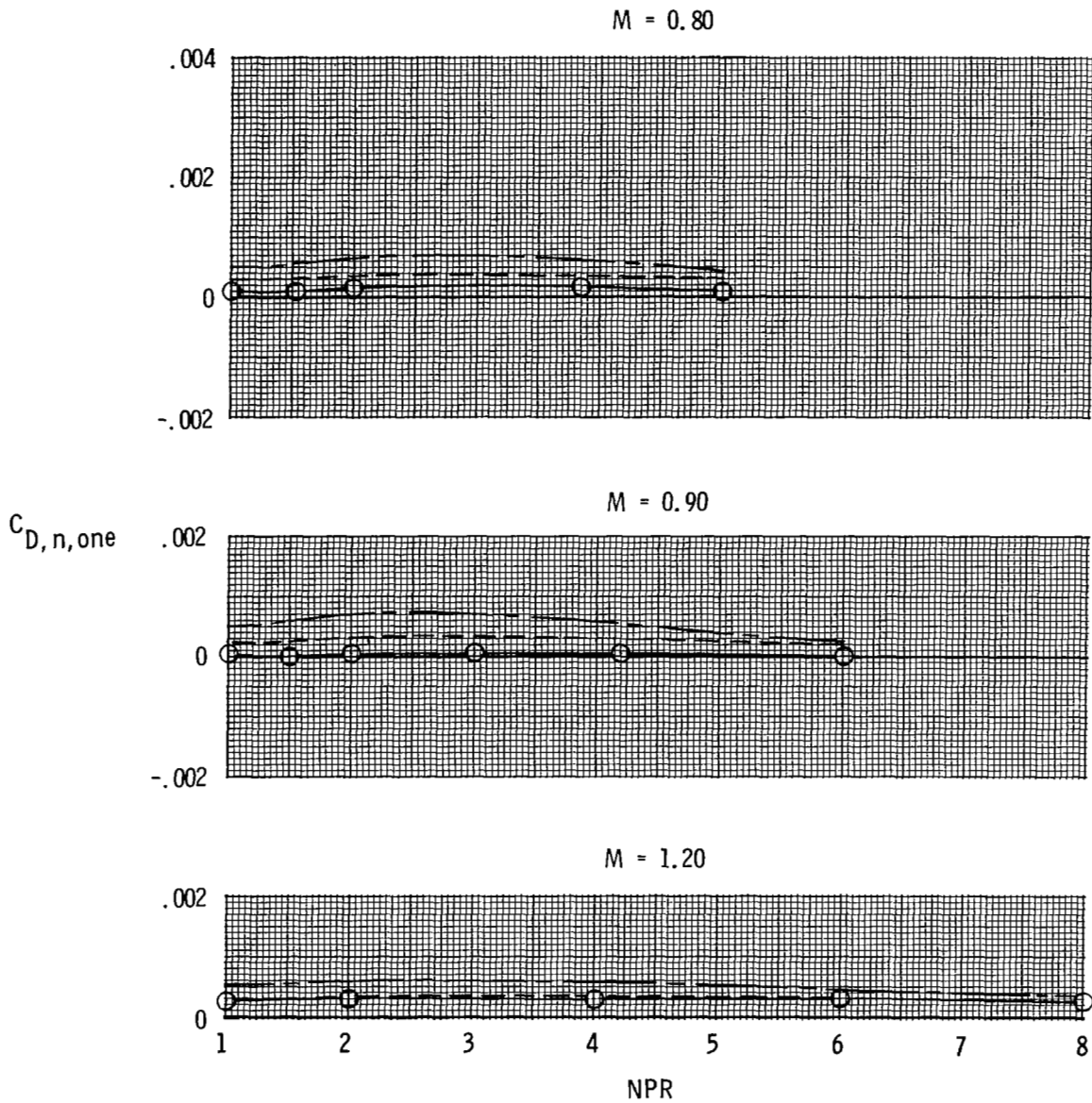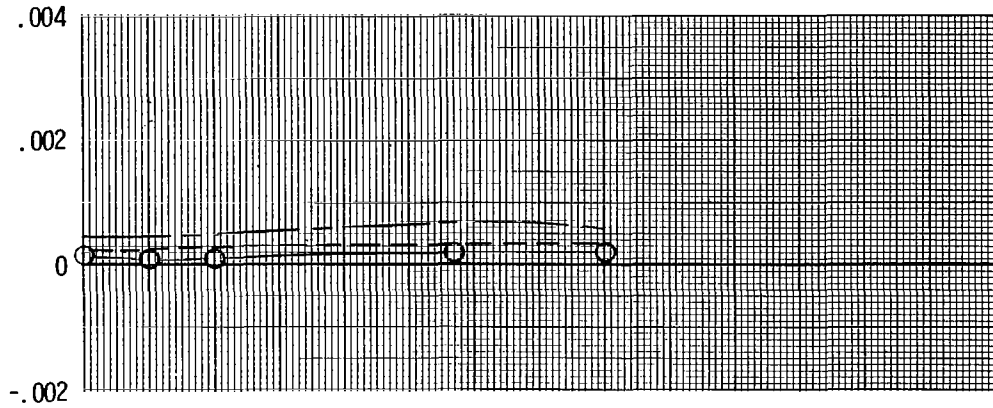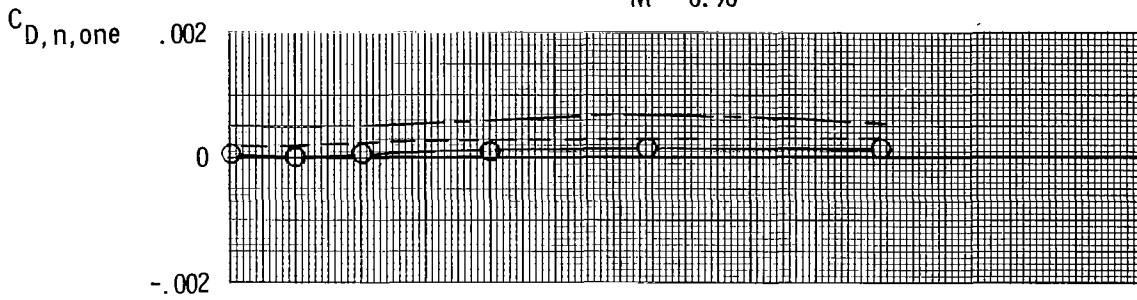
M = 1.20

NPR

(e) Short supersonic (A_e/A_t = 2.24) partial A/B power nozzle.

Figure 36.- Continued.
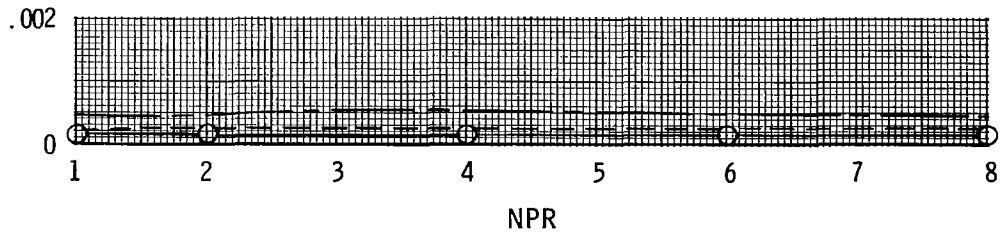
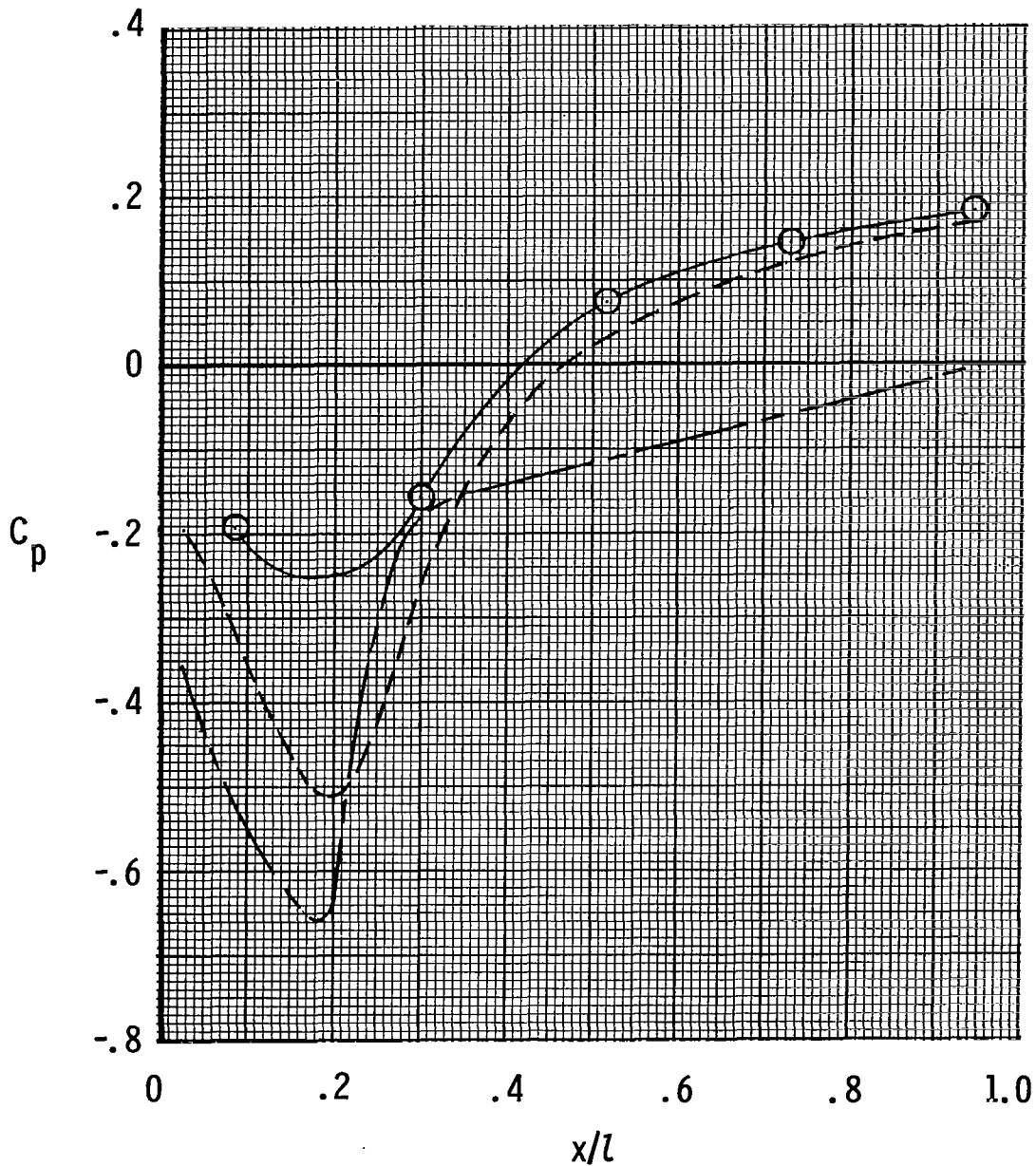(f) Long supersonic (A_e/A_t = 2.24) partial A/B power nozzle.

Figure 36.- Concluded.

Figure 37.- Comparison of installed and isolated nozzle static-pressure
distributions. Short subsonic dry power nozzle; tails off; M = 0.90;
NPR = 4.2; ϕ = 0°; α = 0°.

1. Report No. NASA TP-2205	2. Government Accession No.	3. Recipient's Catalog No.
4. Title and Subtitle INVESTIGATION OF INSTALLATION EFFECTS ON TWIN-ENGINE CONVERGENT-DIVERGENT NOZZLES		5. Report Date November 1983
		6. Performing Organization Code 505-43-23-01
7. Author(s) E. Ann Bare and Bobby L. Berrier		8. Performing Organization Report No. L-15609
		10. Work Unit No.
9. Performing Organization Name and Address NASA Langley Research Center Hampton, VA 23665		11. Contract or Grant No.
		13. Type of Report and Period Covered Technical Paper
12. Sponsoring Agency Name and Address National Aeronautics and Space Administration Washington, DC 20546		14. Sponsoring Agency Code

15. Supplementary Notes

16. Abstract

An investigation has been conducted in the Langley 16-Foot Transonic Tunnel to determine installation effects on convergent-divergent nozzles applicable to twin-engine reduced-power supersonic cruise aircraft. Tests were conducted at Mach numbers from 0.50 to 1.20, angles of attack from -5° to 9°, and at nozzle pressure ratios from jet off (1.0) to 8.0. The effects of empennage arrangement, nozzle length, and afterbody closure on total and component drag coefficients were investigated.

17. Key Words (Suggested by Author(s)) Twin engine Convergent-divergent nozzle Empennage interference Nozzle drag Afterbody drag	18. Distribution Statement Unclassified - Unlimited Subject Category 02

19. Security Classif. (of this report) Unclassified	20. Security Classif. (of this page) Unclassified	21. No. of Pages 189	22. Price A09

National Aeronautics and
Space Administration

Washington, D.C.
20546

Official Business
Penalty for Private Use, $300

U.S.MAIL

5   1 1U,A,   831031 S00903JS
DEPT OF THE AIR FORCE
AF WEAPONS LABORATORY
ATTN: TECHNICAL LIBRARY (SUL)
KIRTLAND AFB NM 87117

NASA

POSTMASTER: If Undeliverable (Section 158
Postal Manual) Do Not Return